Optical design of perovskite materials and solar cells

Miguel Anaya

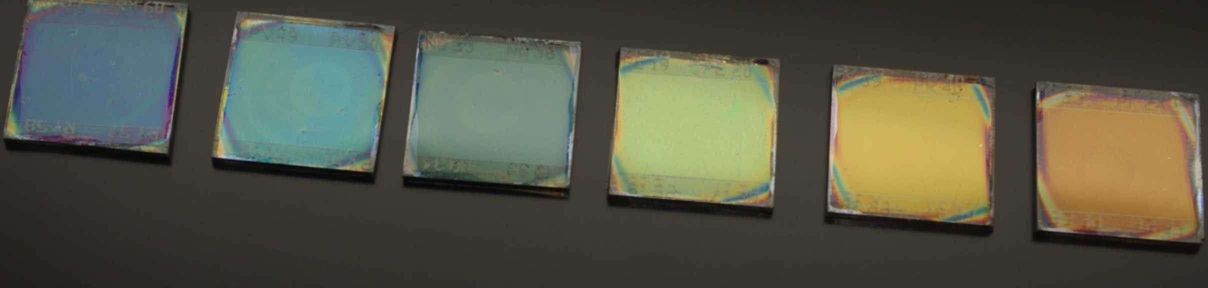

Optical design of perovskite materials and solar cells

Doctoral thesis presented by

Miguel Anaya Martín

Supervised by

Prof Dr Hernán Ruy Míguez García

Dr Mauricio Ernesto Calvo Roggiani

Inorganic Chemistry Department

Faculty of Chemistry

University of Seville

Multifunctional Optical Materials Group

Institute of Materials Science of Seville

Spanish National Research Council – University of Seville

MOM Multifunctional Optical Materials Group

CSIC
CONSEJO SUPERIOR DE INVESTIGACIONES CIENTÍFICAS

This PhD thesis was defended on the 17th of May 2018 at 11am in the auditorium of cicCartuja2 under the evaluation of:

Carmen Gallardo
Anders Hagfeldt
Monica Lira
Iván Mora
Annamaria Petrozza

receiving the distinction of *cum laude*.

In addition, Prof Anders Hagfeldt and Dr Sam Stranks, world experts in the research field of perovskites for optoelectronics, have reviewed this manuscript. Both of them consider the dissertation to have the quality necessary to be awarded with the *international doctorate* distinction.

The cover image is a digital camera picture of a selection of perovskite solar cells displaying colours on-demand through the use of different photonic structures.

ISBN: 978-84-09-03184-9

A mi familia

General considerations

Results concerning the investigation conducting to this PhD thesis and the evolution of the perovskite solar cell field itself have progressed contemporary. Although in the general introduction of this dissertation I will review the state-of-the-art of the field, at the beginning of my doctoral project there was no report on the optical design of this kind of materials and solar cells. Indeed, results presented along the different chapters can be considered seminal in the perovskite community.

Some results have been obtained in collaboration with laboratories around the world. I acknowledge the different individuals in the notes sections of each chapter, indicating at which grade they have contributed. In the discussion, I will present only materials, devices, and characterization techniques developed by myself. In Appendix D, I have included some micrographs taken in the laboratory of Prof Hagfeldt (EPFL) that are necessary for the argumentation in Chapter 3.

Similarly, I will explain in detail the characterization techniques and protocols that I have conceived and setup during my investigations. Commercial equipment is specified where necessary.

Table of contents

Chapter 1

General introduction

The as-known Paris Agreement reached in December 2015 at the conference of the United Nations Framework Convention on Climate Change (COP 21) indicates the will of the parties to reduce CO_2 emissions in order to hold the increase in the global average temperature to well below 2ºC above pre-industrial levels.[1] In a world in which 80% of global energy demand is generated from fossil fuels, any realistic path to attaining such a climate objective must have renewable energy at its core.[2] In this scenario, great efforts are going into the development of environmentally innocuous technologies that, moreover, will serve as solutions for the resource shortage produced by the historically unabated use of coal and oil, among others.

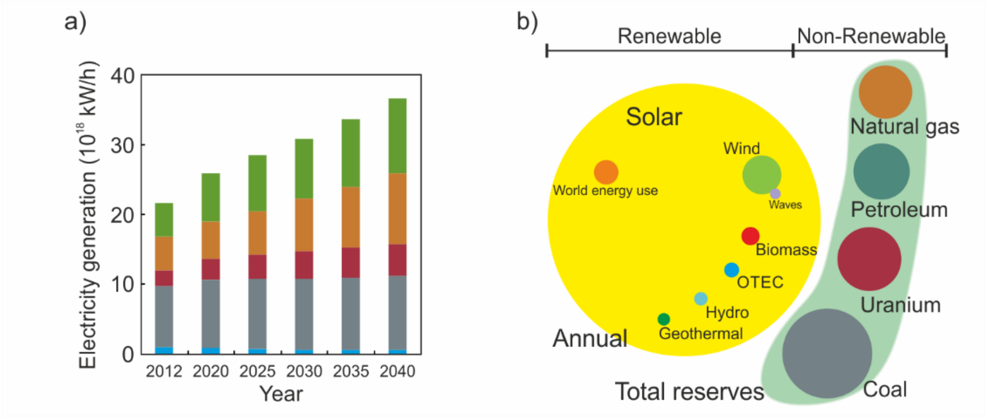

Figure 1.1. Global energy resources. a) World net electricity generation by energy source: renewables (green), natural gas (orange), nuclear (pink), coal (grey), and liquids (blue). b) Comparative of finite and renewable planetary energy reserves in 2015. Total recoverable reserves are shown for the finite resources. Yearly potential is shown for the renewables.

Predictions for the world net electricity generation, the most versatile energy vector, place renewables as the protagonists in the prospective investments proposed, enhancing their weight in the sector three times by 2040 (see Figure 1.1a).[2] Albeit hydro-, geothermal- or wind-based alternative energy technologies are of great importance, solar energy is particularly crucial in the purpose of slowing down climate change for two main reasons. On one hand, nowadays annual world electricity demand surpass 20 TW-yr, something that can be easily afforded by the 23,000 TW-yr per annum provided by the sun.[3] In this sense, solar energy surpasses by orders of magnitude the potential of all other renewable alternatives combined, as it is displayed in Figure 1.1b. Indeed, it represents the logical future energy supply future that will face the finite character of coal or gas reserves. On the other hand, if we consider economic viability, solar is further lowering the threshold of other sources. In particular, solar photovoltaic (PV) is taking centre stage due to a 60% cost reduction in the last five years up to $1200/kW. Contemporary to the writing process of this manuscript, PV is reaching the zone of grid parity with very promising estimates for further cost reductions.[2] Furthermore, solar panels represent a very functional tool for energy production, being easily installable in remote areas with minor environmental impact. Consequently, PV is attracting tremendous interest: markets are rapidly increasing their investments, and academia is devoting tireless efforts to study the mechanisms of solar to electrical energy conversion in order to push efficiency limits. As evidence thereof, we display in Figure 1.2 the evolution of the number of scientific articles related to PV published since 1980, which reflects a continuously growing interest towards the development of PV.[4]

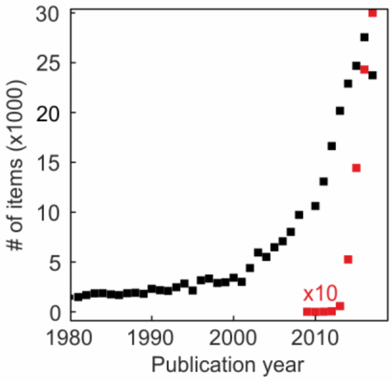

Figure 1.2. Analysis of PV-related literature. Results of the searches ‘photovoltaic or solar cell’ (black squares), and “perovskite solar cell” (red squares) in the Web of Science (February 20, 2018) for papers published between the 1st of January 1988 and the 1st of January of 2018.

Up to the present day, we have witnessed the appearance of three different solar technology generations. First generation solar cells, which are based on crystalline silicon (c-Si) wafers, were developed in the 1950s. They have a dominant position in market share due to the production chain optimization of c-Si occasioned by its massive use for electronics.[5] However, they require a lot of energy in terms of high temperature fabrication processes, which can eventually question its green character. Twenty years later, the second generation PV arose, comprising the as-known thin film solar cells that are based on amorphous Si (a-Si), CdTe or copper indium gallium selenide (CIGS) cells.[6-8] They represent a plausible way of costs reduction compared to the first generation since they have a lower material consumption, also being flexible and thus procurable by roll-to-roll techniques. Nevertheless, they still require large energy consumption due to the vacuum processes and high temperature treatments involved in their production. Finally, in the late 1980s, a series of technologies arrived on the scene and were classified as third generation PVs. These emerging PVs, whose predominant value is their versatility, include dye-sensitized solar cells (DSSCs),[9,10] organic solar cells,[11] quantum dot solar cells,[12] and perovskite solar cells.[13] In this context, solar cells based on metal halide (ABX_3) perovskites emerged in the last decade as a new technology that demonstrates both high performance and low cost. This type of cells are driving a revolution in PV, holding great promise for the generation of green energy at large scale. Indeed, perovskite solar cells (PSCs) represent more than 10% of all papers published in the field of PV, as noted in Figure 1.2.

1.1. Perovskite solar cells

PSCs have evolved from featuring a modest 3.81% in 2009 to over 20% in several works nowadays, which reveals PSCs as the most efficient emerging PV devices. Indeed, the World Economic Forum considered PSCs one of the top 10 emerging technologies in his Meta-Council in 2016.[14] This is due to the natural abundance of the precursors employed to synthesize perovskite absorbers, their low weight and, above all reasons, the swift rise in power conversion efficiency (PCE) demonstrated for this technology. All these facts make perovskite devices potential competitors of well-established technologies such as those based on silicon. In the next subsections, we will give an overview of the generalities involving ABX_3 perovskite materials and solar cells.

1.1.1. General properties of ABX_3 Materials

In the most simplified description, these perovskite materials are crystallised from halide salts to form crystals in the ABX_3 structure, where B is a hexa-coordinated metal (typically

Pb, but also Sn or Ge) occupying the centres of octahedra which share their halide-type (Cl, Br, I, or mixtures) corners X. A is a large cation (typically methylammonium, MA; CH_3NH_3, formamidinium, FA; $HC(NH_2)_2$, caesium Cs, rubidium Rb, or mixtures) that fill the voids left by every eight of those octahedral located at the corners of a classical cubic cell (see Figure 1.3). In this regard, methyl-ammonium lead triiodide ($CH_3NH_3PbI_3$ or $MAPbI_3$) served as starting point material for the field, representing the only composite with true interest in 2013-14 when this thesis started. Indeed, among perovskite materials developed for PV, $MAPbI_3$ is the most widely-employed compound.

$MAPbI_3$ has a tetragonal structure (space group *I4cm*) at 300K. It presents a phase transition at 160K to an orthorhombic structure (space group *Pnma*), and other at 327K to a cubic phase.[15-17] At room temperature, its absorption onset is placed at λ=780 nm (E=1.6 eV), harvesting photons very efficiently. Indeed, its absorption coefficient is high enough to absorb 100% of the photons provided by the sun with energies higher than the bandgap with only 1 μm of material.[18] This is a crucial feature for its implementation in thin film optoelectronic applications. Absorbed photons promote electrons to the conduction band, resulting in excitons (electron-hole pairs) that exhibit a binding energy 6 meV at room temperature. Such a low binding energy allow excitons to be separated in free carriers very quickly.[19] In addition, these carriers feature diffusion lengths in the order of microns, which lead to efficient charge extraction.[20] From a complementary point of view, perovskite materials show high radiative recombination rates that make them very interesting for light emission applications.[21-24] In consequence, the characterization and comprehension of the photophysical properties of the material can shed light into their formation and working mechanisms.

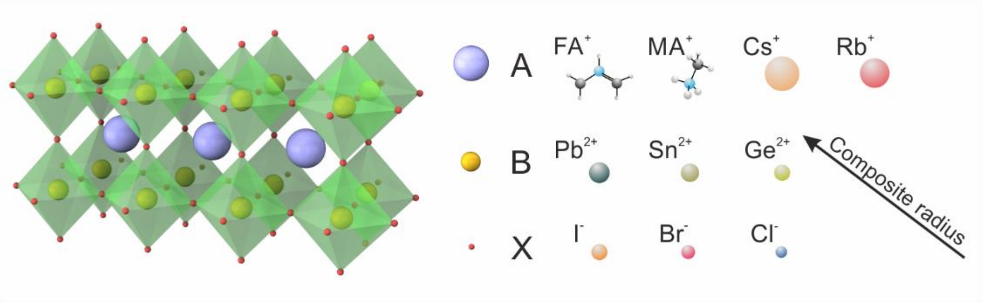

Figure 1.3. Perovskite structure. Schematic illustration of an ABX_3 perovskite and typical elements occupying the different positions in the structure.

1.1.2. Processing methods

ABX_3 perovskites precursors are earth-abundant and cost-effective. ABX_3 perovskite films are processed as thin layer using spin coating,[25-28] dip coating,[29] spray coating,[30] thermal co-evaporation,[31,32] chemical vapour deposition,[33] and vapour phase conversion,[34] among others. Solution processing methods amenable to mass production can be employed due to the large tolerance perovskites feature against structural defects in contrast to most semiconductors.[35] Among all preparation methods reported, spin coating dominates the scenario, being an anti-solvent approach that leads to better film quality and reproducibility.[27,28]

1.1.3. Architecture of perovskite solar cells and working principles

As we mentioned before, the versatility of the electro-optical properties and the ease of processing are the factors that explain the irruption of ABX_3 perovskites for PV applications. Figure 1.4 shows a scheme of the typical perovskite based device. The solar cell is composed of a glass substrate covered with a transparent conductive electrode, usually fluorine-doped tin oxide (FTO) or indium tin oxide (ITO). Then, an electron-selective layer (ESL), a perovskite film and a hole-selective layer (HSL) are sequentially deposited. Finally, a thermally evaporated metallic film is commonly used as a back contact to electrically close the cell. Perovskite material can be supported by a mesoporous scaffold that can be a photoconductor, such as n-TiO_2[26], or an insulator, such as Al_2O_3.[25] A selection of conventional materials employed in the fabrication of perovskite solar cells is presented in Figure 1.4. Since the complete device is a complex multilayer architecture, orthogonal solvents are employed to deposit the precursors of the different layers. With this, redissolving effects are avoided in materials predeposited from the different solvents. Although the described architecture is the dominant form and therefore considered standard in the perovskite community, there are examples in which the relative position of the ESL and HSL with respect to the perovskite layer are interchanged. This latter architecture is called inverted.[36]

As a historical note, ABX_3 perovskites were first employed as ‘sensitizers’ in a dye-sensitized solar cell (DSSC).[37,38] In this kind of systems, photogenerated electrons in perovskite are injected into the conduction band of the TiO_2, within which they are extracted to an external circuit though the front contact. A liquid redox electrolyte then regenerates from the perovskite material, closing the electrical circuit. The biggest jump in perovskite solar cell performance and stability was attained when the liquid electrolyte was substituted by a solid hole-conductor.[25,39]

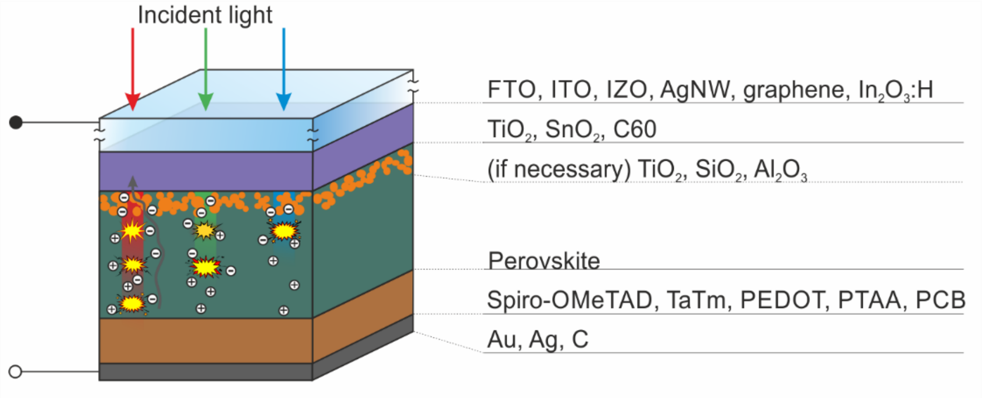

Figure 1.4. Perovskite solar cell. Illustration of the charge generation process in a perovskite solar cell and a catalogue of materials employed for the preparation of the different layers comprising the device.

In parallel to the evolution of the field, it is becoming apparent that the mesoporous TiO_2 layer possesses a scaffolding function in order to attain a seemly interfacial contact with the perovskite. Indeed, it was soon reported that perovskite acts as both electron and hole conductors, thus merging light absorption, and charge generation and transport in just one material.[25,31,40] With this in mind, the scaffold becomes thinner, if not removed entirely, and the device designs are converging on a planar architecture. Nevertheless, the use of a scaffold configuration provides the system with versatility, since it can be nanostructured in order to provide it with additional functionalities.

1.2. Optical design in photovoltaic devices

The efficiency of PV devices is intimately linked to the way in which the absorption of photons takes place in the system. Indeed, the larger the amount of photons harvested in the photoactive material the higher the potential efficiency of the solar cell. It can therefore be easily concluded that a route to boost the performance of solar cells relies on the optical design of their architecture.[41] In particular, this approach becomes crucial when dealing with third generation PV. Since their multilayered architecture, where the thicknesses of the components are on the order of the wavelength of the incoming light, gives rise to strong interference phenomena.

1.2.1. Optical properties of a monolayer

In Figure 1.5, we show a simplified scheme explaining how an incident light beam partially reflects and transmit when reaching a perovskite layer, giving rise to interference phenomena.

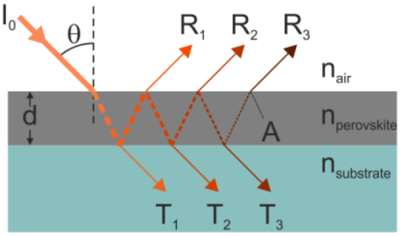

Figure 1.5. Scheme showing how light propagates in a stratified medium.

From this picture, it is easy to conclude that attaining a rational optical description of ABX_3 perovskites demands the extraction of their complex refractive index, something that was missed at the starting date of my PhD program.

The complex refractive index, *N*, is defined by

$$N = n - ik \tag{1.1}$$

where *n* and *k* are known as the real and the imaginary parts. *k* is also referred to as the extinction coefficient and it is related to the absorption coefficient, α, by

$$\alpha = \frac{4\pi\nu k}{c} \tag{1.2}$$

with ν being the frequency of the light and *c* the speed of light.

The set of parameters (*n*, *k*) of thin layers is usually determined by variable angle spectroscopic ellipsometry,[42] or by optical spectroscopy in the ultraviolet-visible-near infrared region of the spectrum.[43] The first technique detects changes in the polarization of the transmitted or reflected light that impinges over a thin layer. The second method requires the spectral measurement of reflectance and/or transmittance.

1.2.2. Optical properties of a multilayer

In general, one can describe thin film PV devices as a succession of layers one stacked on top of the other. One can optimize light harvesting by adjusting the composition of materials (refractive indexes) along the system and their layer thicknesses. This can be done in terms of a theoretical method based on the transfer matrix formalism, which has been successfully applied in the past for several types of layered solar cells.[44,45,46,47] In Figure 1.6, we display an example in which the mentioned model was employed to describe the optical behaviour of a thin DSSC. The method calculates the transmission and reflection of light of the complete device. Furthermore, it allows describing how the electric field intensity is spatially and spectrally distributed across the cell. This calculation delivers useful information, such as the fraction of the light absorbed in each component of the solar cell, providing insight into productive (which could generate photocurrent) and parasitic absorption (which cannot generate photocurrent).

In principle, if the composition of the materials comprising the device is fixed, one can find the combination of layer thicknesses that give rise to an optimized harvesting of incident light. This would be the result of the convenient interaction of light with the device, which is translated into: i) antireflective phenomena that augment the amount of harvestable light, ii) a decrease in the parasitic absorption due to light localization in the absorber, and iii) an increased optical path thanks to the utilization of the back layers as mirrors. It is worth mentioning that this kind of optical design is key to drive PSCs to greater heights in terms of efficiency.[18,48,49] The propagation of the radiation provided by the sun within the device will be highly sensitive to changes in the multilayered system since the total thickness of a PSC is around one micron. Thus, the realization of a fine optical design of the architecture of PSCs becomes fundamental.

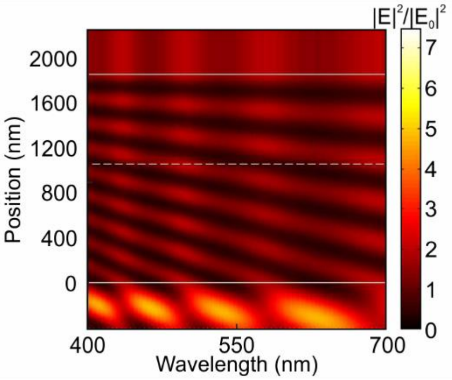

Figure 1.6. Spatial distribution of the electric field intensity along the cross section of a Dye Sensitized Solar Cell. Light enters the system from the bottom FTO glass substrate and passes through a 1 μm-thick TiO_2 electrode embedded with a dye, a 800 nm-thick electrolyte, and a seminfinite top FTO glass contact.

1.3. Integration of nanostructured optical components in photovoltaic devices

Additionally to the concepts discussed in the previous section, one can modify the optical response of a solar cell by means of the introduction of different elements in the device. On one hand, this is motivated by the aim to manage and deliver light to the absorbing layer in a highly efficient way.[50] On the other, there exists an urgency to make PV aesthetically attractive, hence allowing its integration in quotidian elements (backpacks or mobile phones) and buildings. The various strategies carried out by the PV community consist of the integration of metallic,[51] or dielectric nanostructures[52] (nanoparticles, textured surfaces, light scatters, etc.) in different solar cells. In the next paragraphs, we will give an overview of the different approaches that can be applied in PSCs. Although we will explain the concepts referring to different examples reported in the literature, we would like to note that they have been published during the development of this PhD project.

1.3.1. Dielectric particles

Sub-micron dielectric particles can induce an increase of the diffusive scattering and enhance the light absorbed in the active layer of a device.[53,54] This approach relies on the increase of the traveling distance of photons within the absorber as a result of randomizing the light path.[55] In Figure 1.7a, we propose different configurations that would serve to evaluate the potential of this strategy with the aim of improving light collection in PSCs. Initial attempts have already been employed in PSCs by embedding TiO_2 nanoparticles with typical size of ~160 nm in the mesoporous TiO_2 scaffold.[56] Although an absorption enhancement is observed in the $550<\lambda<750$ nm range, this research area remains almost unexplored and more exhaustive theoretical models and calculations are needed in order to discern the scatter effect on the near and far electromagnetic field.

1.3.2. Plasmonic particles

Noble metals can support surface plasmons, which are optically induced collective oscillations of free electrons occurring at the interface between a metal and a dielectric. These resonances result in the confinement of the electromagnetic field, mediating strong light-matter interactions in a nanoscale volume. For this reason, metallic nanoparticles have been proposed to enhance light absorption in the active layer of different solar cell technologies.[57-

[60] In particular, silver and gold nanoparticles have been successfully integrated in PSCs to enhance the PCE.[61,62] However, it has been recently demonstrated that neither near field nor scattering effects are responsible of the electrical improvements taking place in those systems.[63] In this regard, numerical simulations indicate that only particles featuring certain combinations of shapes and sizes will lead to plasmonic-promoted improvements in the solar devices (Figure 1.7b).[63]

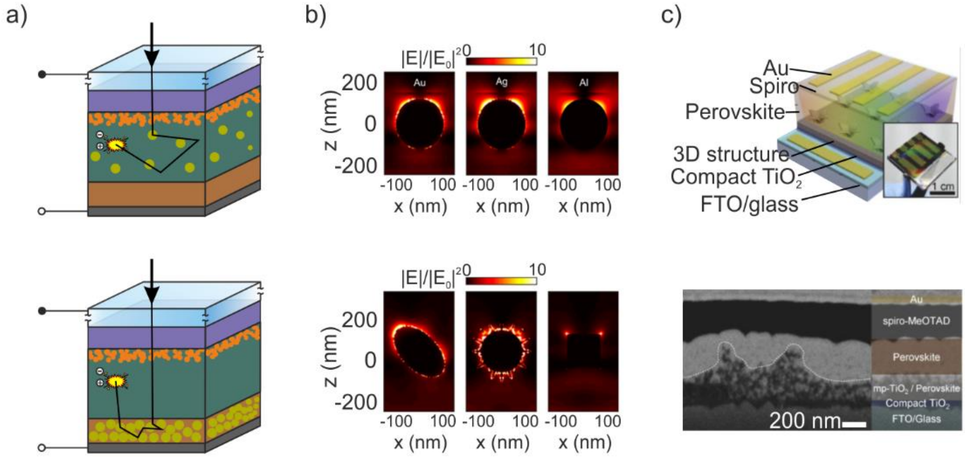

Figure 1.7. Integration of optical elements in perovskite solar cells. a) Schemes showing different strategies in which nanoparticles are employed as diffuse scattering layers. b) Spatial distribution of the normalized electric field intensity for a 300 nm $MAPbI_3$ film containing nanoparticles with different compositions (top panel) and shapes (bottom panel). c) Schematic illustration (top panel) and scanning electron microscopy image (bottom panel) of a 3D patterning-based perovskite solar cell. Reproduced with permission from references 63 and 69.

1.3.3. Diffraction gratings

An alternative approach to the use of randomly distributed particles as those afore mentioned involves the introduction of grating structures in the solar cell. This optical systems diffract incident light into highly oblique angles, increasing its optical path and the probability to be absorbed within the device. These periodic structures have been extensively employed in the past to enhance the efficiency of silicon solar cells and DSSCs.[64-67] More recently, this strategy has been introduced in the PSCs field by patterning the selective charge carrier layers. Different periodic motifs reproducing flowers[68] or moth eyes[69] were moulded on the ESL by soft-lithography techniques (see Figure 1.7c). In addition, Paetzold *et al.* demonstrated that the inner face of the frontal glass can be patterned,[70] and this motif is preserved even after the deposition of ITO and ESL. In all cases, PSCs that incorporate these motifs present an enhancement in photoconversion efficiencies that can be attributed to antireflection effects or diffraction of light.

1.3.4. Photonic crystals

In the framework of this PhD thesis, it is of special relevance the periodic combination of dielectric layers to cause a modification of the photonic response of the solar cell. In this context, solution processed dielectric nanostructures for light management have increasingly attracted interest due to their potential to improve the performance of optoelectronic devices.[71-73] Within the large family of dielectric optical materials, one-dimensional photonic crystals (PCs) are among the first and most basic designs that have been employed for this purpose.[74-80] A PC typically consists of two different compounds alternately stacked to produce a periodic modulation of the refractive index in one dimension of the space. As a consequence, strong interference phenomena occur and selective light reflection at certain wavelengths ranges is achieved.[81] Both the spectral position and the intensity of the reflectance peak (or Bragg peak) depend on the thickness, refractive index and number of slabs deposited. The larger the dielectric contrast between alternate layers is, the lower the number of slabs required in the stack to achieve a certain reflectance value and the wider the spectral width at which it occurs.

For PCs operating in the visible range, silicon oxide (SiO_2) and titanium oxide (TiO_2) are typical materials of choice due to the large refractive index difference they present. The Multifunctional Optical Materials group in which I have developed my work is internationally-recognized for the development of a porous PC based on SiO_2 and TiO_2 nanoparticles. The novelty of these nanostructures was their accessible interconnected mesoscopic porosity. This made them suitable for their integration in DSSCs as back reflectors in order to increase the optical path at selective wavelengths and enhancing the efficiency of the device (see Figure 1.8a).[82,] Moreover, they have been proposed with the aim of providing this third generation PV system with colour a la carte (see Figure 1.8b).[83]

An alternative approach to high refractive index contrast PCs is based on the alternation of layers with different porosity. This idea has been put into practice for the creation of PCs made of a variety of compositions,[84-88] including those in which a single compound is used.[89] In this regard, during my Master Thesis, we developed a conductive PC based on the periodic alternation of TiO_2 layers of different particle size. This allowed us to integrate it as a photonic electrode in the DSSC and show experimental evidence of resonant photocurrent generation by matching the electromagnetic field confinement with the sensitizer absorption band (see Figure 1.8c).[90]

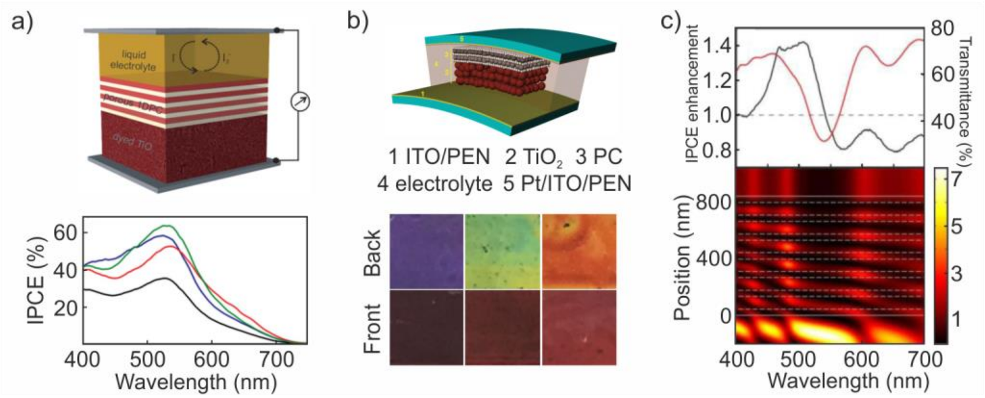

Figure 1.8. Photonic crystal based Dye Sensitized Solar Cells. a) Design of a DSC in which a highly porous 1DPC has been implemented. The multilayer structure acts as an efficient back reflector under front illumination conditions. Hence, it increases the probability of photocurrent generation at certain wavelength range as displayed in the bottom panel. b) Schematic of a PC integrated flexible DSSCs presenting a wide palette of colours as shown in the bottom panel. c) Spectral variation of the photocurrent enhancement factors (black solid lines) for a dye-sensitized conductive multilayer. Transmittance spectra are also included for the sake of comparison. In the bottom panel, the calculated spatial distribution of the electric field along a cross section of the structure is plotted as a function of the incident wavelength. Reproduced with permission from references 82, 83 and 90.

Although ABX_3 perovskite based solar cells harvest light excellently, the integration of PC is imperative to provide them with colours on demand while preserving their operational range. This would open the path to their application for building integration purposes, which would decrease to a great extent the fixed costs related to this technology. In this regard, the scaffold present in the standard perovskite-based device constitutes a great opportunity itself to be nanostructured as a PC.

1.3.5. Periodically ordered mesoporous structures

Another radically different approach to modify the optical response of a given semiconductor, such as ABX_3 perovskites, consists in the reduction of its dimensions to the quantum regime.[91] At this scale, the size of the compound is comparable to the wavelength of electron and holes, restricting their random movement to specific energy levels. This discreteness of the energy levels results in a widening of the bandgap of the semiconductor, which scales with the reduction of the nanocrystal.

This approach has been widely employed in the past for the demonstration of Cd- and Pb-sulphides and selenides with tuneable bandgaps dictated by the dimensions of the composite.

The principal approach to this end is colloidal synthesis, giving rise to either liquid or solid dispersions of nanocrystals. Although the former is more common for its ease of processing, reproducibility and scalability, its application in PV is subject to the subsequent deposition of the material as a high optical quality film.[92] In this regard, the latter strategy provides a two-in-one goal: quantum confinement effects intrinsically arise from thin films.

The methodology consists in the use of periodically ordered mesoporous structures as nanoreactors for the formation of semiconductor nanocrystals.[93] These materials are synthesized via the polymerization of inorganic species around a periodic organic template, which could be surfactant micelles or copolymers. After a thermal treatment under controlled humidity, a porous material is obtained whose pores are the perfect replica of the organic species. The ordered voids entail a very narrow distribution of their size. Thus, if the precursors of the semiconductor material fill the pores of the matrix, its formation is finely controlled in a deterministic way.

The application of this kind of materials to the synthesis of ABX_3 perovskites would provide the possibility of blue shifting their bandgap on demand without modifying their chemical composition.

1.4. Motivation and objectives

As we have been introducing throughout this text, in order to achieve a better solar cell performance in terms of either efficiency or aesthetic, the precise cell designs based on the in-depth understanding of the optical properties of the materials are crucial. In this regard, by September 2014, when the research contributing to this doctorate began, there was an evident lack in knowledge of the optics surrounding ABX_3 perovskite materials. In part, this was a consequence of the novelty of the field (see Figure 1.2), but it also stemmed from the inherent uniqueness of the optoelectronic properties of this family of perovskites. Indeed, it became imperative to re-establish the standard concepts, simulation tools and characterization techniques in order to satisfy what was required to optically describe and design perovskite-based materials and devices.

Hence, the general objective of this dissertation is to provide the community with the necessary tools that allow the discernment of the optical properties of ABX_3 perovskites in order to design devices of superior performance. A series of photophysical characterization techniques are applied with the aim of explaining the perovskite formation and stability under different conditions. This comprehension of the intrinsic properties of the compounds serves as a starting point for developing optical models to extract their refractive indices. Further, the optical model is employed to describe and optimize perovskite-based devices with different architectures. Finally, we give yet another turn of the screw to the complexity of the optics related to PSCs. This revolves on the combination of perovskites and porous films in order to modify the optical behaviour of the perovskite on demand. In this regard, we will present new routes that ensure fine control over the porosity of photonic crystals and scaffolds acting as host materials for the perovskite formation. This will result in perovskite showing structural colour and strong quantum confinement effects, respectively.

1.5. Overview

This thesis, entitled *Optical Design of Perovskite Materials and Solar Cells*, is the result of more than three years of research, comprising from September 2014 to January 2018. The investigations herein presented have been performed mainly at the Institute of Materials Science of Seville under the supervision of Prof Hernán Míguez and Dr Mauricio E. Calvo. I acknowledge La Caixa Foundation for its financial support. I am also grateful for the facilities provided by the Multifunctional Optical Materials Group under the framework of different projects, especially POLIGHT (ERC-Consolidator Grant) and MAT2014 54852-R (Spanish Ministry of Economy and Competitiveness). I have visited several laboratories abroad and contributed with oral presentations in 15 international conferences for the correct development and dissemination of my investigations. In this regard, I thank the travel funding provided by the International Society for Optics and Photonics and the University of Seville's Research Program.

Results are discussed in the next five chapters, which are followed by some notes. These notes describe the theoretical basis of the optical models and present an experimental result which is necessary to understand the dissertation but has not been conducted by me.

In Chapter 2, we establish the foundation of the basic characterization and synthesis protocols that we will employ within this thesis. We analyse the optical behaviour of $MAPbI_3$ perovskite films during their synthesis and when exposed to different atmospheres. Further, we present a protocol to extract their optical constants.

In Chapter 3, we model the optical behaviour of single-junction perovskite solar cells of different architectures. This allows us to describe how the electric field is distributed across the device and discern between efficient and parasitic absorption.

In Chapter 4, we discuss the possibilities that an optical model opens to improve the efficiency of perovskite-based solar cells within the framework of the Shockley-Queisser theory. Firstly, we present perovskites in which Pb is gradually substituted by Sn as optimum materials for single-junction solar devices. Afterwards, we propose perovskite based tandem solar cells, providing a roadmap towards their optical optimization.

In Chapter 5, we employ photonic crystals as scaffolds in perovskite solar cells in order to provide them with tuneable structural colour. This goal is experimentally achievable by means of a new technique to control the porosity of each stack constituting the periodic multilayers on demand.

In Chapter 6, we develop a synthetic route to obtain stabilized $MAPbI_3$ nanocrystals embedded in thin metal oxide films that display well-defined and adjustable quantum confinement effects over a wide range of 0.34 eV. This objective is attained by the fabrication of TiO_2 and SiO_2 layers performing a 3D network of size-adjustable pores.

1.6. References

1 Paris Agreement, 21st Conference of the Parties, European Commission **2015**.

2 World energy outlook, *International Energy Agency* **2016**.

3 Perez, R.; Perez, M. A fundamental look at supply side energy reserves for the planet. *The IEA SHC Solar Update* **2015**, *62*, 4–6.

4 Result of the search ‘Photovoltaic or solar cell’ and “perovskite solar cell” in the Web of Science, February 20, **2018**.

5 Green, M. A. The path to 25% silicon solar cell efficiency: history of silicon cell evolution. *Prog. Photovolt: Res. Appl.* **2009**, *17*, 183–189.

6 Stuckelbergera, M.; Birona, R.; Wyrscha, N.; Hauga, F.-J.; Ballif, C. Review: Progress in solar cells from hydrogenated amorphous silicon. *Renew. Sust. Energ. Rev.* **2017**, *76*, 1497-1523.

7 Green, M. A. Thin-film solar cells: review of materials, technologies and commercial status. *J. Mater. Sci.: Mater. Electron*. **2007**, *18*, 15-19.

8 Contreras, M. A.; Egaas, B.; Ramanathan, K.; Hilter, J.; Swartzlander, F. H.; Noufi, R. Progress toward 20% efficiency in Cu(In,Ga)Se_2 polycrystalline thin-film solar cells. *Prog. Photovolt: Res. Appl.* **1999**, *7*, 311–316.

9 Hagfeldt, A.; Boschloo, G.; Sun, L.; Kloo, L.; Pettersson, H. Dye-sensitized solar cells. *Chem. Rev.* **2010**, *110*, 6595-6663.

10 Gong, J.; Sumathy, K.; Qiao, Q.; Zhou, Z. Review on dye-sensitized solar cells (DSSCs): advanced techniques and research trends. *Renew. Sust. Energ. Rev.* **2017**, *68*, 234-246.

11 Lu, L.; Zheng, T.; Wu, Q.; Schneider, A. M.; Zhao, D.; Yu, L. Recent Advances in Bulk Heterojunction Polymer Solar Cells. *Chem. Rev.* **2015**, *115*, 12666-12731.

12 Kamat, P.V. Quantum dot solar cells. Semiconductor nanocrystals as light harvesters. *J. Phys. Chem. C* **2008**, *112*, 18737-18753.

13 Green, M. A.; Ho-Baillie, A.; Snaith, H. J. The emergence of perovskite solar cells. *Nat. Photon.* **2014**, *8*, 506-514.

14 Top 10 Emerging Technologies of 2016. *World Economic Forum* **2016**.

15 Onoda-Yamamuro, N.; Matsuo, T.; Suga, H. Dielectric study of $CH_3NH_3PbX_3$ (X = Cl, Br, I). *J. Phys. Chem. Solids.* **1992**, *53*, 935–939.

16 Stoumpos, C. C.; Malliakas, C. D.; Kanatzidis, M. G. Organic tin and lead iodide perovskites with organic cations: unique semiconductors, with phase transitions and near-infrared photoluminescent properties. *Inorg. Chem.* **2013**, *52*, 9019–9038.

17 Baikie, T.; Fang, Y.; Kadro, J. M.; Schreyer, M.; Wei, F.; Mhaisalkar, S. G.; Graetzel, M.; White, T. J. Synthesis and crystal chemistry of the hybrid perovskite $(CH_3NH_3)PbI_3$ for solid-state sensitised solar cell applications. *J. Mater. Chem. A.* **2013**, *1*, 5628–5641.

18 Anaya, M.; Lozano, G.; Calvo, M. E.; Zhang, W.; Johnston, M. B.; Snaith, H. J. Optical description of mesostructured organic-inorganic halide perovskite solar cells. *J. Phys. Chem. Lett.* **2015**, *6*, 48–53.

19 Miyata, A.; Mitioglu, A.; Plochocka, P.; Portugall, O.; Wang, J. T.-W.; Stranks, S. D.; Snaith, H. J.; Nicholas, R. J. Direct measurement of the exciton binding energy and effective masses for charge carriers in organic-inorganic tri-halide perovskites. *Nat. Phys.* **2015**, *11*, 582–587.

20 Stranks, S. D.; Eperon, G. E.; Grancini, G.; Menelaou, C.; Alcocer, M. J. P.; Leijtens, T.; Herz, L. M.; Petrozza, A.; Snaith, H. J. Electron-hole diffusion lengths exceeding Micrometer in an Organometal Trihalide Perovskite Absorber. *Science* **2014**, *342*, 341–344.

21 Deschler, F.; Price, M.; Pathak, S.; Klintberg, L. E.; Jarausch, D.; Higler, R.; Hu, S.; Leijtens, T.; Stranks, S. D.; Snaith, H. J.; Atatüre, H. J.; Philips, R. T.; Friends, R. H. High photoluminescence efficiency and optically pumped lasing in solution-processed mixed halide perovskite semiconductors. *J. Phys. Chem. Lett.* **2015**, *5*, 1421–1426.

22 Xing, G.; Mathews, N.; Lim, S. S.; Yantara, N.; Liu, X.; Sabba, D.; Grätzel, M.; Mhaisalkar, S.; Sum, T. C. Low-temperature solution-processed wavelength-tunable perovskites for lasing. *Nat. Mater.* **2014** *13*, 476–480.

23 Tan, Z.-K.; Moghaddam, R. S.; Lai, M. L.; Docampo, P.; Higler, R.; Deschler, F.; Price, M.; Sadhanala, A.; Pazos, L. M.; Credgington, D.; Hanusch, F.; Bein, T.; Snaith, H. J.;

Friend, R. H. Bright light-emitting diodes based on organometal halide perovskite. *Nat. Nanotechnol.* **2014**, *9*, 687–692.

24 Cho, H.; Jeong, S.; Park, M.; Kim, Y.; Wolf, C.; Lee, C.; Heo, J. H.; Sadhanala, A.; Myoung, N.; Yoo, S.; Im, S. H.; Friend, R. H.; Lee, T.-W. Overcoming the electroluminescence efficiency limitations of perovskite light-emitting diodes. *Science* **2015**, *350*, 1222–1225.

25 Lee, M. M.; Teuscher, J.; Miyasaka, T.; Murakami, T. N.; Snaith, H. J. Efficient hybrid solar cells based on meso-superstructured organometal halide perovskites. *Science* **2012**, *338*, 643–647.

26 Burschka, J.; Pellet, N.; Moon, S-J.; Humphry-Baker, R.; Gao, P.; Nazeeruddin, M. K.; Grätzel, M. Sequential deposition as a route to high-performance perovskite-sensitized solar cells. *Nature* **2013**, *499*, 316–320.

27 Xiao, M.; Huang, F.; Huang, W.; Dkhissi, Y.; Zhu, Y.; Etheridge, J.; Gray-Weale, A.; Bach, U.; Cheng, Y. B.; Spiccia, L. A fast deposition-crystallization procedure for highly efficient lead iodide perovskite thin-film solar cells. *Angew. Chemie Int. Ed.* **2014**, *53*, 9898–9903.

28 Jeon, N. J.; Noh, J. H.; Kim, Y. C.; Yang, W. S.; Ryu, S.; Seok, S. l. Solvent engineering for high-performance inorganic-organic hybrid perovskite solar cells. *Nat. Mater.* **2014**, *13*, 1–7.

29 Huang, L.; Li, C.; Sun, X.; Xu, R.; Du, Y.; Ni, J.; Cai, H.; Li, J.; Hu, Z.; Zhang, J. Efficient and hysteresis-less pseudo-planar heterojunction perovskite solar cells fabricated by a facile and solution-saving one-step dip-coating method. *Org. Electron. Physics Mater. Appl.* **2017**, *40*, 13–23.

30 Das, S.; Yang, B.; Gu, G.; Joshi, P. C.; Ivanov, I. N.; Rouleau, C. M.; Aytug, T.; Geohegan, D. B.; Xiao, K. High-performance flexible perovskite solar cells by using a combination of ultrasonic spray-coating and low thermal budget photonic curing. *ACS Photonics* **2015**, *2*, 680–686.

31 Liu, M.; Johnston, M. B.; Snaith, H. J. Efficient planar heterojunction perovskite solar cells by vapour deposition. *Nature* **2013**, *501*, 395–398.

32 Malinkiewicz, O.; Yella, A.; Lee, Y. H.; Espallargas, G. M. M.; Graetzel, M.; Nazeeruddin, M. K.; Bolink, H. J. Perovskite solar cells employing organic charge-transport layers. *Nat. Photonics.* **2014**, *8*, 128–132.

33 Leyden, M. R.; Ono, L. K.; Raga, S.; Kato, Y.; Wang, S.; Qi, Y. High performance perovskite solar cells by hybrid chemical vapor deposition. *J. Mater. Chem. A* **2014**, *2*, 18742-18745.

34 Raga, S.; Ono, L. K.; Qi, Y. Rapid perovskite formation by CH_3NH_2 gas-induced intercalation and reaction of PbI_2. *J. Mater. Chem. A* **2016**, *4*, 2494-2500.

35 Brandt, R. E.; Stevanović, V.; Ginley, D. S.; Buonassisi, T. Identifying defect-tolerant semiconductors with high minority-carrier lifetimes: beyond hybrid lead halide perovskites. *MRS Commun.* **2015**, *5*, 265–275.

36 Wu, C.-G.; Chiang, C.-H.; Tseng, Z.-L.; Mohammad, K. N.; Hagfeldt, A.; Grätzel, M. High efficiency stable inverted perovskite solar cells without current hysteresis. *Energy Environ. Sci.* **2015**, *8*, 2725–2733.

37 Kojima, A.; Teshima, K.; Shirai, Y.; Miyasaka, T. Organometal halide perovskites as visible-light sensitizers for photovoltaic cells. *J. Am. Chem. Soc.* **2009**, *131*, 6050-6051.

38 Im, J. H.; Lee, C.R.; Lee, J. W.; Park, S. W.; Park, N. G. Park, 6.5% efficient perovskite quantum-dot-sensitized solar cell. *Nanoscale* **2011**, *3*, 4088-4093.

39 Kim, H. S.; Lee, C. R.; Im, J.H.; Lee, K. B.; Moehl, T.; Marchioro, A.; Moon, S. J.; Humphry-Baker, R.; Yum, J. H.; Moser, J. E.; Grätzel, M.; Park, N. G. Lead iodide perovskite sensitized all-solid-state submicron thin film mesoscopic solar cell with efficiency exceeding 9%. *Sci. Rep.* **2012**, *2*, 591.

40 Ball, J. M.; Lee, M. M.; Hey, A.; Snaith, H. J. Low-temperature processed meso-superstructured to thin-film perovskite solar cells. *Energy Environ. Sci.* **2013**, *6*, 1739–1743.

41 Polman, A.; Atwater, H. A. Photonic design principles for ultrahigh-efficiency photovoltaics. *Nat. Mater.* **2012**, *11*, 174-177.

42 Irene, E. A. Applications of spectroscopic ellipsometry to microelectronics. *Thin Solid Films* **1993**, *233*, 96–111.

43 Poelman, D.; Smet, P. F. Methods for the determination of the optical constants of thin films from single transmission measurements: a critical review. *J. Phys. D: Appl. Phys*. **2003**, *1850*, 1850–1857.

44 Pettersson, L. A. A.; Roman, L. S.; Inganäs, O. Modelling photocurrent action spectra of photovoltaic devices based on organic thin films. *J. Appl. Phys.* **1999**, *487*, 487–496.

45 Burkhard, G. F.; Hoke, E. T.; McGehee, M. D. Accounting for interference, scattering, and electrode absorption to make accurate internal quantum effi ciency measurements in organic and other thin solar cells. *Adv. Mater.* **2010**, *22*, 3293–3297.

46 Lozano, G.; Colodrero, S.; Caulier, O.; Calvo, M. E.; Míguez, H. Theoretical analysis of the performance of one-dimensional photonic crystal-based dye-sensitized solar cells. *J. Phys. Chem. C* **2010**, *114*, 3681–3687.

47 Chang, J.-H.; Wang, H.-F.; Lin, W.-C.; Chiang, K.-M.; Chen, K.-C.; Huang, W.-C.; Huang, Z.-Y.; Meng, H.-F.; Ho, R.-M.; Lin, H.-W. Efficient inverted quasi-bilayer organic solar cells fabricated by using non-halogenated solvent processes. *J. Mater. Chem. A* **2014**, *2*, 13398–13406.

48 Anaya, M.; Correa-Baena, J. P.; Lozano, G.; Saliba, M.; Anguita, P.; Roose, B.; Abate, A.; Steiner, U.; Grätzel, M.; Calvo, M. E.; Hagfeldt, A.; Míguez, H. Optical analysis of $CH_3NH_3Sn_xPb_{1-x}I_3$ absorbers: a roadmap for perovskite-on-perovskite tandem solar cells. *J. Mater. Chem. A* **2016**, *4*, 11214–11221.

49 Correa-Baena, J. P.; Anaya, M.; Lozano, G.; Tress, W.; Domanski, K.; Saliba, M.; Matsui, T.; Jacobsson, T. J.; Calvo, M. E.; Abate, A.; Grätzel, M.; Míguez, H.; Hagfeldt, A. Unbroken perovskite: interplay of morphology, electro-optical properties, and ionic movement. *Adv. Mater.* **2016**, *28*, 5031–5037.

50 Arpin, K. A.; Mihi, A.; Johnson, H. T.; Baca, A. J.; Rogers, J. A.; Lewis, J. A.; Braun, P. V. Multidimensional architectures for functional optical devices. *Adv. Mater.* **2010**, *22*, 1084– 1101.

51 Atwater, H. A.; Polman, A. Plasmonics for improved photovoltaic devices. *Nat. Mater.* **2010**, *9*, 205-213.

52 Zeng, L.;. Bermel, P.; Yi, Y.; Alamariu, B. A.; Broderick, K. A.; Liu, J.; Hong, C.; Duan, X.; Joannopoulos, J.; Kimerling, L. C. Demonstration of enhanced absorption in thin film Si solar cells with textured photonic crystal back reflector. *Appl. Phys. Lett.* **2008**, *93*, 221105.

53 Enrique Galvez, F.; Kemppainen, E.; Míguez, H.; Halme, J. Effect of diffuse light scattering designs on the efficiency of dye solar cells: an integral optical and electrical description. *J. Phys. Chem. C* **2012**, *116*, 11426-11433.

54 Miranda-Muñoz,J. M.; Carretero-Palacios, S.; Jiménez-Solano, A.; Li, Y.; Lozano, G.; Míguez, H. Efficient bifacial dye-sensitized solar cells through disorder by design. *J. Mater. Chem. A* **2016**, *4*, 1953-1961.

55 Enrique Galvez, F.; Barnes, P. R. F.; Halme, J.; Miguez, H. Dye sensitized solar cells as optically random photovoltaic media. *Energy Environ. Sci.* **2014**, *7*, 689-697.

56 Yin, J.; Qu, H.; Cao, J.; Tai, H.; Li, J.; Zheng, N. Light absorption enhancement by embedding submicron scattering TiO_2 nanoparticles in perovskite solar cells. *RSC Adv.* **2016**, *6*, 24596-24602.

57 Derkacs, D.; Lim, S. H.; Matheu, P.; Mar, M.; Yu, E. T. Improved performance of amorphous silicon solar cells via scattering from surface plasmon polaritons in nearby metallic nanoparticles. *Appl. Phys. Lett*. **2006**, *89*, 093103.

58 Ferry, V. E.; Verschuuren, M. A.; Li, H. B. T.; Verhagen, E.; Walters, R. J.; Schropp, R. E. I.; Atwater, H. A.; Polman, A. Light trapping in ultrathin plasmonic solar cells. *Opt. Express* **2010**, *18*, A237.

59 Standridge, S. D.; Schatz, G. C.; Hupp, J. J. Distance dependence of plasmon-enhanced photocurrent in dye-sensitized solar cells. *J. Am. Chem. Soc*. **2009**, *131*, 8407–8409

60 Brown, M. D.; Suteewong, T.; Kumar, R. S.; D'Innocenzo, V.; Petrozza, A.; Lee, M. M.; Wiesner, U.; Snaith, H. J. Plasmonic dye-sensitized solar cells using core−shell metal−insulator nanoparticles. *Nano Lett.* **2011**, *11*, 438–445.

61 Zhang, W.; Saliba, M.; Stranks, S. D.; Sun, Y.; Shi, X.; Wiesner, U.; Snaith, H. J. Enhancement of perovskite-based solar cells employing core–shell metal nanoparticles. *Nano Lett.* **2013**, *13*, 4505–4510.

62 Saliba, M.; Zhang, W.; Burlakov, V. M.; Stranks, S. D.; Sun, Y.; Ball, J. M.; Johnston, M. B.; Goriely, A.; Wiesner, U.; Snaith, H. J. Plasmonic-induced photon recycling in metal halide perovskite solar cells. *Adv. Func. Mater.* **2015**, *25*, 5038-5046.

63 Carretero-Palacios, S.; Jiménez-Solano, A.; Míguez, H. Plasmonic nanoparticles as light harvesting enhancers in perovskite solar cells: a user’s guide. *ACS Ener. Lett.* **2016**, *1*, 323-331.

64 Zeng, L.; Bermel, P.; Yi1, Y.; Alamariu, B. A.; Broderick, K. A.; Liu, J.;. Hong, C.; Duan, X.; Joannopoulos, J.; Kimerling, L. C. Demonstration of enhanced absorption in thin film Si solar cells with textured photonic crystal back reflector. *Appl. Phys. Lett.* **2008**, *93*, 221105.

65 Dewan, R.; Knipp, D. Light trapping in thin-film silicon solar cells with integrated diffraction grating. *J. Appl. Phys.* **2009**, *106*, 074901.

66 Wooh, S.; Yoon, H.; Jung, J.-H.; Lee, Y.-G.; Koh, J. H.; Lee, B.; Kang, Y. S.; Char, K. Efficient light harvesting with micropatterned 3D pyramidal photoanodes in dye-sensitized solar cells. *Adv. Mater.* **2013**, *25*, 3111.

67 López-López, C.; Colodrero, S.; Jiménez-Solano, A.; Lozano, G.; Ortiz, R.; Calvo, M. E.; Míguez, H. Multidirectional light-harvesting enhancement in dye solar cells by surface patterning. *Adv. Opt. Mater.* **2014**, *2*, 879-884.

68 Jang, S.; Yoon, J.; Ha, K.; Kim, M.; Kim, D. H.; Kim, S. M.; Kang, S. M.; Park, S. J.; Jung, H. S.; Choi, M.. Facile fabrication of three-dimensional TiO_2 structures for highly efficient perovskite solar cells. *Nano Energy* **2016**, *22*, 499–506.

69 Kang, S. M.; Jang, S.; Lee, J. K.; Yoon, J.; Yoo, D. E.; Lee, J. W.; Choi, M.; Park, N. G. Moth-eye TiO_2 layer for improving light harvesting efficiency in perovskite solar cells. *Small* **2016**, *12*, 2443–2449.

70 Paetzold, U. W.; Qiu, W.; Finger, F.; Poortmans, J.; Cheyns, D. Nanophotonic front electrodes for perovskite solar cells. *Appl. Phys. Lett.* **2015**, *106*, 173101.

71 Yeh, P. Optical Waves in Layered Media, John Wiley & Sons, Hoboken, New Jersey, **2005**.

72 Kang, G.; Yoo, J.; Ahn, J.; Kim, K. Transparent dielectric nanostructures for efficient light management in optoelectronic applications. *Nano Today*, **2015**, *10*, 22–47.

73 Yoshimura, M.; Suchanek, W.L.; Byrappa, K. Soft solution processing: a strategy for one-step processing of advanced inorganic materials. *MRS Bull*. **2000**, *25*, 17-25.

74 Almeida, R.M.; Portal, S. Photonic band gap structures by sol–gel processing. *Curr. Opin. Solid State Mater. Sci.;***2003**, *7* , 151–157.

75 Hou, L.; Hou, Q.; Mo, Y.; Peng, J., Cao, Y. All-organic flexible polymer microcavity light-emitting diodes using 3M reflective multilayer polymer mirrors. *Applied Phys. Lett.;* **2005**, *87*, 243504.

76 Betancur, R.; Romero-Gomez, P.; Martinez-Otero, A.; Elias, X.; Maymó, M.; Martorell, J. Transparent polymer solar cells employing a layered light-trapping architecture. *Nat. Photonics*, **2013** , *7,* 995-1000.

77 Bermel, P.; Luo, C.; Zeng, L.; Kimerling, L. C.; Joannopoulos, J. D. Improving thin-film crystalline silicon solar cell efficiencies with photonic crystals. *Opt. Express*, **2007**, *15*, 16986-17000.

78 Xie, K.; Guo, M.; Huang, H. Photonic crystals for sensitized solar cells: fabrication, properties, and applications. *J. Mater. Chem. C*, **2015**, *3*, 10665-10686.

79 Jiménez-Solano, A.; Delgado-Sánchez, J.M.; Calvo, M.E.; Miranda-Muñoz, J.M.; Lozano, G.; Sancho, D.; Sánchez-Cortezón, E.; Míguez, H. Design and realization of transparent solar modules based on luminescent solar concentrators integrating nanostructured photonic crystals. *Prog. Photovolt: Res. Appl.;* **2015**, *23*, 1785–1792.

80 Shen, H.; Wang, Z.; Wu, Y.; Yang, B. One-dimensional photonic crystals: fabrication, responsiveness and emerging applications in 3D construction. *RSC Adv*.; **2016**, *6*, 4505-4520.

81 Joannopoulos, J. D. Photonic crystals: molding the flow of light, Princeton University Press, Princeton, 2nd ed.; **2008**.

82 Colonna, D.; Colodrero, S.; Lindstrom, H.; Di Carlo, A.; Míıguez, H. Introducing structural colour in DSCs by using photonic crystals: interplay between conversion efficiency and optical properties. *Energy Environ. Sci.* **2012**, *5*, 8238-8243.

83 Li, Y.; Calvo, M. E.; Míguez, H. Integration of photonic crystals into flexible dye solar cells: a route toward bendable and adaptable optoelectronic devices displaying structural color and enhanced efficiency. *Adv. Opt. Mater.* **2016**, *4*, 464-471

84 Steele, J.J.; van Popta, A.C.; Hawkeye, M.M.; Sit, J.C.; Brett, M.J. Nanostructured gradient index optical filter for high-speed humidity sensing. *Sens. Actuators B,* **2006**, *120*, 213-219.

85 Passoni, L.; Criante, L.; Fumagalli, F.; Scotognella, F.; Lanzani, G.; Di Fonzo, F. Self-assembled hierarchical nanostructures for high-efficiency porous photonic crystals. *ACS Nano*, **2014**, *8*, 12167-12174.

86 Fuertes, M.C.; López-Alcaraz, F.J.; Marchi, M.C.; Troiani, H.E.; Míguez, H.; Soler Illia, G.J.A.A. Photonic crystals from ordered mesoporous thin-film functional building blocks. *Adv. Funct. Mater*. **2007**, *17*, 1247.

87 Colodrero, S.; Ocaña, M.; Míguez. H. Nanoparticle-based one-dimensional photonic crystals. *Langmuir* **2008**, *24*, 4430.

88 Bonifacio, L. D.; Puzzo, D. P.; Breslav, S.; Willey, B. M.; McGeer, A.; Ozin, G. A. Towards the photonic nose: a novel platform for molecule and bacteria identification. *Adv. Mater*. **2010**, *22*, 1351-1354.

89 Calvo, M. E.; Colodrero, S.; Rojas, T. C.; Ocaña, M.; Anta, J. A.; Míguez, H. Photoconducting Bragg mirrors based on TiO_2 nanoparticle multilayers. *Adv. Func. Mater.* **2008**, *18*, 2708.

90 Anaya, M.; Calvo, M. E.; Luque-Raigón, J. M.; Míguez, H. Resonant Photocurrent Generation in Dye-Sensitized Periodically Nanostructured Photoconductors by Optical Field Confinement Effects. *J. Am. Chem. Soc.* **2013**, *135*, 7803-7806.

91 Yoffe, A. D. Low-dimensional systems: quantum size effects and electronic properties of semiconductor microcrystallites (zero-dimensional systems) and some quasi-two-dimensional systems. *Adv. Phys.* **1993**, *42*, 173.

92 Kovalenko, M. V. Opportunities and challenges for quantum dot photovoltaics. *Nat. Photon.* **2015**, *10*, 993-997.

93 Besson, S.; Gacoin, T.; Ricolleau, C.; Jacquiod, C.; Biolot, J. P. 3D Quantum dot lattice inside mesoporous silica films. *Nano Lett.* **2002**, *4*, 409-414.

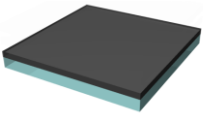

Chapter 2

Optical description of perovskite films

In this chapter, we focus on the understanding of the optical behaviour of $MAPbI_3$ *perovskite films. First, we demonstrate that the different processes occurring during perovskite film formation can be identified and analysed by a combined in-situ analysis of their photophysical and structural properties. This allows us to determine when the material is completely formed and exhibits the best optical performance, hence when the annealing step must be finalised. Thereafter, we describe how the interplay between photo-induced activation and darkening processes affect the photophysical properties of the films, which strongly depend on the atmosphere surrounding the samples. Finally, we determine the optical constants of* $MAPbI_3$ *films. In this regard, herein, we cover the optical characterization of the material by reflectance, transmittance and absorptance spectrally resolved. The use of a code based on the transfer matrix model combined with a genetic algorithm will serve to extract the optical constants of the perovskite, which are consistent with the Forouhi-Bloomer formalism. Conclusions extracted from this chapter provide a basis for the following chapters in order to synthesise and handle* ABX_3 *perovskite materials in the most suitable conditions, and model solar cells based on them.*

2.1. Introduction

Ever since the first evidence that ABX_3 perovskites could outperform all other solution process approaches to fabricate photovoltaic devices,[1-5] strong research efforts have been directed towards exploring questions essential to translate the current perovskite solar cell rush into a well-established technology. The latter include the nature of photoexcited species, stability of the material under operating conditions, the synthesis of the material, etc.[6-8] In this regard, the analysis of the photophysical properties of a semiconductor provides a powerful background to understand such mechanisms. Particularly, the detection of the re-radiated photons stimulated by charge photoexcitation entails a direct evidence of the optical processes present in the perovskite material. Consequently, this requires illuminating the samples with light designed to promote photon absorption, charge excitation and radiative recombination in ABX_3 perovskites (see Figure 2.1). Rather than being problematic, in fact, it implies actually a method to reproduce the in-operando light conditions (i.e. $350<\lambda<800$ nm) for the perovskites as a PV material.

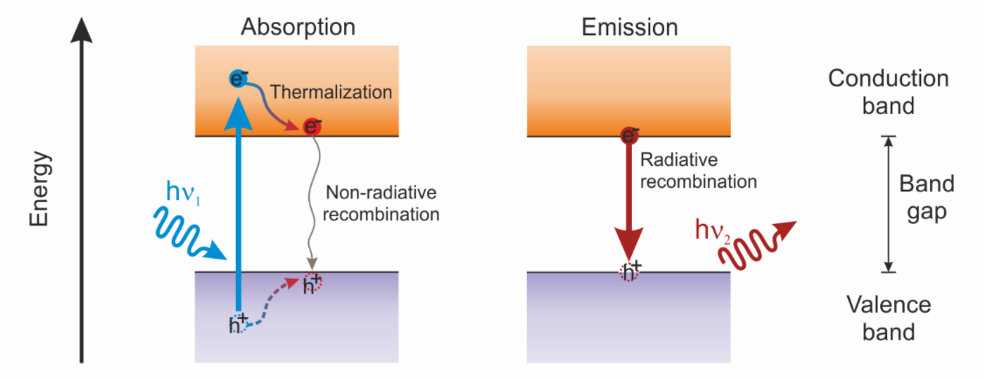

Figure 2.1. Absorption and emission of light. Energy diagram showing absorption of light and the relaxation processes involved in the emission of light in a semiconductor.

As introduced in Chapter 1, a number of approaches have been explored to prepare high quality perovskite films ranging from vacuum evaporation[9,10] to solution process techniques.[8,11,12] Among the latter, spin coating is the most widespread approach, representing the best compromise between material quality, feasibility of mass-production and low-cost processing, leading to high performance photovoltaic devices as well as light-emitting ones with outstanding efficiency.[13] The morphology of the fabricated material (crystal size distribution and shape, as well as of their connectivity and final film texture), which dictates its operation for photovoltaics, is strongly determined by the growth process.

In this respect, a number of studies[7,14-23] have recently examined the steps which link the initial precursors to the final material during the solution processing of metal halide perovskite films. These investigations, carried out mainly from structural information concerning electron microscopy images and X-ray diffraction (XRD) experiments, have focused on different aspects of the material formation. These include the effect of annealing rate and conditions,[14,15,19] the evolution of the crystallization process[7,17,20,23] and the nature of the intermediate precursor species which precede perovskite formation[7,16,18,20,21] all of them leading to the fabrication of samples with better crystalline quality. Beside the interest in the processes taking place at its fabrication stage, concern for perovskite stability under illumination has risen since it potentially hampers device performance.[24-26] The control over the optical response of the material would allow the extraction of its optical constants, something that was not reported when this PhD project started.

In this chapter, we focus the discussion on the optical properties of $MAPbI_3$ films. First, we will introduce the protocols applied to the perovskite film preparation and we will give a basic description of the samples in terms of both structural and optical behaviour. This section will serve as starting point for the entire dissertation, providing the reader with the necessary background concerning the $MAPbI_3$ material. Afterwards, we will monitor its photophysical behaviour in a broad time scale: from the moment just after the deposition of the precursors takes place, up to several hours after the complete formation of the perovskite structure. This will allow us to identify the nucleation and growth regimes while the perovskite forms, as well as environmental effects on its photophysical performance. Finally, we will present a protocol to extract the complex refractive index of perovskite materials. To this end, we will characterize angularly the spectral dependence of light reflected and transmitted by the films. Subsequently, we will obtain their optical constants by fitting the curves with a code based on the transfer matrix model (TMM).

2.2. Preparation and characterization of $MAPbI_3$ films

2.2.1. Synthesis of precursor materials

Methylammonium iodide (CH_3NH_3I, MAI) was prepared by dissolving 12.4 ml of methylamine (Sigma-Aldrich 534102) in 50 ml absolute ethanol, and reacting with 6 ml hydroiodic acid (Sigma-Aldrich 210021), in an ice bath. After 60 minutes, the solvent was removed by rotary evaporation and the obtained white powder was washed with anhydrous diethyl ether, and dried overnight under vacuum at 80°C. Finally, MAI and $PbCl_2$ (Sigma-Aldrich 268690) were dissolved at a final concentration of 40 wt%.in anhydrous N,N-Dimethylformamide (DMF) (molar ratio between MAI and $PbCl_2$ was 3:1).

2.2.2. Deposition method

$MAPbI_3$ films were deposited onto clear white glass substrates (ProScitech) previously cleaned sequentially in ethanol, acetone, 2-propanol and finally treated with oxygen plasma during 300 seconds. The use of a low fluorescence glass is crucial to ensure that no PL artifacts arise from the substrate in forthcoming sections. The perovskite films were prepared following a solvent-annealing (or antisolvent) crystallization method.[8] $MAPbI_3$ precursor solution (100 μL) was deposited (substrate area ~2 cm x 2 cm) by spin-coating at 5000 rpm (see Figure 2.2). After six seconds, while the spinning process takes place, 200 μL of anhydrous chlorobenzene (CBZ) was dropped onto the center of the substrate. The resulting films were then annealed at 100°C for 1 hour, until a pure $MAPbI_3$ layer was obtained.

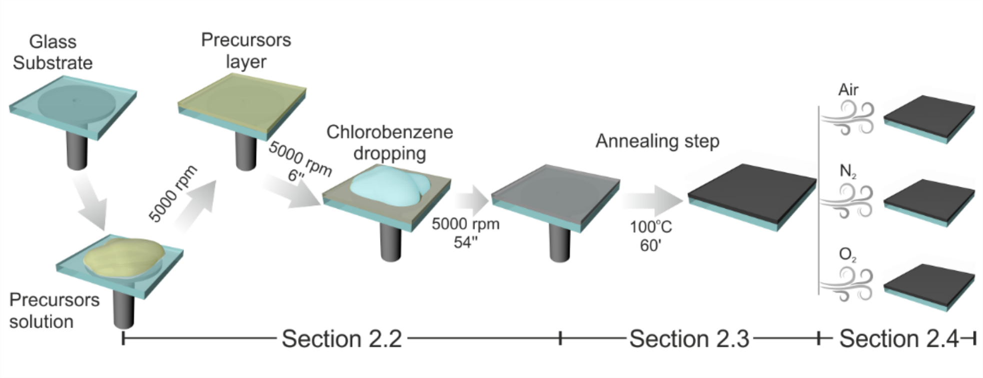

Figure 2.2. Scheme of the $MAPbI_3$ film preparation. Description of the antisolvent method employed for the deposition of the perovskite films. Complete crystallization occurs after a subsequent annealing step. A general timeline of the chapter is also added in the Figure.

2.2.3. Structural characterization

In order to verify the presence of the perovskite structure, X-Ray diffraction (XRD) measurements were carried out in a X'pert PRO (PANalytical) system in a glancing angle (ω=1°). Diffraction patterns were recorded with $Cu_{\kappa\alpha}$ radiation (λ=1.54 Å, 40mA, 45 kV) over a 2θ range from 5° to 90° and a pixel detector, using a step size of 0.05° and an acquisition time of 60s. The obtained XRD pattern (see Figure 2.3a) shows peaks characteristic of crystalline $MAPbI_3$ at 14.088º, 23.488º, 28.408º, and 31.868º which correspond to Bragg diffraction by the (110), (211), (220), and (310) planes of the tetragonal phase of this metal halide perovskite.[27]

The approach described previously gives rise to ~300 nm-thick perovskite films as noticed in the Scanning Electron Microscopy (SEM, S5200, Hitachi) image in Figure 2.3b. A (poly)methyl methacrylate (PMMA) layer was deposited by spin coating on top of the $MAPbI_3$ film in order to prevent degradation during the cross-section preparation. In order to further analyse the sample quality, we employed an Atomic Force Microscope (AFM, Pico Plus) in tapping mode to prevent any structural modification of the perovskite film surface. Figure 2.3c shows a topographic image of the top interface of the perovskite layer. A fine control over the AFM parameters, such as cantilever resonance frequency or scanning speed, leads to a clear and noiseless mapping. From the data analysis (software WSxM 5.0 Develop 8.0), the films present a narrow crystal size distribution around an average controlled value of hundreds of nanometers, estimated to be 300 nm in our particular case. Moreover, the roughness is below 20 nm (Figure 2.3d), assuring an appropriate film quality.

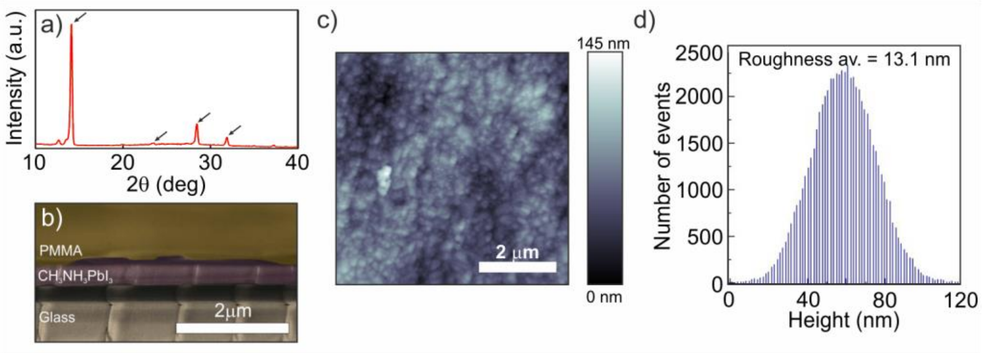

Figure 2.3. Structural characterization of a $MAPbI_3$ film. a) XRD pattern of a $MAPbI_3$ film deposited on glass. Arrows point to angular positions of diffraction peaks expected for crystalline $MAPbI_3$ (see text). b) Scanning Electron Microscopy (SEM) image of the cross section of a typical $MAPbI_3$ film. c) Atomic Force Microscopy (AFM) image displaying the topography of the perovskite layer. d) Statistical analysis of the relative surface high of the different regions of the sample displayed in panel c). Results are fitted with a Gaussian distribution, which brings a roughness of 13 nm.

2.2.4. Optical characterization

We have performed an analysis of the spectral dependence of the light reflected and transmitted by $MAPbI_3$ samples. In particular, we have measured total reflectance (R_t), diffuse reflectance (R_d), total transmittance (T_t) and diffuse transmittance (T_d) with a commercial system comprised of an integrating sphere attached to an UV-VIS spectrophotometer (UV-2101 PC, Shimadzu). These measurements allowed us to determine the fraction of incident light absorbed (absorptance, A) by the film by making use of the formula $A=1-R_t-T_t$ (see Figure 2.4a). A sharp band edge at λ=770 nm was observed. Additionally, the diffuse reflectance spectrum revealed the high optical quality of the thin film due to the negligible fraction (<5%) of diffusely scattered light (see Figure 2.4b).

Once light absorption by the $MAPbI_3$ perovskite was understood, we focused the attention on its emissive properties. To this end, we carried out a characterization of the photoluminescence (PL) in a commercial fluorometer (Fluorolog 3, Horiba) with a tunable picosecond laser source (SC400, Fianium) delivering low power (sub-mW) 900 ps long pulses with a 1 kHz repetition rate. A PL peak at 775 nm with a full width at half maximum (*FWHM*) of 45 nm under optical excitation with a λ=450 nm light was measured (see Figure 2.4a). Then, the evolution of the PL maximum was monitored with a scanning monochromatic excitation provided by a Xenon lamp. The spectral trend of this photoluminescence excitation (PLE) is displayed in Figure 2.4a. The spectrum presented two clear maxima, at 510 nm and 750 nm. The marked spectral difference between absorptance and PLE evidences that photocarriers generated at large energy have a higher contribution to the PL than photocarriers produced at low energy.

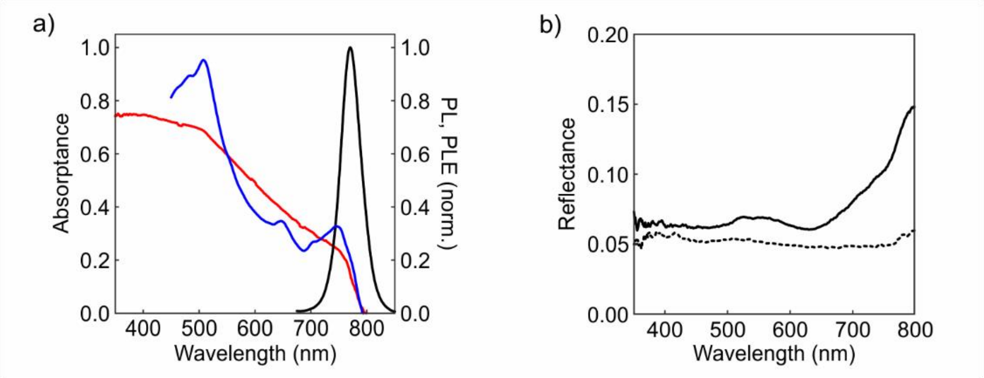

Figure 2.4. Optical characterization of a $MAPbI_3$ film. a) Normalized PL and PLE (black and blue, respectively) and absorptance (red line) spectra from a 200 nm-thick perovskite films. Please notice that PLE spectrum is recorded from λ=450 nm to avoid the PL arising from the substrate. b) Total (solid black) and diffuse (dashed black) reflectance spectra of the film.

The combination of features described in Sections 2.2.3. and 2.2.4. (i.e. film homogeneity, high absorptance and PL, and low diffuse light) permits us to conclude that the obtained $MAPbI_3$ material exhibits properties that make it suitable for developing photophysical studies.

2.3. Photophysics of MAPbI$_3$ films during formation

In order to gain further knowledge into the formation process of the perovskite films, we have studied the photophysics of the samples during the thermal annealing step.

2.3.1. Steady-state photoluminescence

After 20 seconds spin step ended, samples were placed on top of a Peltier Cell set at 100 ºC, to monitor their optical properties in an air atmosphere (see Figure 2.2). A scheme of the experimental setup is displayed in Figure 2.5. A black metal plate was placed between the cell and the sample in order to avoid reflections of the pump beam. The sample was illuminated with a pulsed femtosecond laser source (OPerA-Solo from Coherent, delivering 150 fs long pulses with a repetition rate of 1 kHz and a λ=532 nm) focused with an achromatic 10 cm focal length lens producing a spot size of 40 µm which also acted as collection optics. PL spectra were collected with a fibre-coupled spectrophotometer (USB4000 from Ocean Optics).

The MAPbI$_3$ sample was pumped with a power of 500 nW. Under these conditions recombination dynamics are dominated by the filling of trap states associated with the presence of defects, leading to a monomolecular regime.[28,29] Further, for the power and small duty cycle associated with these pump conditions, no changes in intensity due to photoinduced processes (as the ones presented in Section 2.4) were observed.

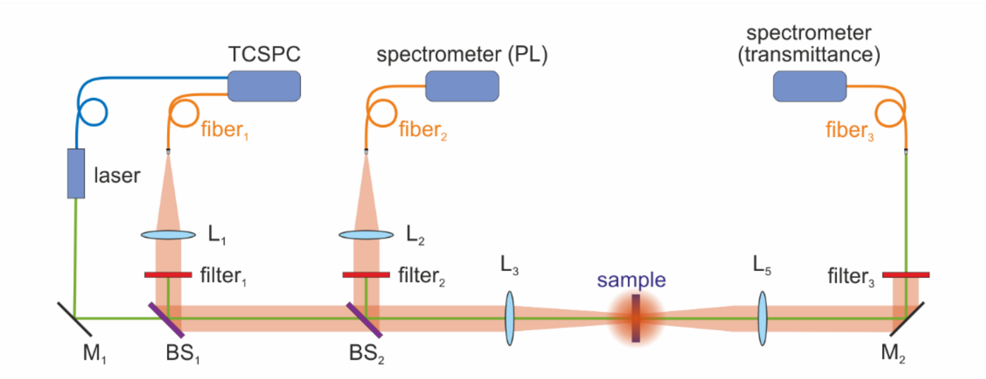

Figure 2.5. Set-up. Sketch of the experimental set-up in order to measure steady-state and time-resolved PL as well as transmittance in an optical bench.

Figures 2.6a and 2.6b show the spectral position and amplitude of the PL peak as a function of annealing time. Here four different regimes can be clearly observed. For a time interval (i) the PL peak remains fixed in spectral position but monotonically increases its intensity.

After a 10 minutes interval where the PL intensity slightly decreases while maintaining its spectral position, stage (ii), the PL further rises in amplitude and is accompanied by a redshift in the peak. This period (iii) lasts nearly 30 minutes and then a final stage is achieved (iv) which we identified with the end of the annealing process.

2.3.2. Time resolved photoluminescence

We have performed time resolved measurements in order to obtain the PL decay dynamics of the material during its formation in the annealing process. In this regard, we used a Time Correlated Single Photon Counting card (TCSPC, SPC-130, Becker & Hickl) coupled to the setup presented in Figure 2.5. Under the above mentioned pump conditions, which are associated with the monomolecular recombination regime, the presence of defects determines the dynamics of the PL and thus changes in the density of trap states are expected to be reflected in the PL lifetime. Indeed, the dynamics of the PL of the deposited samples were observed to strongly vary as the annealing time increased. In order to correlate these changes with those described above, the data was fitted to a decay rate distribution and extracted the most frequent value for each annealing time (Γ_{MF}). Figure 2.6c shows the time evolution of the decay rates, where measurements were collected over a period of five minutes in order to have enough signal.

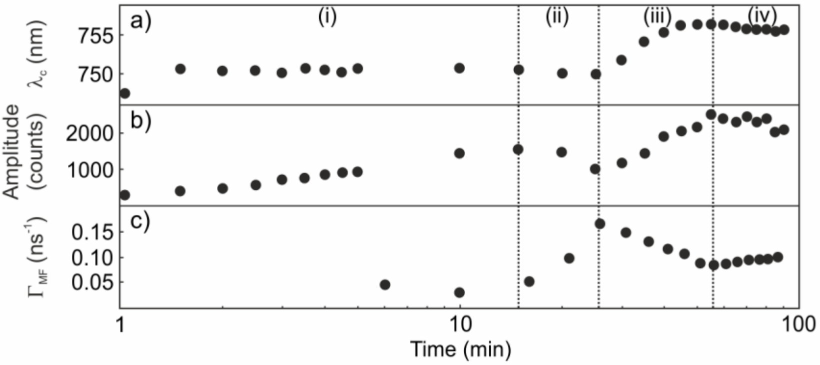

Figure 2.6. Photoluminescence characterization during the calcination step. Time evolution during the annealing process of spectral position (a) and amplitude (b) of the PL peak and most frequent value of the decay rate distribution (c). Please note that each decay rate measurement took 5 minutes. Four regimes corresponding to four different perovskite film formation stages (see text) are separated by vertical dashed lines.

2.3.3. XRD measurements

We accomplished a temperature dependent XRD characterization of the freshly deposited films with the aim of extracting information on the structural modifications that took place during the thermal annealing of the MAPbI$_3$ film. XRD data were collected as a function of time in a high temperature chamber (ANTON PAAR HTK 1200) attached to a diffractometer (X'pert PRO, PHILIPS) while the sample was heated at 100 °C.

Figures 2.7a and 2.7b show data acquired at two times of the heating process, 1 and 100 minutes after precursor deposition. This time interval allows the sample to achieve a state where material formation seems complete and no signs of degradation, such as the characteristic color change to yellow, were observed. In the angular range under consideration, two peaks were studied: one around $2\theta=14°$ characteristic of the (110) planes of the tetragonal MAPbI$_3$ phase or the (100) of the cubic phase and another just below $2\theta=12°$ associated with intermediate PbI$_2$-related precursor species which will be consumed during perovskite formation.[17,30] Both peaks appear highlighted by arrows in the figure. In order to follow the evolution of both species during annealing we have extracted the intensity maxima of each peak as a function of time.

A monotonic increase of the MAPbI$_3$ related peak is accompanied by a drop in the peak associated to the presence of the intermediate precursor species (see Figure 2.7c). Such trends indicate the formation of the perovskite species as the lead precursor disappears. We have further extracted the angular position of the peaks corresponding to the two species, a small shift in the position being evident (Figure 2.7d). We will come back on this point later on.

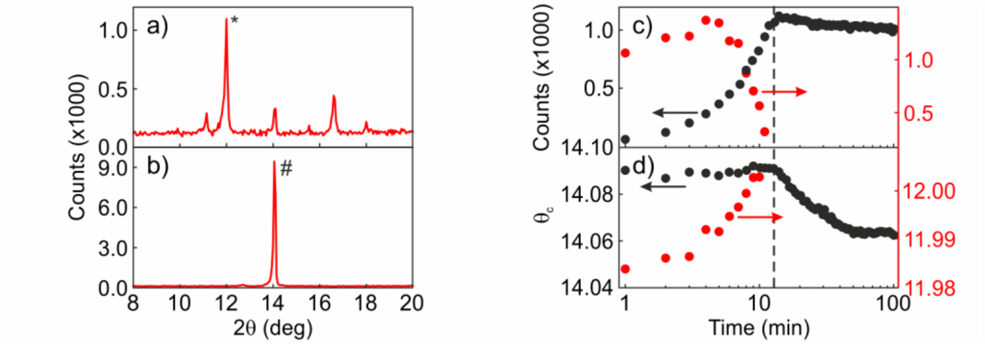

Figure 2.7. XRD characterization during the calcination step. XRD data of thin film perovskites collected at two points of the annealing process: 1 minute (a) and 100 minutes (b) after precursor deposition. Diffraction peaks associated with MAPbI$_3$ (#) and PbI$_2$-related precursors (*) are highlighted. Evolution of the intensity maximum of the XRD peak (c) corresponding to MAPbI$_3$ (black) and precursor species (red circles) and angular position (d) as a function of anneal time.

2.3.4. General picture of $MAPbI_3$ formation

The combined optical and structural study allows us to propose a full timeline for the $MAPbI_3$ perovskite formation, in which the nucleation and growth regimes are unequivocally differentiated.

2.3.4.1. First stage

During stage (i) the increase in PL intensity (Figure 2.6b) coincides with the rise of the amplitude of the XRD peak corresponding to the perovskite (Figure 2.7c), evidencing the formation of $MAPbI_3$ as more crystals contribute to Bragg diffraction. Also during this interval, the angular position, as seen in Figure 2.7d (black dots), of the XRD peak does not vary. This data indicates that stage (i) corresponds to the nucleation of perovskite crystallites during the annealing process.

2.3.4.2. Second stage

Considering now the PL decay dynamics (Figure 2.6c), a rapid increase in the decay rate takes place during stage (ii). This is accompanied by a decrease in the PL intensity. These changes point to a decrease in the quantum yield (QY) of the material, likely related to the presence of non-radiative recombination paths associated with crystalline defects. This drop in the PL coincides with the vanishing of the XRD intensity of the PbI_2-related precursor (Figure 2.7c) which seems to be acting as a trap-passivating agent of the formed crystallites. If one considers the angular position of the precursor XRD peak (red dots in Figure 2.7d), the drop of its intensity is accompanied by a slight shift to larger angles closer to the value expected for pure PbI_2.[31] A plausible explanation for this behavior is illustrated in Figure 2.8, where a schematic description of the crystal growth process is provided along with the concomitant changes in the precursor and perovskite structures.

The perovskite crystallites form in the presence of a precursor whose nature are PbI_2 planes intercalated with DMF as well as MAI molecules, which separate the crystallographic planes of the inorganic material (Figure 2.8a and 2.8b).[32] As nucleation proceeds, new perovskite crystallites form and the intercalated DMF molecules evaporate, causing the PbI_2 planes to become closer together, this being at the origin of the narrower interplanar spacing revealed in Figure 2.7d (red dots). At a certain point, corresponding to the stage (ii), all crystallites are formed at the expense of the precursor. As it disappears, the newly formed grain boundaries (Figure 2.8c) introduce carrier traps that act as non-radiative decay paths that yield the sudden drop of photoemission efficiency observed (Figure 2.6b). This time interval corresponds to the early stages of the annealing process for which other works have reported the existence of intermediate precursor species.[7,16,18,20,21]

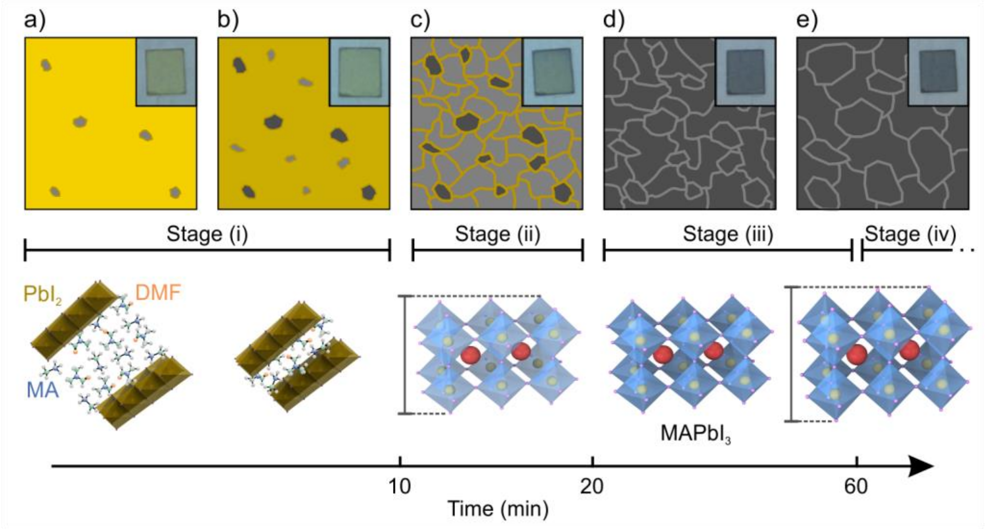

Figure 2.8. $MAPbI_3$ formation picture. Schematic representation of the $MAPbI_3$ formation during the annealing process. a-b) Perovskite crystallites (grey regions) form in a medium comprising a PbI_2-related precursor (yellow region). c) All crystallites form at the expense of the precursor. d-e) Crystal growth takes place as different crystallites coalesce. Insets show photographs of the samples at different stages of the annealing process: 5, 10, 20, 40 and 90 minutes.

2.3.4.3. Third and fourth stages

When perovskite formation enters the third regime (iii), the PL decay rate decreases until it reaches a constant value (region (iv)). This is accompanied by a number of changes in some of the other properties we have monitored. As the amplitude of the XRD peak associated with the crystalline $MAPbI_3$ remains constant, we assume that the total amount of perovskite does not change. At this point, $MAPbI_3$ crystal grows at the expense of smaller crystallites (Figure 2.8d and 2.8e). This is in agreement with the fact that the PL intensity further increases (see Figure 2.6b), as larger crystallites present a smaller density of surface defects that act as non-radiative recombination centres. The hypothesis of crystal growth is further supported by a redshift of the PL peak (Figure 2.6a) and a decrease in the decay dynamics. This behaviour is attributed to the release of strain present in the crystalline lattice as a consequence of the distortion of the Pb-I-Pb bond.[33] This is in agreement with the enlargement of the interplanar spacing revealed by the change in the position of the XRD peak associated with the $MAPbI_3$ (see black dots in Figure 2.7d) during this third time interval.

2.4. Environmental effects on the photophysics of $MAPbI_3$ films

Once the formation processes resulting in the perovskite structure were understood, we analysed the photophysics of $MAPbI_3$ films under different environmental conditions. First, samples may cool down under ambient temperature. As the annealing process took place well above the cubic-to-tetragonal transition temperature (~50ºC),[34] the phase of the as-prepared films was cubic, changing to tetragonal as the sample cooled down. In this process, the PL underwent a slight redshift of 15 nm (see Figure 2.9).

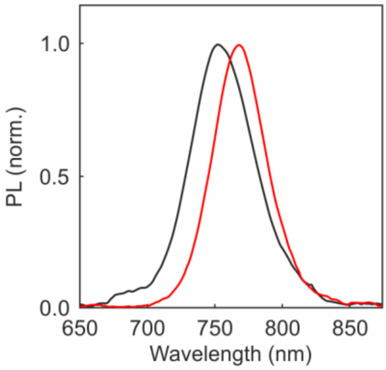

Figure 2.9. Photoluminescence at different temperatures. PL spectra of a $MAPbI_3$ thin film at the end of the annealing process (60 minutes at 100ºC) and after cooling at room temperature for an hour are shown as black and red curves respectively.

2.4.1. Photoluminescence transient of $MAPbI_3$ films in air

The most evident feature that one can observe in the photoemission of a $MAPbI_3$ film is the existence of a PL transient under continuous light illumination (0.3 W/cm^2). Indeed, it occurs under optical pump conditions, which are those comparable to the in-operando conditions for a perovskite-based device. The PL peak presents a slow (in the range of minutes) dynamics with an initial photo-activation stage followed by a photo darkening one. As a matter of fact, both processes are likely taking place simultaneously. This feature becomes evident when one plots the PL maximum (λ=775nm) (see Figure 2.10a) as a function of illumination time.

Simultaneously with the PL measurements, we monitored the absorption at the excitation wavelength (see Figure 2.10b). In order to do so, we followed the setup from Figure 2.5 in which another spectrophotometer was placed behind the sample. It is evident that large changes in PL intensity were accompanied by a nearly constant pump absorption (fluctuations of ~ 2%). This behavior indicated that the variation in the sample emission was due to changes of radiative and non-radiative decay paths of the photogenerated carriers. Further, PL spectra collected at three different stages of the collection period presented no changes in the spectral shape (see Figure 2.10c), which indicated that the electronic transitions involved in the time evolution observed in the PL had a non-radiative character.

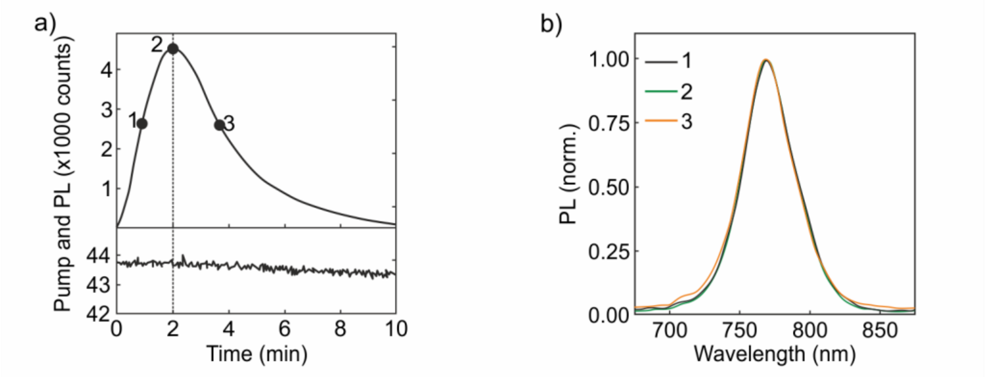

Figure 2.10. Photoluminescence transient in air. a) PL maximum (λ=775nm) as a function of time under excitation with monochromatic light λ=500nm. Bottom panel displays the transmitted pump intensity. b) Normalized PL spectra at three stages of the time evolution (marked by dots in (a)).

On the one hand, photo-activation emission dynamics are not a result of any change in the material morphology since no changes in the PL spectral shape are observed. On the other, the photo-darkening of the perovskite film is not a product of photoinduced high temperatures (which could be caused by local heating by the pump beam) since no physical change associated with the color of the perovskite film was observed. Indeed, PbI_2 should arise as a sub-product of the degradation, giving rise to a characteristic PL peak at λ=500 nm, and it is not observed.

2.4.2. Photoluminescence transient of $MAPbI_3$ films in the presence of N_2 and O_2

With the aim of discerning whether the photo-activation and photo-darkening of the $MAPbI_3$ film PL were related to the environment, we studied the photophysics of the samples under N_2 and O_2 atmospheres. Samples were kept in a closed chamber that can be filled with different gasses. The time evolution of the PL was measured by sequentially changing the atmosphere. Between each measurement the sample was exposed to the corresponding gas flux without any illumination for a period of 5 minutes in order to guarantee a complete replacement of the atmosphere. Figure 2.11 shows the evolution of the PL maximum as the samples were exposed to O_2/N_2 and N_2/O_2 sequential fluxes. From these results, it is evident that the photo-activation of the PL strongly depended on the surrounding atmosphere. In particular, the activation is more effective in the presence of O_2 than N_2.

Meanwhile, from Figure 2.11, it is apparent that the strong photo-darkening was mainly due to the presence of moisture in the atmosphere surrounding the samples when the sample was illuminated in air. When the evolution of the PL under air/N_2/O_2 was tracked, it could be found that the drop in PL of over 90% observed in air was reduced to 15%-20% when the sample was placed in N_2 or O_2 (see Figure 2.12). Further, it can be noticed that the photo-darkening during illumination in air was partially reversible when the sample was placed in O_2 at a later time. It can be also noted that such recovery upon changing the atmosphere from air to O_2 demands illumination, that is, it is a photo-activated process.

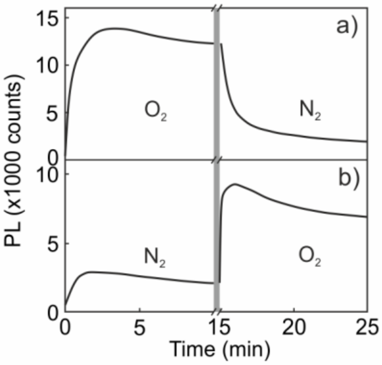

Figure 2.11. Photoluminescence transient in N_2 and O_2. Dynamics of the PL maximum under constant pump conditions for bulk perovskites under different atmospheric conditions. a) Passing an O_2 flux followed by a N_2 one. b) Passing a N_2 flux followed by an O_2 one. Note that before each measurement with a given gas the sample is exposed to it for 5 minutes in dark (break in the x-axis and grey band).

The origin of such moisture-related photo-activation and photo-darkening is likely related to the formation of oxidized species at the perovskite surface. Such oxide composites would lead to a gradient in the electric charge distribution along the perovskite layer, which would act as driving force for the halide (iodide) ion migration. This ionic movement activates the photoemission since the crystal structure is healed by halide vacant filling: i) superficial iodides are pushed down to load bulk defects, while ii) oxide species occupy the superficial vacant and the space left by migrant halides. It seems that the described process reaches a saturation point in which the perovskite structure is so distorted that an irreversible degradation of the sample arises. This later mechanism may result in photo-darkening.

Nevertheless, further experiments may be performed to confirm this hypothesis and to reach a complete picture of the mechanisms underlying the $MAPbI_3$ perovskite PL transient. Indeed, this is a very active topic in the community nowadays.[35-38] In this regard, we are involved in new experiments that combine in-situ PL and X-ray Photoemission Spectroscopy (XPS), which are pointing out towards the described interpretation.

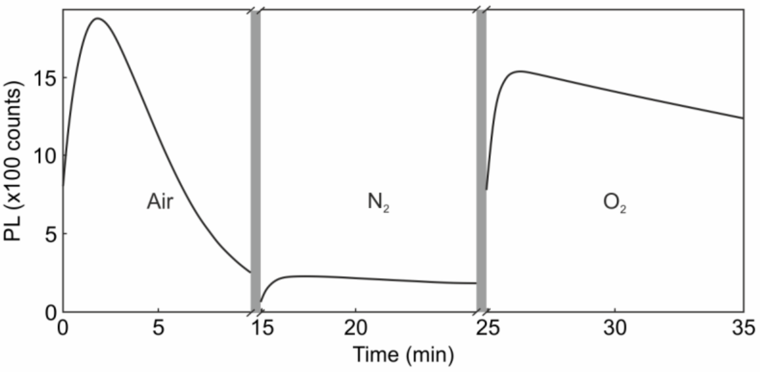

Figure 2.12. Sequence of photoluminescence transients. PL evolution of the PL maximum with the sample exposed to different atmospheres. Note that before each measurement with a given gas the sample is exposed to it for 5 minutes (break in the x-axis and grey band).

2.5. Optical constants of $MAPbI_3$ perovskite films

We have investigated the films presented in Section 2.2 as well as samples provided by the leading European groups in the field. Identical samples in terms of chemical formulation ($MAPbI_3$), but differing in their synthetic routes, were employed to compare the eventual variation in their optical response. The groups led by Prof Anders Hagfeldt at the École Polytechnique Fédérale de Lausanne (EPFL, Switzerland) and by Prof Henry Snaith at the University of Oxford (United Kingdom) supplied the materials.[39,40]

2.5.1. Characterization protocol

We have investigated perovskite films with two different thicknesses, i.e. ~100 nm and ~500 nm, deposited on glass. First of all, we measured R_t, R_d, T_t, and T_d as was described in Section 2.2.4. However, in this case, we decided to mount a setup in the optical bench, as displayed in Figure 2.13. Measurements were carried out using an integrating sphere (Labsphere RTC-060-SF), a halogen lamp (Ocean Optics, HL-2000) as the light source, and two spectrometers working in the visible (Ocean Optics, USB 2000+) and the near infrared (Ocean Optics, NIRQuest 512) regions of the electromagnetic spectrum as detectors. With this setup, we could confirm that the optical response of the samples was spatially homogeneous (~0.25 cm^2 spot size). Besides, in line with Figure 2.4b, the diffuse reflectance spectra revealed the high optical quality of the thin films due to the negligible fraction of diffusely scattered light. This feature assures the plane-parallel conditions of the interfaces of the samples that will serve to simplify the optical model.

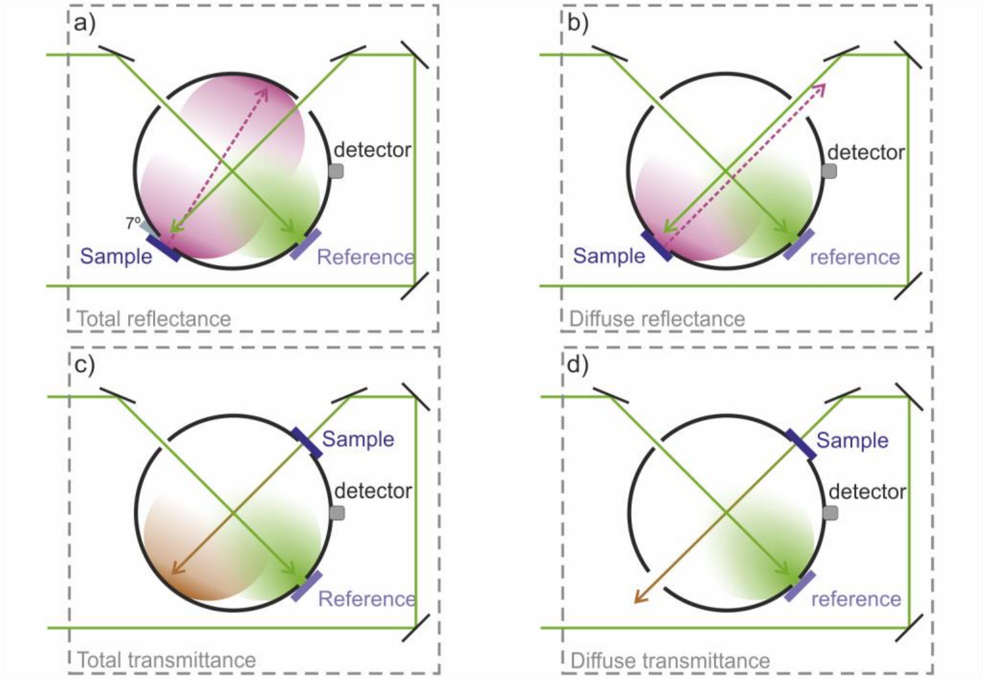

Figure 2.13. Set-up integrating sphere. Sketch of the experimental set-up employed to measure the spectral dependence of both the total and the diffuse reflectance and transmittance.

Since the optical quality of the films was assured, we then performed an angular characterization at specular incidence by using a commercial spectrophotometer (Cary 5000 in which a Universal Measurement Accessory, UMA, is attached). In particular, specular reflectance and transmittance at three different angles of the incident light beam, i.e. 6°, 30°, and 50°, for *s*- and *p*-polarized light, were obtained (see Figure 2.14). Spectral range measured is broad enough to observe sufficient optical features (200 nm < λ < 2000 nm).

2.5.2. Calculation of the complex refractive index

Based on the described characterization, we extracted Kramers-Kronig (K-K) consistent *n* and *k* parts of the complex refractive index (n+ik) of the $MAPbI_3$ films. To do so, we employed a homemade MatLab code based on the transfer matrix formalism to model the perovskite film. We considered air as the incoming and outgoing media and two layers: i) a perovskite film, and ii) a 1 mm-thick glass substrate. If necessary, we added an extra very thin layer consisting of perovskite and air to account for the surface roughness of the film. We used a Forouhi-Bloomer[41] model in the parametrization of Jobin Yvon[42] that consists of 3 oscillators (with E_i, f_i, Γ_i the position, strength and width of each oscillator, respectively), which has been already employed to account for the spectral dependence of the complex refractive index elsewhere.[43] This model is applicable to nanocrystalline semiconductors, and it makes use of as many oscillators as peaks are observed in the absorption spectrum of a material. With a genetic algorithm,[44] we simultaneously fitted to the TMM equations the angular dependence of the *s* and *p* polarizations of the reflectance and transmittance spectra for the two different thicknesses of perovskite films provided. As in the experiments, the calculation considered an incident wave vector that impinged perpendicularly to the electrode and therefore to the stacking of dielectric layers, although the description of angular and polarization effects would also be possible if necessary. To obtain the *R* and *T* of the cell, the intensity of the electric field in the incident and outgoing medium, respectively, were calculated by solving the set of equations established by imposing the continuity of the electric and magnetic fields across each interface. A full theoretical framework is provided in the theoretical notes (see Appendixes).

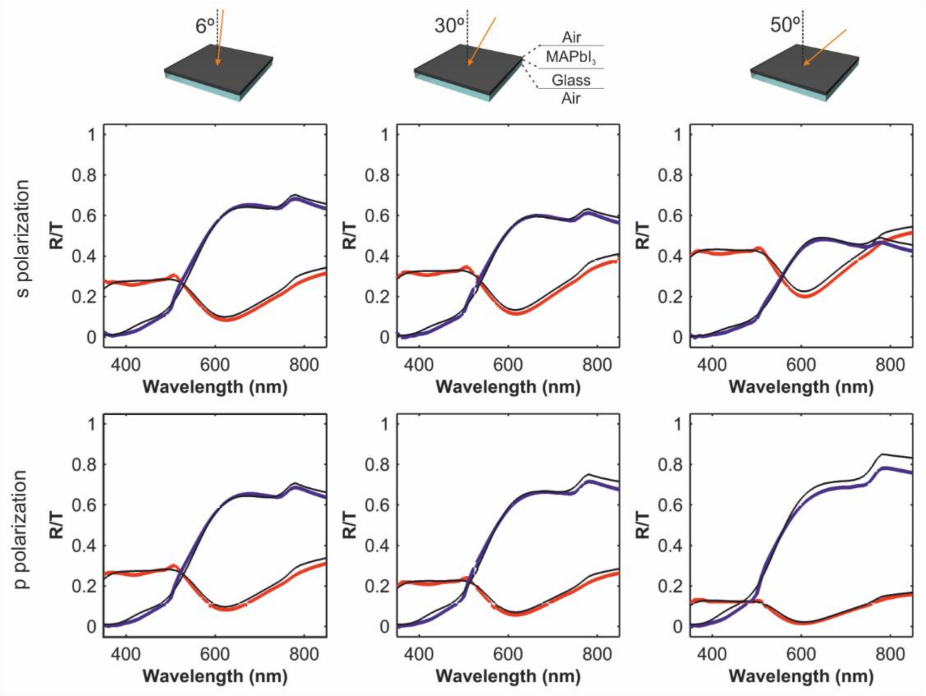

Figure 2.14. Fittings. Experimental (colour lines) and calculated (black lines) reflectance (red) and transmittance (blue) spectra of a 120 nm-thick $MAPbI_3$ film. *p* and *s* polarizations are shown.

Please note in Figure 2.14 the excellent agreement between experimental and calculated reflectance and transmittance for one of the $MAPbI_3$ layers. We show spectra from λ=400 nm to λ=850 nm, the region where the perovskite absorbs light. No degradation of the perovskite was observed during the full characterization process.

2.5.3. Analysis of the complex refractive index

The spectral dependence of *n* and *k* are shown in Figure 2.15a and 2.15b, respectively. Similar spectral shapes for the different samples are observed in the real and in the imaginary part of the refractive index. However, they show clear differences in their mean values. We attribute this discrepancy to the different experimental routes followed to prepare the perovskite absorber, even if they are all based on wet chemistry approaches. Recently, it has been publish an article suggesting there is a photo-induced change in reflectivity of the perovskites, but it is not the case in our study since intensities we use are several order of magnitudes lower.[45]

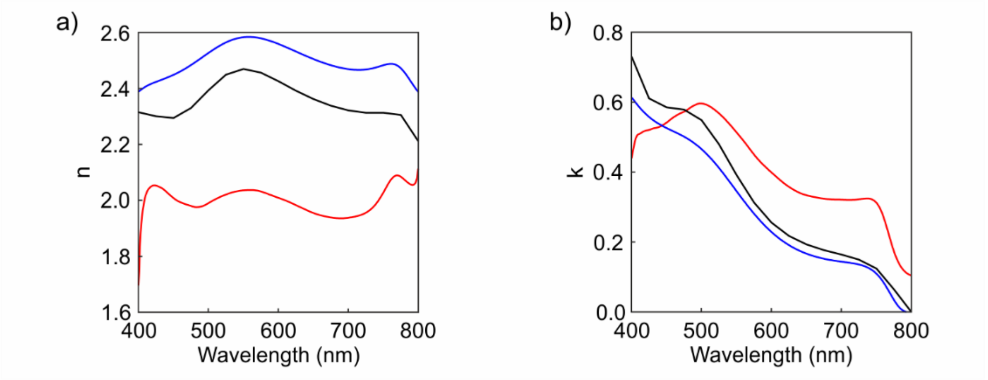

Figure 2.15. Optical constants of $MAPbI_3$ films. Spectral dependence of real (a) and imaginary part (b) of the herein calculated complex refractive index of the $MAPbI_3$ perovskite films developed according to Section 2.2. (blue lines), at the EPFL (black lines) and the University of Oxford (red lines).

We would like to highlight the case of the extinction coefficient, *k*, which is mainly responsible for the absorption of light by the perovskite material. The absorption onset is located at 780 nm regardless the origin of the sample and two preeminent regions can be distinguished. The first of them covers from 600 nm to 780 nm, and then an abrupt increase in the 500-600 nm range is observed. This behaviour indicates that the studied perovskite materials absorb significantly better in the blueish range than in the reddish one. Having said that, the material provided by the group of Prof Snaith ($PbAc_2$ route) is a better absorber. Indeed, its extinction coefficient does not even fall to zero for photon energies below the bandgap energy (E_g). However, far for being a favourable property, it reveals that there exist allowed electronic states within the E_g. These states could eventually give rise to traps that hamper the electronic performance of the perovskite. In conclusion, different preparation methods lead to different values of the optical constants of the $MAPbI_3$ perovskite, affecting light-matter interaction.

2.6. Conclusions

In summary, in this chapter we have studied the process of $MAPbI_3$ perovskite formation during annealing by simultaneously carrying out real-time *in-situ* structural and photophysical characterization. The combination of both types of experiments proves crucial to unveil different mechanisms taking place during the material formation. This latter comprises the nucleation of small crystallites (i), a transitional stage during which a large number of grain boundaries are formed as precursors vanish (ii), an actual crystal growth period where different crystals coalesce (iii) and a final stage (iv) where the material is eventually formed. Then, we have studied the photophysics of perovskite films under different atmospheres. A combination of photo-induced activation and darkening processes has been shown to determine their luminescence. By exposing the perovskite films to different atmospheres while optically pumping them, it has been isolated the predominant role of oxygen during the photo-activation and that of moisture in the photo-darkening. Finally, we have established a protocol with the objective of determining the spectral variation of the complex refractive index of the $MAPbI_3$ perovskite film. To this end, we fit the angular behaviour of the light reflected and transmitted by perovskite films by making use of a code based on the transfer matrix model in which n and k are variables. The application of a genetic algorithm accelerates the process and results in very accurate fittings. In particular, we have extracted the n and k values of $MAPbI_3$ perovskites for the first time. Indeed, we have observed that the synthetic routes employed to prepare the perovskite film has a strong impact on the optical behaviour of the final material. Further, we note that while applied for a specific synthetic route and material, the presented tools can be generalized to explore the optical behaviour of any metal halide perovskite (being solution or vacuum processed).

2.7. Notes

The photophysical characterization presented in Sections 2.3.1. and 2.3.2. has been performed in the facilities of the Photonic Crystals Group headed by Prof. Cefe López at the Institute of Materials Science of Madrid (Spanish National Research Council). I am very grateful for his kind reception during my secondment in his department in August 2015.

The $MAPbI_3$ perovskite films studied in Section 2.5. were provided by the groups headed by Prof Henry Snaith and Prof Anders Hagfeldt at the University of Oxford and the EPFL, respectively. I would like to thank them for their collaboration.

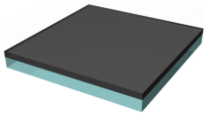

2.8. References

1 Kojima, A.; Teshima, K.; Shirai, Y.; Miyasaka, T. Organometal halide perovskites as visible-light sensitizers for photovoltaic cells. *J. Am. Chem. Soc.* **2009**, *131*, 6050–6051.

2 Im, J. H.; Lee, C. R.; Lee, J. W.; Park, S. W.; Park, N. G. 6.5% efficient perovskite quantum-dot-sensitized solar cell. *Nanoscale* **2011**, *3*, 4088–4093.

3 Chung, I.; Lee, B.; He, J., Chang, R. P. H.; Kanatzidis, M. G. All-solid-state dye-sensitized solar cells with high efficiency. *Nature* **2012**, *485*, 486–489.

4 Kim, H. S.; Lee, C. R.; Im, J. H.; Lee, K. B.; Moehl, T.; Marchioro, A.; Moon, S. J.; Humphry-Baker, R.; Yum, J. H.; Moser, J. E.; Grätzel, M.; Park, N. G. Lead iodide perovskite sensitized all-solid-state submicron thin film mesoscopic solar cell with efficiency exceeding 9%. *Sci. Rep.* **2012**, *2*, 591.

5 Lee, M. M.; Teuscher, J.; Miyasaka, T.; Murakami, T. N.; Snaith, H. J. Efficient hybrid solar cells based on meso-superstructured organometal halide perovskites. *Science* **2012**, *338*, 643–647.

6 Burschka, J.; Pellet, N.; Moon, S.-J.; Humphry-Baker, R.; Gao, P.; Nazeeruddin, M. K.; Grätzel M. Sequential deposition as a route to high-performance perovskite-sensitized solar cells. *Nature* **2013**, *499*, 316-319.

7 Jeon, N. J.; Noh, J. H.; Kim, Y. C.; Yang, W. S.; Ryu, S.; Seok, S. I. Solvent engineering for high-performance inorganic–organic hybrid perovskite solar cells. *Nat. Mater.* **2014**, *13*, 897-903.

8 Xiao, M.; Huang, F.; Huang, W.; Dkhissi, Y.; Zhu, Y.; Etheridge, J.; Gray-Weale, A.; Bach, U.; Cheng, Y.-B.; Spiccia, L. A. Fast deposition-crystallization procedure for highly efficient lead iodide perovskite thin-film solar cells. *Angew. Chem.* **2014**, *53*, 9898-9903.

9 Liu, M.; Johnston, M. B.; Snaith, H. J. Efficient Planar Heterojunction Perovskite Solar Cells by Vapour Deposition. *Nature* **2013**, *501*, 395-398.

10 Chen, C-W.; Kang, H-W.; Hsiao, S-Y.; Yang, P-F.; Chiang, K-M.; Lin, H-W. Efficient and uniform planar-type perovskite solar cells by simple sequential vacuum deposition. *Adv. Mater.* **2014**, *15*, 6647-6652.

11 Burschka, J.; Pellet, N.; Moon, S.-J.; Humphry-Baker, R.; Gao, P.; Nazeeruddin, M. K.; Grätzel M. Sequential deposition as a route to high-performance perovskite-sensitized solar cells. *Nature* **2013**, *499*, 316-319.

12 Jeon, N. J.; Noh, J. H.; Kim, Y. C.; Yang, W. S.; Ryu, S. and Seok, S. I. Solvent engineering for high-performance inorganic–organic hybrid perovskite solar cells. *Nat. Mater.* **2014**, 13, 897-903.

13 Cho, H.; Jeong, S-H.; park, M-H.; Kim, Y-H.; Wolf, C.; Lee, C-L.; Heo, J. H.; Sadhanala, A.; Myoung, N.; Yoo, S.; Im, S. H.; Friend, R. H.; Lee, T-W. Overcoming the electroluminescence efficiency limitations of perovskite light-emitting diodes. *Science* **2015**, *350*, 1222-1225.

14 Dualeh, A.; Tétreault, N.; Moehl, T.; Gao, P.; Nazeeruddin, M. K.; Grätzel, M. Effect of annealing temperature on film morphology of organic−inorganic hybrid pervoskite solid-state solar cells. *Adv. Funct. Mater.* **2014**, *24*, 3250−3258.

15 Saliba, M.; Tan, K. W.; Sai, H.; Moore, D. T.; Scott, T.; Zhang, W.; Estroff, L. A.; Wiesner, U.; Snaith, H. J. Influence of thermal processing protocol upon the crystallization and photovoltaic performance of organic−inorganic lead trihalide perovskites. *J. Phys. Chem. C.* **2014**, *118*, 17171-17177.

16 Tan, K. W.; Moore, D. T.; Saliba, M.; Sai, H.; Estroff, L. A.; Hanrath, T.; Snaith, H. J.; Wiesner, U. Thermally induced structural evolution and performance of mesoporous block copolymer-directed alumina perovskite solar cells. *ACS Nano* **2014**, *8*, 4730-4739.

17 Unger, L. E.; Bowring, A. R.; Tassone, C. J.; Pool, V. L.; Gold-Parker, A.; Cheacharoen, R.; Stone, K. H.; Hoke, E. T.; Toney, M. F.; McGehee, M. D. Chloride in lead chloride-derived organo-metal halides for perovskite-absorber solar cells. *Chem. Mater.* **2014**, *26*, 7158-7165.

18 Moore, D. T.; M.; Sai, H.; Tan, K. W.; Smilgies, D-M.; Zhang, W.; Snaith, H. J.; Wiesner, U.; Estroff, L. A. Crystallization kinetics of organic−inorganic trihalide perovskites and the role of the lead anion in crystal growth. *J. Am. Chem. Soc.* **2014**, *137*, 2350-2358.

19 Xiao, Z.; Dong, Q.; Bi, C.; Shao, Y.; Yuan, Y.; Huang, J. Solvent annealing of perovskite-induced crystal growth for photovoltaic-device efficiency enhancement. *Adv. Mater.* **2014**, *26*, 6503-6509.

20 Zhang, W.; Saliba, M.; Moore, D. T.; Pathak, S. K.; Hörantner, M. T.; Stergiopoulos, T.; Stranks, S. D.; Eperon, G. E.; Alexander-Webber, J. A.; Abate, A.; Sadhanala, A.; Yao, S.; Chen, Y.; Friend, R. H.; Estroff, L. A.; Wiesner, U.; Snaith, H. J. Ultrasmooth Organic–inorganic perovskite thin-film formation and crystallization for efficient planar heterojunction solar cells. *Nat. Commun.* **2015**, *6*, 6142.

21 Manser, J. S.; Reid, B.; Kamat, P. V. Evolution of organic-inorganic lead halide perovskite from solid-state iodoplumbate complexes. *J. Phys. Chem. C.* **2015**, *119*, 17065-17063.

22 Grancini, G.; Marras, S.; Prato, M.; Giannini, C.; Quarti, C.; Angelis, F. D.; Bastiani, M. D.; Eperon, G. E.; Snaith, H. J.; Manna, L.; Petrozza, A. J. The impact of the crystallization processes on the structural and optical properties of hybrid perovskite films for photovoltaics. *J. Phys. Chem. Lett.* **2014**, *5*, 3836−3842.

23 Moore, D. T.; Tan, K. W.; Sai, H.; Barteau, K. P.; Wiesner, U.; Estroff, L. A. Direct crystallization route to methylammonium lead iodide perovskite from an ionic liquid. *Chem. Mater.* **2015**, *27*, 3197-3199.

24 Galisteo-López, J. F.; Anaya, M.; Calvo, M. E.; Míguez, H. Environmental effects on the photophysics of organic−inorganic halide perovskites. *J. Phys. Chem. Lett.* **2015**, 6, 2200−2205.

25 Tian, Y.; Peter, M.; Unger, E.; Abdellah, M.; Zheng, K.; Pullerits, T.; Yartsev, A.; Sundström, V.; Scheblykin, I. G. Mechanistic insights into perovskite photoluminescence enhance-ment: light curing with oxygen can boost yield thousand fold. *Phys. Chem. Chem. Phys.* **2015**, 17, 24978−24987.

26 Fang, H.-H.; Adjokatse, S.; Wei, H.; Yang, J.; Blake, G. R.; Huang, J.; Even, J.; Loi, M. A. Ultrahigh sensitivity of methylammonium lead tribromide perov-skite single crystals to environmental gases. *Sci. Adv.* **2016**, 2, e1600534.

27 Xiao, M.; Huang, F.; Huang, W.; Dkhissi, Y.; Zhu, Y.; Etheridge, J.; Gray-Weale, A.; Bach, U.; Cheng, Y-B.; Spiccia, L. A Fast Deposition-Crystallization Procedure for Highly Efficient Lead Iodide Perovskite Thin-Film Solar Cells. *Angew. Chem.* **2014**, 53, 9898-9903.

28 Stranks, S. D.; Burlakov, V. M.; Leijtens, T.; Ball, J. M.; Goriely, A.; Snaith, H. J. Recombination kinetics in organic−inorganic perovskites: excitons, free charge, and subgap states. *Phys. Rev. Appl.* **2014**, *2*, 034007.

29 Yamada, Y.; Nakamura, T.; Endo, M.; Wakamiya, A.; Kanemitsu, Y. Photocarrier recombination dynamics in perovskite $CH_3NH_3PbI_3$ for solar cell applications. *J. Am. Chem. Soc.* **2014**, *136*, 11610−11613.

30 Baikie, T.; Fang, Y.; Kadro, J. M.; Schreyer, M.; Wei, F.; Mhaisalkar, S. G.; Graetzel, M.; White, T. J. Synthesis and crystal chemistry of the hybrid perovskite $(CH_3NH_3)PbI_3$ for solid-state sensitised solar cell applications. *J. Mat. Chem. A* **2013**, *1*, 5628-5641.

31 Zheng, Z.; Liu, A.; Wang, S.; Wang, Y.; Li, Z.; Lau, W. M.; Zhang, L. In situ growth of epitaxial lead iodide films composed of hexagonal single crystals. *J. Mat. Chem.* **2005**, *15*, 4555-4559.

32 Shen, D. et al. In situ growth of epitaxial lead iodide films composed of hexagonal single crystals. *J. Mat. Chem.* **2005**, 15, 4555-4559.

33 D'Innocenzo, V.; Kandada, A. R. S.; De Bastiani, M.; Gandini, M.; Petrozza, A. Tuning the light emission properties by band gap engineering in hybrid lead halide perovskite. *J. Am. Chem. Soc.* **2014**, *136*, 17730-17733.

34 Milot, R. L.; Eperon, G. E.; Snaith, H. J.; Johnston, M. B.; Herz, L. M. Temperature-dependent charge-carrier dynamics in $ch_3nh_3pbi_3$ perovskite thin films. *Adv. Funct. Mater.* **2015**, *25*, 6218-6227.

35 Hoke, E. T.; Slotcavage, D. J.; Dohner, E. R.; Bowring, A. R.; Karunadasa, H. I.; McGehee. M. D. Reversible photo-induced trap formation in mixed-halide hybrid perovskites for photovoltaics. *Chem. Sci.* **2015**, 6, 613.

36 Slotcavage, D. J.; Karunadasa, H. I.; McGehee, M. D. Light-induced phase segregation in halide-perovskite absorbers. *ACS Energy Lett.* **2016**, 1, 1199.

37 Brivio, F.; Caetano, C.; Walsh, A. Thermodynamic origin of photoinstability in the $ch_3nh_3pb(i_{1-x}br_x)_3$ hybrid halide perovskite alloy. *J. Phys. Chem. Lett.* **2016**, 7, 1083.

38 Barker, A.J.; Sadhanala, A.; Deschler, F.; Gandini, M.; Senanayak, S. P.; Pearce, P. M.; Mosconi, E.; Pearson, A. J.; Wu, Y.; Kandada, A. R. S.; Leijtens, T.; De Angelis, F.; Dutton, S. E.; Petrozza, A.; Friend, R. H. Defect-assisted photoinduced halide segregation in mixed-halide perovskite thin films. *ACS Energy Lett.* **2017**, 2, 1416.

39 Anaya, M.; Correa-Baena, J. P.; Lozano, G.; Saliba, M.; Anguita, P.; Roose, B.; Abate, A.; Steiner, U.; Grätzel, M.; Calvo, M. E.; Hagfeldt, A.; Míguez, H. Optical analysis of

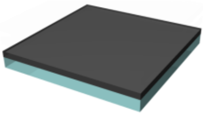

$CH_3NH_3Sn_xPb_{1-x}I_3$ absorbers: a roadmap for perovskite-on-perovskite tandem solar cells. *J. Mater. Chem. A* **2016**, *4*, 11214–11221.

40 Anaya, M.; Lozano, G.; Calvo, M. E.; Zhang, W.; Johnston, M. B.; Snaith, H. J.; Míguez, H. Optical description of mesostructured organic-inorganic halide perovskite solar cells. *J. Phys. Chem. Lett.* **2015**, *6*, 48–53.

41 Forouhi, A.; Bloomer, I. Optical dispersion relations for amorphous semiconductors and amorphous dielectrics. *Phys. Rev. B* **1986**, *34*, 7018−7026.

42 JobinYvon New Amorphous Dispersion Formula. http://www.horiba.com/fileadmin/uploads/Scientific/Downloads/OpticalSchool_CN/TN/ellipsometer/New_Amorphous_Dispersion_Formula.pdf.

43 Löper, P.; Stuckelberger, M.; Niesen, B.; Werner, J.; Filipič, M.; Moon, S.-J.; Yum, J.-H.; Topič, M.; De Wolf, S.; Ballif, C. Complex refractive index spectra of $CH_3NH_3PbI_3$ perovskite thin films determined by spectroscopic ellipsometry and spectrophotometry. *J. Phys. Chem. Lett.* **2015**, *6*, 66-71.

44 Jiménez-Solano, A.; Anaya, M.; Calvo, M. E.; Alcon-Camas, M.; Alcañiz, C.; Guillén, E.; Martínez, N.; Gallas, M.; Preussner, T.; Escobar-Galindo, R; Míguez, H. Aperiodic metal-dielectric multilayers as highly efficient sunlight reflectors. *Adv. Opt. Mater*. **2017**, *9*, 1600833

45 Price, M. B.; Butkus, J.; Jellicoe, T. C.; Sadhanala, A.; Briane, A.; Halpert, J. E.; Broch, K.; Hodgkiss, J. M.; Friend, R. H.; Deschler, F. Hot-carrier cooling and photoinduced refractive index changes in organic–inorganic lead halide perovskites. *Nat. Commun.* **2015**, *6*, 8420.

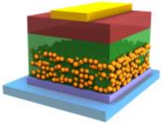

Chapter 3

Optical description of perovskite solar cells

This chapter is concerned with the optical model of solar cells based on $APbX_3$ *perovskite materials with the aim of correlating their optical behaviour with the performance of actual solar devices. First, we model the mesostructured perovskite solar cell to study the optical effects that arise from the presence of all layers comprising the device. Results are in very good agreement with the experimental reflectance, transmittance and absorptance spectra of actual cells. Then, we discuss the case of state-of-the-art solar cells based on a mixed-cation mixed-halide lead perovskite. The possibility of calculating the electric field distribution along the cells ensures extraction of accurate absorption profiles. This leads to interpret the scaffold effect and the perovskite grain size in the optical behaviour of the devices. This chapter hence opens an avenue for the optical design of perovskite solar cells with either improved efficiency or aesthetical aspect, which will be presented in next chapters.*

3.1. Introduction

Not long after their inception, as commented before, perovskite solar cells were already striding ahead in the emerging PV efficiency race, having reached in the last years certified efficiency values that significantly surpass those attained for all other cells based on solution-processed materials, and rapidly approaching existing commercial thin-film technologies.[1] On one hand, improvements of the morphology and crystallinity of the perovskite thin films, and their proper encapsulation, as discussed in Chapter 2,[2,3] have favoured this rapid progress.[4-6] On the other hand, new charge-selective materials and device architectures have pushed the performance of this technology even further.[7-10]

Another route to boost the efficiency of solar cell devices consists in the optimization of their optical design to maximize light harvesting and charge collection.[11] In this regard, a detailed description of the optical behaviour of the perovskite device was missing at the beginning of my doctorate. Of course, this was related to the early stage of the technology. Especially, there existed a misunderstanding of the optical behaviour of the material. In this regard, in Chapter 2, we developed a rigorous study of the optical properties of perovskite films and presented the first report of the optical constants of the $MAPbI_3$ perovskite. This opened up new possibilities to understand the optical behaviour of solar cells based on this material.

In this chapter, we will present an optical model of the PSC based on the TMM. We will confirm the theoretical calculations with experimental measurements from actual devices that we fabricate following already reported methods. Finally, we will employ the aforementioned tools in order to model and characterize state-of-the-art PSCs in which a clear interplay between morphology of the perovskite film and optoelectronic performance of the device is established.

3.2. Optical description of mesostructured perovskite solar cells

In this section, we will present an optical model of the complete perovskite photovoltaic device. We will focus on the mesostructured PSC since champion devices in the field are recurrently achieved with this architecture. General conclusions can be directly extended to the whole typologies of solar cell architectures, with only slight spectral differences arising.

3.2.1. Fabrication of the device

In order to confirm the calculations, we fabricated a PSC that follows the scheme shown in Figure 3.1. To do so, we employed an already reported procedure, which uses the $PbCl_2$ route to prepare $MAPbI_3$ perovskite.[12]

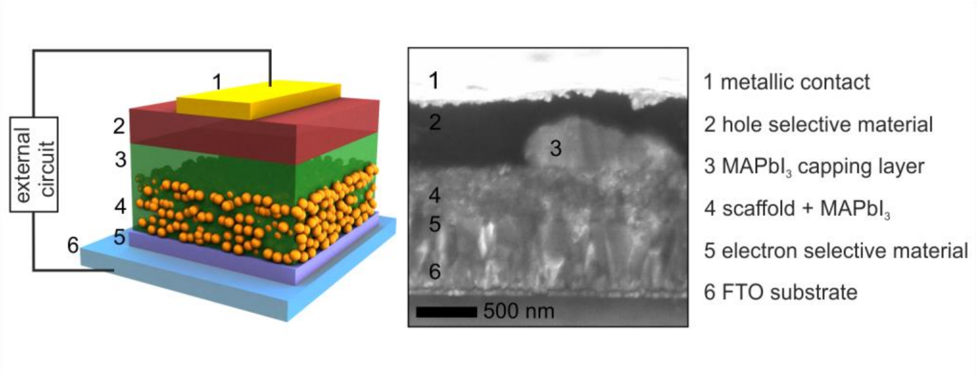

Figure 3.1. Schematic and Scanning Electron Microscopy micrograph of the device.

First of all, a FTO patterned glass (Pilkington TEC 7, 7 Ω/sq) was cleaned sequentially in Hellmanex, milliQ water, acetone, ethanol and oxygen plasma. Then, a TiO_2 compact layer was deposited by spin coating a 253 mM titanium isopropoxide (diluted in a mildly acidic anhydrous ethanol solution) at a speed of 2000 rpm for 60 s followed by sintering at 500°C during 45 minutes. This TiO_2 compact layer acted as electron selective material, thus blocking holes and avoiding short circuits in the device.

After cooling the structure to room temperature, an Al_2O_3 layer was spin coated at 2500 rpm for 45s. To this end, a colloidal dispersion of Al_2O_3 nanoparticles with a diameter <50 nm (Sigma-Aldrich, product number 702129) was diluted in ethanol in a 1:2 volume ratio. Since this layer served as scaffold for the perovskite precursors, it was dried at 150°C to evaporate any remaining solvent that could be a potential degradation source for the perovskite. To fabricate the solar cells, Al_2O_3 scaffolds were infiltrated using a 40 wt% perovskite solution prepared according to Section 2.2.1. A spin-coating program at 2000 rpm for 45 s was performed in a nitrogen-filled glovebox. After the spin-coating process, samples were annealed at 100°C for 2 hours to assure a complete crystallization of the perovskite structure.

The hole selective layer was Spiro-OMeTAD. It was diluted in a 80 mM chlorobenzene solution containing additives of lithium bis(trifluoromethanesulfonyl)imide and 4-tert-butylpyridine. It was spun at 2000 rpm for 60 s in the nitrogen-filled glovebox and kept drying overnight in a drybox. This long time was experimentally proven to be beneficial for the performance of the cell since Spiro-OMeTAD requires hours to be properly oxidized. Finally, gold electrodes were thermally evaporated under a pressure of 10^{-6} Torr at a rate of 0.1 nm/s, to complete the devices.

3.2.2. Performance of the device

We conducted a photovoltaic characterization of the devices in order to confirm their validity prior to accomplish an exhaustive optical description. As displayed in Figure 3.2a, we measured current density-voltage, I-V, curves (Keithley Instruments, 2400 Series SourceMeter) under simulated AM 1.5 sunlight at 100 $\text{mW}\cdot\text{cm}^{-2}$ irradiance generated by an Abet Class AAB sun 2000 simulator. The intensity was calibrated with an NREL-calibrated KG5 filtered Si reference cell. The mismatch factor was calculated to be less than 1%. The solar cells were masked with a metal aperture to define the active area, typically 0.0625 cm^2 (measured individually for each mask). We employed a light-tight sample holder to minimize any edge effects and ensure that the reference and test cells were located in the same spot under the solar simulator during measurement. The fabricated PSCs were stable for minutes (see Figure 3.2b) with efficiencies approaching 14% (2014). These properties were reproducible for a batch of 25 devices.

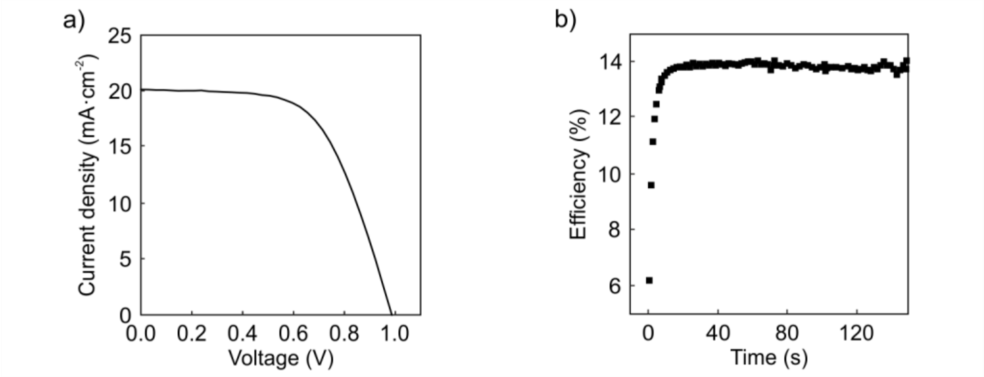

Figure 3.2. Photovoltaic characterization. I-V (b) and stabilized power output (c) of a typical device.

3.2.3. Optical model of the device

The perovskite cell was modeled through a layered structure, as depicted in Figure 3.1. To this end, we adapted the TMM-based code presented in Section 2.5.2. As it was mentioned before, the incoming and outgoing media were considered to be air. In the model, the optical effects that arise from the presence of all layers comprising the PV device were accounted for. The optical constants of the different constituents of the stack, i.e. glass, FTO, TiO_2, Spiro-OMeTAD and Au, were taken from literature.[13-15] As discussed in Section 2.5, there

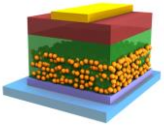

are a broad variety of chemical routes to attain the $MAPbI_3$ perovskite. Since they result in different optical features, the determination of the particular n and k is crucial to understand light propagation in solar cells based on them. In the case of the perovskite employed in this device, the spectral dependence of the complex refractive index is analogous to the one represented in red line in Figure 2.15 ($PbAc_2$ route).

We employed an effective medium approximation to account for different features observed in the SEM image from Figure 3.1: i) the rough FTO surface coated by the thin compact layer, ii) the perovskite infiltrated mesostructured scaffold, and iii) the non-uniform nature of the interface between the perovskite capping layer and the Spiro-OMeTAD layer. In order to determine the effective refractive index of such media, we considered different equations, i.e. volume-weighted average, Bruggeman, and Maxwell-Garnett. Regarding i) and iii), in view of the cross sections observed in the SEM, considering an equal contribution to the refractive index of the transition middle layer from the materials at both sides of the interface seemed reasonable. In the case of the mesostructured Al_2O_3 scaffold, a 46% porosity prior to perovskite infiltration was attained from the fitting of its experimental reflectance, assuming that the thickness and the permittivity of alumina layer were estimated from SEM images and obtained from the scientific literature,[16] respectively. The very similar results attained from the different effective medium equations employed led us to consider the simplest approximation, i.e. the volume-weighted average, to calculate the effective optical constants.

3.2.3.1. Reflectance, transmittance and absorptance of the device

The theoretical model served to describe the optical response, i.e. R, T and A, of the cell shown as, respectively, red, blue, and black dashed lines in Figure 3.3. Total absorptance was determined as the fraction of light that was neither reflected nor transmitted as $A=1-R-T$. Measurements performed in an integrating sphere (see Section 2.5.1) showed that the A of the device reaches values above 90% at 500 nm, where the extinction coefficient of the perovskite is maximum, showed values above 80% from 400 to 700 nm, and significantly diminished at around 800 nm, at the edge of electronic bandgap of the perovskite.

A genetic algorithm was employed to fit the experimental R and T. We considered the thickness of the different layers comprising the multilayer stack as fitting parameters. The values extracted from SEM images were taken as initial values. Fair agreement between theory (dashed lines) and experiment (solid lines) was found as displayed in Figure 3.3. It can be clearly seen the correspondence between experimental and theoretical spectral features in R, T, and A. As the wavelength increases, the extinction coefficient of the perovskite diminishes and both *R* and *T* increase. It is important to mention that the model does not account for the effect of diffuse scattering. In fact, the diffuse reflectance may well explain the small discrepancy observed between measured and calculated *R* and, consequently, between measured and calculated *A* in the spectral range 700<λ<800 nm. This resulted in an overestimation of the fraction of light absorbed by the device at those wavelengths. Note that the solar radiation in this range is greatly reduced, and therefore the impact of the inaccuracy of the model in the overall response of the solar cell is not significant.

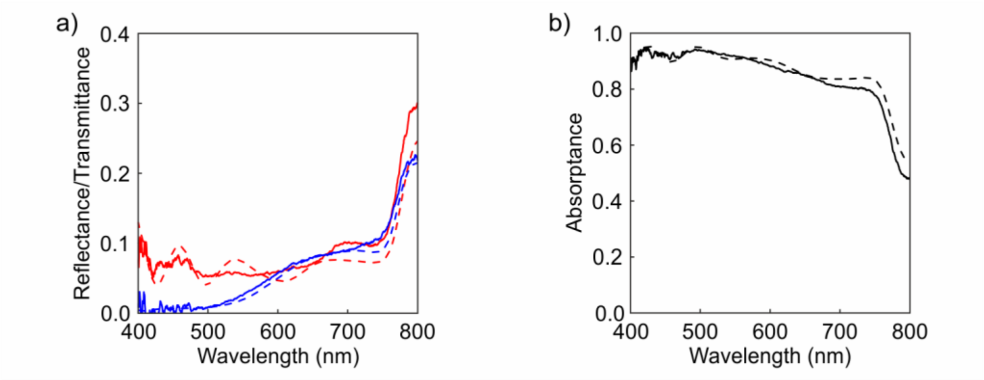

Figure 3.3. Reflectance, transmittance and absorptance of a PSC. a) Reflectance (red lines) and transmittance (blue lines) spectra calculated (dashed lines) and measured (solid lines) from a representative device. b) Corresponding total absorptance obtained by the expression 1-R-T.

3.2.3.2. Absorption profile in the device

Since the light absorbed in the device is responsible for the generated current, we performed an exhaustive analysis in this direction. The developed optical model allows calculating the spatial distribution of the square magnitude of the electric field in the device and correlating it with the absorption of light. Figure 3.4a shows the calculated spatial (vertical axis) and spectral (horizontal axis) distribution of the electric field intensity enhancement ($|E|^2/|E_0|^2$), i.e. near-field intensity normalized by the incident intensity, along a cross section of the PV device. Light impinges from the bottom of the scheme. The glass-FTO interface is sited at y=0 nm. The interference of all beams reflected and transmitted at each interface determines the way in which the radiation distributes over the solar cell for each wavelength. Different wavelengths propagate distinctly through the device.

We can observe that the intensity at 500 nm decreases very rapidly in the absorbing perovskite filling the scaffold voids until it vanishes within the perovskite capping layer. In contrast, at 750 nm, where the extinction coefficient of the perovskite absorber reduces, the penetration of the optical field in the device is significantly larger. The incoming light reaches the last layers of the solar cell, which yields a non-zero transmittance (see Figure 3.3).

The calculation of the spatial distribution of the electric field intensity inside the solar cell allows computing the fraction of light absorbed by each constituent of the PV device (A_j) according to

$$A_j = 2\pi \int_{x_j}^{x_{j+1}} \frac{I(x_j, \lambda)}{I_0(\lambda)} \frac{2n_j k_j}{\lambda} dx_j \tag{3.1}$$

, where the subscript j refers to each layer comprising the cell, and λ is the wavelength of the radiation. The integral extends over the volume occupied by each medium, which can be reduced to one dimension (x_j) due to the symmetry of the system. The right panel in Figure 3.4a displays the absorption profile in the PSC. Although light is mainly absorbed in the regions occupied by perovskite, there is a non-negligible amount of light absorbed in other domains.

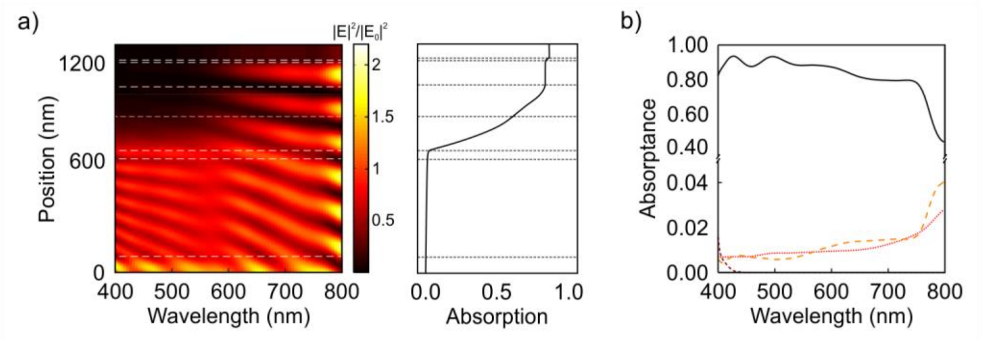

Figure 3.4. Absorption profile in a PSC. a) Calculated spatial (vertical axis) and spectral (horizontal axis) distribution of the electric field intensity enhancement along a cross section of the perovskite solar cell. Horizontal dashed lines are guides to the eye to delimit the interfaces between media in the device. From top to bottom: air, Au, Spiro-OMeTAD, perovskite capping layer, perovskite-infiltrated Al_2O_3 scaffold, TiO_2 compact layer and FTO. Right panel shows the absorption profile in the device. b) Spectral dependence of the fraction of light absorbed by the different absorbing materials comprising the device: FTO (red dotted line), Spiro-OMeTAD (brown short dashed line), perovskite (black solid line), and Au (orange dashed line).

In Figure 3.4b, we disclose the fraction of light absorbed by the different absorbing materials that constitute the cell, i.e. FTO, Spiro-OMeTAD, perovskite, and Au. Thus, the model permits one to quantify the optical losses in a perovskite solar cell, and discriminate between productive and parasitic, or non-productive, absorption in the other component layers. The solar spectrum weighted integrated absorptance (*SSWIA*),

$$SSWIA = \frac{\int_{400}^{800} A(\lambda) \cdot AM1.5(\lambda)\, d\lambda}{\int_{400}^{800} AM1.5(\lambda)\, d\lambda} \tag{3.2}$$

defined as the fraction of light absorbed by the perovskite weighted across the solar spectrum, between 400 nm to 800 nm, is 82.9% for the cell under investigation. Note that the total fraction of non-productive light absorbed is below 6% throughout the spectrum, being around 2% at 500 nm. This means that light harvested within the PSC is very high. In contrast, the specular reflectance is above 5% across the spectrum, reaching values as high as 15% at 750 nm.

3.2.3.3. Scaffold effect on the optical performance of the device

We made use of the theoretical model to extrapolate the *SSWIA* of devices featuring infiltrated mesostructured Al_2O_3 scaffolds as a function of the thickness of the HSL. In Figure 3.5a, it can be observed that the *SSWIA* is larger for thicker scaffolds, due to a larger amount of perovskite material. More interestingly, the *SSWIA* shows an oscillatory behaviour with the Spiro-OMeTAD layer thickness for a fixed scaffold. Similar oscillatory profiles were attained for scaffolds of different thickness. As an example, in a 300 nm-thick perovskite infiltrated scaffold, the *SSWIA* is 72% for cells comprising a HSL with thickness of 100 or 320 nm, whereas it reaches 75% for a 220 nm-thick HSL. Hence, a complete description of layer thicknesses is necessary in order to architecture high efficient devices.

Moreover, we investigated the performance of the device under different scaffold compositions. In particular, we calculated the fraction of the light absorbed by perovskite ($A_{perovskite}$) when the scaffold is a 300 nm-thick layer of Al_2O_3, SiO_2 or TiO_2 (see Figure 3.5b). The differences observed are attributed to the different refractive indices of the scaffolds, being n_{TiO2} the highest and n_{SiO2} the lowest in the visible range among the materials considered. One may notice that the larger the refractive index, the higher the reflectance, and therefore, the lower the absorptance of light. Such variations can be further quantified through the *SSWIA* parameter, attaining values of 72%, 75% and 76%, for the perovskite infiltrated TiO_2, Al_2O_3 and SiO_2 scaffolds, respectively.

In Figure 3.5b, we also plot the $A_{perovskite}$ for a solar cell that integrates a solid perovskite film of the same thickness (300 nm). The presence of a larger amount of perovskite absorber leads to almost full absorption, reaching a *SSWIA* value as high as 88%. The model also served to calculate the thickness of the scaffold that would provide a similar *SSWIA*, attaining thickness values of 600, 570 and 540 nm for mesostructured scaffolds made of TiO_2, Al_2O_3 and SiO_2, respectively. In conclusion, this analysis provides the possibility of finding the material features needed to attain mesostructured PSCs in which light harvesting is as efficient as in flat PSCs.

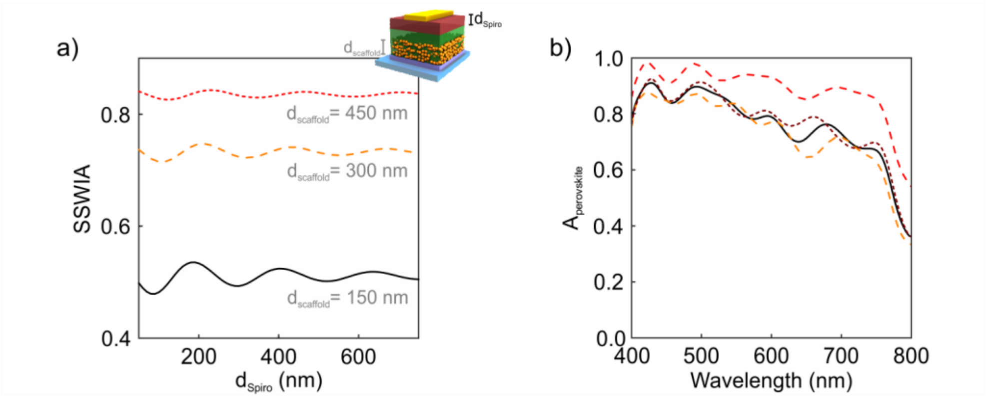

Figure 3.5. Scaffold effect in a PSC. a) Calculated solar spectrum weighted integrated absorptance (*SSWIA*) as a function of the Spiro-OMeTAD layer thickness for photovoltaic devices comprising perovskite-infiltrated mesoporous Al_2O_3 scaffolds with a thickness of 150 nm (black solid line), 300 nm (orange dashed line), and 450 nm (red short dashed line). b) Spectral dependence of the productive absorptance ($A_{perovskite}$) of solar cells, in which the perovskite infiltrates a 300 nm-thick mesostructured scaffold made of: SiO_2 (brown short-dashed line), Al_2O_3 (black solid line) and TiO_2 (orange dashed line). For comparison we present (red dashed line) the $A_{perovskite}$ of a solar cell that integrates a solid perovskite film of the same thickness, i.e. 300 nm. We note that the perovskite absorber only occupies 50% of the volume within the photoactive region and that there is no capping layer considered in the calculations.

3.3. Optical description of state-of-the-art perovskite solar cells

Several studies have focused on the effect of perovskite morphology on its electro-optical properties.[17-19] Although they indicated a strong dependence on the crystal size, a comprehensive study on the relation to one another in an actual PSC was missed. For this reason, in this section we will present how the electro-optical characteristics of the devices rely on the thickness of the perovskite capping layer, which in turn determines the grain size. We will perform optical calculations and compare them with the electro-optical characterization of PSCs based on a mixed-halide mixed-cation material (from now on referred to as 'mixed perovskite') that have been prepared by the group of Prof Anders Hagfeldt. These devices are considered state-of-the-art in the field, reaching PCE values approaching 22%. In consequence, results herein discussed have strong implications for the eventual implementation of PSCs with efficiencies competing with those achieved by mature technologies such as silicon PV.

3.3.1. Notes concerning the material

The mixed perovskite was comprised of two organic cations and two halide anions. The former was a combination of $HC(NH_2)_2^+$ (formamidinium, FA) and MA, while the latter was a combination of Br and I. The final chemical formula was $FA_{0.85}MA_{0.15}Pb(I_{0.85}Br_{0.15})_3$.[20]

On this basis, PSCs were prepared in a typical stack very similar to the one shown in Figure 3.1: glass/FTO/TiO_2/mesoporous-TiO_2/mixed perovskite/Spiro-OMeTAD/gold. Here, the compact TiO_2 and the thin mesoporous TiO_2 layers were used as ESL since this material gives rise to better PSCs efficiencies.[20] The Spiro-OMeTAD was used as HSL. By varying the concentration of the perovskite precursor solution, the thickness of the perovskite capping layer was varied. Figure in the Appendix D summarizes the change in perovskite thickness, as extracted from SEM micrograph. As clearly seen in the cross-sectional images, perovskite capping layers from 40 nm to 480 nm sat atop the perovskite-filled mesoporous layer. Another effect associated to the thickness variation was observed for the crystal size in the capping layer. From the top view of the perovskite films (see Appendix D), it was concluded that the smallest crystals were about 40 nm in size and the largest ones about 400 nm, as the perovskite layer thickness was increased. Perovskite crystals for the thickest samples (380 and 480 nm) grew as a single grain from the top of the mesoporous ESL to the HSL (this metric will be used throughout the text), scaling with perovskite capping layer thickness. For samples with thinner layers, it was not very clear whether single crystals were sandwiched between the contacts or if there were a few crystals on top of each other. However, it could be deduced that only one or a few crystals were found in this dimension of the capping layer. Therefore, we could study the optical properties of small and large crystals by varying the thickness of the mixed perovskite.

3.3.2. Optical constants of mixed perovskite

Throughout this thesis, the optical constants of each particular perovskite compound have proven to be highly dependent on the synthetic route employed. This behaviour will be even more noticeable when changing the perovskite composition, as is the case herein. The protocol described in Section 2.5 allowed us to extract *n* and *k* for the $FA_{0.85}MA_{0.15}Pb(I_{0.85}Br_{0.15})_3$ from the simultaneous fitting of the reflectance and transmittance spectra measured from perovskite films of different thicknesses.

Good agreement was found between the calculated and measured absorptance spectra as displayed in Figure 3.6a. The spectral dependence of the extracted *n* and *k* values is shown in Figure 3.6b. The absorptance onset for this mixed perovskite material is at 780 nm. An enhancement in the extinction coefficient of the mixed absorber is observed throughout the visible range, reaching values as high as 20% in comparison with standard $MAPbI_3$. Mixed perovskite thus showed improved optical properties, which should translate to improved current densities in a PSC.

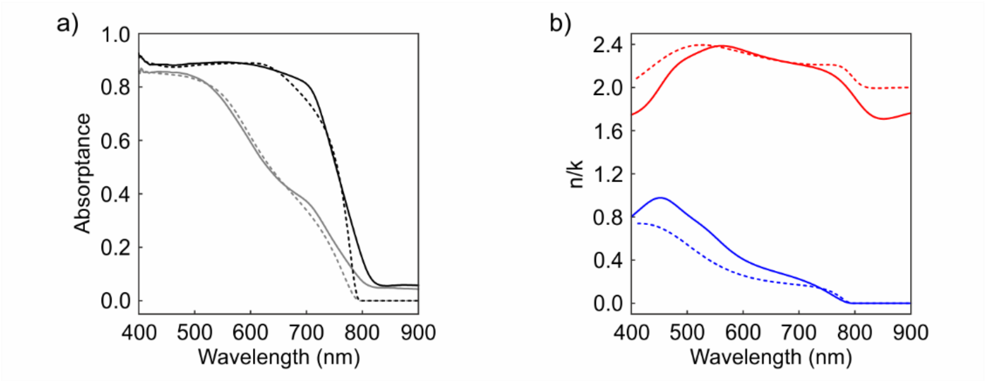

Figure 3.6. *n* and *k* values for the mixed perovskite. Absorptance spectra measured (solid lines) and calculated (dashed lines) from mixed perovskite films with thicknesses of 200 nm (grey) and 400 nm (black). Spectral dependence of the real (n, red lines) and imaginary (k, blue lines) parts of the complex refractive index for $MAPbI_3$ (dashed) and mixed (solid) perovskites.

3.3.3. Optical characterization of mixed perovskite-based solar cells

Direct measurements of the spectral dependence of the fraction of light absorbed from full devices using different mixed perovskite capping layer thicknesses are displayed in Figure 3.7a. The absorptance of the cells at wavelengths below 500 nm was close to 95% regardless of the perovskite layer thickness. This originates from the high values of the imaginary part of the complex refractive index of the mixed perovskite (see Figure 3.6b) and, to a lesser extent, from the parasitic absorption generated in the transparent conductive oxide layer and in the gold contact, especially for the thinnest devices. As a result, nearly all light transmitted through the substrate in the blue was absorbed within the PSC. In contrast, between 500 nm and 795 nm, where the extinction coefficient of the perovskite reduces, the fraction of the incident light absorbed by the cell increased with the perovskite thickness. Notice that a saturated behaviour was found for a perovskite capping layer thickness of 480 nm, for which the absorptance reached values as high as 95% from 400 nm to 740 nm.

3.3.4. Quantum efficiency of mixed perovskite-based solar cells

In order to have a complete picture on how the perovskite grain size influenced the electro-optical performance of the devices, we carried out a characterization of their external quantum efficiency (*EQE*). *EQE* is defined as the ratio of collected carriers to the incident photons in a device and we carried out an experiment on the optical bench to obtain its spectral behaviour. We set up a 300 W Xenon lamp, controlled by a digital scan drive system (McPherson 789A-3), that provided a white light source. A monochromator with a 1140 g/mm grating (McPherson 272) was employed to select the light wavelength with which the devices where excited. Second order harmonics arising from the monochromator were removed by a short pass filter with a cut-off wavelength of 400 nm. With the aim of getting absolute values, a calibrated silicon photodiode (D8-Si-100 TO-8 detector, Sphere Optics) was employed to correct the measurements.

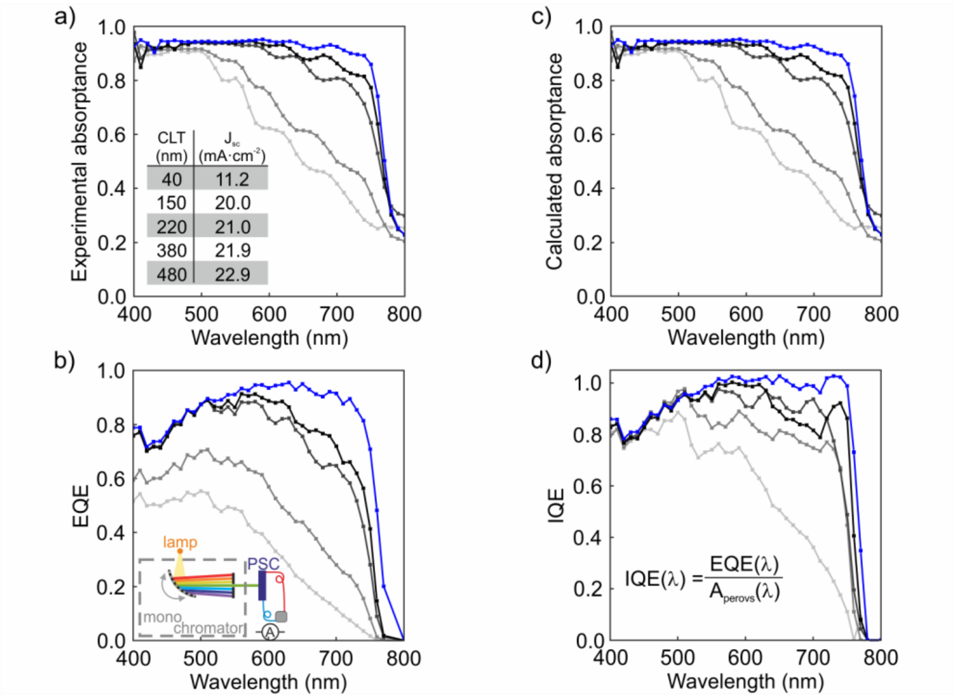

CLT (nm)	J_{sc} (mA·cm^{-2})
40	11.2
150	20.0
220	21.0
380	21.9
480	22.9

Figure 3.7. Quantum efficiency of mixed perovskite solar cells. Spectral dependence of the experimental absorptance (a), external quantum efficiency (b), calculated absorptance (c) and internal quantum efficiency (d) of devices in which different 'mixed' perovskite capping layer thicknesses have been deposited. Grey-to-black curves represent increments in thickness of the perovskite capping layer: 40 nm, 150 nm, 220 nm and 380 nm. Blue curve corresponds to the optimized case in which a 480 nm thick 'mixed' perovskite capping layer is employed to maximize light absorption. Inset in (a) displays the dependence of the measured short circuit current on the perovskite capping layer thickness (CLT). Inset in (b) shows a sketch of the setup employed to measure the external quantum efficiency. For the sake of clarity, in (d), we display the formula that led us to determine the internal quantum efficiency.

The spectral dependence of the *EQE* of the devices is presented in Figure 3.7b. The area under each curve, which represents the number of carriers created by the device under solar illumination at no bias (that is the so-called short circuit current, J_{SC}), increases with the capping layer thickness (see inset of Figure 3.7a), as it is expected from the absorptance measurements. The extremely high optical quality of the layers comprising the devices enables the observation of spectral fringes arising from the interference between light reflected and transmitted at the different interfaces of the cell. Indeed, the *EQE* spectrum measured for each perovskite thickness features well-defined oscillations matching the ones noted in the absorptance curves. Please notice that *EQE* deviation from 100% could be the result of two complementary effects: i) the reflected and the non-productively absorbed light, and ii) the imperfect collection of charges photogenerated in the mixed perovskite. While designing appropriate antireflective and non-absorbing materials can overcome the formers, respectively, the latter is an intrinsic property of the active material.

In order to gain insight into the way these cells made use of the absorbed light, we modelled the device as described in the previous section. In this case, we assigned the following thicknesses to the different layers comprising the devices: 1 mm of glass substrate, 650 nm of FTO layer, 50 nm of TiO_2 compact layer, 85 nm of 50% porous TiO_2 scaffold fully infiltrated by perovskite, 40-480 nm of perovskite capping layer, 240 nm of Spiro-OMeTAD, and 50 nm of gold contact. The model, which did not account for crystal size variations, fairly reproduced the absorptance measured from the complete devices (see Figure 3.7c). Furthermore, it allowed the discrimination of the fraction of light absorbed only by the mixed perovskite (A_{perovs}) by applying equation 3.1. This opened the way to determine the internal quantum efficiency (*IQE*),

$$IQE(\lambda) = \frac{EQE(\lambda)}{A_{perovs}(\lambda)} \tag{3.3}$$

as shown in Figure 3.7d for the different devices under analysis. This parameter is fundamental to knowing how adequately the photogenerated carriers are extracted from a device. For thick perovskite capping layers, the *IQE* was close to 100% from 500 to 770 nm, indicating that photogenerated carriers were collected with equal efficiency at both contacts. In contrast, *IQE* values diminished considerably as the thickness of the perovskite layer decreased. This feature can be associated to the reduction of perovskite crystal size affecting the electric properties of the material. On top of this, *IQE* reduced at shorter wavelengths (below 500 nm), which did not originate from a lower optical absorption. Consequently, such behaviour could be due to absorption into lead iodide states or should find an explanation in the efficiency of injection, transport or collection of photogenerated carriers close to the ESL/perovskite interface where charges were predominantly generated by blue light.

3.4. Conclusions

In conclusion, we have extended the optical model with the aim of describing the optical behaviour of complete solar devices. The theoretical results were confirmed with experimental measurements from mesostructured solution-processed $MAPbI_3$ devices. Nevertheless, the proposed model could be also employed to describe the optical response of planar heterojunction solar cells prepared by evaporation or wet approaches, as it was done in contemporaneous works.[21,22] It serves to visualize the spatial distribution of the radiation within the cell, which allows quantifying the fraction of light absorbed by each constituent of the device. Furthermore, we have extrapolated the model to estimate the influence of the HSL and the scaffold on the light harvesting of solar radiation by the PV device. Finally, we have analysed the electro-optics of state-of-the-art mixed PSCs. We have found that the trend and spectral features of the optoelectronic performance of the devices were strongly influenced by the perovskite grain size, which is dependent on the capping layer thickness. we model the optical behaviour of the systems in order to discern the radiation that actually contributes to generate photocurrent in the devices. This allows us to perform an accurate estimation of the *IQE* of the solar cell and conclude that bigger perovskite grains give rise to an enhanced charge extraction. The results discussed in this chapter hence open a new avenue for the optical design of PSCs with improved performance. In this regard, in the next two chapters, we will show examples in which we optimize optically the device architecture in order to either boost its efficiency or provide it with better aesthetical aspect.

3.5. Notes

The synthesis of materials and fabrication of devices carried out in Section 3.2. was performed throughout a secondment (June 2014) at the Photovoltaic and Optoelectronic Device Group led by Prof Henry Snaith. I appreciate his kind reception and Dr Wei Zhang's guidance during my stay. I would also like to acknowledge Dr Juan Pablo Correa-Baena for supplying me the devices analysed in Section 3.3.

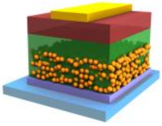

3.6. References

1 Research Cell Efficiency Records. NREL (http://www.nrel.gov/ncpv/).

2 Anaya, M.; Galisteo-López, F. J.; Calvo, M. E.; López, C.; Miguez, H. Photophysical analysis of the formation of organic-inorganic trihalide perovskite films: identification and characterization of crystal nucleation and growth. *J. Phys. Chem. C*, **2016**, *120*, pp 3071–3076.

3 Galisteo-López, J. F.; Anaya, M.; Calvo, M. E.; Míguez, H. Environmental Effects on the Photophysics of Organic-Inorganic Halide Perovskites. *J. Phys. Chem. Lett.* **2015**, *6*, 2200−2205.

4 Jeon, N. J.; Noh, J. H.; Kim, Y. C.; Yang, W. S.; Ryu, S.; Seok, S. Solvent engineering for high-performance inorganic–organic hybrid perovskite solar cells. *Nat. Mater*. **2014**, *13*, 897-903.

5 Xiao, M.; Huang, F.; Huang, W.; Dkhissi, Y.; Zhu, Y.; Etheridge, J.; Gray-Weale, A.; Bach, U.; Cheng, Y. B.; and Spiccia, L. A fast deposition-crystallization procedure for highly efficient lead iodide perovskite thin-film solar cells. *Angew. Chemie Int. Ed.* **2015**, *53,* 9898–9903.

6 Bella, F.; Griffini, G.; Correa-Baena, J.-P.; Saracco, G.; Grätzel, M.; Hagfeldt, A.; Turri, S.; Gerbaldi, C. Improving efficiency and stability of perovskite solar cells with photocurable fluoropolymers. *Science* **2016**, *354*, 203-206.

7 Liu, M.; Johnston, M. B.; Snaith, H. J. Efficient planar heterojunction perovskite solar cells by vapour deposition. *Nature* **2013**, *501*, 395-398.

8 Heo, J. H.; Im, S. H.; Noh, J. H.; Mandal, T. N.; Lim, C.-S.; Chang, J. A.; Lee, Y. H.; Kim, H.; Sarkar, A.; Nazeeruddin, et al. Efficient inorganic-organic hybrid heterojunction solar cells containing perovskite compound and polymeric hole conductors. *Nat. Photon.* **2013**, *7*, 486-491.

9 Zhou, H.; Chen, Q.; Li, G.; Luo, S.; Song, T.; Duan, H.-S.; Hong, Z.; You, J.; Liu, Y.; Yang, Y. Interface engineering of highly efficient perovskite solar cells. *Science* **2014**, *345*, 542-546.

10 Hu, Q.; Wu, J.; Jiang, C.; Liu, T.; Que, X.; Zhu, R.; Gong, Q. Engineering of electron-elective contact for perovskite solar cells with efficiency exceeding 15%. *ACS Nano* **2014**, *10*, 10161-10167.

11 Polman, A.; Atwater, H. A. Photonic design principles for ultrahigh-efficiency photovoltaics. *Nat. Mater.* **2012**, *11*, 174-177.

12 Lee, M. M.; Teuscher, J.; Miyasaka, T.; Murakami, T. N.; Snaith, H. J. Efficient Hybrid Solar Cells Based on Meso-Superstructured Organometal Halide Perovskites. *Science* **2012**, *338*, 643–647.

13 Wenger, S.; Schmid, M.; Rothenberger, G.; Gentsch, A.; Grätzel, M.; Schumacher, J. O. Coupled optical and electronic modeling of dye-sensitized solar cells for steady-state parameter extraction. *J. Phys. Chem. C* **2011**, *115*, 10218-10229.

14 Moule, A. J.; Snaith, H. J.; Kaiser, M.; Klesper, H.; Huang, D. M.; Grätzel, M.; Meerholz, K.; Optical description of solid-state dye-sensitized solar cells. I. Measurement of layer optical properties. *J. Appl. Phys.* **2009**, *106*, 073111.

15 Palik, E. D. *Handbook of optical constants of solids*; Academic Press: San Diego, U.S.A.; 1985.

16 Malitson, I. H.; Refraction and dispersion of synthetic sapphire. *J. Opt. Soc. Am.* **1962**, *52*, 1377-1379.

17 D'Innocenzo, V.; Grancini, G.; Alcocer, M. J. P.; Kandada, A. R. S.; Stranks, S. D.; Lee, M. M.; Lanzani, G.; Snaith, H. J.; Petrozza, A. Excitons versus free charges in organo-lead tri-halide perovskites. *Nat Commun* **2014**, *5*, 3586.

18 Grancini, G.; Srimath Kandada, A. R.; Frost, J. M.; Barker, A. J.; De Bastiani, M.; Gandini, M.; Marras, S.; Lanzani, G.; Walsh, A.; Petrozza, A. Role of microstructure in the electron–hole interaction of hybrid lead halide perovskites. *Nat Photon* **2015**, *9*, 695-701.

19 Kim, H.-S.; Park, N.-G. Parameters Affecting I–V Hysteresis of $CH_3NH_3PbI_3$ Perovskite Solar Cells: Effects of Perovskite Crystal Size and Mesoporous TiO_2 Layer. *The Journal of Physical Chemistry Letters* **2014**, *5*, 2927-2934.

20 Correa-Baena, J. P.; Anaya, M.; Lozano, G.; Tress, W.; Domanski, K.; Saliba, M.; Matsui, T.; Jacobsson, T. J.; Calvo, M. E.; Abate, A.; Grätzel, M.; Míguez, H.; Hagfeldt, A. Unbroken perovskite: interplay of morphology, electro-optical properties, and ionic movement. *Adv. Mater.* **2016**, *28*, 5031–5037.

21 Lin, Q.; Armin, A.; Nagiri, R. C. R.; Burn, P. L.; Meredith, P. Electro-optics of perovskite solar cells. *Nat. Photonics* **2015**, *9*, 106-112.

22 Ball, J. B.; Stranks, S. D.; Hörantner, M. T.; Hüttner, S.; Zhang, W.; Crossland, E. J. W.; Ramirez, I.; Riede, M.; Johnston, M. B.; Friend, R. H.; Snaith, H. J. Optical properties and limiting photocurrent of thin-film perovskite solar cells. *Energy Environ. Sci.* **2015**, *8*, 602-609.

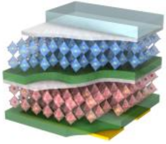

Chapter 4

Optical optimization of single- and double-junction perovskite solar cells

In this chapter, we discuss the possibilities that an optical model opens to improve the efficiency of perovskite-based solar cells within the framework of the Shockley-Queisser theory. Firstly, we present perovskites in which Pb is gradually substituted by Sn as promising materials due to their tuneable bandgap. Indeed, they show absorption onsets shifted towards the infrared region of the electromagnetic spectrum, which make them more favourable light absorbers according to thermodynamics. We employ the optical model presented in the previous chapter to demonstrate that a solar device based on a $MASn_{0.15}Pb_{0.85}I_3$ perovskite would significantly surpass the efficiencies shown by standard $MAPbI_3$ solar cells. Furthermore, we identify $MASn_{0.85}Pb_{0.15}I_3$ as the ABX_3 perovskite with the lowest energy absorption edge. This opens the path to the proposal of perovskite/perovskite tandem devices, which we model and design in depth in this chapter. Finally, we conclude with a roadmap towards the achievement of optically optimized tandem solar cells, where the combination of materials is designed to maximize light harvesting within the system. This kind of approach promises to be of great importance for the immediate future of this rapidly growing field.

4.1. Introduction

Shockley-Queisser (SQ) theory sets the maximum PCE achievable for single junction cells depending on the E_g of the absorbing material.[1] The voltage (V) dependence of the current (I) extracted from devices based on light absorbing materials with different E_g can be calculated assuming that radiative recombination (RR) is the only source of electron and hole recombination:

$$I(V, E_g) = I_{ph}(E_g) - RR(V, E_g) \tag{4.1}$$

Being the photogenerated current (I_{ph})

$$I_{ph}(E_g) = q \int_{E_g}^{\infty} N(\lambda) EQE(\lambda) d\lambda \tag{4.2}$$

with q the electron charge, λ the wavelength of light, $N(\lambda)$ the number of photons provided by the Sun at Air Mass 1.5, and $EQE(\lambda)$ the external quantum efficiency. RR is given by

$$RR(V, E_g) = e^{qV/k_BT} \frac{2\pi}{c^2 h^3} \int_{E_g}^{\infty} \frac{E^2}{e^{(E/k_BT)} - 1} dE \tag{4.3}$$

with c the speed of light, h the Planck constant and k_B the Boltzman constant. T is the temperature and E is the energy. The PCE of a device is determined by

$$PCE\ (E_g) = \frac{P_{max}(E_g)}{P_{in}} = \frac{I(V, E_g) \cdot V\big|_{max}}{P_{in}} \tag{4.4}$$

where P_{max} is the maximum power extracted from the cell and P_{in} is the incident sunlight power. In this picture, one can also estimate the ideal J_{sc} as $J_{sc} = I(0, E_g)$, while the maximum voltage, i.e. open circuit voltage (V_{oc}), is given by $I(V_{oc}, E_g) = 0$. Then, the PCE can be redefined as

$$PCE\ (E_g) = \frac{J_{sc} \cdot V_{oc} \cdot FF}{P_{in}} \tag{4.5}$$

where FF is the fill factor.

The ideal J_{sc} increases as the E_g is reduced since a larger fraction of the incident sunlight is harvested by the absorbing material. In contrast, charge recombination increases with the reduction of E_g. As a consequence, at 300K a limiting PCE over 33% could be attained for

$E_g = 1.14$ eV or $E_g = 1.34$ eV, considering an idealized system without additional losses, such as parasitic absorption or non-radiative recombination (see Figure 4.1a).

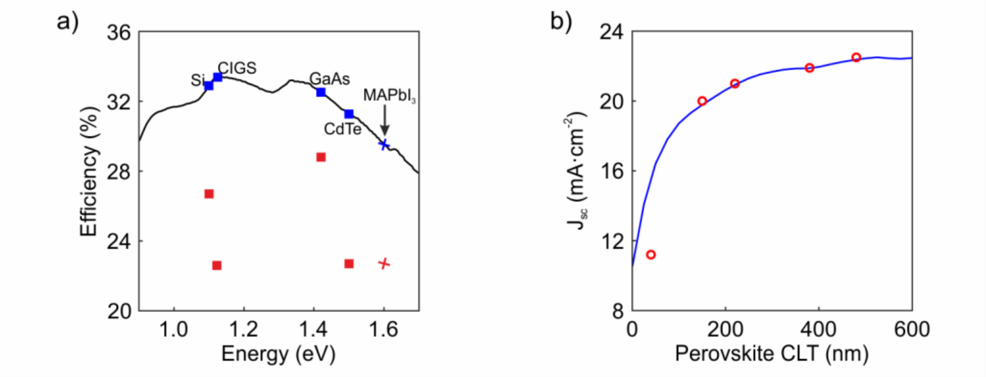

Figure 4.1. Shockley-Queisser limit. a) Ideal calculated power conversion efficiency as a function of the absorber bandgap energy according to Shockley-Queisser theory. Theoretically predicted (blue) and experimentally attained (red) efficiency for different photovoltaic technologies are also displayed. b) Calculated (blue line) and experimental (red circles) short circuit current of the mixed-perovskite based solar cells presented in Figure 3.7. CLT refers to Capping Layer Thickness.

In this context, record photo-conversion efficiencies of PSCs are approaching the thermodynamic limit established by the SQ theory, which reveals them as the most efficient emerging PV devices.[2] Indeed, from the calculus of the ideal J_{sc} for the different devices discussed in Section 3.3., it can be noticed that the experimental values reach the maximum values predicted by SQ (see Figure 4.1b). This estimation assumes that all photons absorbed in the perovskite layer are converted into carriers with a 100% charge collection. Furthermore, the PCE of the record device in this experiment is 20.8% (November 2015). This means that the loss-in-efficiency (difference between experimental and ideal efficiency) is a relative 30%, which is one of the lowest values recorded for any PV material.[3] Please note that there are several losses sources such as non-radiative recombination, radiative recombination below 100% and parasitic absorption.

Since the performance of standard perovskite devices is reaching the theoretical limits, ABX_3 perovskites with more favourable E_g in terms of the SQ theory represent a very promising route to achieve even higher PCEs.[4] This entails the attainment of perovskites in which the absorption edges are shifted towards the near infrared (NIR) region of the electromagnetic spectrum (SQ maxima are found at $E_g = 1.14$ eV and $E_g = 1.34$ eV). In Figure 4.2, we show how the bandgap energy of the ABX_3 material is modified for different compositions.[5-13] In particular, perovskites in which Pb is gradually substituted by Sn are the only ones that permit extending the bandgap to the NIR, which is more favourable according to the SQ theory (see Figure 4.1a).

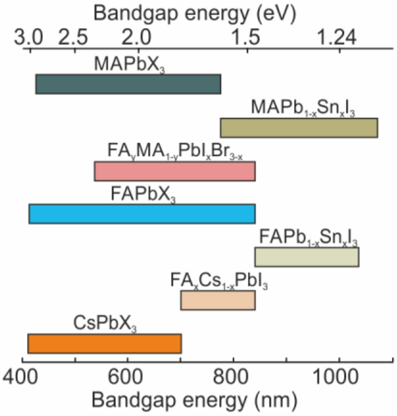

Figure 4.2. Bandgap tunability of ABX_3 perovskites. Bandgap energies that can be attained with the different combinations of elements in an ABX_3 perovskite structure. X refers to the halide site, being I (reddish bandgap), Br, or Cl (blueish bandgap).

In the first part of this chapter, I will use the optical model described in Chapter 3 in order to study the optical behaviour of different perovskites compositions and devices based on Sn/Pb alloys. We will present the complex refractive index for a series of $MASn_xPb_{1-x}I_3$ perovskites, demonstrating that they are able to harvest photons in the NIR. Then, we will predict the performance of a solar device integrating these materials and estimate the maximum short circuit current expected for each Sn/Pb ratio. In particular, we will show that a $MASn_{0.15}Pb_{0.85}I_3$-based PSC exhibits optimum optical properties regarding SQ theory, giving rise to a maximised efficiency. In the second part of the chapter, we will introduce perovskite/perovskite tandem solar cells that have the potential to surpass the theoretical ceiling established by the SQ limit. We will propose a device architecture in which $MAPbI_3$ and $MASn_{0.85}Pb_{0.15}I_3$ perovskite films are employed as active layers for the top and bottom cell, respectively. This design makes a more efficient use of the solar radiation in comparison with traditional PSCs, although a number of concerns arise from the optical point of view. For this reason, I will then identify which are the effects that the different components have in the optical performance of the perovskite/perovskite cell. This discussion will lead us to finish the chapter presenting an integral optical design of a fully optimized $FA_{0.83}Cs_{0.17}PbI_{1.8}Br_{1.2}/MASn_{0.85}Pb_{0.15}I_3$ tandem device. This kind of architectures promise to be of great importance in the PV scenario and it already represents a very active topic in the community.

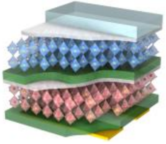

4.2. Optical design of $MASn_xPb_{1-x}I_3$ perovskite solar cells

4.2.1. Synthesis and structural properties of Sn/Pb-based perovskite films

Perovskite materials with changing Sn and Pb compositions in $MASn_xPb_{1-x}I_3$, where x is varied from 0 to 1 (otherwise denoted throughout the text as 0% and 100%, respectively), were provided by the group of Prof Anders Hagfeldt at the EPFL. Although full details can be found elsewhere,[7] it is worth mentioning that optical quality films were only attained by means of a combination of precursor solvent engineering and anti-solvent deposition method, which induces fast crystallization of the Sn/Pb perovskite. Figure 4.3a-c shows the cross-sectional SEM images of perovskite films with 0%, 50% and 100% in mol content of Sn. The synthetic route advanced to layers that presented a thickness variation small enough to consider perovskite-air interface plane-parallel for the impinging light. From top-view SEM images (see Figure 4.3d-f), it can be observed that crystalline grains were densely packed, forming continuous films.

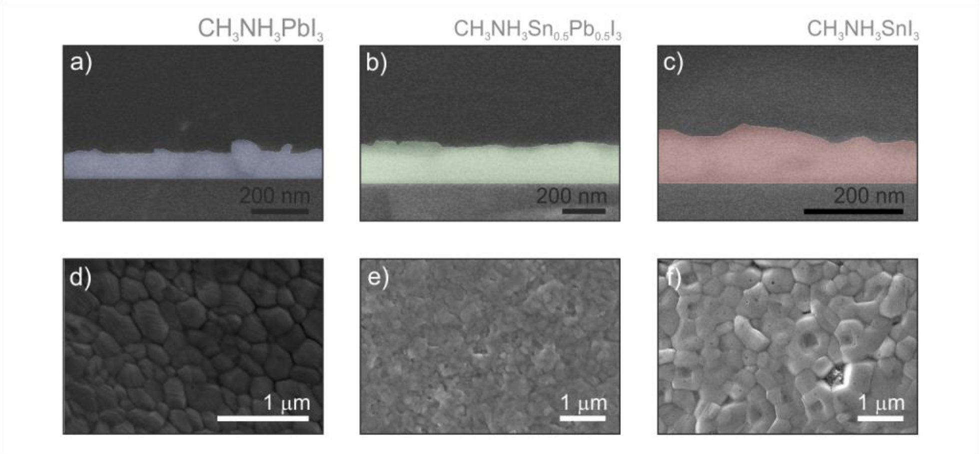

Figure 4.3. Structural characterization of $MASn_xPb_{1-x}I_3$ films. Cross-sectional (a-c) and top view (d-f) scanning electron microscopy images of the perovskite materials with different compositions as deposited on a glass substrate for optical analysis. Perovskite layers have been shaded with colour for the sake of clarity.

4.2.2. Optical properties of Sn/Pb-based perovskite films

The pin-hole free, dense and planar character of the films allowed us to conduct a thorough study on the optical properties of perovskite films with different metal composition, $MAPbI_3$, $MASn_{0.15}Pb_{0.85}I_3$, $MASn_{0.5}Pb_{0.5}I_3$, $MASn_{0.85}Pb_{0.15}I_3$ and $MASnI_3$. A spectroscopic analysis analogous to the one presented in Section 2.5.1. revealed the high optical quality of the perovskite films (see Figure 4.4a). The small fraction of the incident light absorbed at wavelengths larger than the bandgap discarded the existence of intraband states, indicating a low density of defects being present in the fabricated films. Moreover, optical properties were preserved over time when the samples were encapsulated within two glass substrates sealed with epoxy (see Figure 4.4b).

The evolution of the absorption onset of the $MASn_xPb_{1-x}I_3$ films is displayed in Figure 4.4c. As expected, the bandgap of the pure Pb perovskite was found at E_g=1.60 eV. As the fraction of Sn in the precursor solution increased, the band edge shifted to longer wavelengths. A minimum value in energy, E_g=1.17 eV, was reached when the Sn content was 85%. However, the bandgap energy increased for the pure Sn-based perovskite up to E_g=1.21 eV. Such bandgap evolution, discussed in detail elsewhere, originates from a difference in the spin-orbit coupling and a crystal phase change from tetragonal to cubic.[14]

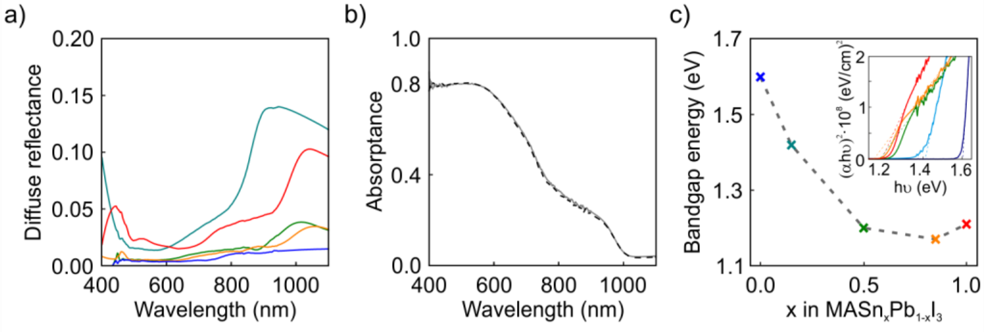

Figure 4.4. Optical characterization of $MASn_xPb_{1-x}I_3$ films. a) Experimental diffuse reflectance for perovskite films in which the percentage of Sn was increased at the expense of Pb: 0% Sn (blue), 15% Sn (blue green), 50% Sn (green), 85% Sn (orange), and 100% Sn (red). b) Experimental total absorptance spectra of a fresh (black dashed line) and aged (grey solid line) $MASn_{0.5}Pb_{0.5}I_3$ film. Aging was done in air atmosphere during four weeks. c) Bandgap energy of the different perovskites versus the amount of Sn in the composition. The dashed grey line is only a guide for the eye. Inset shows the Tauc plots employed to estimate the direct bandgap energy. Colour code from (a) is preserved.

The optical measurements enabled the analysis of the gradual change of the optical constants of the composites as the amount of Sn increases at the expense of Pb. To this end, we followed the protocol described in Section 2.5.2. K−K consistent *n* and *k* values for perovskite thin films with different composition are displayed in Figure 4.5a-e. Perovskite materials under analysis featured complex refractive indices of similar order of magnitude regardless of the specific perovskite composition. However, mixed metal perovskites presented slightly lower *k* values, resulting in light harvesting efficiencies inferior to those

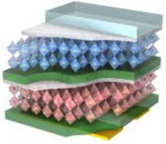

of the pure Pb- or Sn-based perovskites. Fair agreement between theory (dashed lines) and experiment (solid lines) was found for the reflectance and transmittance spectra attained for the different Sn/Pb ratios, as displayed in Figure 4.5f-j. Although some mismatches between the experiment and model can be found, which are produced by the non-perfect uniformity of the films, they are assumable and do not affect the conclusions extracted hereafter.

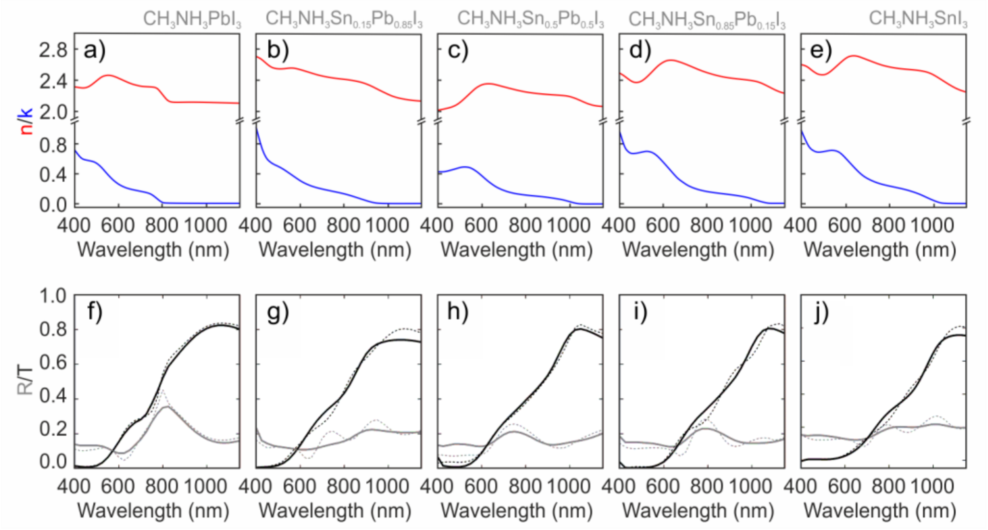

Figure 4.5. *n* and *k* values of $MASn_xPb_{1-x}I_3$ perovskites. a-e) Real (red) and imaginary (blue) parts of the complex refractive index of the perovskite materials herein studied. f-j) Experimental (dashed) and calculated (solid) spectra of the reflectance (grey) and transmittance (black) corresponding to the different films.

4.2.3. Optical performance of Sn/Pb-based perovskite solar cells

Tuning of the bandgap of $MASn_xPb_{1-x}I_3$, between 1.60 eV (x=0) and 1.17 eV (x=0.85), brings the opportunity to develop the ideal absorber to maximize solar conversion efficiency. In order to evaluate the impact of the integration of these perovskites in actual solar cells, we introduced their optical constants in the model previously employed to describe the performance of PSCs (see Section 3.2.3.). By this means, we estimated the fraction of incident sunlight absorbed by the perovskite in a standard cell, which was based on the architecture of a state-of-the-art PSC (see Section 3.3.) and whose scheme is represented in the inset of Figure 4.6a. Please note that the scheme of the cell is flipped in this chapter for the sake of clarity, especially in the sections related to tandem devices. This allowed us to calculate the J_{sc} of the eventual devices for all the different perovskite compositions, according to equation 4.1. at V=0. We would like to remind the reader that the model considers (i) parasitic losses associated to the different absorbing materials present in the cell

(FTO, Spiro-OMeTAD or gold), (ii) reflection losses at the entrance of the cell, and (iii) ideal charge transport and charge collection. This last item implies that the internal quantum efficiency equals the light harvesting efficiency, $IQE(\lambda)=LHE(\lambda)$. In Figure 4.6a, it can be noted that J_{sc} slightly oscillates when increasing perovskite film thickness due to light interference phenomena. Moreover, J_{sc} almost saturates for perovskite capping layer thicknesses larger than 600 nm for all the considered compositions.

With this in mind, we focused the study on devices with a 600 nm perovskite capping layer, which are currently producible.[15] In Figure 4.6b, we present the calculated PCE and J_{sc} for devices in which the Sn/Pb ratio was varied, assuming a FF=0.85. It can be noticed that the J_{sc} followed the same trend as the E_g (see Figure 4.4c), i.e. perovskites with lower bandgaps would generate higher photo-generated currents. In particular, when $MASn_{0.85}Pb_{0.15}I_3$ was used as light harvester in a PSC, a J_{sc}=34 mA·cm^{-2} was foreseen. Notice that, as displayed in Figure 4.1, the J_{sc} measured from a state-of-the-art pure Pb perovskite devices is nearly the theoretical value.[16] However, record devices feature PCEs that do not meet the values estimated according to the SQ theory, i.e. PCE of 22.7% vs 27.9%.[2] In order to provide a more realistic estimation of the efficiency of the PSC, it would be necessary to consider a thorough model of its electrical behaviour, which is out of the scope of this dissertation. However, the optical analysis indicated that a relative PCE enhancement of ~10% with respect to the standard Pb perovskite material may be attained just by substituting 15% Pb by Sn in the perovskite film (PCE of 27.9% vs. 30.4%). This is due to a 25% increase in the J_{sc} (23.5 mA·cm^{-2} vs. 29.5 mA·cm^{-2}) together with a more favourable E_g stated in the SQ theory. Contrarily, the estimations performed using a real device architecture indicated that the film with 85% Sn content (E_g = 1.17 eV) would give rise to a PCE far from that predicted for the ideal one according to SQ theory (PCE of 28% vs. 33% expected).

In order to explain this behaviour, in Figure 4.6c we plot the fraction of light that the different components of the $MASn_{0.85}Pb_{0.15}I_3$-based PSC absorb. It can be observed that the ratio between parasitic absorption, caused by optical losses occurring in Spiro-OMeTAD and FTO, and productive absorption, increased significantly in the NIR spectral range, which resulted in a J_{sc} that was far from the ideal according to SQ theory (J_{sc} of 34 mA·cm^{-2} vs 41 mA·cm^{-2} expected). In view of this result, in order to minimize optical losses, it might be helpful to engineer novel transparent contacts and HSLs for cells operating in the NIR.

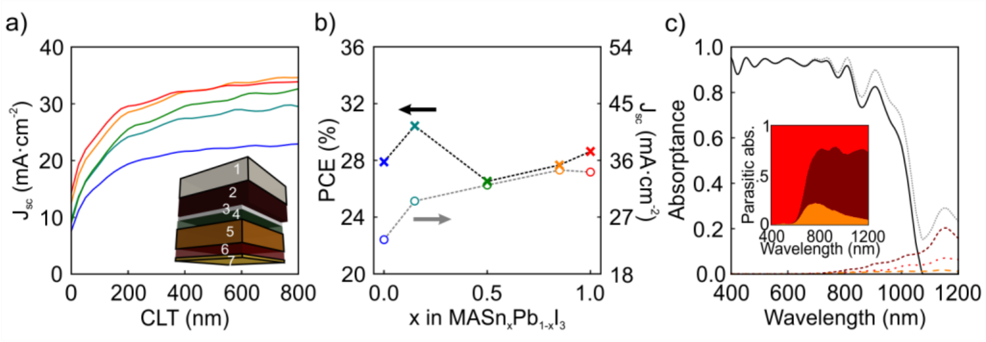

Figure 4.6. Optical performance of $MASn_xPb_{1-x}I_3$ perovskite solar cells. a) Calculated maximum short circuit current (J_{sc}) that an ideal $MASn_xPb_{1-x}I_3$ perovskite solar cell would have depending on the capping layer thickness (CLT): 0% Sn (blue). 15% Sn (blue-green). 50% Sn (green). 85% Sn (orange) and 100% Sn (red). Inset shows the architecture of the simulated device: 1 mm of glass substrate (1), 650 nm of FTO layer (2), 50 nm of TiO_2 compact layer (3), 85 nm of 50% porous TiO_2 scaffold fully infiltrated by perovskite (4), perovskite capping layer (5), 240 nm of Spiro-OMeTAD (6), and 50 nm of gold contact (7). b) Calculated PCE and J_{sc} for simulated devices in which the percentage of Sn was increased at the expense of Pb. Perovskite capping layer was fixed at 600 nm. c) Spectral dependence of the fraction of light absorbed by the different layers comprising a cell: FTO (red dotted line), $MASn_{0.85}Pb_{0.15}I_3$ (black solid line), Spiro-OMeTAD (brown short-dashed line), and gold contact (orange dashed line). Inset shows a detail of the spectral dependence of the parasitic absorption given in the FTO, Spiro-OMeTAD and gold.

4.3. Optical design of perovskite/perovskite tandem solar cells

One of the most appealing properties of $MASn_xPb_{1-x}I_3$ perovskites is their narrow bandgap ($1.17 < E_g < 1.6$ eV) that opens the door to the creation of double-junction devices in which either one or both top (front) and bottom (rear) cells are based on perovskite absorbers. Tandem configurations have already proven to improve PCEs over the limits imposed by SQ theory and have been widely employed in several PV technologies such as Si, III-V semiconductor or organic solar cells in order to boost their performance.[17-19] In fact, the most efficient PV device ever fabricated is based on expensive multi-junction configurations based on different semiconductors,[2] whose primarily application is related to self-powered systems installed in outer space.[20] In this context, all the processing techniques mentioned in the introduction of this thesis for ABX_3 perovskites are compatible with tandem configurations as they prevent the deterioration of the pre-deposited structures.

4.3.1. Working principle

The working principle of tandem solar cells is based on the combination of different subcells, each of them able to absorb a different part of the electromagnetic spectrum, which allows minimizing losses and reaching higher PCEs. In a standard single-junction solar cell, photons with energies lower than the E_g of the active material cannot be absorbed while those with higher energies lead to carriers that eventually thermalize to band edges from where they are extracted to their respective selective layers. These undesirable effects result in current and potential losses, respectively. In contrast, a double-junction configuration combines top and bottom subcells based on materials with absorption onsets at relative shorter and longer wavelengths (see Figure 4.7a). In Figure 4.7b we present canonical energy diagrams for a double-junction tandem cell. Photons with higher energies are harvested in the front cell while those of lower energies penetrate deeper in the device and are absorbed by the rear cell.

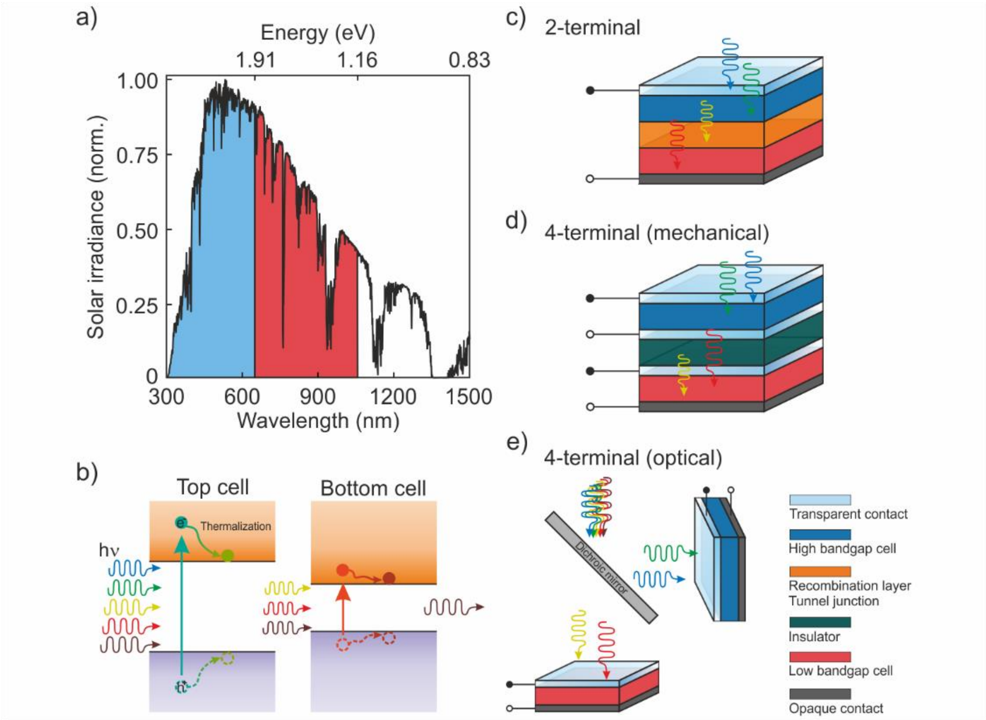

Figure 4.7. Working principle of tandem solar cells. a) Spectral response of generic top (blue) and bottom (red) subcells comprising a tandem device working in different regions of the reference solar spectral irradiance AM1.5. b) Canonical energy diagram for a double-junction tandem solar cell. Scheme of the three most common double-junction configurations: (c) two terminal, (d) mechanically stacked four terminal, and (e) optically coupled four terminal.

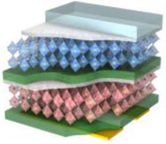

It is possible to classify double junction cells as two- or four-terminal devices based on the electric connection among subcell electrodes. In a two-terminal device, subcells are monolithically stacked requiring a recombination layer or a tunnel junction in order to achieve charge neutrality (see Figure 4.7c). In this series connection scheme, currents through top and bottom cells must be the same, being thus limited by the subcell that produces a lower photocurrent. The voltage across the device is the sum of the voltages across each of the constituent cells. A four-terminal tandem solar cell is composed of two self-working cells that are externally connected in series or in parallel. As displayed in Figures 4.7d and 4.7e, they can be either mechanically stacked or coupled by optical filters. From a fabrication perspective, four-terminal devices are more convenient since the preparation techniques of the different junctions do not need to be compatible. Nevertheless, two terminal configurations are more attractive from an industrial point of view since they present lower parasitic absorption and costs are reduced due to the less amount of transparent conductive material required. For these reasons, in the next paragraphs we will focus our discussion on two-terminal, otherwise named monolithic, tandem solar cells.

4.3.2. Architecture of a $MAPbI_3$-$MASn_{0.85}Pb_{0.15}I_3$ tandem solar cell

Although PSCs can be combined as front subcells with well-established technologies,[21] the achievement of all-perovskite tandem devices represent a unique opportunity to develop third-generation PV for widespread use. They hold the potential of surpassing 30% efficiency while maintaining low costs. For this reason, we now develop a roadmap for the realistic design of perovskite/perovskite tandem devices. To this goal, we considered a tandem solar cell with mesostructured configuration, as displayed in Figure 4.8a. The active material chosen for the top cell was the standard $MAPbI_3$ perovskite, which absorbed the incident light very efficiently up to 800 nm. Less energetic photons passed through the system and reached the $MASn_{0.85}Pb_{0.15}I_3$ perovskite in the bottom cell, which presents the lowest E_g among the ABX_3 perovskites and harvests light up to 1100 nm.

4.3.3. Current-matching condition in a $MAPbI_3$-$MASn_{0.85}Pb_{0.15}I_3$ tandem solar cell

Finding the configuration that gives rise to a similar fraction of the incident light harvested by the top and bottom cells, the so-called current-matching condition, is of utmost importance to propose realistic tandem designs. The satisfaction of this constraint is not intuitive since the spatial profile of the absorption of light in the device depends on numerous variables, e.g.

optical constants and thicknesses of the materials and optical interference phenomena. In order to visualize it, we calculated the fraction of incident light that each perovskite layer absorbs using the optical model. Figure 4.8a displays the current mismatch between top and bottom cells (ΔJ_{sc}) as a function of the thickness of each perovskite capping layer (D_1 and D_2, respectively). The white dotted line indicates graphically the current-matching condition between both subcells. The thicknesses of the different non-active layers were kept constant in order to simplify the calculations. Figure 4.8b shows the J_{sc} that flows through the tandem device as a function of D_1 and D_2. It can be observed that the photogenerated current increases with D_1. Notice that for values of D_1>250 nm, *D2* became significantly thicker to attain current matching. For this reason, in order to maintain the experimental feasibility of the proposed architecture, the analysis will be focused on a perovskite/perovskite device in which D_1=240 nm and D_2=600 nm, which leads to J_{sc} = 16.5 mA·cm^{-2}. The V_{oc} for the top and bottom cells were 1.32 V and 0.92 V, respectively, according to the SQ theory, which would bring the voltage of the double-junction device to 2.24 V. Consequently, the theoretical efficiency of such perovskite/perovskite tandem device is 31% assuming a *FF* of 0.85.

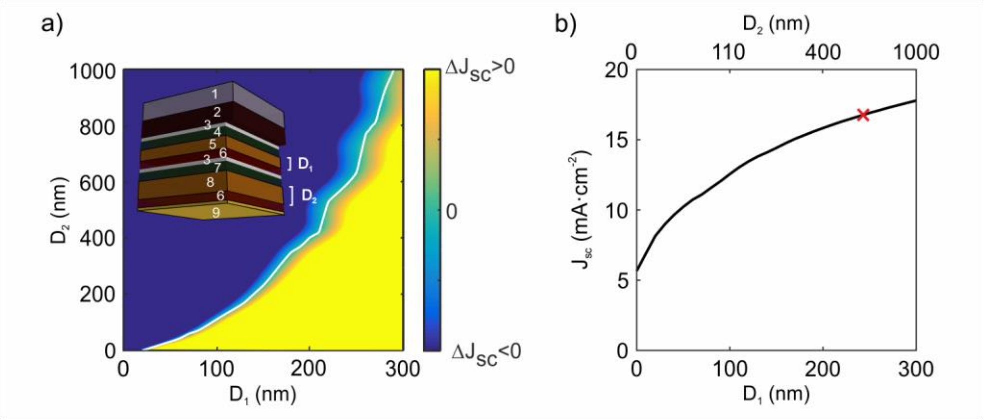

Figure 4.8. Current matching condition. a) Difference between short circuit currents extracted from the top and bottom cells composing a tandem device with mesostructured architecture, in which the $MAPbI_3$ (D_1) and $MASn_{0.85}Pb_{0.15}I_3$ (D_2) thicknesses are varied. White line indicates the particular thicknesses for which the current matching is attained. Inset shows the architecture of the simulated device: 1 mm of glass substrate (1), 650 nm of FTO layer (2), 50 nm of TiO_2 compact layer (3), 85 nm of 50% porous TiO_2 scaffold fully infiltrated by $MAPbI_3$ (4), D_1 nm of $MAPbI_3$ capping layer (5), 240 nm of Spiro-OMeTAD (6), 50 nm of TiO_2 compact layer (3), 85 nm of 50% porous TiO_2 scaffold fully infiltrated by $MASn_{0.85}Pb_{0.15}I_3$ (7), D_2 nm of $MASn_{0.85}Pb_{0.15}I_3$ capping layer (8), 240 nm of Spiro-OMeTAD (6), and 50 nm of gold contact (9). b) Matched short circuit current values for each pair of D_1-D_2 thicknesses. Red mark points out the configuration analysed in the next figures (D_1=240 nm and D_2=600 nm).

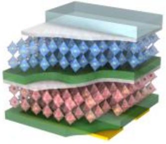

4.3.4. External quantum efficiency of a $MAPbI_3$-$MASn_{0.85}Pb_{0.15}I_3$ tandem solar cell

In order to know how light was spectrally absorbed along the proposed tandem solar cell, we calculated the spectral dependence of the spatial distribution of the electric field intensity calculated inside the device (see Figure 4.9a). Bright and dark fringes arose from the interference between light reflected and transmitted by each layer of the multi-layered system. The calculations indicated that: i) $\lambda<600$ nm barely reached the bottom cell; ii) $600<\lambda<800$ nm were absorbed by top and bottom cells simultaneously; and iii) $\lambda>800$ nm reached the metallic contact of the cell. Additionally, light distribution across FTO, HSL and gold suggests the presence of parasitic absorption. In order to assess this effect, we calculated the *EQE* of the tandem solar cell. Figure 4.9b displays the *EQE* of the tandem device together with the ones of the constituent subcells. The total *EQE* remains over 90% for most of the spectral range until $\lambda=780$ nm that is the absorption onset of the $MAPbI_3$ material. It is also important to stress that the *EQE* gradually diminishes from $\lambda=850$ nm because $MASn_{0.85}Pb_{0.15}I_3$ perovskite performs a *k* value that is not high enough to absorb all incident photons in the NIR. Indeed, calculations show that it would be necessary to increase its thickness up to 1 μm with the aim of harvesting all the incident radiation. Moreover, both FTO and Spiro-OMeTAD contribute to this non-optimum effective light absorption since they absorb a non-negligible fraction of photons in the NIR (see Figure 4.9c). Finally, it is remarkable that the *EQE* features a dramatic drop from $\lambda=1000$ nm. This is caused by an increase in the light reflected at the entrance of the cell produced by interference phenomena.

As aforementioned, the optical design of the tandem device yielded a photocurrent matching value of 16.5 $mA\cdot cm^{-2}$. However, around 8 $mA\cdot cm^{-2}$ were lost, which indicated there was still room for improvement in the device performance. Hereof, a proper choice of absorbers, contacts, charge selective layers and antireflective films may be of great importance for the demonstration of tandems of superior efficiencies.

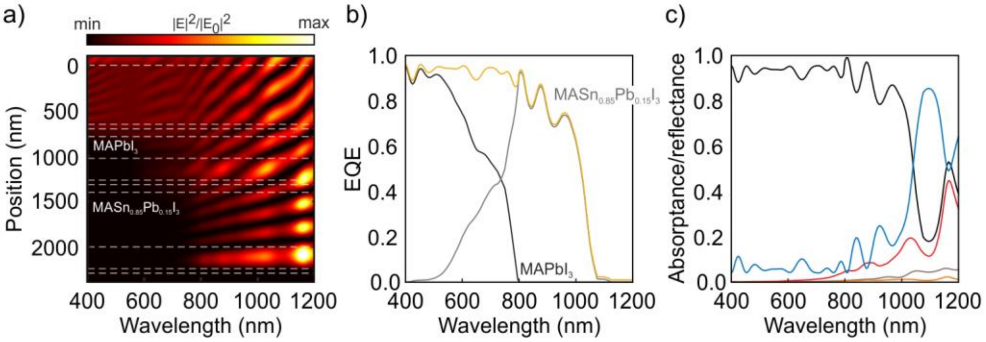

Figure 4.9. Optical performance of a $MAPbI_3$/$MASn_{0.85}Pb_{0.15}I_3$ tandem device. a) Calculated spatial (y-axis) and spectral (x-axis) distribution of the electric field intensity enhancement along the cross section of the selected perovskite/perovskite tandem solar cell. White dashed lines specify the interfaces between the different layers. b) Calculated external quantum efficiency corresponding to the top (black line) and bottom (grey line) cells, and the complete tandem device (red line). c) Spectral dependence of the reflectance (blue line) and absorptance (black line) of the total device, and of the fraction of the incident light absorbed by the Spiro-OMeTAD (red line), FTO (grey line), and Au (orange line).

4.4. Optical optimization of perovskite/perovskite tandem solar cells

Different aspects may be addressed in order to drive perovskite-based tandem solar cells to superior efficiencies. In this regard, the choice of light harvesters plays the most critical role in the performance of a tandem device, although charge selective layers and contacts with proper transparency windows also would make a difference when proposing optimized architectures.

4.4.1. Most adequate light absorbers in a tandem solar cell

Similar to what happens in a single-junction device, pairs of optimum absorption onsets for both top and bottom absorbers can be found according to SQ theory in order to achieve maximized performances. Figure 4.10 displays the expected efficiency for ideal two-terminal double-junction devices as a function of the E_g of both top and bottom harvesters. For example, the optimal top subcell E_g for a Si bottom subcell is close to 1.7 eV, which corresponds to different ABX_3 perovskites families as shown in Figure 4.2.[22] Analogously, for a CIS subcell with E_g=1.0 eV, optimal top subcell E_g should be around 1.6 eV, which would be the case of $MAPbI_3$. In the case of a perovskite/perovskite tandem solar cell, the right selection of compositions (bandgaps), e.g. $FA_{0.83}Cs_{0.17}PbI_{1.8}Br_{1.2}$ and $MAPb_{0.15}Sn_{0.85}I_3$, would lead to efficiencies above 40% in the ideal case, which represents a theoretical ceiling. However, other electro-optical considerations must be taken into account with the aim of proposing actual devices. All device components need to be designed in order to: i) achieve low resistance (high conductivity) and adequate energy band alignment from the electrical point of view, and ii) minimize both parasitic absorption, which takes place at the substrate, contacts, ESLs and HSLs, and reflectance losses from the optical. Therefore, in the next sections, we will discuss the role of the each constituent in the perovskite/perovskite tandem device, and in extension in the PSC, and their influence on the electro-optical performance of the system.

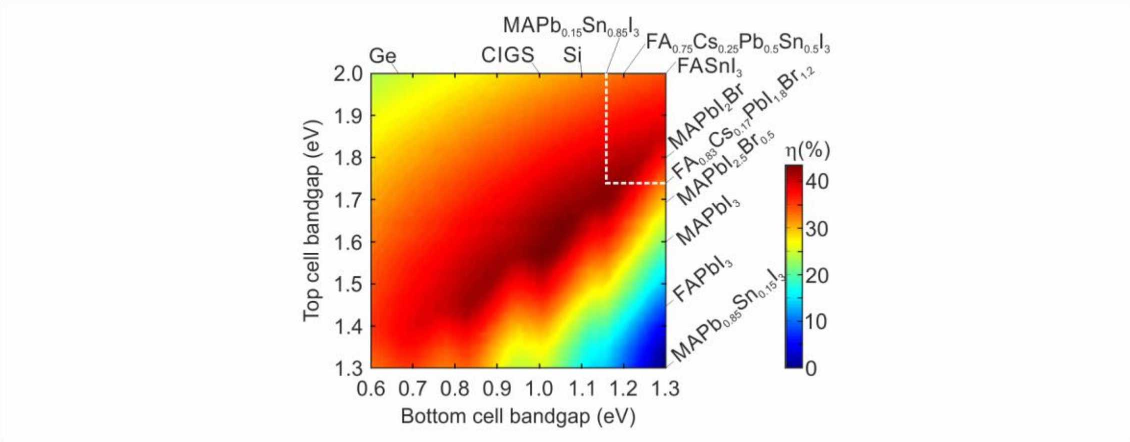

Figure 4.10. Shockley-Queisser limit for tandem solar cells. Expected efficiency for ideal double-junction devices as a function of E_g of both top and bottom light harvesters. A selection of well-established and perovskite absorbers are displayed.

4.4.1.1. Transparent contact

Ideally, materials employed as transparent contacts should minimize absorption and reflection in the 350-to-1200 nm spectral range. Regarding the materials comprising the cell described in Figure 4.9, the front transparent contact was the one leading to higher optical losses. Although FTO is widely employed for the fabrication of PSCs, alternative materials have been reported such as ITO, indium zinc oxide (IZO), Ag nanowires (NWs) or Au thin film.[23,24,25] We present in Figure 4.11a the calculated spectral dependence of the transmittance of each of these layers deposited on a glass substrate assuming optical constants reported elsewhere. [7,26,27] In order to allow a realistic comparison, film thicknesses were set to be similar to the ones that these materials typically feature. In addition, Figure 4.11a displays the photogenerated current loss associated with each material. ITO, AgNWs and FTO showed similar transparency, yet the best compromise in terms of optical properties, sheet resistance and material necessities was found for the ITO contact. Please note that, although these results allowed the comparison of the performance of different materials employed as contacts, the calculation of the actual fraction of the incident light wasted by such contacts in a device would require the full simulation of the complete system.

4.4.1.2. Electron and hole selective layers

As in the previous section, we present in Figure 4.11b the calculated spectral dependence of the fraction of light absorbed by ESL and HSL materials typically employed by the PSC community. Thicknesses of the layers were those considered standard in the field. Although TiO_2 and Spiro-OMeTAD are the most widely-used ESL and HSL materials in single junction devices, the calculations revealed that SnO_2, and PEDOT are very promising ESL and HSL, respectively. Indeed, they showed less absorption than Spiro-OMeTAD while preserving good electrical properties and ease of processing. Moreover, SnO_2 electronic structure results in a better conduction band alignment.[28] Finally, we would like to mention that evaporated organic semiconductors, such as C60 and TaTm, hold great potential in the field due to their tuneable electro-optical properties by means of doping.[29,30]

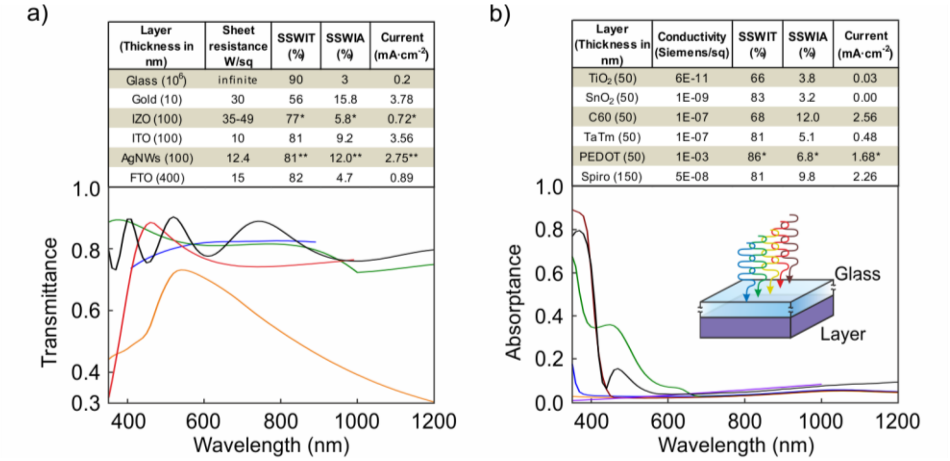

Layer (Thickness in nm)	Sheet resistance W/sq	SSWIT (%)	SSWIA (%)	Current ($mA \cdot cm^{-2}$)
Glass (10^6)	infinite	90	3	0.2
Gold (10)	30	56	15.8	3.78
IZO (100)	35-49	77*	5.8*	0.72*
ITO (100)	10	81	9.2	3.56
AgNWs (100)	12.4	81**	12.0**	2.75**
FTO (400)	15	82	4.7	0.89

Layer (Thickness in nm)	Conductivity (Siemens/sq)	SSWIT (%)	SSWIA (%)	Current ($mA \cdot cm^{-2}$)
TiO_2 (50)	6E-11	66	3.8	0.03
SnO_2 (50)	1E-09	83	3.2	0.00
C60 (50)	1E-07	68	12.0	2.56
TaTm (50)	1E-07	81	5.1	0.48
PEDOT (50)	1E-03	86*	6.8*	1.68*
Spiro (150)	5E-08	81	9.8	2.26

Figure 4.11. Shockley-Queisser limit for tandem solar cells. a) Calculated spectral dependence of the transmittance of a selection of transparent contacts: gold (orange), IZO (red), ITO (green), AgNWs (blue) and FTO (black). Sheet resistance, *SSWIT*, *SSWIA*, and current associated to the fraction of the incident light absorbed at each material are displayed. (e) Calculated spectral dependence of the absorptance of a selection of charge selective layers: TiO_2 (blue), SnO_2 (orange), C60 (green), TaTm (red), PEDOT:PSS (purple) and Spiro-OMeTAD (black). Conductivity, *SSWIT*, *SSWIA* and current associated to the fraction of the incident light absorbed in each material are displayed. *SSWIT* and *SSWIA* refer to solar spectrum weighted integrated transmittance and absorptance, respectively. *SSWIA* was calculated as presented in Section 3.2.3.2. We employed an analogous expression for *SSWIT*. Calculations are made for wavelengths from 350 nm to 1200 nm, except for * (350-1000) and ** (400-900). Please note that electrical properties (sheet resistance and conductivity) were extracted from the literature.

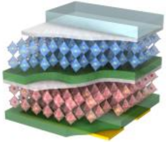

4.4.1.3. Antireflective layer

Light reflected at the entrance of the system represented approximately half of the light that could not be harvested in the device proposed in Figure 4.9. Reflection losses are caused by the sudden change in the refractive index perceived by the light beam when passing from one medium to another, in this case from air (n=1) to glass (n=1.51). Designing optimized antireflective layers that work throughout the full operational spectral range represents a big challenge. Nevertheless, we propose a very simple approach that would consisti a ~100 nm-thick porous SiO_2 layer on top of the glass substrate to enhance the incident light in-coupling. This SiO_2 film would perform a refractive index $1<n_{SiO2}<1.51$ for the entire operational wavelength range, and could be prepared using cost-effective SiO_2 nanoparticles that are easily processable and amenable to large-scale solution processing.[31]

4.4.2. Optimized $FA_{0.83}Cs_{0.17}PbI_{1.8}Br_{1.2}$ / $MAPb_{0.15}Sn_{0.85}I_3$ tandem solar cell

Considering all the criteria described in the previous paragraphs, we now present a full optical optimization of a perovskite/perovskite tandem device. In Figure 4.12a, we show the calculated spectral dependence of the absorptance and reflectance of an optimized device formed by glass / ITO / SnO_2 / $FA_{0.83}Cs_{0.17}PbI_{1.8}Br_{1.2}$ / PEDOT / SnO_2 / $MAPb_{0.15}Sn_{0.85}I_3$ / PEDOT / Au. We omitted the presence of scaffolds since they would require thicker perovskite layers to harvest as much light as a flat absorber layer, thus producing a detrimental impact in the final performance caused by charge recombination. Indeed, best experimental demonstrations of working perovskite/perovskite tandem devices employ planar configurations for both top and bottom subcells.[10,29] ITO thickness was fixed at 100 nm, while ESL, HSL and Au thicknesses were limited to be less than 100 nm. The choice of the perovskite compounds was the optimum according to the SQ theory (Figure 4.10), considering that the perovskite with the lowest bandgap reported (E_g=1.17 eV) was the one discussed in Section 4.2.2. They were restricted to be up to 600 nm thick. Each layer thickness was optimized combining the optical model with the genetic algorithm already presented within this thesis. In the optimization target, we maximized J_{sc} of both top and bottom cells, while minimizing the current mismatch. Currents at each subcell were calculated assuming no electrical losses in the perovskite materials, i.e. IQE=1. The grade of freedom given to the thickness of the different materials was crucial to find the device configuration in which optical interference derived in optimal light absorption within the perovskite layers.

In Figure 4.12b, we display the thickness obtained for each layer comprising the tandem device. We also present the photocurrent associated to the fraction of the incident light absorbed at each component. In particular, 1.40 mA·cm^{-2} and 0.75 mA·cm^{-2} were wasted by ITO and charge selective contacts, which led us to conclude that the improvement of the contacts transparency in the NIR will be essential for attaining perovskite/perovskite tandems of superior performance. In addition, 5.38 mA·cm^{-2} were lost at the device entrance. To mitigate this deleterious reflectance, we added to the calculated system a 110 nm-thick antireflective layer as the one suggested in Section 4.4.1.3. This resulted in an extra 1.20 mA·cm^{-2} available to be extracted from the solar cell as shown in Figure 4.12c, giving rise a 33.3% efficiency device. This value is significantly higher than the one attained in Section 4.3, where several restrictions were imposed to the system. Consequently, the integral optical optimization herein proposed is proven to be a realistic and powerful tool to potentially achieve monolithic perovskite-based tandem solar cells with performances approaching the theoretical limits, while employing materials a-la-carte.

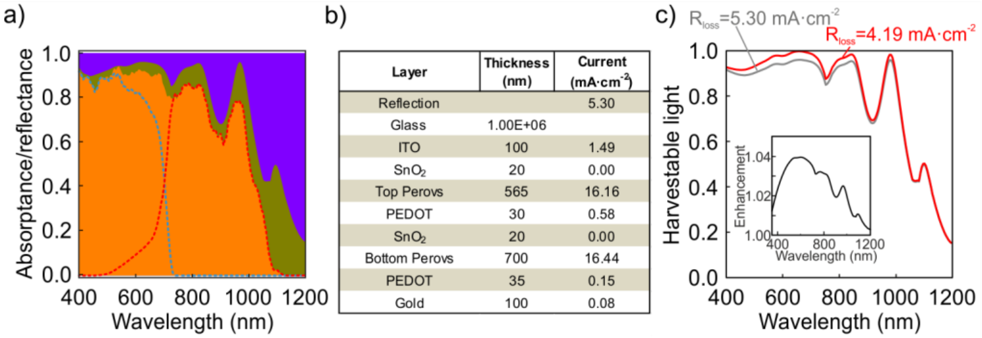

Layer	Thickness (nm)	Current (mA·cm^{-2})
Reflection		5.30
Glass	1.00E+06	
ITO	100	1.49
SnO_2	20	0.00
Top Perovs	565	16.16
PEDOT	30	0.58
SnO_2	20	0.00
Bottom Perovs	700	16.44
PEDOT	35	0.15
Gold	100	0.08

Figure 4.12. Optical design of an optimized perovskite/perovskite tandem device. a) Calculated spectral dependence of effective (orange) and parasitic (green) absorptance and reflectance (purple) of a perovskite/perovskite device formed by glass / ITO / SnO_2 / $FA_{0.83}Cs_{0.17}PbI_{1.8}Br_{1.2}$ / PEDOT / SnO_2 / $MAPb_{0.15}Sn_{0.85}I_3$ / PEDOT / Au. Blue and red dashed lines represent light absorbed by the top and bottom perovskite material, respectively. b) Layout of the device, thickness and current associated to the fraction of the incident light absorbed at each component. c) Calculated spectral dependence of the fraction of the incident light that is harvestable by the device with (red) and without (grey) a SiO_2 based antireflective layer. Inset shows the ratio between the spectral harvestable light with and without antireflective layer.

4.5. Conclusions

In this chapter, we have performed an in-depth optical characterization to attain the complex refractive index of a series of $MASn_xPb_{1-x}I_3$ perovskite films. The performance of

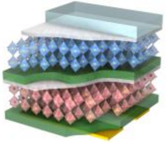

hypothetical solar cells based on these light harvesters, which perform absorption onsets more favourable according to SQ theory, is estimated. The results, based on realistic device parameters, indicate that a fine-tuning of the composition will eventually lead to significant enhancement of the power conversion efficiency of perovskite solar cells. In particular, adding a 15% of Sn to the perovskite absorber results in a 25% increase of the photo-generated current. This may yield a 10% increase of the performance of state-of-the-art perovskite devices. The bandgap tunability of the materials herein discussed may also allow the fabrication of monolithic perovskite/perovskite tandem solar cells of even superior efficiencies. We have shown how the use of an optical model provides a straightforward path towards device architectures in which current matching is attained, eventually preventing the field from time-consuming trial and error experiments. Finally, we have determined charge selective and contact materials whose combination of properties would result in devices with a better compromise between electro-optical properties and costs. Based on the conclusions attained, we have merged the optical model and the genetic algorithm to fully optimise a $FA_{0.83}Cs_{0.17}PbI_{1.8}Br_{1.2}/MAPb_{0.15}Sn_{0.85}I_3$ tandem device that outperforms 30% efficiency. Although we have focused on two-terminal perovskite/perovskite tandem devices, the model and the discussion can be immediately extended to any solar cell architecture based on any combination of light-harvesting materials. Indeed, our proposal is intended to promote the use of ABX_3 perovskites that would give rise to considerable cost reductions in multi-junction technology while potentially featuring performances exceeding those theoretically achievable by single junction solar cells. These findings should encourage further research to attain Sn-based working devices of improved chemical stability that could surpass the performance of pure Pb-based solar cells.

4.6. Notes

The $MASn_xPb_{1-x}I_3$ perovskite films studied in Section 4.2. were provided by Dr Juan Pablo Correa-Baena. I would like to thank him and his colleagues from the EPFL for their collaboration.

4.7. References

1 Shockley, W.; Queisser, H. J. *J. Appl. Phys.* **1961**, *32*, 510-519.

2 See NREL's Efficiency Chart: http://www.nrel.gov/ncpv/images/efficiency_chart.jpg for the latest certified efficiency update.

3 Green, M. A.; Hishikawa, Y.; Dunlop, E. D.; Levi, D. H.; Hohl-Ebinger, J.; Ho-Baillie, A. W. Y. Solar cell efficiency tables (version 51). *Prog. Photovolt. Res. Appl*. **2017**, *26*, 3-12.

4 Walsh, A. Principles of Chemical Bonding and Band Gap Engineering in Hybrid Organic–Inorganic Halide Perovskites. *J. Phys. Chem. C* **2015**, *119*, 5755-5760.

5 Noh, J. H.; Im, S. H.; Heo, J. H.; Mandal, T. N.; Seok, S. I. Chemical management for colorful, efficient, and stable inorganic-organic hybrid nanostructured solar cells. *Nano Lett.* **2013**, *13*, 1764–1769.

6 Sadhanala, A.; Ahmad, S.; Zhao, B.; Giesbrecht, N.; Pearce, P. M.; Deschler, F.; Hoye, R. L. Z.; Gödel, K. C.; Bein, T.; Docampo, P.; Dutton, S. E.; De Volder, M. F. L.; Friend, R. H. Blue-green color tunable solution processable organolead chloride-bromide mixed halide perovskites for optoelectronic applications. *Nano Lett.* **2015**, *15*, 6095–6101.

7 Anaya, M.; Correa-Baena, J. P.; Lozano, G.; Saliba, M.; Anguita, P.; Roose, B.; Abate, A.; Steiner, U.; Grätzel, M.; Calvo, M. E.; Hagfeldt, A.; Míguez, H. Optical analysis of $CH_3NH_3Sn_xPb_{1-x}I_3$ absorbers: a roadmap for perovskite-on-perovskite tandem solar cells. *J. Mater. Chem. A* **2016**, *4*, 11214–11221.

8 Eperon, G. E.; Stranks, S. D.; Menelaou, C.; Johnston, M. B.; Herz, L. M.; Snaith, H. J. Formamidinium lead trihalide: a broadly tunable perovskite for efficient planar heterojunction solar cells. *Energy Environ. Sci.* **2014**, *7*, 982–988.

9 Levchuk, I.; Osvet, A.; Tang, X.; Brandl, M.; Perea, J. D.; Hoegl, F.; Matt, G. J.; Hock, R.; Batentschuk, M.; Brabec, C. J. Brightly luminescent and color-tunable formamidinium lead halide perovskite $FAPbX_3$ (X = Cl, Br, I) Colloidal Nanocrystals. *Nano Lett.* **2017**, *17*, 2765–2770.

10 Eperon, G. E.; Leijtens, T.; Bush, K. A.; Prasanna, R.; Green, T.; Wang, J. T.-W.; Mc Meekin, D. P.; Volonakis, G.; Milot, R. L.; May, R., Palmstrom, A.; Slotcavage, D. J.;

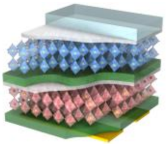

Belisle, R. A.; Patel, J. B.; Parrott, E. S.; Sutton, R. J.; Ma, W.; Moghadam, F.; Conings, B.; Babayigit, A.; Boyen, H.-G.; Bent, S.; Giustino, F.; Herz, L. M.; Johnston, M. B.; McGehee, M. D.; Snaith H. J. Perovskite-perovskite tandem photovoltaics with optimized band gaps. *Science* **2016**, *354*, 861–865.

11 Li, Z.; Yang, M.; Park, J. S.; Wei, S. H.; Berry, J. J.; Zhu, K. Stabilizing perovskite structures by tuning tolerance factor: formation of formamidinium and cesium lead iodide solid-state alloys. *Chem. Mater.* **2016**, *28*, 284–292.

12 Protesescu, L.; Yakunin, S.; Bodnarchuk, M. I.; Krieg, F.; Caputo, R.; Hendon, C. H.; Yang, R. X.; Walsh, A.; and Kovalenko, M. V. Nanocrystals of cesium lead halide perovskites ($CsPbX_3$, X = Cl, Br, and I): novel optoelectronic materials showing bright emission with wide color gamut. *Nano Lett.* **2015**, *15*, 3692–3696.

13 Jacobsson, T. J.; Correa-Baena, J.-P.; Pazoki, M.; Saliba, M.; Schenk, K.; Grätzel, M.; and Hagfeldt, A. Exploration of the compositional space for mixed lead halogen perovskites for high efficiency solar cells. *Energy Environ. Sci.* **2016**, *9*, 1706–1724.

14 Im, J.; Stoumpos, C. C.; Jin, H.; Freeman, A. J.; Kanatzidis, M. G. Antagonism between spin–orbit coupling and steric effects causes anomalous band gap evolution in the perovskite photovoltaic materials $CH_3NH_3Sn_{1-x}Pb_xI_3$. *J. Phys. Chem. Lett.* **2015**, *6*, 3503.

15 Momblona, C.; Malinkiewicz, O.; Roldán-Carmona, C.; Soriano, A.; Gil-Escrig, L.; Bandiello, E.; Scheepers, M., Edri, E.; Bolink, H. J. Efficient methylammonium lead iodide perovskite solar cells with active layers from 300 to 900 nm. *APL Mater.* **2014**, *2*, 081504.

16 Correa-Baena, J. P.; Anaya, M.; Lozano, G.; Tress, W.; Domanski, K.; Saliba, M.; Matsui, T.; Jacobsson, T. J.; Calvo, M. E.; Abate, A.; Grätzel, M.; Míguez, H.; Hagfeldt, A. Unbroken perovskite: interplay of morphology, electro-optical properties, and ionic movement. *Adv. Mater.* **2016**, *28*, 5031–5037.

17 Yu, Z.; Leilaeioun, M.; and Holman, Z. Selecting tandem partners for silicon solar cells. *Nat. Energy.* **2016**, *1*, 16137.

18 Tanabe, K. A review of ultrahigh efficiency III-V semiconductor compound solar cells: Multijunction tandem, lower dimensional, photonic up/down conversion and plasmonic nanometallic structures. *Energies* **2009**, *2*, 504–530.

19 Ameri, T.; Li, N.; Brabec, C. J. Highly efficient organic tandem solar cells: a follow up review. *Energy Environ. Sci.* **2013**, *6*, 2390-2413.

20 Torchynska, T. V.; and Polupan, G. (2004). High efficiency solar cells for space applications. Superf. Vacío 17, 21–25.

21 Anaya, M.; Lozano, G.; Calvo, M. E.; Míguez, H. ABX_3 perovskites for tandem cells. *Joule* **2017**, *4*, 769-793.

22 Bush, K. A.; Palmstrom, A. F.; Yu, Z. J.; Boccard, M.; Cheacharoen, R.; Mailoa, J. P.; McMeekin, D. P.; Hoye, R. L. Z.; Bailie, C. D.; Leijtens, T.; Peters, I. A.; Minichetti, M. C.; Rolston, N.; Prasanna, R.; Sofia, S.; Harwood, D.; Ma, W.; Moghadam, F.; Snaith, H. J.; Buonassisi, T.; Holman, Z. C.; Bent, S. F.; McGehee, M. D. 23.6%-Efficient monolithic perovskite/silicon tandem solar cells with improved stability. *Nat. Energy.* **2017**, *2*, 17009.

23 You, J.; Hong, Z.; Yang, Y.; Chen, Q.; Cai, M.; Song, T.-B.; Chen, C.-C.; Lu, S.; Liu, Y.; Zhou, H.; Yang, Y. Low-Temperature Solution-Processed Perovskite Solar Cells with High Efficiency and Flexibility. *ACS NANO* **2014**, *8*, 1674-1680.

24 Werner, J.; Weng, C.H.; Walter, A.; Fesquet, L.; Seif, J.P.; De Wolf, S.; Niesen, B.; and Ballif, C. J. Efficient monolithic perovskite/silicon tandem solar cell with cell area >1 cm^2. *Phys. Chem. Lett.* **2016**, *7*, 161–166.

25 Bailie, C.D., Christoforo, M.G., Mailoa, J.P., Bowring, A.R., Unger, E.L., Nguyen, W.H., Burschka, J., Pellet, N., Lee, J.Z., Grätzel, M.; Noufi, R.; Buonassisi, T.; Salleo, A.; McGehee, M. D. Semi-transparent perovskite solar cells for tandems with silicon and CIGS. *Energy Environ. Sci.* **2015**, *8*, 956–963.

26 Khanarian, G.; Joo, J.; Liu, X. Q.; Eastman, P.; Werner, D.; O'Connell, K.; Trefonas, P. The optical and electrical properties of silver nanowire mesh films. *J. Appl. Phys.* **2013**, *114*, 024302.

27 Jean, J.; Wang ,A.; Bulovic, V. In situ vapor-deposited parylene substrates for ultra-thin, lightweight organic solar cells. *Org. Electron. Physics Mater. Appl.* **2016**, *3*1, 120–126.

28 Correa-Baena, J.-P.; Steier, L.; Tress, W.; Saliba, M.; Neutzner, S.; Matsui, T.; Giordano, F.; Jacobsson, T. J.; Kandada, A. R. S.; Zakeeruddin, S. M.; Petrozza, A.; Abate, A.; Nazeeruddin, M. K.; Grätzel, M.; Hagfeldt, A. Highly efficient planar perovskite solar cells through band alignment engineering. *Energy Environ. Sci.* **2015**, *8*, 2928-2934.

29 Forgács, D.; Gil-Escrig, L.; Pérez-del-Rey, D.; Momblona, C.; Werner, J.; Niesen, B.; Ballif, C.; Sessolo, M.; Bolink, H. J. Efficient monolithic perovskite/perovskite tandem solar cells. *Adv. Energy. Mater.* **2017**, *7*, 1602121.

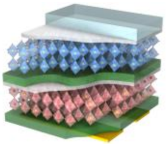

30 Momblona, C.; Gil-Escrig, L.; Bandiello, E.; Hutter, E. M.; Sessolo, M.; Lederer, K.; Blochwitz-Nimoth, J.; Bolink, H. J. Efficient vacuum deposited p-i-n and n-i-p perovskite solar cells employing doped charge transport layers. *Energy Environ. Sci.* **2016**, *9*, 3456–3463.

31 Prosser, J. H.; Brugarolas, T.; Lee, S.; Nolte, A. J.; Lee, D. Avoiding cracks in nanoparticle films. *Nano Lett.* **2012**, *12*, 5287–5291.

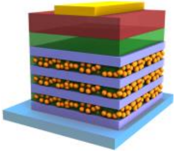

Chapter 5

Perovskite solar cells with structural colour

Herein, we present how the use of photonic crystals as scaffolds provides the perovskite solar cells with bright and tuneable structural colour. This goal is experimentally achievable by means of a new technique to produce periodic multilayers with a very high refractive index contrast. We explore the limit of a sacrificial polymer approximation to build photonic crystals with maximized reflectance based on the alternation of quasi-dense sol-gel processed TiO_2 *films and highly porous* SiO_2 *nanoparticle layers. This allowed us to obtain very thin photonic crystal scaffolds for highly-efficient perovskite devices. This important result constitutes the first report of the integration of a photonic structure in this kind of solar cell. We make use of optical modelling to design the nanostructured scaffold that provides the system with any particular colour of the visible range of the electromagnetic spectrum. We support the results with a detailed structural and electro-optical characterization that sheds light on the fundamental processes underlying the working mechanisms of this new class of perovskite solar cells. Turning the brownish tone of the standard device into a brightly attractive colour will give rise to a significant increment of their commercial interest, as they can be used for building integration in facades, awnings, bus shelters, etc.*

5.1. Introduction

The definitive step to make a technology attractive for the PV industry is the maximization of the compromise between the efficiency of the final product and the costs involved for its accomplishment. Along the previous chapters, we have presented the highly beneficial attributes that an optical model can provide to the optimization of the perovskite solar cells in terms of efficiency, even when they are combined to yield tandem devices. Although ABX_3 perovskite materials themselves and the fabrication processes they require are inexpensive, other factors may affect the overall expenses related to this emerging technology. Among the more important of these aspects are: i) the materials employed to process all the other layers in the device; ii) the stability of the components under temperature and atmospheric operational conditions; and iii) the adaptability of the technology to satisfy the different necessities of the consumers. The first two circumstances are the exclusive domain of chemistry and engineering through the search for new composites and assembling protocols. With respect to the last, however, optics have a crucial role since the adoption of any device, solar cells in particular, strongly depend on their aesthetic appearance.

A large fraction of the cost of solar energy is not the solar cells, but the fixed cost of land, frames, supports and services. A smart move to slash these fixed costs is to build the PV directly into the infrastructure and supports already constructed for other purposes, such as building facades, fences, walls, awnings and automotive skins. Moreover, it would imply the generation of power where it is actually demanded, ensuring equal access to energy resources in all corners of the globe. However, for widespread uptake of building integrated photovoltaics (BIPV),[1] the installed solar module has to be aesthetically versatile. In this regard, the colour pallet available in PSCs is very sparse, and notably absent of greens and blues,[2,3] highly desirable in the built environment.

A solution may be to follow the route often employed by nature: structural colours, in contrast to pigments or dyes, arise from the interference of coherently scattered light waves. With the aim of endowing this type of device with colour, we propose a versatile approach based on photonics rather than on chemical management. The latter consists on the modification of the perovskite composition to shift its absorption onset as discussed in Section 4.1. (see Figure 4.2). However, it has demonstrated limited success in the blue-to-green region of the spectrum since solar radiation drops dramatically for those photon energies.[2,3] In contrast, the method herein presented is based on the substitution of the

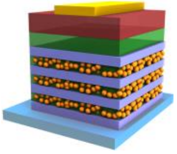

standard scaffold existing in the PSC by a multi-layered scaffold that exhibits PC properties. This strategy simultaneously provides optical reflection at selected visible wavelength ranges and allows good electrical contact with the charge collecting layers, while maintaining the bandgap of the ABX_3 perovskite of choice.

In this chapter, we devise multilayers in which the refractive index contrast between layers in the PC is maximized while accessible porosity is preserved. We employ layers of SiO_2 and TiO_2 in different aggregation states that permit us to tune the open porosity of each alternate layer. In this way, the number of layers, and therefore the thickness, required to achieve a strong reflection peak, can be reduced below the optimum scaffold size in terms of charge diffusion within the perovskite material (i.e. 500 nm), but the perovskite precursors is still capable of soaking the photonic matrix. Then, we fabricate PSCs in which the photonic scaffold is employed to provide them with colour. We attain fine control over the colour tunability of the devices along the entire visible range of the electromagnetic spectrum. Optical behaviour of the colourful PSCs correlate with the optical response of the PC-based scaffolds of choice, which can be fitted by means of the aforementioned optical model. Indeed, we find a clear correspondence between the photonic properties of the devices and their impact in the spectral features of the electrical performance. Finally, we investigate how the use of this kind of multilayered system affect to recombination processes and charge transfer occurring within the solar cells.

5.2. Perovskite solar cells based on a nano-particulated photonic scaffold

Similarly to what was introduced in Section 1.2., our initial attempts involved the substitution of the porous scaffold in the device by a PC made by stacking nanoparticle layers of TiO_2 and SiO_2 (see Figure 5.1a).[4] A first attempt was made based on a recipe that had permitted the successful integration of coloured mirrors in dye-sensitized solar cells.[5] In particular, we substituted the standard scaffold of the $MAPbI_3$-based PSC developed in Section 3.2.1. by the nanoparticulated PC. Despite the fact that efficient PSCs were attained by this approach, the colour they displayed was not different to that of standard ones since the refractive index contrast after perovskite infiltration was largely diminished as we confirmed by employing the optical model. A potential solution to this problem is to increase the number of layers, so the reflections arising from the photonic mirrors are stronger and colour could be preserved after infiltration. Unfortunately, such approach rendered the device performance very poor, as we show in Figure 5.1b, as the total scaffold thickness was around 1 μm, hence compromising charge diffusion. Thus, a balance between minimization of the photonic skeleton thickness and preservation of its high reflectance after infiltration was required.

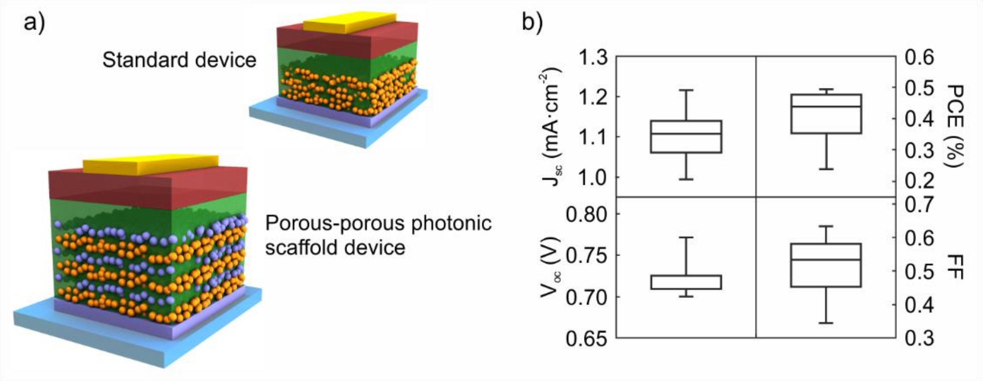

Figure 5.1. Porous-porous photonic scaffold based perovskite solar cell. a) Scheme of the device. b) Device performance of perovskite solar cells based on PCs comprising alternated mesoporous nanoparticle-based TiO_2 and SiO_2 layers with lattice parameter of 180 nm and total multilayer thickness around 800 nm, for which performance is significantly poorer.

5.3. Porous photonic crystals with high refractive index contrast

In this section, we describe a general synthetic procedure to obtain high refractive index contrast PCs based on the alternation of dense sol-gel processed TiO_2 films and highly porous SiO_2 nanoparticle layers. During the deposition of the liquid precursors of the dense layers, the porosity of the low refractive index ones is preserved by prior filling of the interstitial voids with a sacrificial polystyrene (PS) layer that is eliminated at the end of the process. The choice of TiO_2 and SiO_2 to build colored PCs with enhanced refractive index contrast is supported by the fact that they present one of the highest and lowest, respectively, refractive indexes among all transparent materials in the visible range. Besides, they present other attractive properties such as ease of processing, low toxicity and low cost, which make them amenable to device integration and mass production.

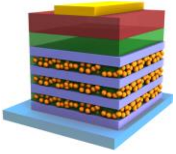

5.3.1. Synthesis of TiO_2-, SiO_2- and Polystyrene-based films precursors

The TiO_2 precursor solution was prepared following a recipe analogous to the one presented in Section 3.2.1. Since the perovskite community widely employs the material as ESL, it ensured the correct charge extraction in an eventual device. In particular, a dispersion of TiO_2 was prepared by adding a solution containing 0.034 ml of 2M hydrochloric acid in 1.690 ml to a solution in which 0.254 ml (named T1) or 0.381 ml (named T2) of titanium tetraisopropoxide (TTIP, Sigma Aldrich, 377996) were diluted in 1.690 ml of ethanol. 10 minutes of stirring are required, avoiding humidity exposure, before filtering the final solution.

Regarding the low refractive index material, we employed a strategy based on the deposition of SiO_2 nanoparticles that have been previously demonstrated values as low as n=1.22 in the visible spectrum.[6] The SiO_2 nanoparticle suspension was obtained by diluting Ludox (Sigma-Aldrich, 420859) in methanol to a final concentration between 1% and 4%.

The PS solution was made by dissolving solid polystyrene (Sigma-Aldrich, 182427) in toluene to a 0.5 wt%.

5.3.2. Deposition procedure of the quasi-dense/porous photonic crystal

In Figure 5.2, we show the procedure that gives rise to the sought quasi-dense/porous multilayered system. In order to make the photonic structure, 200 μl of the TiO_2 precursor dispersion was spin coated at 2500 rpm for 60 seconds onto a clean glass substrate, and then calcined at 500ºC for 5 minutes (Figures 5.2a and 5.2b). Afterwards, 150 μl of a SiO_2 nanoparticle suspension was deposited on top of the quasi-dense TiO_2 film at final rotation speeds from 3000 rpm to 8000 rpm for 60 seconds by spin coating (Figure 5.2c). Next, we placed 150 μl of the PS solution and started the spin coating for 30 seconds. Polystyrene was forced to fill the voids of the SiO_2 nanoparticulated layer and block the access to the pore network (Figure 5.2d). It is worth mentioning that the parameters related to the deposition of the PS layer were set to obtain a complete filling of the porous underlying layer and, at the same time, minimize the accumulation of polystyrene on the top. Otherwise, the eventual thermal annealing of that excess of polystyrene could compromise the mechanical stability of the ensemble. In that way, final rotation speed for PS deposition was varied from 2000 rpm (thicker SiO_2 layers) to 4000 rpm (thinner SiO_2 layers). As PS is insoluble in isopropanol, the precursors of a new TiO_2 layer deposited on top of that hybrid SiO_2-PS layer could not percolate through them (Figure 5.2e). Finally, a shock thermal treatment at

T=500ºC further densified the TiO_2 layer and caused the thermal decomposition and removal of the PS from the SiO_2 layer pores (Figure 5.2f). This process lead to a 3-layer scaffold, which can be promoted to a 5-, 7- or 9-layer one by repeating the described sequence. The higher the concentration of the TiO_2 solution or SiO_2 suspension, the thicker the resulting deposited layer. Similarly, the slower the spin coating velocity, the thicker the deposited film. The final multilayer structures were stabilised at 500 ºC for 30 min.

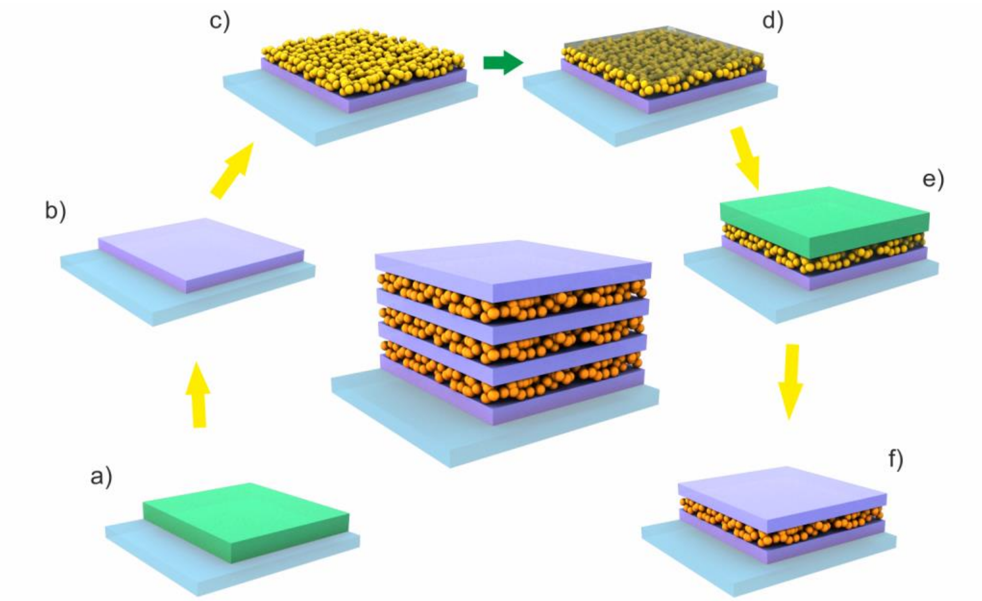

Figure 5.2. Scheme of the deposition pathway that leads to the photonic crystal. a) Deposition of TiO_2 layer. b) Thermal treatment. c) Deposition of SiO_2 particles. d) Protection of SiO_2 particles with polystyrene. e) Deposition of TiO_2 layer. f) Thermal treatment. Sequential repetition of these steps until the desired number of slabs is deposited leads to the formation of a multilayer.

In Figure 5.3, we show secondary electron (Figures 5.3a and 5.3c) and backscattered electron (Figures 5.3b and 5.3d) images simultaneously taken from the same area of a cross section of a 9-layer PC made by alternating compact TiO_2 and porous SiO_2. Figure 5.3a and 5.3b reveal smooth and continuous interfaces between both types of layers with high uniformity at the microscale. Each type of layer can be recognized by their different morphology in secondary electron images as well as by their different response in backscattering electron ones. In the latter, brighter regions indicates the presence of elements of higher atomic number. High magnification images (Figures 5.3c and 5.3d) reveal the spherical morphology of the SiO_2 nanoparticles and the homogeneity and continuity of the compact TiO_2 layer, as well as the absence of interpenetration between both types of layers. We will come back to this point in Section 5.4.

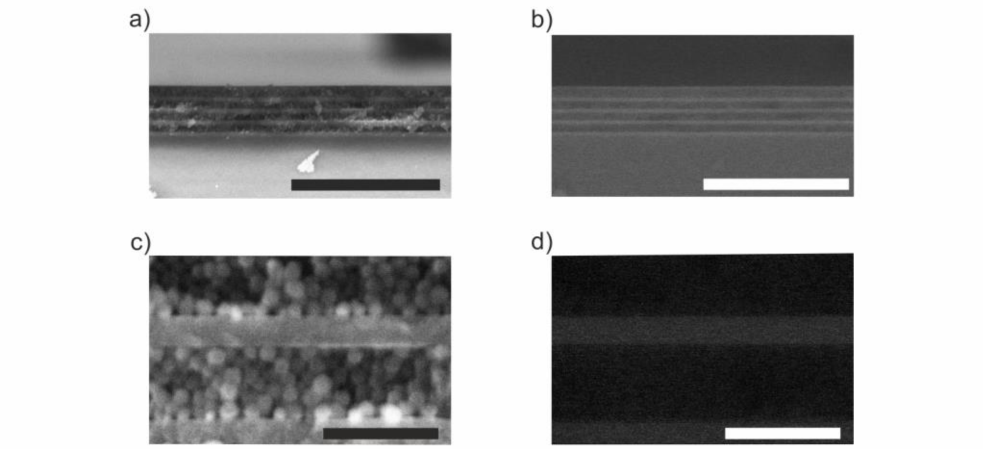

Figure 5.3. Scanning electron micrographs of the photonic crystal. Images were obtained using secondary (a) and backscattered (b) electrons detectors. Scale bar is 2 μm in both images. Magnification of a section of the top images is shown in (c) and (d). Scale bar is 200 nm for both images.

5.3.3. Optical properties of quasi-dense/porous photonic crystals

As introduced in Chapter 1, the modulation of the refractive index along one dimension of the space leads to the occurrence of strong interference effects. When these effects are spectrally located in the visible region of the electromagnetic spectrum, bright colours can be seen by the naked eye. In Figure 5.4, a picture of a series of 7-layer PCs supported on glass slides is displayed, with a colour gamut covering the whole visible range.

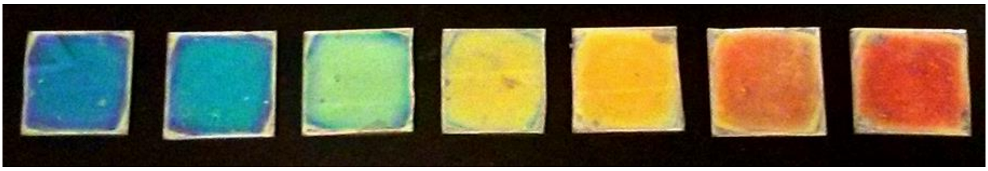

Figure 5.4. Digital camera images obtained from a series of photonic crystals.

The evolution of the reflectance of this type of PCs with the number of layers can be seen in Figure 5.5a. It can be observed that with only 3 layers ($TiO_2/SiO_2/TiO_2$, blue solid line) the measured reflectance reached values as high as 50%, increasing up to 75% and 90% when two and four extra layers were added, respectively (red and black solid lines). Porosity of the individual layers comprising the PC can be estimated through the fitting of the reflectance spectra using the TMM based code that was presented in previous chapters.[7] The simulated spectra (dashed lines in Figure 5.5a) are in fair agreement with the experimental ones. Refractive indexes of 2.35 and 1.25 for TiO_2 and SiO_2 layers, respectively, were considered for $400nm<\lambda<800nm$ for these calculations. The refractive index values implied porosities of 4% and 50%, respectively. It is important to remark that the optical constants of both types of layers remained unaltered as the PC was constructed. In Figure 5.5b, we plot the experimental reflectance spectra obtained from a series of 7-layer PCs prepared combining quasi-dense TiO_2 and highly porous SiO_2. It can be observed that the values of the maximum oscillate between 86% and 96%, covering from the UV to the red. The infiltration of PS within the nanoparticulated SiO_2 films is key to create the stack with high structural quality that allows the subsequent deposition of layers on top. Moreover, it has a moderate impact on the optical quality of the photonic structure, which makes the difference in the realisation of highly reflecting selective mirrors. In Figure 5.5c, we display how the final rotation speed of the PS deposition affected the optical properties of a complete multilayer stack. In consequence, spin coating parameters associated with PS film formation were optimized for each SiO_2 layer thickness, as indicated in the previous subsection.

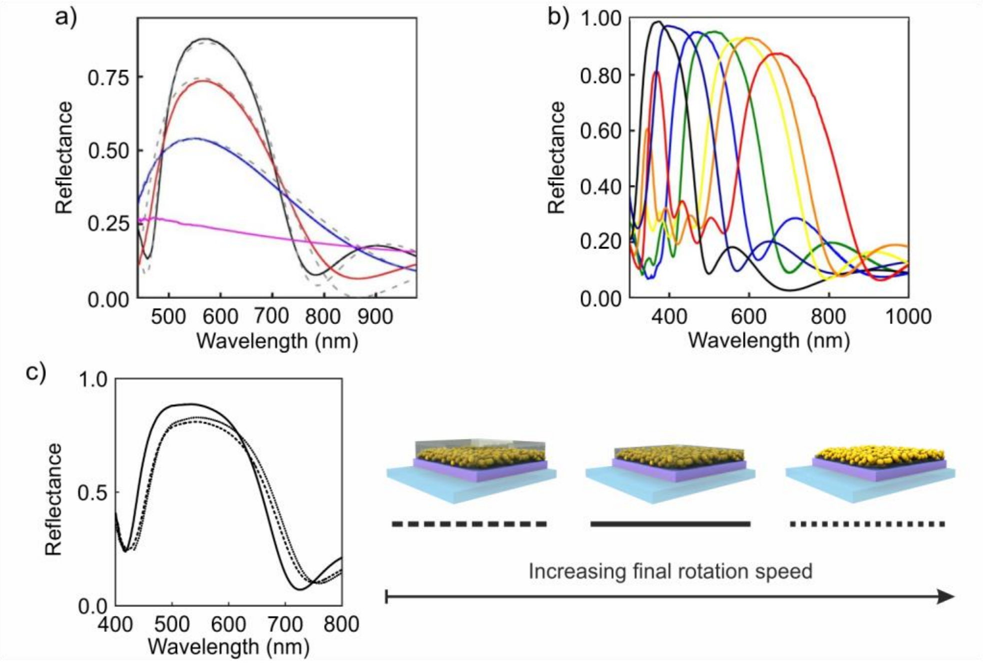

Figure 5.5. Reflectance of the quasi-dense/porous photonic crystals. a) Evolution of the reflectance spectra as the number of stacked layers increases. Experimental data are plotted in solid line being the number of layers: 1 (violet line); 3 (blue line); 5 (red line); 7 (black line). Theoretical calculated spectra are depicted in dashed grey lines. b) Reflectance spectra of a series of high porous SiO_2/low porous TiO_2 PCs built with 7 layers starting with TiO_2. Samples were obtained using different solutions: T1 and $[SiO_2]=1.0\%$ (black line); T2 and: $[SiO_2]=1.0\%$ (violet line), $[SiO_2]=1.5\%$ (blue line), $[SiO_2]=2.0\%$ (green line), $[SiO_2]=2.5\%$ (yellow line), $[SiO_2]=3.0\%$ (orange line), $[SiO_2]=3.5\%$ (red line). c) Reflectance spectra obtained for identical PC infiltrated with PS solution deposited at different final rotation speed (ω). Values of ω are 2000 rpm (dashed line), 3000 rpm (solid line) and 4000 rpm (dotted line).

5.3.4. Infiltration of $MAPbI_3$ within quasi-dense/porous photonic crystals

The development of a porous PC with high refractive index contrast led to exploring its application as a photonic scaffold in a PSC. To achieve this goal, the first step was to synthesise $MAPbI_3$ perovskite within the voids of the SiO_2 and TiO_2 layers, while preserving a selective reflection of light in the complete photonic structure. Despite the low porosity of the quasi-dense TiO_2 layers, ~5%, $MAPbI_3$ perovskite precursors could get through and fill the voids of SiO_2 layers. After a standard thermal annealing at 100ºC for 60’, a red-shift of the reflectance peak of the multilayers was obtained (see Figure 5.6). This was an evidence for the increase in the effective refractive index of the different layers, which indicated the presence of the perovskite semiconductor in the PC. In fact, we employed the optical model to confirm that $MAPbI_3$ completely filled the voids in both SiO_2 and TiO_2 layers, demonstrating the accessibility and interconnectivity of the inorganic structure.

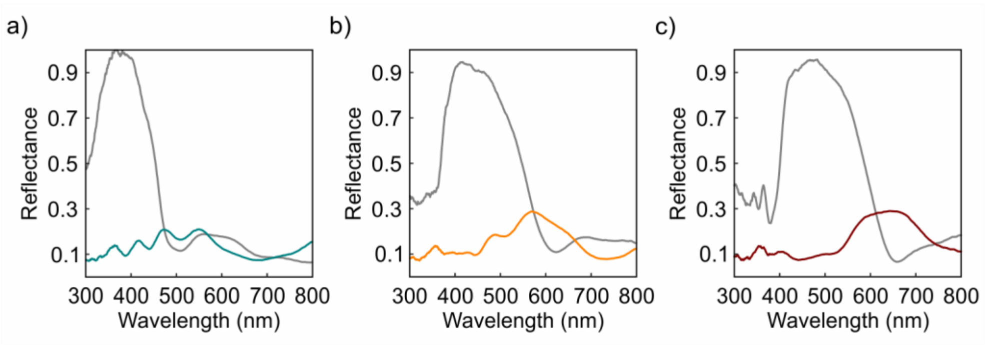

Figure 5.6. Reflectance of quasi-dense/porous photonic crystals infiltrated with perovskite. Reflectance spectra of three PCs (grey lines) obtained using different solutions: T_1 and $[SiO_2]$=1.0% (a); T_2 and: $[SiO_2]$=1.0% (b), $[SiO_2]$=1.5% (c). After the infiltration and thermal annealing of $MAPbI_3$ precursors, structures exhibited different colours (coloured lines): blue-green in (a), orange in (b), and red in (c). All structures were deposited onto FTO glass in order to assure their suitability for device assembly.

5.4. Integration of quasi-dense/porous photonic crystals in perovskite solar cells

The embedding and formation of $MAPbI_3$ perovskite within the quasi-dense/porous PC, allowed us to employ it as a scaffold in actual PSCs. To do so, we followed the protocol detailed in Section 3.2.1. to fabricate perovskite-based devices in which the standard scaffold was substituted by the high refractive index contrast PC. We show a schematic of the structure of a device incorporating a 7-layer PC in Figure 5.7.

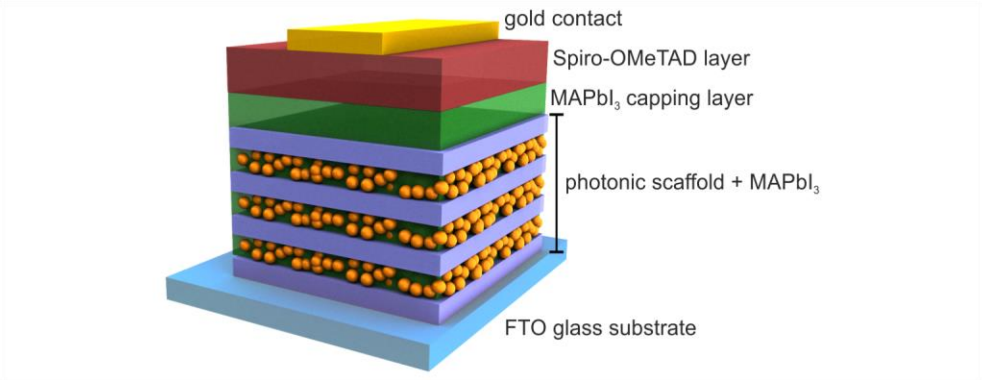

Figure 5.7. Schematic of the photonic crystal-based perovskite solar cell.

5.4.1. Structural characterization of colourful perovskite solar cells

In Figure 5.8a, we display a secondary electron SEM image of a cross section of a PSC that incorporates a PC scaffold. This image reveals that the first SiO$_2$ nanoparticle layer is capable of levelling the roughness, characteristics of the FTO coating, thus providing a flat surface for subsequent layer deposition. This is important for conferring the desirable photonic properties to the system. Furthermore, backscattered electron image analysis shows that the infiltrated perovskite percolates through the void network of the photonic structure, which can then act as an electronic bridging path between the solid perovskite capping layer and the FTO anode (see Figure 5.8b).

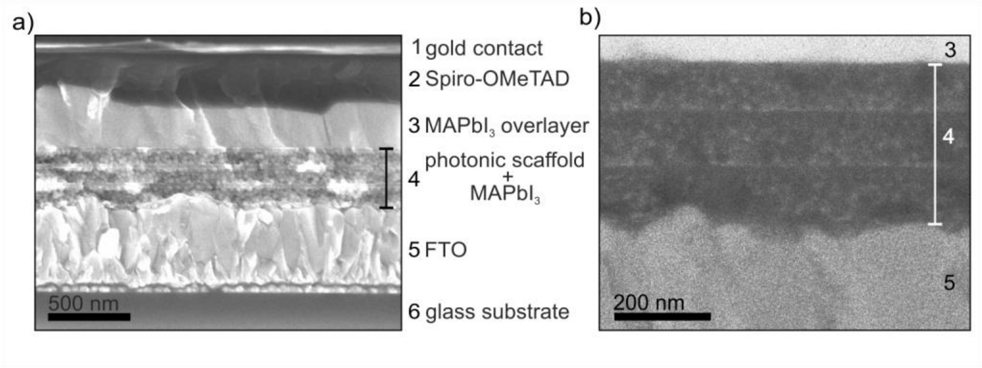

Figure 5.8. Scanning electron microscopy imaging of the photonic crystal-based perovskite solar cell. Secondary electron (a), and backscattered electron (b) scanning electron micrographs of a cross section of a perovskite solar cell with structural colour.

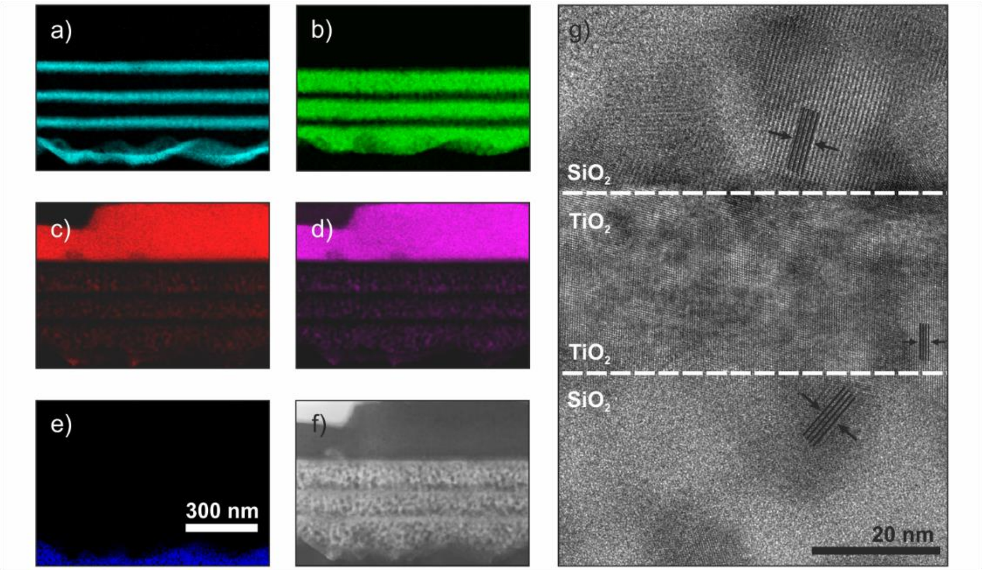

Figure 5.9. MAPbI$_3$ distribution within the photonic crystal based perovskite solar cell. Energy-dispersive X-ray spectroscopy mappings corresponding to Ti (a) and Si (b) identifying, respectively, the TiO$_2$ and the SiO$_2$ layers comprising the photonic structure. Mapping of Pb (c) and I (d) elements allows identifying the regions where perovskite is above the detection limit (capping layer and SiO$_2$ scaffold layers). e) Mapping of Sn that is associated to the FTO glass substrate. f) Transmission electron microscopy image of the same area. Scale bar is the same for panels (a) to (f) and has been only included in panel (e) for the sake of clarity. g) A detail of SiO$_2$-TiO$_2$-SiO$_2$ interfaces in which the crystal planes of MAPbI$_3$ perovskite can be distinguished.

The distribution of MAPbI$_3$ perovskite along the PC-based PSC constitutes a crucial point since it will be related with the performance of the device. In order to shed light on this, we performed an Energy-Dispersive X-Ray Spectroscopy (EDS) analysis by scanning a 0.64 μm^2 area of the cross section of a device. Spot diameter for the elemental analysis was set to 3 nm. High spatial resolution was achieved by employing a 50 nm-thick lamella of the device. It was prepared with a Focused Ion Beam (FIB-SEM, Zeiss Auriga) in order to have a clean cut and thus prevent degradation of the materials and the collapse of the layers. Figures 5.9a-e show an analysis of the spatial distribution of Ti, Si, Pb, I, and Sn elements. The perovskite precursors percolate through the multilayered structure and crystallize in the voids of the SiO$_2$ layers. Interestingly, perovskite levels within the TiO$_2$ layers were below the detection limit, although it must be present as its precursors embed the whole PC (see Figure 5.9c,d). Indeed, it was corroborated by a Transmission Electron Microscopy (TEM) analysis of the perovskite crystallization around the different interfaces (see Figures 5.9f-g). Characteristic MAPbI$_3$ perovskite crystal planes within the porous and amorphous SiO$_2$ nanoparticle layers could be observed. This fact confirmed the good perovskite infiltration in the voids of SiO_2. On the other hand, some small perovskite crystals were detected throughout the TiO_2 film.

5.4.2. Optical performance of colourful perovskite solar cells

In Figure 5.10a-I, we show images of the colour palette obtained with PC-based PSCs. I employed the optical model to design the photonic structures according to the colour sought for the complete device.

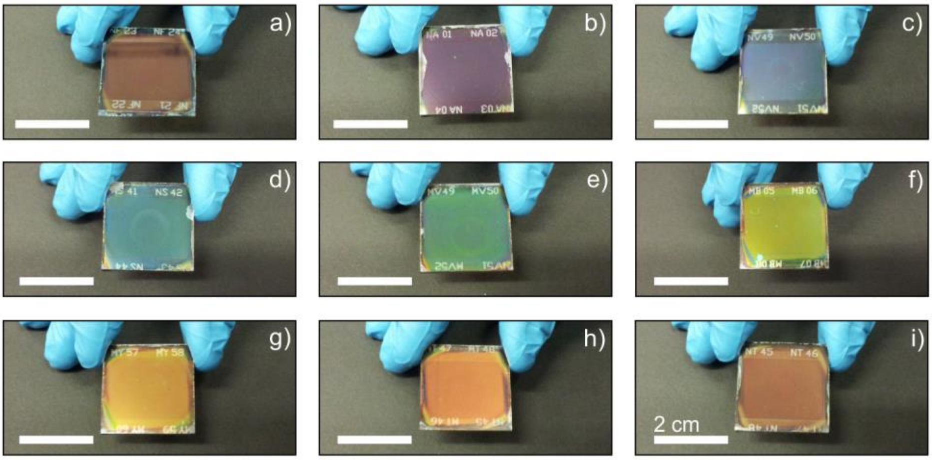

Figure 5.10. Digital camera pictures of the colourful perovskite solar cells integrating different photonic crystals. a) Reference device with no photonic scaffold. b-i) Colourful devices covering the entire visible range of the electromagnetic spectrum.

We performed an in-depth experimental and theoretical analysis of the optical effects occurring in perovskite solar cells that integrate PCs. We employed the theoretical model described in previous chapters to calculate the electric field intensity within the layered structure and, thus, to visualize the effect of integrating the PC on the spatial distribution of the radiation in the photovoltaic device.[8] To check the suitability of the proposed theoretical model, we fitted the experimental reflectance spectra of PC based cells measured at normal incidence, using the thickness of each layer in the structure extracted from the SEM as input parameters. Small variations of these values were permitted in the genetic algorithm function in order to attain a fine tuning of the calculated reflectance and hence a proper fitting. Good agreement between theory and experiment was attained, as displayed in Figure 5.11a. From the calculation, the unit cells of the periodic stacks were estimated to be 129 nm (d_{TiO2} = 39 nm, d_{SiO2} = 90 nm, for all the TiO_2 and SiO_2 layers comprising the unit cell, respectively) for the PC based *blue-green* cell (see TEM image in Figure 5.9f), and 145 nm (d_{TiO2} = 58 nm,

d_{SiO2} = 87 nm) for the *orange* cell (see SEM image in Figure 5.8). Please note that the notation for the ranges herein employed to identify the colour of the cells is the one commonly employed in CIE (*Comission Internationale de l´Éclairage*) colour diagrams. Such reflectance spectra can also be considered as the complement of the absorptance spectra, since light transmission through the cells is null. In that regard, each photonic design led to a different field intensity distribution along the cell and hence to a different spatial and spectral distribution of optical absorption in the device. In Figure 5.11b-c, we show the way in which the square of the electric field was distributed within the multilayer for the two cases chosen as examples. For comparison, we note the strong difference of light field distribution for photons with wavelength around 700 nm, whose penetration was much enhanced in the *blue-green* case, in comparison to the *orange* structure.

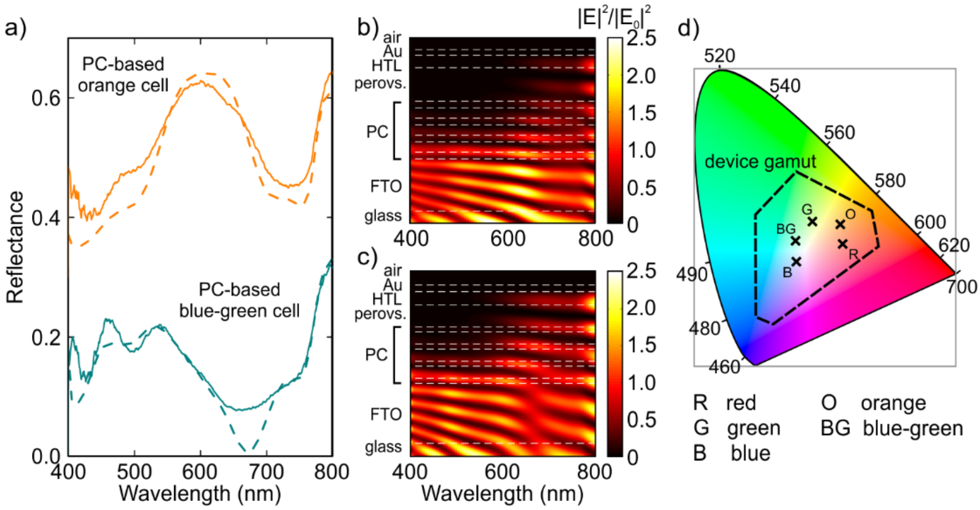

Figure 5.11. Optical description of photonic crystal-based perovskite solar cells. a) Experimental (solid lines) and theoretical reflectance (dashed lines) of the PC-based orange (orange lines) and blue-green (dark cyan lines) perovskite solar cells. Orange curves are vertically shifted by ΔR=0.3 for the sake of clarity. b-c) Calculated spatial (vertical axis) and spectral (horizontal axis) distribution of the square of the electric field enhancement ($|E|^2/|E_0|^2$), i.e. square of the electric field normalized by the square of the electric field in the incoming medium, along a cross section of the solar cell, for the PC-based orange (b), and blue-green (c) cells. Horizontal dashed lines are guides to the eye to delimit the interfaces between layers in the solar cells. d) CIE 1931 chromaticity space, showing the color hues of the PC-based (R) red (0.41, 0.34), (O) orange (0.41, 0.40), (G) green (0.33, 0.41), (BG) blue-green (0.29, 0.35) and (B) blue (0.29, 0.30) cells. The dashed black line delimits the device color gamut. It encompasses all different hues that can be achieved tuning the lattice parameter from 20 to 300 nm, and the thickness ratio of the high and low index material of the PC.

The device owed its colour to the convolution of the reflectance spectrum that resulted from the interference of all beams partially transmitted and reflected at each interface in the device with the photopic response of the human eye. In order to characterize the colour hue of the PC based photovoltaic, we calculated their colour coordinates and displayed the results as black symbols on the CIE 1931 chromaticity diagram in Figure 5.11d. By making use of the theoretical model, we also extrapolated the full range of colours that can be eventually achieved by varying the thickness of the layers comprising the PCs infiltrated by perovskite. Such colours are encompassed by the dashed polygon in Figure 5.11d, which represents the PC based cell tone gamut.

5.4.3. Photovoltaic performance of colourful perovskite solar cells

In Figure 5.12, we show the photovoltaic performance of perovskite solar cells displaying different colours. Measurements were made as we described in Chapter 3 (Sections 3.3.2. and 3.4.4.). If the light is being reflected, it is not being absorbed, and hence we expected there to be a trade-off between colour and photocurrent generation for these solar cells. In Figure 5.12a-c, we show the different spectral response of the *EQE* measured from a reference PSC, made using a mesoporous SiO_2 scaffold with a thickness of around 370 nm, as well as from PSCs integrating orange and blue-green reflecting PCs. As expected, the *EQE* curves showed clear depletions in those spectral regions for which the PC scaffold presented its reflectance maximum (shaded in grey in Figure 5.12b and c). Other potentially relevant effects such as photonic bandgap edge absorption enhancement,[9] were not readily detectable in these measurements. In Figure 5.12d-g, we present the performance parameters for a series of solar cells, see Figure 5.10, made using photonic scaffolds that displayed a range of optical reflectance peaks.

The first encouraging observation was that the solar cells operated well, despite the requirement for conduction through the PC, consistent with the perovskite absorber or the TiO_2 bridging the conduction through the photonic scaffold. We will stress this operational viability in the next section. The J_{sc} decreased in conjunction with the increase in PC thickness, as the colour shifted from blue to red. However, the V_{oc} and *FF* were only slightly varied, displaying independence of the PC thickness. We also observed that for blue, blue-green, green and orange hues, the *PCE* of the best performing devices were all above 6%, with the peak of 8.8% being achieved for the blue cells, showing good potential for making efficient working devices with vivid and tuneable colours. As a comparison, we would like to mention that the performance of the reference cell exhibited a peak and average *PCE* of 10.5% and 9.5% respectively, indicating reasonable retention of the expected performance for the perovskite devices with structural colour. In addition, PC-based PSCs showed a good stabilised power output, which was the *PCE* measured under constant load and illumination.[10] As an example, a blue cell which showed a maximum JV-determined efficiency of 7.9%, exhibited a stabilised power output of 6.6% (see Figure 5.12h-i).

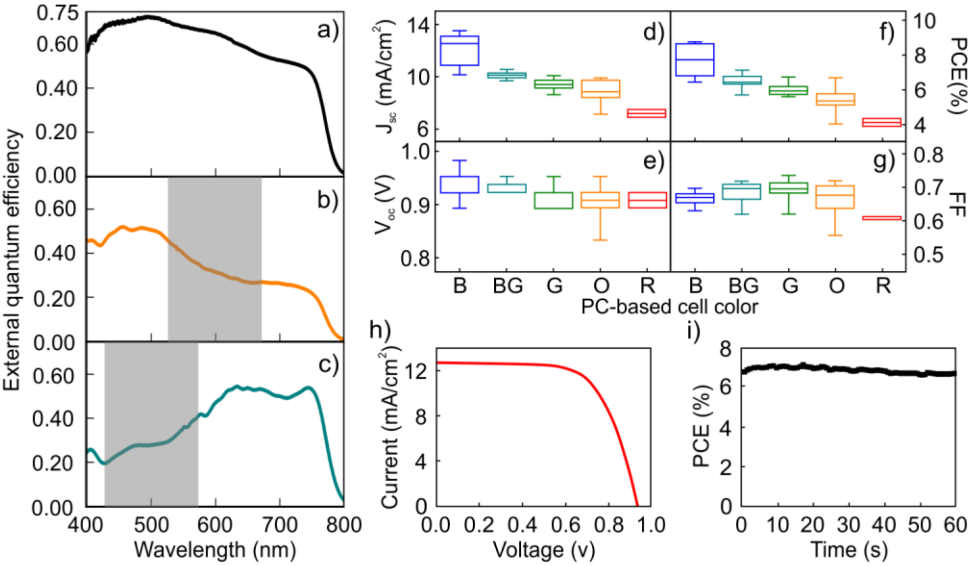

Figure 5.12. Electrical characterization and device performance analysis. a-c) Spectral dependence of the external quantum efficiency of a non-photonic structured SiO_2 scaffold-based perovskite solar cell (a), which acts as a reference, an orange PC-based cell (b), and blue-green PC-based cell (c). The shaded areas correspond to the spectral regions in which the PC-based cells show high reflectance. d-g) Box-plot of the device performance indicators for the different PC-based cells: short-circuit current density (d), open circuit voltage (e), power conversion efficiency (f), and fill factor (g). h Current-density/voltage curve of a PC-based perovskite solar cell. i) Stabilised power conversion efficiency of the same device. Measurements were taken under simulated AM1.5 sun light, at 100 $mW\cdot cm^{-2}$ irradiance.

5.5. Operation of colourful perovskite solar cells

The combined analysis of both the structural properties and the electro-optical performance of the colour perovskite solar cells demonstrates that photonics represents a powerful tool to provide the device with attractive aesthetical character. Indeed, in contrast to chemical management, this approach preserves the absorption onset of the perovskite light harvester, keeping the standard operational range (see Figure 5.12a-c). Nevertheless, we observed a decrease in the J_{sc}, hence in the *PCE*, of the devices as the photonic scaffold thickness increased, as the reflectance peak red-shifted. However, if we integrate the spectral absorptance of all the devices we can conclude that they presented comparable light harvesting efficiency. In consequence, the observed differences in photovoltaic performance did not have a photonic origin exclusively.

In addition, the elemental analysis from Figure 5.9 pointed to an inhomogeneous distribution of perovskite material along the photonic structure. In particular, perovskite presence within the quasi-dense TiO_2 films was below 5%. This observation suggests that, in PC-based devices, electrons may find an easier pathway to reach the electron collecting contact through the TiO_2 rather than percolating through the low amount of infiltrated perovskite, increasing the ratio between electrons injected into TiO_2 and electrons being transported just through the perovskite. This means that part of the electron populations should experience more than one perovskite-TiO_2, and *vice versa*, injection processes in order to get to the FTO. This hypothesis is supported by recent experimental analysis that indicates that the energy levels of hybrid perovskite compounds and TiO_2 are close.[11] Indeed, the effect of electron injection processes in the PC-based PSCs can be amplified due to the quasi-dense/porous layers alternation. At the same time, the transport of holes to the collection contact must be carried by the low amount of perovskite infiltrated in TiO_2 allows the transport of holes to the collecting contact. In addition, the simultaneous hole transport through the TiO_2 layers cannot be discarded, as it has recently been demonstrated for electronically defective slabs.[12]

5.5.1. Impedance spectroscopy of colourful perovskite solar cells

In order to test the validity of this hypothesis, we carried out Impedance Spectroscopy (IS) under illumination for a series of different forward applied bias. Measurements were made by means of a FRA equipped PGSTAT-30 from Autolab, under 100 mW/cm^2 illumination conditions using a 150 W Xe lamp. A 20 mV voltage AC perturbation was applied over the constant forward applied bias, between 0 V and 1 V, with the frequency ranging between 1 MHz and 0.05 Hz. It is far from the reach of this thesis to elucidate a definitive electrical model for perovskite solar cells. However, we will present some evidence that allow us to conclude how the charge is transported through the PC-based PSC.

For this experiment, three different green PC-based PSCs with identical layers thicknesses but different number of slabs, i.e. 3, 5 and 7, were characterized. Additionally, we prepared another set of samples with different SiO_2 layer thickness while keeping constant the total number of layers (7). As we demonstrated before, these last set of samples produced blue, green and red PC-based PSCs. Figure 5.13a-d shows impedance patterns of the aforementioned samples measured at V=0.7 V. Impedance spectra present several arcs and loops at positive values of imaginary impedance. The three arcs that appear at different

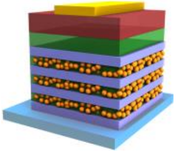

frequency domains can be fitted with an equivalent circuit that has been recently reported (see Figure 5.13e).[13] In that model, the series resistance, R_{series}, is produced by the effect of the FTO substrate and wiring, and can be extracted from the analysis of the high frequency region of the spectra (lower Z' values). The diameter of the arcs determines the resistive elements: successive arcs from high frequency to low frequency (low to high Z') correspond to R_3, R_2 and R_1, respectively. The frequency of the arc maximum and the resistance of each arc determine capacitance values of C_{bulk}, C_1 and C_2. C_{bulk} is the geometric capacitance of the layer due to diverse dipolar mechanisms.

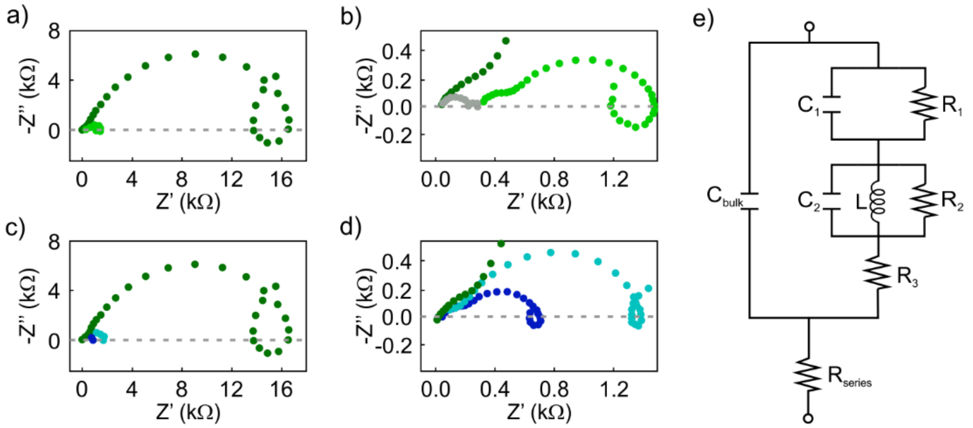

Figure 5.13. Impedance spectra and equivalent circuit of colourful perovskite solar cells. a) Nyquist plot of impedance spectra of a green perovskite solar cell with a photonic scaffold comprising 3 (grey circles), 5 (light green circles), and 7 (dark green circles) layers. b) Zoom of a). c) Nyquist plot of impedance spectra of a green (dark green circles), blue-green (light blue circles), and blue (dark blue circles) perovskite solar cell with a photonic scaffold comprising 7 layers. d) Zoom of c). e) Equivalent circuit employed to fit the impedance spectra.

The PC can be considered a single ESL itself since both TiO_2 and perovskite-infiltrated SiO_2 layers support electron transport. Since R_1 and R_2 are related to recombination resistance and their magnitude depends strongly on the ESL, it was not surprising that R_1 and R_2 increased with both the number of TiO_2 layers and the thickness of SiO_2 layers. Among both, R_2 presented a stronger dependence on the number of TiO_2 layers. R_3 is related to the transport resistance of electrons along the selective contact. Thus, as the number of TiO_2 layers increased, hence the total amount of material in the device, R_3 became larger. Continuing the analysis of the obtained spectra, we could corroborate that C_{bulk} is a voltage-independent parameter, related to the geometrical capacitance of the layer. The low frequency capacitance, C_1, presented very high values that are determined by a majority carrier accumulation at the perovskite-compact TiO_2 layer interface. Accumulation capacitance is proportional to the amount of charge, which is compensated by moving ions. In consequence, this effect was detected at lower frequencies instead of at higher ones, as would be expected from electronic phenomena. The systematic decrease of C_1 capacitance with the increase of total amount of SiO_2 observed for all samples, regardless of the number of TiO_2 layers, indicates a hindering of the ionic motion caused by the use of porous SiO_2 scaffolds. In contrast, C_2 is a surface state capacitance. Thus, as we can observe from the fitting of the impedance spectra, it depends not only on the perovskite-TiO_2 but also the on perovskite-SiO_2 interface.

The most noticeable characteristic of the impedance spectra is the presence of very significant loops (see Figure 5.13). This feature can be conveniently fitted by adding an inductive element, *L*, to the equivalent circuit. Inductance versus applied voltage curves attained from the fitting of the impedance spectra of the different samples under illumination are plotted in Figure 5.14. Figure 5.14a shows a clear increase in *L* with the number of TiO_2 layers. Contrarily, the effect of the total thickness of mesoporous SiO_2 is minor when the number of TiO_2 layers is kept constant (see Figure 5.14b).

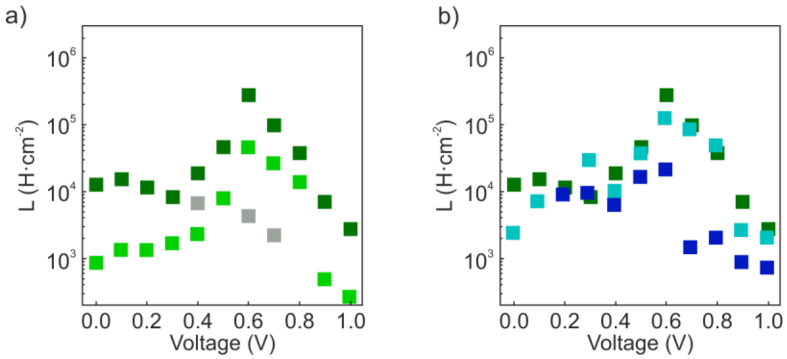

Figure 5.14. Inductance values of colourful perovskite solar cells. a) Inductance for green perovskite solar cells with a photonic scaffold comprising 3 (grey squares), 5 (light green squares), and 7 (dark green squares) layers. b) Inductance for green (dark green squares), blue-green (light blue squares), and blue (dark blue squares) perovskite solar cells with photonic scaffolds comprising 7 layers. The values were obtained from the fitting of the impedance spectra under illumination for the different samples, using the equivalent circuits plotted in Figure 5.13.

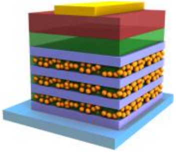

5.5.2. Mechanism of charge injection and recombination in colourful perovskite solar cells

The results show a clear correlation between L and the electron injection processes, augmented with the number of TiO_2 layers (i.e. perovskite/TiO_2 interfaces). They are in good qualitative agreement with inductive effects observed previously in impedance patterns of organic LEDs, which have been attributed to a multistep injection process.[14] This reinforces the hypothesis considered where electrons in the PC-based PSCs reach the FTO contact through a sequence of injection processes taking place at perovskite/TiO_2 and TiO_2/perovskite interfaces as they travel across the cross-section of the device.

Moreover, the analysis indicates that the role of the photonic scaffold goes beyond just providing a suitable matrix to grow perovskite crystals and providing the cell with colour. The presence of the scaffold hinders and/or reduces the ionic migration as the charge accumulation at the TiO_2/perovskite interface and the interfacial recombination is mitigated. This is further confirmed by a reduced hysteresis observed in the J-V curves of the devices. However, the tortuosity of the scaffold not only hinders the ionic motion, but also the diffusion of electrons and holes, resulting overall in a transport resistance increase. An optimum cell design requires an appropriate balance between low charge recombination and a reduction of the ion movement, but keeping transport losses low in order to avoid the decrease of the diffusion length. This compromise requires the use of thin scaffolds as the ones presented in the devices exhibiting the record efficiencies in the field.[15]

5.6. Conclusions

The results presented in this chapter constitute the first demonstration of PSCs displaying bright colour over the entire visible spectrum while retaining their high efficiency. In Summary, we have demonstrated that a porous photonic crystal, built from alternating liquid processed layers of quasi-dense TiO_2 and porous SiO_2, can be constructed and integrated as a substitute scaffold into the active layer of a PSC. The resulting solar cells exhibit well-defined reflectance bands, with the remaining non-reflected light being channelled into the perovskite absorber to undergo photovoltaic conversion at high efficiency. The colours of the devices are attained on demand by means of optical design of the complete multilayer system. The working mechanism consists in an anomalous injection, identified by an inductive loop in the impedance spectra that has been revealed as a succession of charge injection steps taking place at the perovskite/TiO_2 interfaces.

As a result, aesthetically attractive PSCs in blue, blue-green and green hues are achievable and offer a new avenue for efficient and colourful PV for integration into the built environment. We note that a current widely-adopted technology for BIPV is amorphous silicon, where the modules integrated with a red-orange hue are less than 5% efficiency, illustrating potential for much superior performance for the colourful perovskite modules. In addition, we would like to note that state-of-the-art PSCs in March 2018, when this dissertation was submitted for evaluation, surpass 22% efficiency that almost double reference values in 2014, when this work was developed. Therefore, PC-based PSCs nowadays have the potential of achieving efficiencies above 15% for the whole visible spectrum. Key advantages of the route proposed in this chapter, as opposed to employing a colourful absorber layer, are that the structural colour is unlikely to bleach or fade with time, and in addition a single panchromatic photovoltaic absorber optimised for efficiency and stability can be integrated with a broad range of colour hues. An unexpected advantage of the colourful perovskite solar cells for BIPV applications may be that the additional reflected light will reduce the thermal gain within the solar cell and in the building, which may have added benefits of lower operating temperatures of the solar cells, and hence increasing efficiency under real world conditions and reducing the cooling demand in buildings. We expect future improvements to be made by understanding and enhancing the electronic properties of the photonic crystal scaffolds, narrowing the reflectance bands and further optimizing the PSCs. This structure will also lend itself to perovskite-based LEDs, and may prove to be important for the development of perovskite injection lasers.

5.7. Notes

I fabricated the devices from Section 5.4. and 5.5. throughout a series of secondments (June 2014, November 2015, and summer 2016) at the Photovoltaic and Optoelectronic Device Group headed by Prof Henry Snaith. I appreciate his kind reception and Dr Wei Zhang’s guidance during my stay. I performed the impedance spectroscopy characterization in the Group of Advanced Materials and Energy under the supervision of Assistant Prof Iván Mora-Seró.

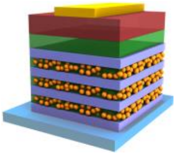

5.8. References

1 Henemann, A. BIPV: Built-in solar energy. *Renewable Energy Focus* **2008**, *9*, 14-19.

2 Noh, J. H.; Im, S. H.; Heo, J. H.; Mandal, T. N.; Seok, S. I. Chemical management for colorful, efficient, and stable inorganic-organic hybrid nanostructured solar cells. *Nano Lett.* **2013**, *13*, 1764–1769.

3 Eperon, G. E.; Stranks, S. D.; Menelaou, C.; Johnston, M. B.; Herz, L. M.; Snaith, H. J. Formamidinium lead trihalide: a broadly tunable perovskite for efficient planar heterojunction solar cells. *Energy Environ. Sci.* **2014**, *7*, 982–988.

4 Colodrero, S.; Ocaña, M.; Míguez, H. Nanoparticle-based one-dimensional photonic crystals. *Langmuir* **2008**, *24*, 4430-4434.

5 Colodrero, S.; Mihi, A.; Häggman, L.; Ocana, M.; Boschloo, G.; Hagfeldt, A.; Miguez, H. Porous one-dimensional photonic crystals improve the power-conversion efficiency of dye-sensitized solar cells. *Adv. Mater.* **2009**, *21*, 764-770.

6 Bravo, J.; Zhai, L.; Wu, Z.; Cohen, R. E.; Rubner, M. F. Transparent superhydrophobic films based on silica nanoparticles. *Langmuir* **2007**, *23*, 7293-7298.

7 Lozano, G.; Colodrero, S.; Caulier, O.; Calvo, M.E.; Míguez, H. Theoretical analysis of the performance of one-dimensional photonic crystal-based dye-sensitized solar cells. *J. Phys. Chem. C.* **2010**, *114*, 3681-3687.

8 Anaya, M.; Lozano, G.; Calvo, M. E.; Zhang, W.; Johnston, M. B.; Snaith, H. J.; Míguez, H. Optical description of mesostructured organic-inorganic halide perovskite solar cells. *J. Phys. Chem. Lett.* **2015**, *6*, 48–53.

9 Anaya, M.; Calvo, M. E.; Luque-Raigón, J. M.; Míguez, H. Resonant photocurrent generation in dye-sensitized periodically nanostructured photoconductors by optical field confinement effects. *J. Am. Chem. Soc.* **2013**, *135*, 7803-7806.

10 Snaith, H. J.; Abate, A.; Ball, J. M.; Eperon, G. E.; Leijtens, T.; Noel, N. K.; Stranks, S. D.; Wang, J. T.-W.; Wojciechowski, K.; Zhang, W. Anomalous Hysteresis in Perovskite Solar Cells. *J. Phys. Chem. Lett.* **2014**, *5*, 1511-1515.

11 Correa Baena, J. P. .; Steier, L.; Tress, W.; Saliba, M.; Neutzner, S.; Matsui, T.; Giordano, F., Jacobsson, T. J.; Srimath Kandada, A. R. S.; Zakeeruddin, M.; Petrozza, A.; Abate, A.; Nazeeruddin, M. K.; Gratzel, M.; Hagfeldt, A. Highly efficient planar perovskite solar cells through band alignment engineering. *Energy Environ. Sci.* **2015**, *8*, 2928-2934

12 Hu, S.; Shaner, M. R.; Beardslee, J. A.; Lichterman, M.; Brunschwig, B. S.; Lewis, N. S. Amorphous TiO_2 coatings stabilize Si, GaAs, and GaP photoanodes for efficient water oxidation. *Science* **2014**, *344*, 1005-1009.

13 Guerrero, A.; Garcia-Belmonte, G.; Mora-Sero, I.; Bisquert, J.; Kang, Y. S.; Jacobsson, T. J.; Correa-Baena, J.-P.; Hagfeldt, A. Properties of contact and bulk impedances in hybrid lead halide perovskite solar cells including inductive loop elements. *J. Phys. Chem. C* **2016**, *120*, 8023−8032.

14 Bisquert, J.; Garcia-Belmonte, G.; Pitarch, Á.; Bolink, H. J. Negative capacitance caused by electron injection through interfacial states in organic light-emitting diodes. *Chem. Phys. Lett.* **2006**, *422*, 184-191.

15 Correa-Baena, J. P.; Anaya, M.; Lozano, G.; Tress, W.; Domanski, K.; Saliba, M.; Matsui, T.; Jacobsson, T. J.; Calvo, M. E.; Abate, A.; Grätzel, M.; Míguez, H.; Hagfeldt, A. Unbroken perovskite: interplay of morphology, electro-optical properties, and ionic movement. *Adv. Mater.* **2016**, *28*, 5031–5037.

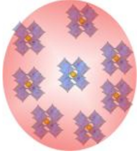

Chapter 6

Strong quantum confinement in perovskite nanocrystals synthesised in mesostructured scaffolds

Herein, we demonstrate a simple, reproducible and scalable method to obtain stabilized $MAPbI_3$ *nanocrystals embedded in thin metal oxide films that display well-defined and adjustable quantum confinement effects over a wide range of 0.34 eV. Supramolecularly templated* TiO_2 *and* SiO_2 *films displaying an ordered three-dimensional pore network are employed for the synthesis of perovskite crystallites.* $MAPbI_3$ *crystallites are attained with narrow size distribution and average radius comprised between 1 and 4 nm, depending on the template of choice. The absorption onset of the resulting ensembles shows stable blue shift on demand with respect to the bulk* $MAPbI_3$ *over a wide range of wavelengths from 640 nm to 775 nm, which is representative of the strong quantum confinement regime. We discuss the distinctive features of these systems in terms of their photophysical properties. The high optical quality of the materials is maintained over areas of several squared centimetres, opening the path to the fabrication of perovskite-based optoelectronic devices free of halide segregation with performances governed by quantum size effects.*

6.1. Introduction

In the previous chapter, $MAPbI_3$ was provided with colour by means of photonics, keeping the bandgap of the material constant and, therefore, maintaining its potential spectral operational range. That finding opened the door to apply this technology in the niche market of BIPV. However, some optoelectronic applications require the modification of the bandgap of the material towards the visible range of the electromagnetic spectrum, not for aesthetical purposes but for operational necessities. This is the case of light emitting devices (LEDs), which demand visible emission for lighting purposes. In addition, a blue-shift in the bandgap of the absorber gives rise to solar cells of superior voltages at the expense of photogenerated current. This is the only way to introduce PV technology for certain uses such as light-promoted water splitting. Moreover, the optimum light harvester for its application as top subcell in double-junction tandem devices would present an absorption onset at λ~700 nm, as we pointed out in Chapter 4. In the ABX_3 field, efforts towards this direction have mainly focused on the synthesis of $APbBr_xI_{3-x}$ perovskites. However, long-term stable devices have not been demonstrated when using this mixed halide materials since a photo-induced ionic segregation occurs.[1-3]

One of the most versatile strategies to tune the optical properties of a semiconductor consists in reducing its particle size until it becomes of the order of the exciton Bohr radius and quantum confinement effects arise.[4] In this framework, the bandgap of the semiconductor blue-shifts following the as-known Brus formula,

$$E_0 \approx E_g + \frac{h^2}{8\mu R^2} - \frac{1.786e^2}{4\pi\varepsilon_0\varepsilon_r R} \tag{6.1}$$

which assumes a hydrogen-like model to describe the interaction between electron-hole pairs strongly confined in spherical semiconductor nanocrystals. [5,6,7] In this expression, E_0 is the energy of the lowest excited state of the exciton inside the nanocrystal, E_g is the energy bandgap of bulk material (E_g=1.60 eV for $MAPbI_3$), h is the Planck constant, μ is the exciton reduced mass, R is the radius of the nanocrystal, and e is the electron charge. ε_0 and ε_r are the dielectric constants of vacuum and the semiconductor, respectively. The second term on the right-hand side of the equation has a kinetic origin and corresponds to the first energy level of a quasiparticle of reduced mass μ confined in a spherical well of radius R limited by a wall of infinite potential. The third term on that same side of the equation is known as the Coulomb energy term, as it arises from considering the electrostatic interaction between the electron and the hole confined in the nanocrystal. The contribution of this term cannot be neglected, although it is less significant than that of the kinetic term due to both the high screening of the interaction in high dielectric constant semiconductors like $MAPbI_3$ and the fact that it scales like R^{-1} instead of R^{-2}.

With this in mind, this approach would imply true colour tunability free of halide segregation in perovskites since it does not require halide mixing, providing a valid path for its application in tandem devices. Evidence of precise control of the optical properties of $MAPbI_3$ over a wide spectral range has been reported from colloidal suspensions attained using a two-step process involving the synthesis of PbI_2 nanocrystals and their subsequent reaction with $MAPbI_3$ to produce the corresponding organic-inorganic lead halide quantum dots.[8] However, its application for tandem solar cells (or any other optoelectronic device) require the use of thin films of high optical quality. As we explained in the introduction of this dissertation, a plausible way to achieve a quantum confined semiconductor deposited as a thin film relies on the use of nanoreactors. The fabrication of such nanocages arise from the precise control over the porosity of thin films that act as host for the formation of semiconductor nanocrystals. By doing so, one can deterministically form nanocrystals whose size is dictated by the voids of scaffolds performing high optical quality, an approach that has not been explored in the field of ABX_3 perovskites.

In this chapter, we present a synthetic route to obtain stabilized $MAPbI_3$ nanocrystals embedded in thin metal oxide films that display well-defined and adjustable quantum confinement effects over a wide range of 0.34 eV. Mesostructured TiO_2 and SiO_2 films displaying an ordered three-dimensional pore network are prepared by evaporation induced self-assembly of a series of organic supramolecular templates in the presence of metal oxide precursors. The pores in the inorganic films obtained after thermal annealing are then used as nanoreactors to synthesize $MAPbI_3$ crystallites with narrow size distribution. High resolution transmission electron microscopy determines average radius comprised between 1 nm and 4 nm, depending on the template of choice. These sizes, which are below the exciton Bohr radius in $MAPbI_3$, result in a controllable blue-shift of the bandgap of the material from the near infrared (λ=780 nm) to the red (λ=640 nm) range of the visible spectrum. This effect is representative of the regime of strong quantum confinement and we analyse its influence on both the static and dynamic photoemission properties of the ensemble. Photoemission maps demonstrate that the optical properties extracted from the perovskite quantum dot loaded films are homogeneous over square centimetre areas. In addition, at variance with their bulk counterparts, constant emission intensity is reached in time scales at least four orders of magnitude shorter. Results in this chapter constitute the first proof of concept of confined perovskite nanocrystals free of halide segregation showing tuneable photophysical properties in high optical quality films.

6.2. Fabrication of periodically mesostructured scaffolds

The preparation of mesoporous structures with different well-defined pore size was made by using a supramolecular templating approach.[9] The synthesis was based on the hydrolysis and condensation (sol-gel method) of TiO_2 and SiO_2 precursors around a 3D arrangement of an organic templating agent. After the removal of the organic pattern by thermal treatment, an oxide mesostructure film arises with an open, ordered and interconnected network of pores with regular shape. This method allows controlling the pore size by changing the organic template.

6.2.1. Synthesis of precursors

First, a dispersion of $TiCl_4$ (Sigma Aldrich) in ethanol (EtOH, VWR Chemical) was prepared in a Ti:EOH 1:40 molar ratio. Then the surfactant was added under strong stirring. The surfactants used were: cethyltrimethylammonium bromide (Sigma-Aldrich, CTAB), two different triblock copolymers (Pluronics F127 and P123) and alkylpoly(ethylene oxide) (Sigma-Aldrich, Brij 58). The surfactant/Ti ratio (in moles) was: 0.100 in CTAB, 0.05 in Brij 58, 0.005 in F127 and P123. The largest pore size was obtained using a combination of the previous method and phase separation. In this case, the dispersion was prepared in 1-butanol using both $TiCl_4$ and F127 in the same molar ratio described above. Thus, 0.24 g of polypropylene glycol 4000 (PPG, Alfa Aesar GMBH&Co KG) and 4 ml of tetrahydrofuran (THF, Panreac) were added to the dispersion. Finally, H_2O was added to the above described dispersion in a H_2O/Ti molar ratio of 10. SiO_2 mesoporous films were prepared in the same way described above, starting from a pre-hydrolyzed tetraethylortosilicate dispersion (TEOS) as inorganic source (instead of $TiCl_4$).

6.2.2. Deposition procedure

All dispersions were aged during two days previous to deposition. Deposition of the precursors was made in low fluorescence slides by dip coating method (ND-R Rotary Dip

Coater, Nadetech Innovations, see Figure 6.1). The withdrawal speed, 2 mm/s, was adjusted to obtain a 200 nm thickness film (100 nm for the cases of F127+PPG-based TiO_2, and CTAB-based SiO_2 scaffolds). Humidity in the deposition chamber was kept constant at values between 40% and 50%. After deposition, the humidity was increased to 80% for 10 s, and then the fresh films were placed in a chamber with 50% humidity during 24 hours. Next, samples were kept at 60°C during 24 hours and then at 120°C for another 24 hours. These steps were needed in order to consolidate the oxide network around the organic template. Finally, the latter was removed by treating the films during one hour at 350°C (ramp of 1°C/min). For the cases of F127+PPG based TiO_2 and CTAB based SiO_2 scaffolds, the deposition process was repeated in order to achieve films around 200 nm thick.

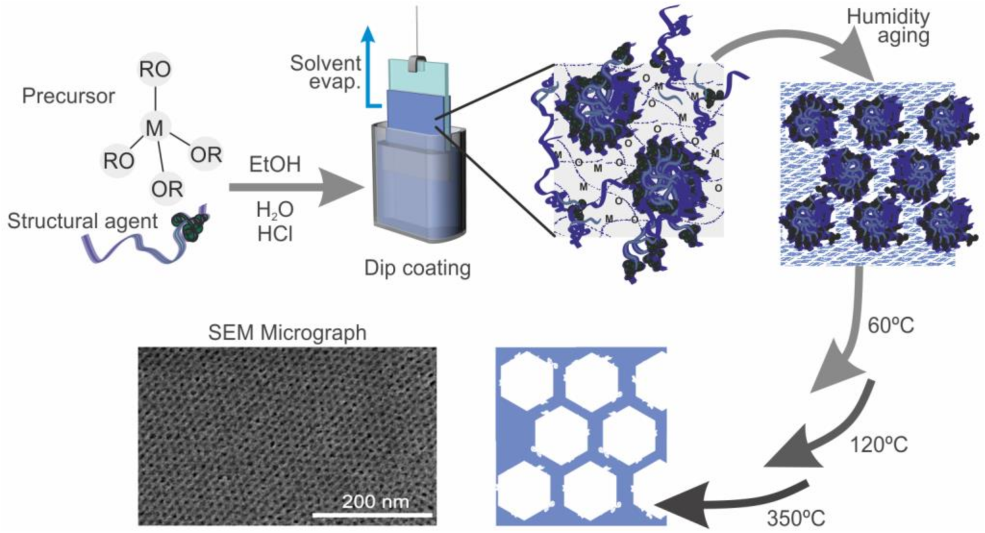

Figure 6.1. Evaporation induced self-assembly process.

6.3. Preparation and structural properties of $MAPbI_3$ nanocrystals

It is well known that the metal oxide films prepared as described above contain a three-dimensional array of pores (see SEM micrograph in Figure 6.1).[9] This ordered distribution of voids implies a very narrow distribution in their sizes, which is directly tuned by the surfactant. Such a feature is ideal for the formation of materials in which their dimensions are deterministically controlled by the nanocage. In the next paragraphs, we will apply this approach to form $MAPbI_3$ perovskite nanocrystals.

6.3.1. Formation of $MAPbI_3$ nanocrystals

We carried out the infiltration of periodic porous mesostructures with $MAPbI_3$ by spin coating the perovskite precursor solutions, as we display in Figure 6.2. Perovskite formation was completed by treating the samples for one hour at 100ºC. To avoid the deposition of a perovskite capping layer, we adjusted the $MAPbI_3$ solution concentration and spin coating deposition parameters. We found that a concentration of 20 wt% and a final rotation speed of 5000 rpm were the optimized parameters. This procedure assured that perovskite nanocrystals were exclusively grown within the inorganic scaffold.

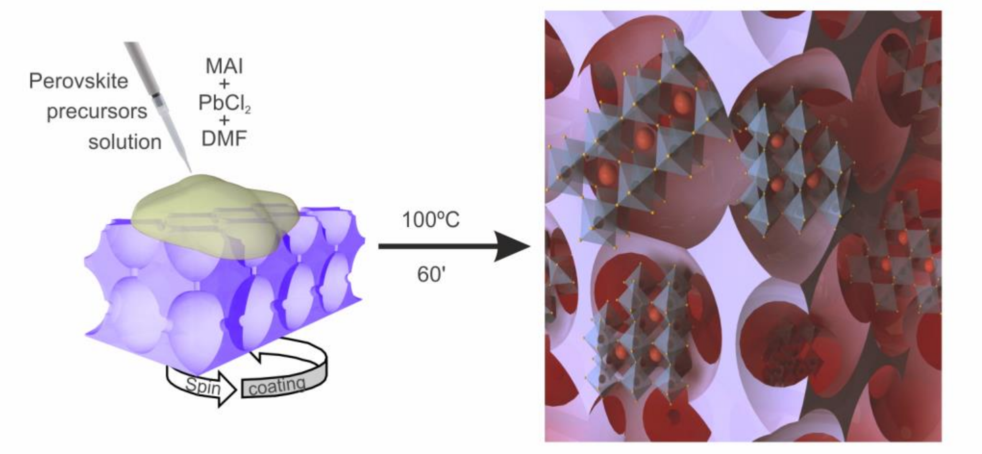

Figure 6.2. Formation of $MAPbI_3$ nanocrystals within the nanoreactors.

6.3.2. X-ray diffraction analysis of the $MAPbI_3$ nanocrystals

Analysis of the X-ray diffractograms, like the one displayed in Figure 6.3a, demonstrated that the stable phase of the crystallites within the cages was tetragonal, which implied that the final structure achieved was the same one observed in bulk $MAPbI_3$ films. Please note that in this chapter we will refer to the standard $MAPbI_3$ films as bulk, in contrast to the nanocrystals. As the pore size decreased, the characteristic diffraction peak intensities of $MAPbI_3$ lowered and widened, as shown in Figure 6.3b. This feature indicated that the crystal size reduced with the decrease of the pore of the structure, as stated by the Scherrer equation:

$$s = \frac{K\lambda}{\beta \cos\theta} \tag{6.4}$$

where s is the size of the nanocrystal, K the shape factor that is close to unity, λ is the X-ray wavelength, β is the *FWHM* of the diffraction peak, and θ is the incident angle of the beam. However, by using this formula, we was only able to roughly guess that perovskite crystal size varied, among the different films prepared, in the range of a few nanometers, as the low intensity of the diffraction maxima prevented a finer estimation.

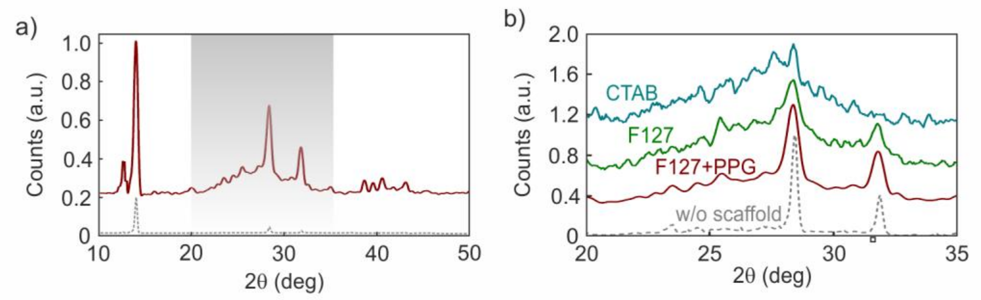

Figure 6.3. X-ray diffraction of MAPbI$_3$ nanocrystals. a) XRD pattern of MAPbI$_3$ perovskite nanocrystals grown within a F127+PPG-templated TiO$_2$ mesostructured scaffold. b) XRD patterns detail of the peak broadening corresponding to {220} reflections (2θ~28°) of MAPbI$_3$ nanocrystals grown within F127+PPG- (red), F127- (green) and CTAB- (blue-green) templated TiO$_2$ mesostructured scaffolds. Grey dashed curves indicate the reference pattern of tetragonal phase bulk MAPbI$_3$ perovskite.

6.3.3. Size of the MAPbI$_3$ nanocrystals

In order to get accurate information regarding the crystallites sizes, we performed TEM characterization of a series of the aforementioned samples. To this end, cross-section lamellas were prepared using a dual FIB (Helios Nanolab 650, FEI). The microstructure of the structures was analysed by scanning TEM (STEM, G2F30, FEG) equipped with a High Angel Annular Dark Field (HAADF, Fischione) detector with a 0.16 nm per point resolution. Arrays of crystallites of similar size and shape, synthesized within porous TiO$_2$ matrices like that shown in Figure 6.4a, could be readily identified on STEM images, as illustrated in Figure 6.4b. Interplanar distances corresponding to the tetragonal structure of MAPbI$_3$ were recognized, as shown in the inset of this Figure.

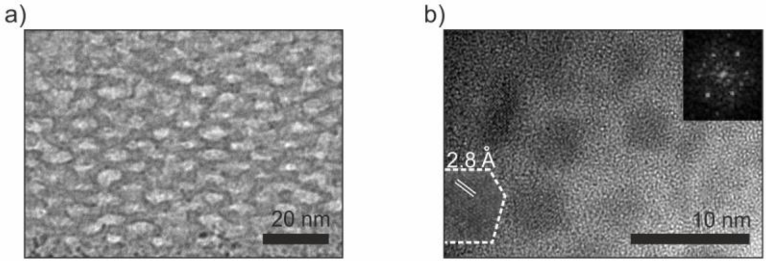

Figure 6.4. Transmission electron microscopy images of MAPbI$_3$ grown within the nanoreactors. a) High resolution transmission electron microscopy image of a cross section of a F127+PPG-templated TiO$_2$ mesostructured scaffold. b) High resolution transmission electron microscopy image showing the crystalline planes of different MAPbI$_3$ nanocrystals. Inset displays the digital diffraction pattern of the highlighted particle planes.

The nanocrystal size distributions, extracted from the analysis of the STEM images, corresponding to each one of the $MAPbI_3$-filled mesostructured films are presented in Figures 6.5a to 6.5e. The estimated crystallite average size correlated with the average pore size expected in each film, which was determined to a good extent by the organic supramolecular template employed. Hence, crystals of radii R=3.10±0.08 nm, R=2.26±0.03 nm, R=2.03±0.07 nm, R=1.70±0.05 nm and R=1.64±0.02 nm were observed inside the void lattice of films made using, respectively, a mixture of F127 and PPG, P123, F127, CTAB and Brij58 as surfactants.

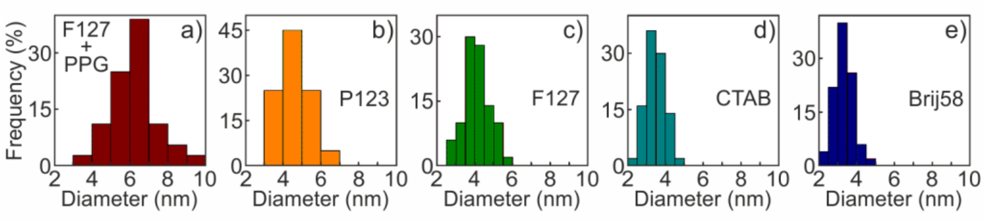

Figure 6.5. Particle size of $MAPbI_3$ nanocrystals grown within the nanoreactors. a-e) Size distribution histograms of $MAPbI_3$ nanocrystals grown within different porous TiO_2 scaffolds in which the voids are ordered by using F127+PPG (a), P123 (b), F127 (c), CTAB (d) and Brij58 (e) as organic template agent.

6.3.4. $MAPbI_3$ distribution within the pore network

In order to confirm that nanocrystals dimensions were deterministically dictated by the TiO_2 voids, we made an analysis on the $MAPbI_3$ spatial distribution within the mesoporous network. Elemental analysis was performed by means of EDS in a region of a cross section of the structure. In this regard, an EDS detector (SSD, INCA X-Max 80) was coupled to the STEM in order to study the spatial distribution of Pb and Ti inside the mesostructured film. Those elemental maps and the corresponding HAADF-STEM images are displayed in Figure 6.6. In this specific case, they were attained from two different inner surfaces of the ordered pore lattice filled with $MAPbI_3$ crystallites. Interestingly, the observations verified that the $MAPbI_3$ crystallite array inherits the order of the pore network in which it was formed, although this had no apparent effect on the optical response of the ensemble. These results confirm that the periodically ordered films can be efficiently infiltrated with the $MAPbI_3$ precursors.

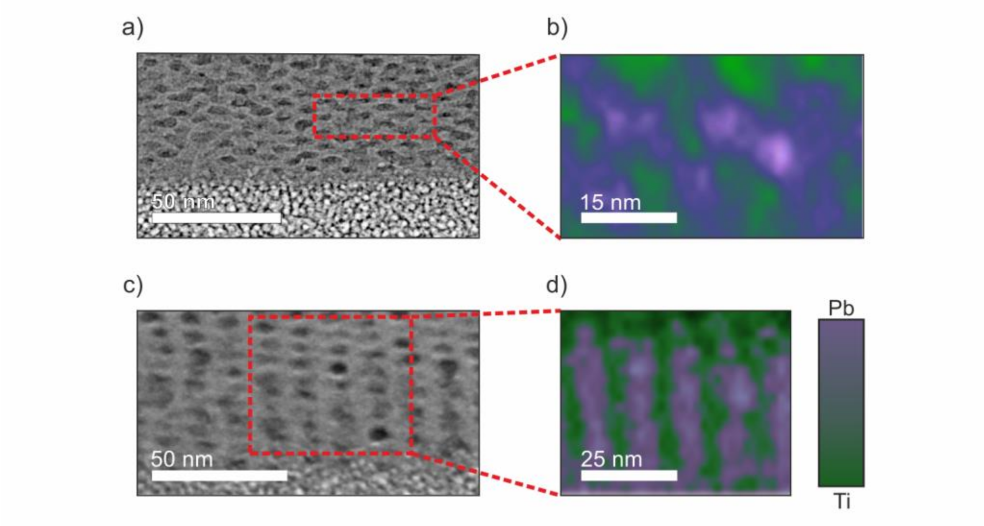

Figure 6.6. Elemental mappings of the $MAPbI_3$ nanocrystals and TiO2 matrix ensembles. a,c) HAADF-STEM image of a hexagonal- (a), and cubic-like (c) pore distribution which can be assigned to different cross section planes of a F127-templated mesostructured scaffold infiltrated by $MAPbI_3$. b,d) XEDS chemical maps of Ti and Pb obtained from the marked regions, for both hexagonal-(b) and cubic-like (d) ordered pore planes infiltrated by $MAPbI_3$.

6.4. Evidences of strong quantum confinement arising from the $MAPbI_3$ nanocrystals

The most direct consequence of the confinement of a semiconductor is the quantization of its energy levels and, consequently, the enlargement of its electronic bandgap. This feature is revealed as a spectral blue-shift of both its optical absorption edge and the corresponding luminescence peak. Hence, the optical properties of the crystallite networks built in periodically mesostructured scaffolds were investigated.

6.4.1. Absorption and static photoluminescence of $MAPbI_3$ nanocrystals

We analysed the absorptance and PL spectra of the perovskite nanocrystals following the procedures described in Section 2.2.4. Results are shown in Figure 6.7a. A single peak at a wavelength of λ_0=775 nm (E_g=1.60 eV) was detected in the PL spectrum of the scaffold-free $MAPbI_3$ film used as reference. In contrast, crystallites synthesized within periodically porous films displayed PL peaks at λ_g=692 nm (E_0=1.79 eV), λ_0=686 nm (E_0=1.81 eV), λ_0=677 nm (E_0=1.83 eV), λ_0=660 nm (E_0=1.88 eV) and λ_0=638 nm (E_0=1.94 eV), where the surfactant employed to achieve each one of the mesostructures is indicated. This implies a maximum blue-shift of $\Delta\lambda_0$=137 nm (ΔE_0=0.34 eV), one of the largest so far reported for $MAPbI_3$ crystallites. Simultaneously, a consistently similar shift was observed at the edge of the absorptance spectra.

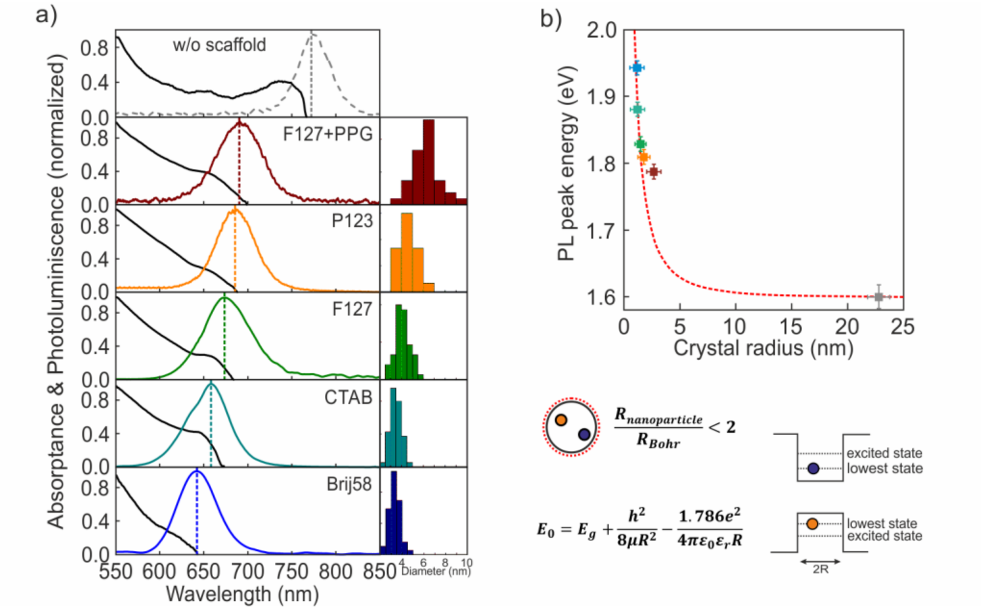

$$\frac{R_{nanoparticle}}{R_{Bohr}} < 2$$

$$E_0 = E_g + \frac{h^2}{8\mu R^2} - \frac{1.786e^2}{4\pi\varepsilon_0\varepsilon_r R}$$

Figure 6.7. Blue-shift of the bandgap of $MAPbI_3$ nanocrystals. a) Normalized absorptance and PL (black and coloured lines, respectively) spectra from $MAPbI_3$ nanocrystals grown in a low-fluorescence glass without scaffold (grey), and with supramolecularly templated TiO_2 scaffolds F127+PPG (dark red), P123 (orange), F127 (green), CTAB (blue-green) and Brij58 (blue). Colourful dashed lines are displayed as a guide to the eye to locate the wavelengths at which absorption onset (PL peak) is in each case. Data from Figure 6.5 are included to allow comparison. b) Spectral position of the absorption onset (PL peak) with respect to the crystal radius of the $MAPbI_3$ nanocrystals grown within the different TiO_2 scaffolds (colour code is preserved from Figure 6.7a). Red dashed line represents the best fit to Brus equation, which is explained in the bottom scheme.

The spectral displacement observed in both absorptance and photoemission spectra increased as the average crystallite size present in the film decreased, as expected for a semiconductor in which quantum confinement of electron-hole pairs takes place. In fact, the comparison between the crystal radii measured by STEM and the reported estimated values of Bohr radius (R_B≈3 nm),[7,10-13] which yielded $\frac{R}{R_B} < 2$ in all cases, as well as the magnitude of the bandgap shift observed for $MAPbI_3$ nanocrystals (ΔE_0=0.34eV), indicated that the observations may be well explained assuming a strong confinement regime, after the classification established by Kayanuma.[14] Within this regime, both electron and hole are expected to be found mainly occupying their respective lowest energy eigenstates and with little spatial correlation between them.

6.4.1.1. Brus equation

In order to provide a deeper insight into the nature of the effects observed, we analysed the dependence between the size of the crystals and their photoluminescence properties. In Figure 6.7b, we plot the energy (eV) at which the absorption onset was detected versus the crystal size as estimated from the STEM analysis. Superimposed, we draw the curve (dashed line) corresponding to the best fit of the data to the Brus formula (Equation 6.1). From the fitting, we estimated an exciton reduced mass of μ=0.27±0.01 m_0, with m_0 being the electron rest mass, and a dielectric constant of ε_r=18.0±0.5. Then, we could make use of the following relations between the exciton binding energy, E_B, and Bohr radius, R_B:

$$E_B = \frac{\mu}{m_0} \cdot \frac{1}{\varepsilon_r^2} \cdot \frac{m_0 e^4}{2(4\pi\varepsilon_o \hbar)^2} = \frac{\mu}{m_0} \cdot \frac{1}{\varepsilon_r^2} \cdot E_{B_{hydrogen}} = \frac{\mu}{m_0} \cdot \frac{1}{\varepsilon_r^2} \cdot 13.6 \tag{6.2}$$

$$R_B = \frac{m_0}{\mu} \cdot \varepsilon_r \cdot R_{B_{hydrogen}} = \frac{m_0}{\mu} \cdot \varepsilon_r \cdot 0.053 \tag{6.3}$$

, to obtain E_B=11.3±1.0 meV and R_B=3.53±0.23 nm for $MAPbI_3$. This set of values for μ, ε_r, E_B and R_B are in fair agreement with previously reported ones based on theoretical estimations that have been demonstrated to well reproduce the behaviour of bulk $MAPbI_3$ at room temperature.[11,15-17] That agreement supported the validity of the use of the Brus approximation to describe the observed trends, although it should be taken into account that, in this expression, the effective mass is considered to be independent of the crystal size, an approximation that might not necessarily hold for extremely small crystallites like the ones presented in this chapter.

6.4.1.2. Photoluminescence activation in $MAPbI_3$ nanocrystals

In Chapter 2, we showed how the emission of perovskite films presented a transient, where a photoactivation preceded a photodarkening of the PL. Similarly, tracking the time evolution of the PL peak from the perovskite nanocrystals, we observed that 10 ms (limited by the time resolution of the setup) after the excitation of the film, it reached a stable emission (see Figure 6.8). This was in contrast with the slow photo-activation of the PL presented by a bulk film of similar thickness (i.e. 200 nm). Such slow dynamics of the PL of bulk $MAPbI_3$ have been previously discussed in this dissertation.[18,19] This was proposed to originate due to trap-filling caused by the photo-induced migration of ions within the perovskite lattice under illumination.[20] Within this picture, it is reasonable to assume that the time needed for ions to traverse the size of the QD should be orders of magnitude smaller than that for the bulk case. This observation suggests that, under similar excitation conditions, the PL of nanocrystals enters the so-called bimolecular regime, in which carrier decay rate is dominated by radiative recombination,[21] much faster than that of bulk crystals, which remains for longer in the monomolecular regime, in which non-radiative trap filling prevails. Furthermore, the confined perovskite nanocrystals are as stable as the bulk perovskite films. Indeed, they conserve their emission properties over weeks although they are conserved under dark ambient conditions.

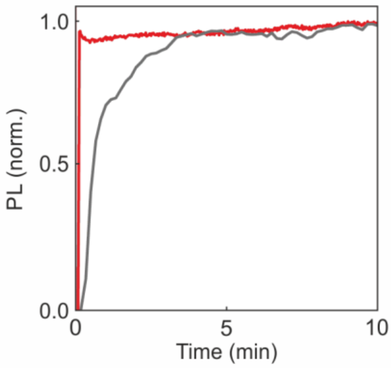

Figure 6.8. Photoluminescence transient from MAPbI$_3$ nanocrystals. Photoluminescence maximum of confined MAPbI$_3$ nanocrystals (λ_{max}=684 nm, red curve) and a bulk MAPbI$_3$ film (λ_{max}=775 nm, grey curve) as a function of time under excitation with monochromatic light of λ=532 nm.

6.4.2. PL decay dynamics of MAPbI$_3$ nanocrystals

Electron-hole pairs confined in nanosized semiconductors are also expected to experience significant modifications in their decay dynamics.[22] Following the procedure introduced in Section 2.3.2., we performed time resolved PL measurements for the series of MAPbI$_3$ crystallites prepared, as well as for a bulk perovskite film, for the sake of comparison. A 532 nm excitation wavelength was employed in all cases, and the time evolution of the emitted intensity was monitored by means of TCSPC within a 5 nm wide spectral window centered at the respective emission maximum. Results shown in Figure 6.9a are representative of each type of sample, since very similar curves were systematically obtained from different regions of the same film. It can be readily seen that the average excited state lifetime (τ_{av}) decreased, hence decay rate (Γ) accelerated, as the crystal size was reduced. A comparative analysis of the widths of the lifetime distributions and those of the MAPbI$_3$ quantum dot size distributions, obtained from Figure 6.5, showed the absence of correlation between them. This implies that the lifetime distribution cannot exclusively be the result of the dispersion observed in quantum dot size, but also of the effect of other non-radiative processes. Measurements of the quantum yield (QY) return values of $QY \approx 1\%$, very similar to those previously reported for other confined $MAPbI_3$ nanocrystals.[23,24] Since $QY = \frac{\Gamma_R}{\Gamma} = \frac{\Gamma_R}{\Gamma_{NR}+\Gamma_R}$, where Γ_{NR} and Γ_R are the non-radiative and radiative decay rates respectively, our QY measurements showed that non-radiative processes were dominant over radiative ones, i.e., $\Gamma_{NR} >> \Gamma_R$. Simultaneously, an analysis of the dependence of the mean decay rate estimated from the PL decay curves with the average nanocrystal radius reveals that $\Gamma \sim R^{-2}$ (see Figure 6.9b). Hence, in our case, Γ_{NR} is inversely proportional to the area of the nanocrystal surface. This could be due to the fact that the smaller the crystal, the larger the surface lattice distortion and thus the higher the density of surface defects, which could give rise to a higher number of non-radiative decay paths. Nevertheless, the influence of the spatial confinement increasing the overlap between the electron and hole wavefunctions, and thus increasing the radiative recombination probability,[25] cannot be discarded.

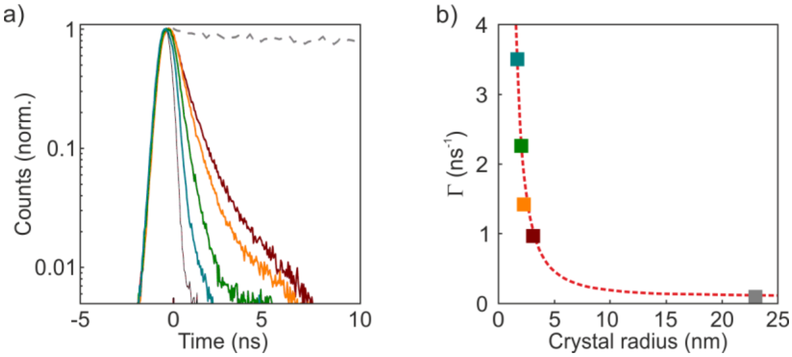

Figure 6.9. Dynamic photoluminescence from $MAPbI_3$ nanocrystals. a) Normalized PL decay curves for the $MAPbI_3$ formed within supramolecularly templated mesoporous TiO_2 scaffolds by using CTAB (blue-green), F127 (green), P123 (orange) and F127+PPG (dark red) as organic template. Grey dashed line belongs to a reference flat perovskite film. Black solid line indicates the instrument response function (IRF) produced by the excitation pulse. b) PL decay rate vs. the frequency at which the PL is maxima for the $MAPbI_3$ infiltrated in the different scaffolds (colour code is preserved from panel (a). The red dashed line is the best fitting curve following an inversely quadratic dependence with crystal radius.

6.4.2.1. Scaffold composition effect on the dynamics of $MAPbI_3$ nanocrystals

We completed our analysis by studying the effect of the matrix in which the nanocrystals were embedded on their decay dynamics. In Figure 6.10a, we show the PL spectra of $MAPbI_3$

crystallites grown in TiO_2 (orange line) and SiO_2 (purple line) scaffolds of similar average pore size and distribution, while Figure 6.10b displays the corresponding characterization of the decay dynamics. While the normalized photoemission intensity spectra were reasonably similar, as expected for collection of crystallites of similar size distribution, it can be seen that the decay rate was approximately 4 times faster in the TiO_2 scaffold than in the SiO_2 one. The expected ratio between the Γ_R attained for two similar emitters located in different media, $\frac{\Gamma_{R,i}}{\Gamma_{R,j}}$, is roughly proportional to the fifth power of the quotient of the refractive indexes, $\frac{n_i}{n_j}$, of such media.[26,27] In this case, refractive indexes should be estimated as the average between those of perovskite nanocrystals and the metal oxide scaffold in each case. By using Bruggeman effective medium approximation, and assuming a 50% fill factor, we obtained $\frac{\Gamma_{R,TiO2}}{\Gamma_{R,SiO2}} \sim \left(\frac{n_{TiO2}}{n_{SiO2}}\right)^5 = 3.5$. This ratio was similar to the $\frac{\Gamma_{TiO2}}{\Gamma_{SiO2}} \approx 4$ experimentally determined. Hence, the changes in the decay rate can be assigned to changes in the radiative term caused by the different matrices employed as host for the perovskite nanocrystals.

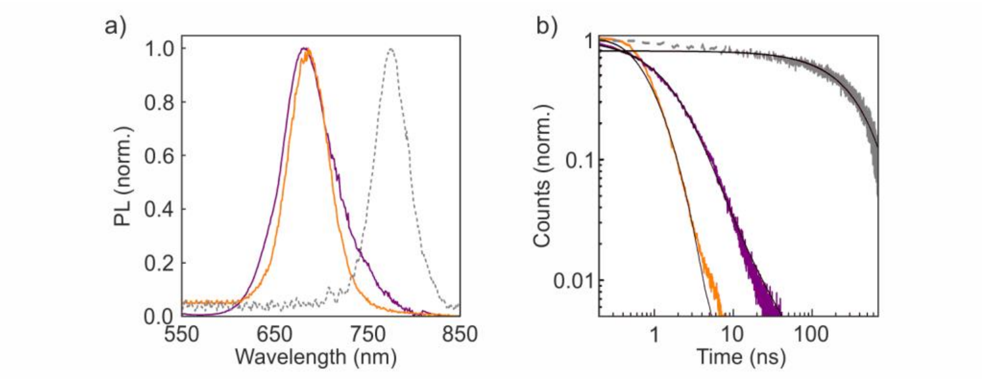

Figure 6.10. Scaffold effect on the dynamic photoluminescence from $MAPbI_3$ nanocrystals. a) Normalized PL spectra from $MAPbI_3$ nanocrystals of similar size grown using supramolecularly templated TiO_2 (orange) and SiO_2 (purple) porous films as scaffolds. Grey dashed line corresponds to the photoemission spectrum of a flat perovskite film. b) Corresponding normalized decay curves for the $MAPbI_3$ formed within both type of scaffolds (colour code is preserved from panel (a).

6.4.3. Macroscopic optical properties of $MAPbI_3$ nanocrystals films

From the point of view of the material performance, the nanocrystal loaded films presented an emission detectable with the naked eye in spite of being only 200 nm thick, as it can be seen in the picture displayed in Figure 6.11a. This photograph was taken under monochromatic light excitation of λ=312 nm from a porous TiO_2 film in which 2.26 nm size $MAPbI_3$ nanocrystals were synthesized. Bright edges resulted from the guiding of the emitted light by the glass substrate. In order to evaluate the homogeneity of the emission, the PL spectrum was measured from 250 μm^2 regions, mapping the whole film surface (2.25 cm^2). The maps obtained reveal the high regularity of the nanocrystal size distribution and density over the entire film, as it can be seen in Figure 6.11b-c. Luminescence peak maximum (λ_{max}) and *FWHM* remained practically constant within very narrow margins, λ_{max}=684±2 nm (i.e. 1.81 eV, standard deviation 0.3%) and *FWHM*=57±2 nm (i.e. 0.15 eV, standard deviation 3.5%).

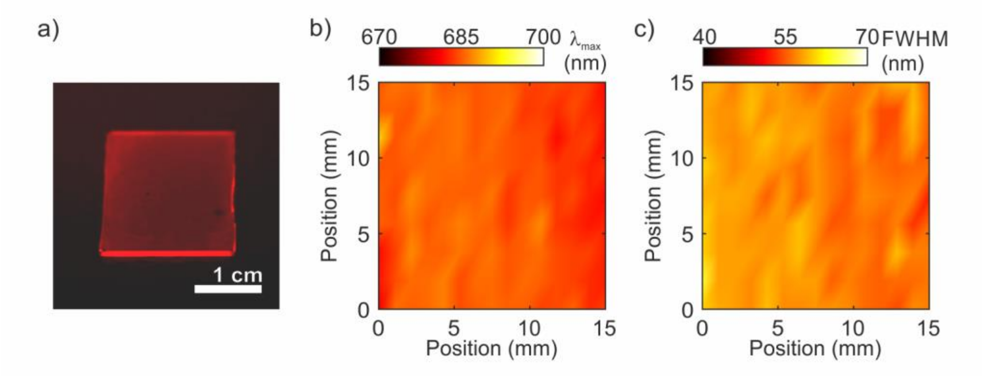

Figure 6.11. Macroscopic photoluminescence homogeneity of films based on $MAPbI_3$ nanocrystals. a) Digital camera picture of a periodically ordered porous film (P123) containing $MAPbI_3$ nanocrystals taken under illumination with UV light of λ=312 nm. b,c) Maps of the photoluminescence maximum (b) and *FWHM* (c) over the 2.25 cm^2 surface of a porous film containing $MAPbI_3$.

6.5. Conclusions

In this chapter, we have demonstrated a simple and reproducible method to obtain solid dispersions of $MAPbI_3$ nanocrystals with tetragonal crystal structure embedded in the periodic porous mesostructure of metal oxide thin films of high optical quality. By synthesizing the perovskite inside the interconnected array of nanocages of the host film, and by using matrices with pores of different average size, we have shown fine-tuning of the absorption onset in a wide spectral range. This has a direct impact on the static and dynamic photoemission properties of the crystallites. Such control over the optical properties arise from the strong quantum size effects characteristic of semiconductor nanocrystals of dimensions comparable to the exciton Bohr radius, as we show by fitting the experimental data to canonical expressions derived for that regime.

We have demonstrated a synthetic route to tune the bandgap, hence the colour, of $MAPbI_3$ perovskite without having to change the chemical formulation of the compound. In contrast to the standard approach that implies halide (Br+I or Cl+Br) mixing, our approach provides a material with a bandgap on demand in which halide segregation is cannot occur. In addition, the host film employed as nanoreactor acts as encapsulator for the $MAPbI_3$ nanocrystals, preventing their degradation under operational atmosphere. These features enhance the stability of the optical properties of the ensembles over time. These results clear the way to the demonstration of a reliable perovskite material with a blue-shifted bandgap optimum for its application as top subcell in tandem solar cells. In another note, we believe that these results open interesting possibilities for the application of $MAPbI_3$ perovskite nanocrystals in lighting devices as they represent a stable visible emitter at the desired frequency range. Furthermore, the technique gives rise to materials with a fast photoactivation and can be easily extended to other hybrid perovskites. In consequence, they represent a great opportunity to attain efficient perovskite based LEDs working at wavelengths a la carte.

6.6. References

1 Slotcavage, D. J.; Karunadasa, H. I.; McGehee, M. D. Light-induced phase segregation in halide-perovskite absorbers. *ACS Energy Lett.* **2016**, 1, 1199.

2 Brivio, F.; Caetano, C.; Walsh, A. Thermodynamic origin of photoinstability in the $CH_3NH_3Pb(I_{1-x}Br_x)_3$ hybrid halide perovskite alloy. *J. Phys. Chem. Lett.* **2016**, 7, 1083.

3 Barker, A.J.; Sadhanala, A.; Deschler, F.; Gandini, M.; Senanayak, S. P.; Pearce, P. M.; Mosconi, E.; Pearson, A. J.; Wu, Y.; Kandada, A. R. S.; Leijtens, T.; De Angelis, F.; Dutton, S. E.; Petrozza, A.; Friend, R. H. Defect-assisted photoinduced halide segregation in mixed-halide perovskite thin films. *ACS Energy Lett.* **2017**, 2, 1416.

4 Yoffe, A. D. Low-dimensional systems: quantum size effects and electronic properties of semiconductor microcrystallites (zero-dimensional systems) and some quasi-two-dimensional systems. *Adv. Phys.* **1993**, *42*, 173.

5 Brus, L. E. Electron–electron and electron-hole interactions in small semiconductor crystallites: The size dependence of the lowest excited electronic state. *J. Chem. Phys.* **1984**, *80*, 4403.

6 Éfros, Al. L.; Éfros, A. L. Interband absorption of light in a semiconductor sphere. *Sov. Phys. Semicond.* **1982**, *16*, 1209.

7 Buin, A.; Comin, R.; Ip, A.; Sargent, E. H. Perovskite quantum dots modeled using ab initio and replica exchange molecular dynamics. *J. Phys. Chem. C* **2015**, *119*, 13965-13971.

8 Hassan, Y.; Song, Y.; Pensack, R. D.; Abdelrahman, A. I.; Kobayashi, Y.; Winnik, M. A.; Scholes, G. D. Structure-tuned lead halide perovskite nanocrystals. *Adv. Mater.* **2016**, *28*, 566.

9 Soler-Illia, G. J. D.; Sanchez, C.; Lebeau, B.; Patarin, J. Chemical strategies to design textured materials: from microporous and mesoporous oxides to nanonetworks and hierarchical structures. *Chem. Rev.* **2012**, *102*, 4093-4138.

10 Hirasawa, M.; Ishihara, T.; Goto, T.; Uchida, K.; Miura, N. Magnetoabsorption of the lowest exciton in perovskite-type compound $(CH_3NH_3)PbI_3$. *Physica B* **1994**, *201*, 427-430.

11 D'Innocenzo, V.; Grancini, G.; Alcocer, M. J. P.; Kandada, A. R. S.; Stranks, S. D.; Lee, M. M.; Lanzani, G.; Snaith, H. J.; Petrozza, A. Excitons versus free charges in organo-lead tri-halide perovskites. *Nat. Commun.* **2014**, *5*, 3586.

12 Menéndez-Proupin, E.; Palacios, P.; Wahnón, P.; Conesa, J. C. Self-consistent relativistic band structure of the $CH_3NH_3PbI_3$ perovskite. *Phys. Rev. B* **2014**, *90*, 045207.

13 Ma, J.; Wang, L.-W. Nanoscale Charge Localization Induced by Random Orientations of Organic Molecules in Hybrid Perovskite $CH_3NH_3PbI_3$. *Nano Lett.* **2015**, *15*, 248-253.

14 Kayanuma, Y. Quantum-size effects of interacting electrons and holes in semiconductor microcrystals with spherical shape. *Phys. Rev. B* **1988**, *38*, 9797.

15 Umari, P.; Mosconi, E.; De Angelis, F. Relativistic GW calculations on $CH_3NH_3PbI_3$ and $CH_3NH_3SnI_3$ perovskites for solar cell applications. *Sci. Rep.* **2014**, *4*, 4467.

16 Even, J.; Pedesseau, L.; Katan, C. Analysis of multivalley and multibandgap absorption and enhancement of free carriers related to exciton screening in hybrid perovskites. *J. Phys. Chem. C* **2014**, *118*, 11566-11572.

17 Giorgi, G.; Yamashita, K. Zero-dimensional hybrid organic–inorganic halide perovskite modeling: insights from first principles. *J. Phys. Chem. Lett.* **2016**, *7*, 888.

18 Galisteo-López, F. J.; Anaya, M.; Calvo, M. E.; Miguez, H. Environmental effects on the photophysics of organic-inorganic halide perovskites. *J. Phys. Chem. Lett.* **2015**, *6*, 2200-2205.

19 Tian, Y.; Peter, M.; Unger, E.; Abdellah, M.; Zheng, K.; Pullerits, T.; Yartsev, A.; Sundström, V.; Scheblykin, I. G. Mechanistic insights into perovskite photoluminescence enhancement: light curing with oxygen can boost yield thousandfold. *Phys. Chem. Chem. Phys.* **2015**, *17*, 24978-24987.

20 DeQuilettes, D. W.; Zhang, W.; Burlakov, V. M.; Graham, D. J.; Leijtens, T.; Osherov, A.; Bulovic, V.; Snaith, H. J.; Ginger, D. S.; Stranks, S. D. Photo-induced halide redistribution in organic-inorganic perovskite films. *Nat. Commun.* **2016**, *7*, 11683.

21 Stranks, S. D.; Burlakov, V. M.; Leijtens, T.; Ball, J. M.; Goriely, A.; Snaith, H. J. Recombination kinetics in organic-inorganic perovskites: excitons, free charge, and subgap states. *Phys. Rev. Appl.* **2014**, *2*, 034007.

22 Takagahara, T. Excitonic optical nonlinearity and exciton dynamics in semiconductor quantum dots. *Phys. Rev. B* **1987**, *36*, 9293.

23 Cadelano, M.; Sarritzu, V.; Sestu, N.; Marongiu, D.; Chen, F.; Piras, R.; Corpino, R.; Carbonaro, C. M.; Quochi, F.; Saba, M.; Mura, A.; Bongiovanni, G. Can trihalide lead perovskites support continuous wave lasing? *Adv. Optical Mater.* **2015**, *3*, 1557-1564.

24 Malgras, V.; Tominaka, S.; Ryan, J. W.; Henzie, J.; Takei, T.; Ohara, K.; Yamauchi, Y. Observation of quantum confinement in monodisperse methylammonium lead halide perovskite nanocrystals embedded in mesoporous silica. *J. Amer. Chem. Soc.* **2016**, *138*, 1384-13881.

25 Ravi, V. K.; Swarnkar, A.; Chakraborty, R.; Nag, A. Excellent green but less impressive blue luminescence from $CsPbBr_3$ perovskite nanocubes and nanoplatelets. *Nanotechnology* **2016**, *27*, 325708.

26 Yablonovitch, E.; Gmitter, T.J.; Bhat, R. Inhibited and enhanced spontaneous emission from optically thin AlGaAs/GaAs double heterostructures. *Phys. Rev. Lett.* **1988**, *61***,** 2546.

27 B. Henderson, G.F. Imbusch, *Optical Spectroscopy of Inorganic Solids*, Oxford University Press, New York, United States **1989**, p. 146.

Appendix A

Light propagation in a stratified medium

The use of simulation tools represents a central point in this dissertation in order to describe the optical behaviour of the materials and solar cells presented. In general, all the systems that we have studied are considered multilayer structures. The determination of the spatial and spectral distribution of the electromagnetic field within them is essential for the calculation of the fraction of light that is reflected, transmitted or absorbed by the systems. The transfer matrix model is widely employed to this end. Its success lies on the analytical expressions that exactly define light propagation through the multilayer system, something that otherwise would be very complex. In this notes, we will give a brief introduction to the theoretical framework that underlies the computational codes in this thesis.

A.1. Fresnel equations

The transmission and reflection of light between two media is described by the Fresnel equations (see Figure 1.5).[1] For purely dielectric incoming and outgoing media being (k=0), Fresnel equations are defined according to

$$R(\lambda) = |r(\lambda)|^2, \qquad (A.1)$$

and

$$T(\lambda) = \frac{n_{out}(\lambda) \cdot \cos(\alpha_{out})}{n_{in}(\lambda) \cdot \cos(\alpha_{in})} |t(\lambda)|^2, \qquad (A.2)$$

where $n_{in}(\lambda)$ and $n_{out}(\lambda)$ are the refractive indices of the incoming and outgoing media, respectively. For example, when we are dealing with perovskite monolayers ($n_{medium}(\lambda) =$

$n_{perovs}(\lambda)$), as in Section 2.5, they are considered to be air ($n_{in} = n_{air} = 1.00$) and glass ($n_{out} = n_{glass} = 1.51$). α_{in} and α_{out} are the incident and outgoing light angles, being 6°, 30° and 50° in our case.

The amplitudes $r(\lambda)$ and $t(\lambda)$ are obtained using the following expressions

$$r(\lambda) = \frac{r_{air,perovs}(\lambda) + r_{perovs,glass}(\lambda)e^{-i2\phi(\lambda)}}{1 + r_{air,perovs}(\lambda) \cdot r_{perovs,glass}(\lambda)e^{-i2\phi(\lambda)}},$$

$$t(\lambda) = \frac{t_{air,perovs}(\lambda) \cdot t_{perovs,glass}(\lambda)e^{-i\phi(\lambda)}}{1 + r_{air,perovs}(\lambda) \cdot r_{perovs,glass}(\lambda)e^{-i2\phi(\lambda)}},$$

being

$$\phi(\lambda) = \frac{2\pi n_{perovs}(\lambda)}{\lambda} \cdot \cos(\alpha_{air}) \cdot d,$$

$$r_{12}(\lambda) = \frac{n_{air}(\lambda) - n_{perovs}(\lambda)}{n_{air}(\lambda) + n_{perovs}(\lambda)},$$

$$r_{23}(\lambda) = \frac{n_{perovs}(\lambda) - n_{glass}(\lambda)}{n_{perovs}(\lambda) + n_{glass}(\lambda)},$$

$$t_{12}(\lambda) = \frac{2n_{air}(\lambda)}{n_{air}(\lambda) + n_{perovs}(\lambda)},$$

$$t_{23}(\lambda) = \frac{2n_{perovs}(\lambda)}{n_{perovs}(\lambda) + n_{glass}(\lambda)},$$

λ is the wavelength of the incoming radiation and d is the thickness of the perovskite layer, which can be estimated from the analysis of SEM images.

In principle, Fresnel equations could be used to describe the optical behaviour of any stratified system. However, the complexity of the expressions increases with the number of layers in the structure, making this mathematical tool a very time-consuming in terms of computational calculations

A.2. Transfer matrix model

In a multilayered system, partial reflections and transmissions occur at each interface, which depend on the thickness and refractive index of the different layers, and give rise to constructive or destructive interference. In this way, total transmittance and total reflectance of the complete stratified medium is the sum of an infinite number of reflections and transmissions of light. The TMM describes the propagation of electromagnetic waves across a stratified medium based on the Maxwell equations, which establish continuity conditions for the electric field across the interface between two media. Hence, one can describe the optical behaviour of a multilayer as the product of a series of matrices that define each layer and each interface in the system. Last step in this model is the conversion of the final matrix to reflection and transmission coefficients.

Let consider a four-layer system, which is stratified in the *z* direction and is homogeneous in the *x* direction. For example a glass substrate, an ESL, a perovskite layer and a HSL, as shown in Figure A.1.

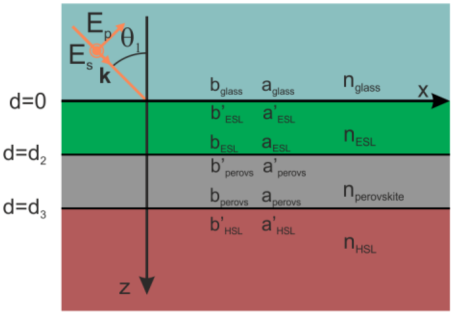

Figure A.1. Scheme of a four-medium multilayer system.

The electric field of an electromagnetic wave propagating in the *xz* plane with an angular frequency ω is given by

$$\boldsymbol{E} = \boldsymbol{E}(z)e^{i(\omega t - k_z z)}, \qquad (A.4)$$

where k_z is the *z* component of the wave vector. We assume a linear polarization of light, either *s* polarization (E_x=E_z=0), or *p* polarization (E_y=0). Assuming that light comes from the glass substrate with an angle θ with respect to *x*-axis, the electric field in the glass, ESL, and perovskite consists of a right- and left-traveling wave expressed as

$$E(z) = ae^{-i(k_z z)} + be^{i(k_z z)} = a(z) + b(z), \qquad (A.5)$$

where $\pm k_z$ are the *z*-components of the wave vector

$$k_z = n_j \frac{2\pi}{\lambda} \cos\theta_j, \qquad (A.6)$$

in a medium *j* with a complex refractive index defined as $n_j = Re(n_j) + i \cdot Im(n_j)$ and incident angle θ_j. The amplitudes *a* and *b* are constant inside each homogeneous layer.

Hence, $a(z)$ and $b(z)$ represent the amplitude of the wave traveling to the right and to the left, respectively. This amplitudes are defined at each interface in the system as

$$a_{glass} = a(0^-),$$

$$b_{glass} = b(0^-),$$

$$a'_{ESL} = a(0^+),$$

$$b'_{ESL} = b(0^+),$$

$$a_{ESL} = a(d^-_{ESL}),$$

$$b_{ESL} = b(d^-_{ESL}),$$

$$a'_{perovs} = a(d^+_{ESL}),$$

$$b'_{perovs} = b(d^+_{ESL}),$$

$$a_{perovs} = a\left(d^-_{perovs}\right),$$

$$b_{perovs} = b\left(d^-_{perovs}\right),$$

$$a'_{HSL} = a\left(d^+_{perovs}\right),$$

$$b'_{HSL} = b\left(d^+_{perovs}\right) = 0,$$

where 0^- (d^-) and 0^+ (d^+) represent the left and right side of the interface at z=0 (z=d). One can relate the vectors at each side of the interface by representing the mentioned amplitudes as column vectors

$$\begin{pmatrix} a_{glass} \\ b_{glass} \end{pmatrix} = \boldsymbol{D}_{glass,ESL} \begin{pmatrix} a'_{ESL} \\ b'_{ESL} \end{pmatrix}, \tag{A.7a}$$

$$\begin{pmatrix} a'_{ESL} \\ b'_{ESL} \end{pmatrix} = \boldsymbol{P}_{ESL} \begin{pmatrix} a_{ESL} \\ a_{ESL} \end{pmatrix}, \tag{A.7b}$$

$$\begin{pmatrix} a_{ESL} \\ a_{ESL} \end{pmatrix} = \boldsymbol{D}_{ESL,perovs} \begin{pmatrix} a'_{perovs} \\ b'_{perovs} \end{pmatrix}, \tag{A.7c}$$

$$\begin{pmatrix} a'_{perovs} \\ b'_{perovs} \end{pmatrix} = \boldsymbol{P}_{perovs} \begin{pmatrix} a_{perovs} \\ b_{perovs} \end{pmatrix}, \tag{A.7d}$$

$$\begin{pmatrix} a_{perovs} \\ b_{perovs} \end{pmatrix} = \boldsymbol{D}_{perovs,HSL} \begin{pmatrix} a'_{HSL} \\ b'_{HSL} \end{pmatrix}, \tag{A.7e}$$

where $\boldsymbol{D}_{glass,ESL}$, $\boldsymbol{D}_{ESL,perovs}$ and $\boldsymbol{D}_{perovs,HSL}$ are the transmission matrices, and $\boldsymbol{P}_{ESL}$ and $\boldsymbol{P}_{perovs}$ are the propagation matrices. One can then generalize the expressions for a j layer as

$$\boldsymbol{D}_{j,j+1} = \frac{1}{t_{j,j+1}}\begin{pmatrix} 1 & r_{j,j+1} \\ r_{j,j+1} & 1 \end{pmatrix}, \qquad (A.8)$$

and

$$\boldsymbol{P}_j = \begin{pmatrix} e^{i\phi_j} & 0 \\ 0 & e^{-i\phi_j} \end{pmatrix}, \qquad (A.9)$$

where $t_{j,j+1}$ and $r_{j,j+1}$ are the Fresnel coefficients for the interface between the layers j and j+1. $\phi_j = \frac{2\pi}{\lambda} n_j \cos(\theta_j d_j)$ is the phase change of light traveling with an angle θ_j through layer j with n_j and d_j being its refractive index and thickness, respectively. λ is the wavelength in the vacuum. From equations 7.7 one can find the relation between a_{glass}, b_{glass}, a_{HSL} and b_{HSL} by operating with the transmission and propagation matrices

$$\begin{pmatrix} a_{glass} \\ b_{glass} \end{pmatrix} = \boldsymbol{D}_{glass,ESL} \cdot \boldsymbol{P}_{ESL} \cdot \boldsymbol{D}_{ESL,perovs} \cdot \boldsymbol{P}_{perovs} \cdot \boldsymbol{D}_{perovs,HSL} \begin{pmatrix} a'_{HSL} \\ b'_{HSL} \end{pmatrix}$$
$$= \begin{pmatrix} \mathrm{M}_{11} & \mathrm{M}_{12} \\ \mathrm{M}_{21} & \mathrm{M}_{22} \end{pmatrix} \begin{pmatrix} a'_{HSL} \\ b'_{HSL} \end{pmatrix}, (7.10)$$

Reflection and transmission of a plane wave coming from the air through the complete system are defined, respectively, as

$$r = (\frac{b_{glass}}{a_{glass}})_{b'_{HSL}=0}, \qquad (A.11)$$

and

$$t = (\frac{a'_{HSL}}{a_{glass}})_{b'_{HSL}=0}, \qquad (A.12)$$

Now, we one uses equations 7.10, 7.11, and 7.12, the reflection and transmission coefficients for this multilayer are

$$r = \frac{M_{21}}{M_{11}}, \qquad (A.13)$$

and

$$t = \frac{1}{M_{11}}, \qquad (A.14)$$

Finally, if we consider air and HSL as pure dielectrics the reflectance (R) and the transmittance (T) of a plane wave propagating through the stratified structure can be written as

$$R = \left|\frac{M_{21}}{M_{11}}\right|^2, \qquad (A.15)$$

and

$$T = \frac{n_{HSL}\cos\theta_{HSL}}{n_{glass}\cos\theta_{glass}}\left|\frac{1}{M_{11}}\right|^2, \qquad (A.16)$$

This formalism can be expanded for systems comprised of m layers by operating with the propagation and transmission matrices corresponding to each layer and each interface. In this thesis, we have employed the TMM for all the calculations involving multilayers systems. In principle, one only needs the thickness of the different components and their refractive indices, which herein are wavelength dependent. However, in several calculations the optical constants of the absorber (the perovskite) was unknown, and we needed to calculate it.

Notice that the glass substrate can be considered in the model as a layer that does not give rise to interference effects since its thickness is larger than the coherence length of the incident light. As a result, the calculated spectra along the thesis (for example, see Figure 2.14) do not show the very short period fringes, which would arise from the presence of an ideal flat 1 mm-thick layer.

When dealing with porous media, we applied different effective medium approximations (volume-weighted average, Bruggeman and Maxwell-Garnett) in order to calculate the corresponding effective refractive indices. The very similar results attained from the different effective medium equations employed led us to consider the simplest approximation, i.e. the volume-weighted average.

1 Hecht, E. Optics. Addisib Wesley, **2002**.

Appendix B

Forouhi-Bloomer model

In order to extract the complex refractive index of the different ABX_3 perovskites, we have employed the Forouhi-Bloomer model.[1] This model considers a nanocrystalline semiconductor, which is ideal for the materials that we have studied. In particular, we have used the Jobin Yvon (new amorphous) parametrization[2]

$$n(E) = n_{\infty} \sum_{j=1}^{N} \frac{B_j\left(E - E_j\right) + C_j}{(E - E_j)^2 + \Gamma_j^2}, \qquad (B.1)$$

$$k(E) = \begin{cases} \displaystyle\sum_{j=1}^{N} \frac{f_j (E - E_g)^2}{(E - E_j)^2 + \Gamma_j^2}; \text{for } E > E_g \\ 0; \text{for } E < E_g \end{cases} \qquad (B.2)$$

with

$$B_j = \frac{f_j}{\Gamma_j}\left(\Gamma_j^2 - \left(E - E_j\right)^2\right) \text{ and } C_j = 2 f_j \Gamma_j \left(E - E_j\right)$$

Where E is the energy, E_g is the bandgap, and E_j, f_j, and Γ_j are the position, strength, and width of one oscillator. In our case, we have employed 3 oscillators (N=3). Please note that this formalism is fully consistent with Kramers-Kronig relations

$$n(\omega) = n_0 + \frac{2}{\pi} \mathrm{P} \int_0^{\infty} \frac{\Omega k(\Omega)}{\Omega^2 - \omega^2} d\Omega, \qquad (\mathrm{B}.3)$$

where $\omega = 2\pi c / \lambda$ is the angular frequency and c is the speed of light in vacuum.

1 Forouhi, A.; Bloomer, I. Optical dispersion relations for amorphous semiconductors and amorphous dielectrics. *Phys. Rev. B* **1986**, *34*, 7018−7026.

2 Jobin Yvon New Amorphous Dispersion Formula. http://www.horiba.com/fileadmin/uploads/Scientific/Downloads/OpticalSchool_CN/TN/ellipsometer/New_Amorphous_Dispersion_Formula.pdf.

Appendix C

Genetic algorithm

Genetic algorithms are one of the more versatile numerical methods to solve optimization problems. In this kind of algorithm, a population of individuals (candidate solutions) evolve through selection, mutation and crossover towards better solutions, inspired by the process of natural selection.[1,2] In each step of the process, the algorithm set the next generation of individuals by picking out the best individuals of the current population (elitism), selecting some individuals (selection), using the best individuals, i.e. parents, to generate an improved offspring (crossover), and mutating some individuals (mutation). After a number of iterations (generations), the population reaches an optimum solution that minimizes the value of the target function. In this regard, the termination conditions are modified depending on the considered problem and include the maximum number of generations, the maximum precision of the target function, or the number of generations in which the precision of the target function keeps constant.

In this thesis, we have combined a genetic algorithm included as a function in MatLab with the TMM for different purposes. For example, we employ it to calculate the imaginary refractive indices of the perovskite materials. To this end, we minimize the difference between the spectral dependences of the experimental reflectance and transmittance of perovskite films, and those extracted from a calculus that considers a generic imaginary refractive index of the material. In this case, the target function f is

$$f = \sum_{i=\lambda} \left(R_i^{exp} + T_i^{exp} - R_i^{theo} - T_i^{theo} \right)^2 \qquad (C.1)$$

The population is comprised by a group of vectors whose elements represent the different parameters included in the Forouhi-Bloomer model (E_g, E_j, f_j, and Γ_j) and the thickness of the perovskite film (d)

$$x_i = \left(E_g, E_1, E_2, E_3, f_1, f_2, f_3, \Gamma_1, \Gamma_2, \Gamma_3, d\right) \qquad (C.2)$$

We set a population of 256 individuals and, after several tens of iterations (generations), the algorithm arrives to the best solution x_{best}. We then consider this x_{best} as the entrance parameters in the Forouhi-Bloomer model in order to extract the actual n and k values of the refractive index of the material under study.

Similarly, we also use the method to minimize parasitic absorption, thus maximizing the absorption of light in the perovskite layers in order to optimize both single junction and double junction perovskite devices.

1 Goldberg, D. E. Genetic algorithims in search, optimization and machine learning. *Addison-Wesley* **1989**.

2 Holland, J. H. Adaptation in natural and artificial systems. *The MIT Press* **1992**.

Appendix D

SEM images of state-of-the-art PSCs

a) SEM images of cross-sectioned PSCs corresponding to Section 3.3. Scale bar is 200 nm. b) Top view of the bare perovskite films, scale bar 400 nm, for different perovskite film thicknesses.

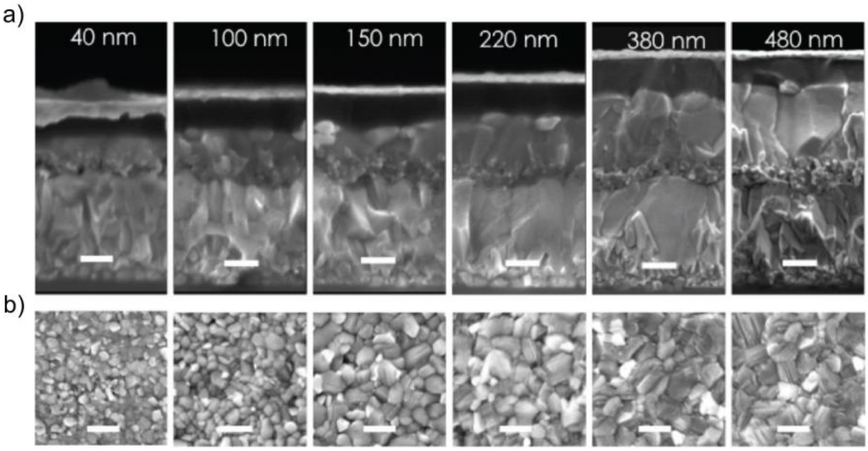

General conclusions

It has been analysed the optical behaviour of $MAPbI_3$ perovskite films. We have unveiled the nucleation and growth regimes taking place during the thermal annealing step of the films by combining X-ray diffraction and photoluminescence characterization. The environmental effects on the photophysics of $MAPbI_3$ have also been discussed. It has been found that a photoactivation followed by a subsequent photodarkening of the photoluminescence strongly correlate with the presence of oxygen in the atmosphere. Finally, we have presented a protocol to extract the optical constants of perovskite films.

The first model to optically describe perovskite solar cells has been developed. We have applied it to predict how the electric field is distributed across the devices and discern between efficient and parasitic absorption.

The combination of the optical model with the Shockley-Queisser theory has served to present the use of Pb/Sn-based perovskites in order to attain efficiencies reaching the theoretical ceilings associated to single-junction perovskite solar cells. Further, we have proposed a roadmap towards the optical optimization of a novel perovskite/perovskite tandem architecture that has the potential to surpass the state-of-the-art performances associated to this technology.

The first photonic structure compatible with $MAPbI_3$ perovskite synthesis has been presented. This new photonic crystal has an enhanced refractive index contrast between the constituent layers and has been integrated in perovskite solar cells in order to provide them with colour. The resulting colourful devices showed performances above 5% for the first time in the field.

A novel route to attain a solid dispersion of $MAPbI_3$ nanocrystals exhibiting quantum confinement effects has been developed. The strategy relies on porous matrices used as nanoreactors to deterministically form the perovskite nanocrystals. High optical quality over several squared centimetre areas is demonstrated.

Abbreviations

AM1.5	Air mass 1.5
AFM	Atomic force microscopy
BIPV	Building integrated photovoltaics
CBZ	Chlorobenzene
CIGS	Copper indium gallium selenide
CLT	Capping layer thickness
DMF	Dimethylformamide
DSSC	Dye sensitized solar cell
EDS	Energy-dispersive X-ray spectroscopy
EQE	External quantum efficiency
FF	Fill factor
FIB	Focussed ion beam
FTO	Fluorine doped tin oxide
FWHM	Full width at half maximum
IQE	Internal quantum efficiency
IS	Impedance spectroscopy
ITO	Indium doped tin oxide
$\mathbf{J_{sc}}$	Short circuit current
NIR	Near infrared
PC	Photonic crystal

PCE	Power conversion efficiency
PL	Photoluminescence
PMMA	(Poly)methyl methacrylate
PS	Polystyrene
PSC	Perovskite solar cell
PV	Photovoltaic
QY	Quantum yield
$\mathbf{R_d}$	Diffuse reflectance
$\mathbf{R_t}$	Total reflectance
RR	Radiative recombination
SEM	Scanning electron microscopy
SQ	Shockley Queisser
$\mathbf{T_d}$	Diffuse transmittance
$\mathbf{T_t}$	Total transmittance
TEM	Transmission electron microscopy
V	Voltage
$\mathbf{V_{oc}}$	Open circuit voltage
XRD	X-ray diffraction

List of publications

This thesis is based on the following publications. Asterisk indicates first co-author.

1. **Anaya, M.**; Calvo, M. E.; Luque-Raigon, J. M.; Míguez, H. Resonant photocurrent generation in dye-sensitized periodically nanostructured photoconductors by optical field confinement effects. *J. Am. Chem. Soc.*, **2013**, *135*, 7803-7806.
2. **Anaya, M.**; Lozano, G.; Calvo, M. E.; Zhang, W.; Johnston, M. B.; Snaith, H. J.; Míguez, H. Optical description of mesostructured organic-inorganic halide perovskite solar cells. *J. Phys. Chem. Lett.* **2015**, *6*, 48–53.
3. Zhang, W.*; **Anaya, M.***; Lozano, G.; Calvo, M. E.; Johnston, M. B.; Míguez, H.; Snaith, H. J. Highly efficient perovskite solar cells with tuneable structural color. *Nano Lett.* **2015**, *15*, 1698-1702. This work has been highlighted in the section "ScienceShots" of the journal *Science (AAAS)*.
4. Galisteo-López, F. J.; **Anaya, M.**; Calvo, M. E.; Míguez, H. Environmental effects on the photophysics of organic-inorganic halide perovskites, *J. Phys. Chem. Lett.* **2015**, *6*, 2200-2205.
5. **Anaya, M.**; Galisteo-López, F. J.; Calvo, M. E.; López, C.; Míguez, H. Photophysical analysis of the formation of organic-inorganic trihalide perovskite films: identification and characterization of crystal nucleation and growth. *J. Phys. Chem. C*, **2016**, *120*, 3071-3076.
6. **Anaya, M.**; Rubino, A.; Calvo, M. E.; Míguez, H. Solution processed high refractive index contrast distributed Bragg reflectors. *J. Mater. Chem. C*, **2016**, *4*, 4532-4537.

7. Correa-Baena, J.P.*; **Anaya, M.*;** Lozano, G.; Tress, W.; Domanski, K.; Saliba, M.; Matsui, T.; Jacobsson, T.J.; Calvo, M.E.; Abate, A.; Grätzel, M.; Míguez, H.; Hagfeldt, A. Unbroken perovskite: interplay of morphology, electro-optical properties and ionic movement. *Adv. Mater.*, **2016**, *28*, 5031-5037. Highlighted in a note in *ChemPhysChem*.

8. **Anaya, M.**; Correa-Baena, J.P.; Lozano, G.; Saliba, M.; Anguita, P.; Roose, B.; Abate, A.; Steiner, U.; Grätzel, M.; Calvo, M.E.; Hagfeldt, A.; Míguez, H. *Optical analysis of $CH_3NH_3Sn_xPb_{1-x}I_3$ absorbers: a roadmap for perovskite-on-perovskite tandem solar cells, J. Mater. Chem. A*, **2016**, *4*, 11214-11221. Highlighted as cover.

9. **Anaya, M.**; Zhang, W.; Clasen Hames, B.; Li, Y.; Fabregat-Santiago, F.; Calvo, M. E.; Snaith, H.; Míguez, H.; Mora Seró, I. *Electron injection and scaffold effect in perovskite solar cells, J. Mater. Chem. C,* **2017**, *5*, 634-644.

10. **Anaya, M.**; Rubino, A.; Rojas, T. C.; Galisteo-López, J. F.; Calvo, M. E.; Míguez, H. Strong quantum confinement and fast photoemission activation in $CH_3NH_3PbI_3$ perovskite nanocrystals grown within periodically mesostructured films, *Adv. Opt. Mater.*, **2017**, *5*, 1601087. Highlighted as cover.

11. **Anaya, M.**; Lozano, G.; Calvo, M. E.; Míguez, H. ABX_3 perovskites for tandem solar cells, *Joule* **2017**, *1*, 769-793.

Resumen en español

Introducción

En el acuerdo de París firmado en diciembre de 2015 en el marco de la Convención de las Naciones Unidas para el Cambio Climático las partes se conminaron a reducir las emisiones de CO_2 de manera que la subida de temperatura del globo se limitara a 2ºC por encima de los niveles preindustriales. [1] Para cumplir tal objetivo, la comunidad científica está enfocando sus esfuerzos en las energías renovables (ver Figura 1). [2] De entre ellas, la energía solar se está erigiendo con un papel protagonista debido a que el Sol es capaz de proveernos en una hora de toda la energía consumida por la humanidad a lo largo de un año.[3] La fotovoltaica (FV) es la principal responsable de esta revolución ya que en los últimos años se está logrando alcanzar unos costes de producción lo suficientemente bajos como para hacerla viable económicamente. En este contexto, en los últimos años las conocidas como celdas solares de perovskita (CSP) han irrumpido con una fuerza inusitada en el escenario.

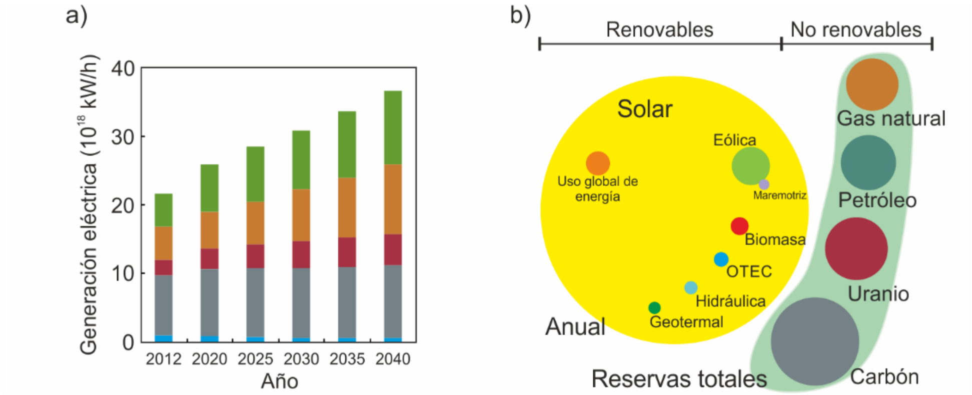

Figura 1 Recursos energéticos globales. a) Generación de electricidad a nivel mundial según el recurso energético: renovables (verde), gas natural (naranja), nuclear (rosa), carbón (gris), y líquidos (azul). b) Comparativa entre los recursos finitos y renovables disponibles en el planeta.

Celdas solares de perovskita

Las CSPs han logrado evolucionar rápidamente para pasar de tener un 3.81% de eficiencia en 2009 a superar con asiduidad el 20% hoy en día. De hecho, el Foro Económico Mundial las ha considerado como una de las 10 tecnologías emergentes más importantes.[4] Este tipo de dispositivos reciben su nombre por el material que les otorga su funcionalidad: las perovskitas ABX_3. Estas perovskitas cristalizan a partir de sales de haluros donde B es un metal hexacoordinado (típicamente Pb, aunque también Sn o Ge) que ocupa los centros de octaedros cuyos vértices están ocupados por un haluro X (Cl, Br, I, o mezclas). A es un catión (típicamente metilamonio, CH_3NH_3, MA; formamidinio, $HC(NH_2)_2$, FA; Cs; Rb; o mezclas) que rellena los huecos que deja cada grupo de ocho octaedros (ver Figura 2).

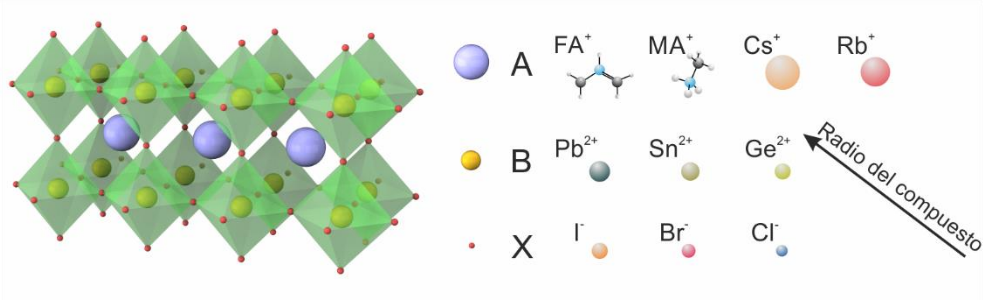

Figura 2. Estructura perovskita. Esquema de las perovskita ABX_3 y los elementos típicos que ocupan las diferentes posiciones en la estructura.

De entre todas las combinaciones, la más empleada es la que da lugar al $MAPbI_3$. Esta presenta una estructura tetragonal a temperatura ambiente.[5-7] Su borde de absorción de luz se da a l=780 nm (E=1.6 eV), absorbiendo fotones muy eficientemente.[8] Estos excitan pares de portadores de carga (electrones y huecos) que poseen unas distancias de difusión del orden de las micras.[9] Todas ellas suponen propiedades únicas para aplicar estos materiales en fotovoltaica. Por otro lado, la tasa de recombinación radiativa es muy alta, lo que las hace muy interesantes también para aplicaciones relacionadas con la emisión de luz.[10-13] En consecuencia, la caracterización y comprensión de las propiedades fotofísicas de estos materiales son esenciales para arrojar luz sobre los procesos de formación y sus mecanismos de funcionamiento.

Los precursores para sintetizar perovskitas ABX_3 son abundantes y económicos y se pueden procesar por diversos métodos.[14-17] De entre todos ellos destaca el procesado por *spin coating*.[18,19] En la Figura 3 muestro un esquema de una CSP típica. El dispositivo está formado por un sustrato trasparente conductor, usualmente óxido de estaño dopado con flúor (FTO) o indio (ITO). A continuación, tenemos una capa selectica de electrones (ESL), una capa de perovskita y una capa selectiva de huecos (HSL). Finalmente, encontramos una capa metálica como contacto trasero. Todas las siglas de los materiales han sido dadas por su denominación en inglés.

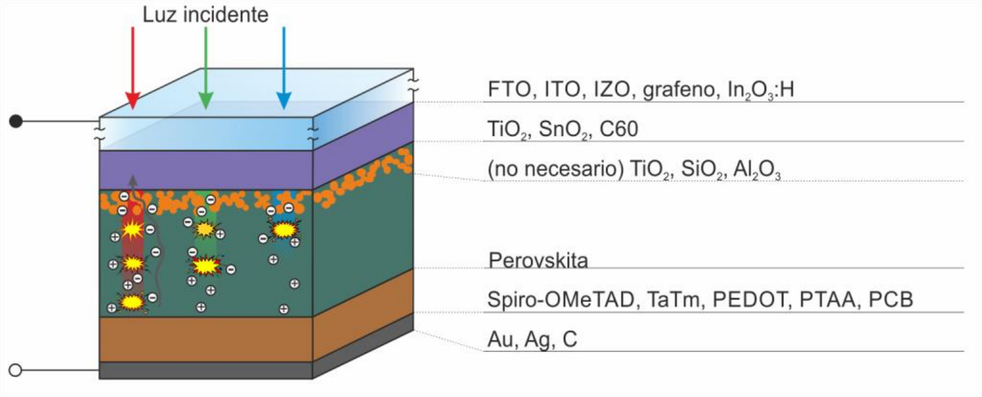

Figura 3. Celda solar de perovskita. Ilustración de la generación de carga en una celda solar de perovskita y un catálogo de los materiales más usuales para su construcción.

Diseño óptico en dispositivos fotovoltaicos

La eficiencia de dispositivos FV está íntimamente ligada a la manera en la que tiene lugar la absorción de fotones en el sistema. Por ello, una de las rutas más importantes para aumentar su desempeño reside en el diseño óptico de su arquitectura para tener un control preciso de la propagación de luz a través de ella. Su disposición en forma de multicapa, donde los grosores de cada componente es del orden de la longitud de onda del haz incidente, origina fenómenos fuertes de interferencia.

Para describir cómo es la interacción radiación materia en las CSP, es esencial conocer tanto la parte real, n, como la imaginaria, k, del índice de refracción de todos los materiales que la componen. En relación a esto, al comienzo del proyecto de tesis doctoral que da lugar a esta disertación, las constantes ópticas de las perovskitas ABX_3 no habían sido reportadas. Una vez conocidas, es posible optimizar el diseño del dispositivo mediante una elección correcta de materiales (índices de refracción) y de los grosores de las capas. Esto se puede llevar a cabo mediante el uso del método de la matriz de transferencia (TMM, por sus siglas en inglés), una herramienta que ya ha sido empleada con éxito en el pasado para diferentes tecnología FV.[20,21,22,23] Con este método es posible calcular la dependencia espectral de la transmisión y reflexión de luz en el sistema. Además, nos permite describir cómo se distribuye la intensidad de campo eléctrico a lo largo de la sección transversal del dispositivo. En la Figura 4 muestro un ejemplo aplicado a las celdas solares de colorante. Gracias a esto último, es posible calcular la fracción de luz absorbida en cada componente y, por tanto, discernir entre absorción efectiva y parasítica. Así, en principio, si la composición de los materiales que componen el dispositivo es fija, uno puede encontrar la combinación de grosores de las capas que resulta en una utilización de la luz óptima. Esto, sería el resultado de: i) fenómenos antirreflectantes que proporcionan mayor luz al interior de la celda, ii) una minimización de la absorción parasítica gracias a un mejor confinamiento de luz en la capa de perovskita, y iii) un aumento del camino óptico al utilizar las capas traseras a modo de espejos. Todos estos efectos son muy sensibles a cambios en el sistema multicapa debido a que el grosor total de las CSP es alrededor de una micra. Por ello, el desarrollo de un diseño óptico de la arquitectura de la CSP se erige como algo fundamental para su evolución.

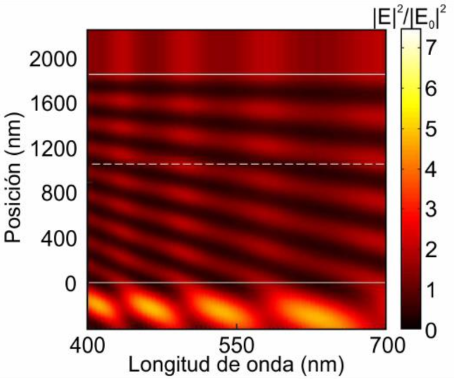

Figura 5. Distribución espacial y espectral de la intensidad de campo eléctrico a través de la sección transversal de una celda solar de colorante.

Integración en dispositivos fotovoltaicos de componentes ópticos nanoestructurados

Adicionalmente a los conceptos descritos en la sección anterior, uno puede modificar la respuesta de una celda solar mediante la introducción de elementos ópticos en el dispositivo. Con ello se pretende o bien mejorar su rendimiento, o bien otorgarle propiedades estéticas que las hagan atractivas para su integración en elementos cotidianos como edificios. A continuación, describo distintas estrategias utilizadas en FV basadas en este concepto.

La integración de partículas dieléctricas da lugar a dispersión difusa de luz y, así, a un aumento de la luz absorbida en la capa activa del dispositivo.[24,25] Por otro lado, se han propuesto partículas plasmónicas para generar interacciones radiación-materia fuertes en volúmenes nanométricos.[26,27] Ambas aproximaciones ya han sido empleadas en CSPs,[28-30] aunque el campo está muy poco explorado y se precisan de herramientas teóricas para una completa comprensión de los efectos observados. Alternativamente a la inclusión de partículas desordenadas, se ha estudiado el efecto de introducir patrones de difracción en los sistemas fotovoltaicos que aumentan el camino óptico en su interior. [31-33]

En el marco de esta tesis, la utilización de estructuras fotónicas multicapa tiene una relevancia especial. Estas se caracterizan por modular el índice de refracción de una forma periódica en una dimensión del espacio. Como consecuencia de esto se origina lo que se conoce como pico de Bragg que no es más que una reflexión de luz cuyos máximo espectral e intensidad pueden ser controlados de manera precisa. El dióxido de silicio y el dióxido de titanio son materiales típicos que se utilizan para que el efecto descrito tenga lugar en el visible. En el grupo de Materiales Ópticos Multifuncionales se desarrolló una versión porosa del cristal fotónico mediante la utilización de nanopartículas. Ello permitió integrarlos en dispositivos solares para (ver Figura 6): i) utilizarlos como espejos traseros y, así, dar una segunda oportunidad de absorber fotones a ciertas longitudes de onda,[34] ii) proveer de color a los dispositivos,[35] y dar lugar a un aumento en la fotocorriente por fenómenos de resonancia.[36] En todos los casos, el control de la porosidad del material resultó crucial para su correcta implementación. Aunque las CSPs son capaces de absorber la luz de una forma muy eficiente, el uso de cristales fotónicos constituye una vía muy prometedora para proveerlas de color a la carta sin necesidad de modificar la composición de la perovskita.

Por último, existe otra estrategia que consiste en reducir el tamaño de un semiconductor, como es el caso de las perovskitas ABX_3, hasta dimensiones en el régimen cuántico. A esta escala, los portadores de carga se confinan y los niveles energéticos se discretizan. Así, cuanto menor es el nanocristal, mayor es el corrimiento hacia el azul de su borde de absorción. Para su consecución, la manera tradicional se basa en síntesis coloidal en medio líquido, pero la posterior deposición de los nanocristales en forma de lámina delgada se hace muy complicada. Esto pone en discusión su empleo para la fabricación de dispositivos optoelectrónicos. Por el contrario, si se emplean materiales porosos como nanoreactores para la obtención de semiconductores confinados, tal problema desaparece. Es por ello, que la utilización de capas cuyo poro es controlado en la escala nanométrica para sintetizar nanocristales de perovskita constituye un método muy prometedor para controlar su borde de absorción.

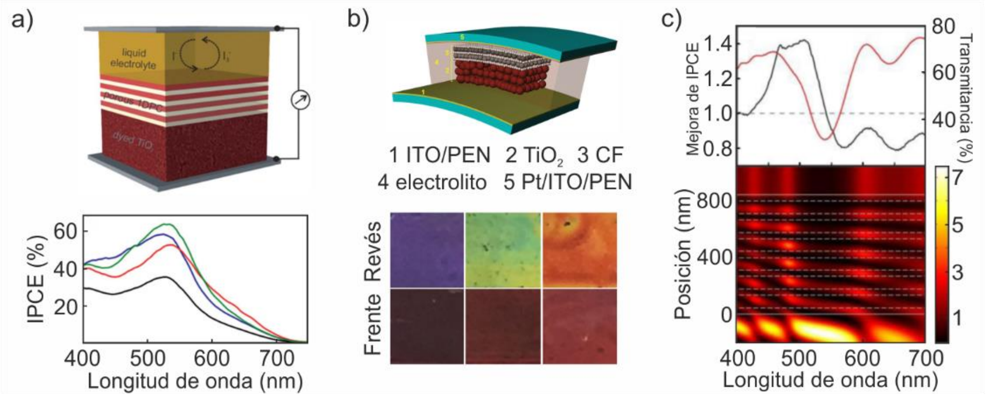

Figura 6. Celdas solares de colorante integrando cristales fotónicos unidimensionales. Diseño de una celda solar de colorante donde un cristal fotónico se incluye como espejo trasero para aumentar su eficiencia (a) y para darle color (b). c) Variación espectral del aumento de fotocorriente (línea negra) para una multicapa conductor sensibilizada por colorante. El espectro de transmitancia también se muestra en rojo. En el panel inferior se muestra la distribución de intensidad de campo en el sistema, Reproducido con autorización de las referencias 34, 35 y 36.

Motivación y objetivos

Como se ha venido introduciendo en el texto, para lograr mejores prestaciones en celdas solares es necesario realizar diseños basados en el conocimiento de las propiedades ópticas de los materiales que las componen. En este sentido, cuando este proyecto de tesis comenzó, había una evidente laguna en torno a la óptica de a las perovskitas ABX_3 y los dispositivos solares basados en ellas. Así, el objetivo general de esta disertación es proveer a la comunidad científica con las herramientas necesarias para entender el comportamiento óptico de las perovskitas ABX_3 para proponer dispositivos con diseños optimizados.

Descripción óptica de láminas de perovskita

El primer paso para estudiar la óptica de las perovskitas ABX_3 es comprender cuáles son los mecanismos que llevan a su formación y cómo estas se comportan después de ser sintetizadas. Para ello lo primero que se hizo fue depositar por *spin coater* los precursores de la perovskita $MAPbI_3$ en forma de lámina delgada siguiendo un procedimiento estándar.[27] Una vez calentado a 100ºC durante una hora, se obtuvo el material deseado tal y como se confirmó por Difracción de Rayos X (DRX), Microcopía Electrónica de Barrido (MEB) y Microscopía de Fuerzas Atómicas (MFA) (ver Figura 7).

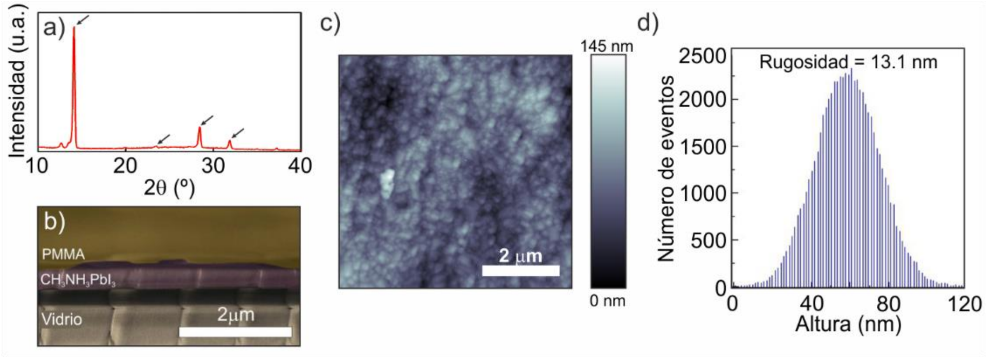

Figura 7. Caracterización estructural de láminas de $MAPbI_3$. a) Patrón de DRX de una lámina de $MAPbI_3$ depositada sobre vidrio. Las flechas marcan las posiciones de los picos de difracción esperados para el material.[37] b) Imagen MEB de una sección transversal de la muestra. c) Imagen MFA de la superficie de la muestra. d) Análisis estadístico de la rugosidad que indica una rugosidad media de alrededor de 13 nm

Como se aprecia en la Figura 7, se obtuvieron muestras uniformes y homogéneas, lo que fue confirmado por mediante espectroscopía ultravioleta-visible. En la Figura 8a se muestra el espectro de absorción, excitación y luminiscencia del material. Asimismo, En la Figura 8b se verifica la calidad óptica de las láminas, ya que la luz que se refleja difusamente es muy baja.

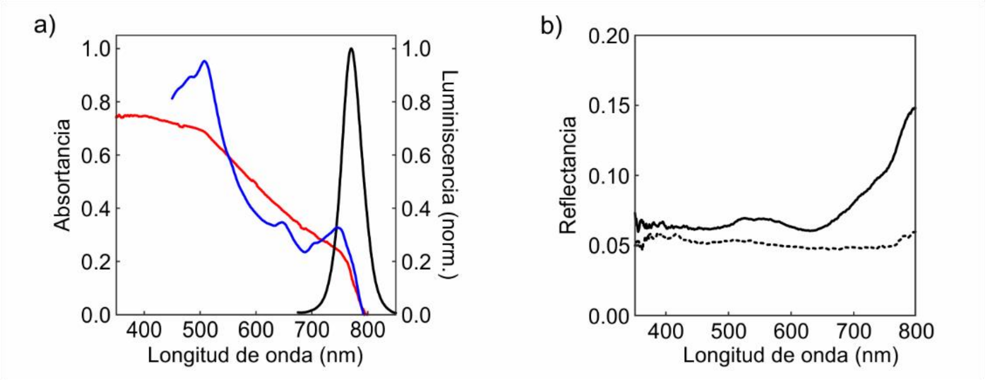

Figura 8. Caracterización óptica de una lámina de $MAPbI_3$. a) Espectros de fotoluminiscencia y excitación (curvas negras y azul, respectivamente) y de absortancia (curva roja) correspondientes a una lámina de 200 nm de $MAPbI_3$. b) Dependencia espectral de la reflectancia total (curva sólida) y difusa (curva punteada) de la lámina.

Fotofísica de la formación de láminas de $MAPbI_3$

Con el objetivo de entender mejor los procesos de formación de las perovskitas ABX_3 se hizo uso de sus propiedades ópticas. De esta manera se midió la fotoluminiscencia tanto estática como dinámica del material $MAPbI_3$ durante la etapa de calentamiento del material que tiene lugar a 100ºC durante una hora (Figura 9a). Además, se tomaron difractogramas de DRX para disponer de otra fuente de información y así poder diferenciar unívocamente cuándo tienen lugar los regímenes de nucleación y crecimiento de la perovskita (Figura 9b).

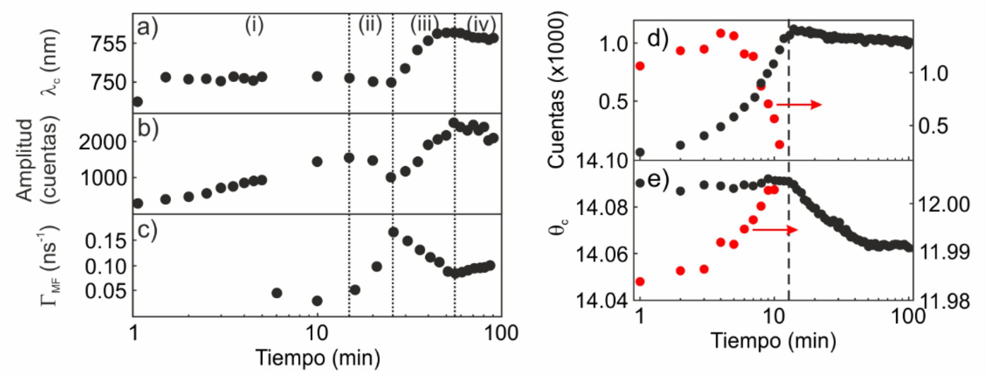

Figura 9. Caracterización de una lámina de perovskita $MAPbI_3$ durante su calcinado. Evolución temporal de la posición (a) y amplitud (b) del máximo de fotoluminiscencia, así como de la tasa de decaimiento (c) de una lámina de $MAPbI_3$. Evolución de la intensidad (d) y posición (e) del máximo de DRX correspondiente a $MAPbI_3$ (puntos negros) y los precursores (puntos rojos)

Como se puede observar, se diferenciaron 4 etapas diferentes durante el proceso de calentamiento de la capa de perovskita. En la primera se forman los cristales de perovskita (nucleación), algo que se evidencia por el aumento del pico de DRX asociado al $MAPbI_3$ y la intensidad en la emisión. En la segunda etapa los precursores comienzan a desaparecer y se observa una caída abrupta en la emisión acompañada de un incremento en la tasa de decaimiento, algo que se asocia a la aparición de bordes de grano que dan lugar a centros de recombinación. En la tercera etapa los granos de perovskita aumentan de tamaño tal y como se confirma por el desplazamiento hacia el rojo del máximo de emisión y hacia ángulos menores en el pico de DRX. Esto origina mayor emisión y una bajada en la tasa de decaimiento ya que la relación entre bordes de grano y material decrece. La cuarta etapa se corresponde con la finalización de la formación del material perovskita. En la Figura 10 se puede observar un esquema con el mecanismo propuesto para la formación de la perovskita.

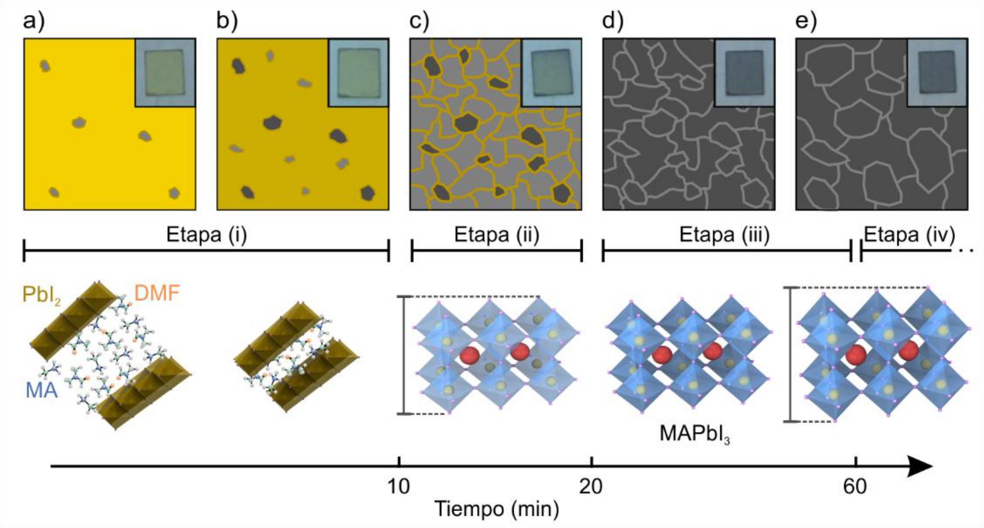

Figura 10. Esquema de la formación de la lámina de perovskita $MAPbI_3$.

Efectos de la atmósfera en la fotofísica de láminas de $MAPbI_3$

Una vez entendidos los procesos de formación de la perovskita $MAPbI_3$ a través del estudio de sus propiedades fotofísicas, nos dispusimos a monitorizar cómo variaba su emisión a lo largo del tiempo. Lo primero que se observó es que, si uno monitorizaba la intensidad del máximo de emisión, esta variaba con el paso del tiempo. De hecho, se pudieron diferenciar dos regímenes: uno que ocurría en pocos minutos y suponía la activación de la emisión y otro que tenía lugar en las decenas de minutos que suponía la desactivación de la misma.

Para poder diferenciar cuál era el origen de dichos procesos de activación y desactivación de la emisión, se colocó una muestra de $MAPbI_3$ en diferentes atmósferas. En concreto se utilizaron atmósferas de N_2 y O_2. En la Figura 11 se puede ver qué efecto tuvieron en la emisión del material. Así, se pudo comprobar que en presencia de O_2 la intensidad de emisión proveniente de la lámina de perovskita se incrementaba un orden de magnitud con respecto al caso en el que la atmósfera era de N_2. El mecanismo propuesto se asienta en la formación de especies oxidadas en la superficie de los granos de perovskita cuando esta se expone a O_2. Este hecho da lugar a un gradiente de distribución de carga que actúa como fuerza para promover la migración de iones haluro hacia el interior del material. Esto se puede ver como una forma de reparación de los defectos en la perovskita que resulta en una mejora en la emisión del mismo.

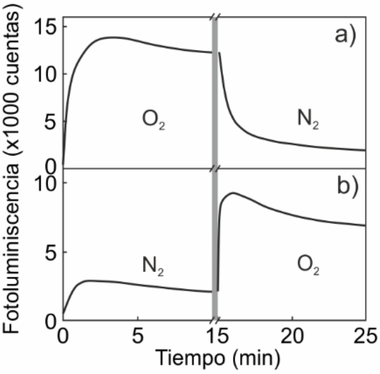

Figura 11. Transiente de fotoluminiscencia en presencia de N_2 y O_2. a) Expuesto a un flujo de O_2 seguido de un flujo de N_2. b) Expuesto a un flujo de N_2 seguido de un flujo de O_2. Las muestras reposaron en oscuridad durante 5 minutos (señalado con francas grises).

Constantes ópticas de láminas de perovskita

Una vez entendidos los procesos de formación y el comportamiento del material a lo largo del tiempo, se modelizaron sus constantes ópticas para, posteriormente, diseñar ópticamente CSPs. Para ello, se diseñó un protocolo en el que se caracterizaba la transmitancia y reflectancia angular de una lámina de $MAPbI_3$. Los espectros resultantes fueron utilizados a modo de parámetros a ajustar en un programa basado en el TMM combinado con un algoritmo genético.[38,39] En él, a través del modelo de Forouhi-Bloomer,[40,41] se encontraron los valores de *n* y *k* asociados a la lámina de $MAPbI_3$ que mejor ajustaban su comportamiento óptico (ver Figura 12). Como se puede observar, las propiedades del material presentan diferencias que dependen del método de preparación empleado.

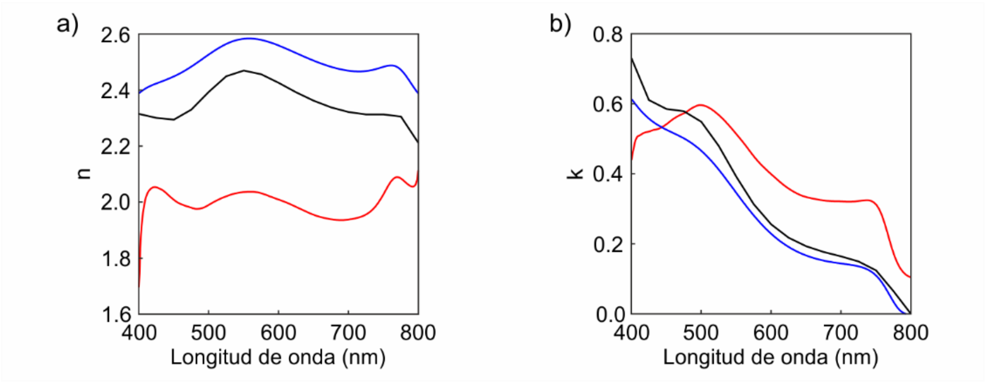

Figura 12. Constantes ópticas de una lámina de $MAPbI_3$. Dependencia espectral de la parte real (a) e imaginaria (b) del índice de refracción complejo de láminas de perovskita $MAPbI_3$ fabricados en el Instituto de Ciencia de Materiales de Sevilla (curvas azules), el École Polytechnique Fédérale de Lausanne (curvas negras) y la Universidad de Oxford (líneas rojas).

Descripción óptica de celdas solares de perovskita

En este capítulo se calculó el comportamiento óptico de una CSP gracias al empleo del modelo óptico basado en el TMM. En particular, se comenzó estudiando una CSP mesostructurada en la que se utilizó Al_2O_3 como andamio para soportar la perovskita. Como se puede observar en la Figura 13, el cálculo reprodujo fielmente los espectros obtenidos experimentalmente.

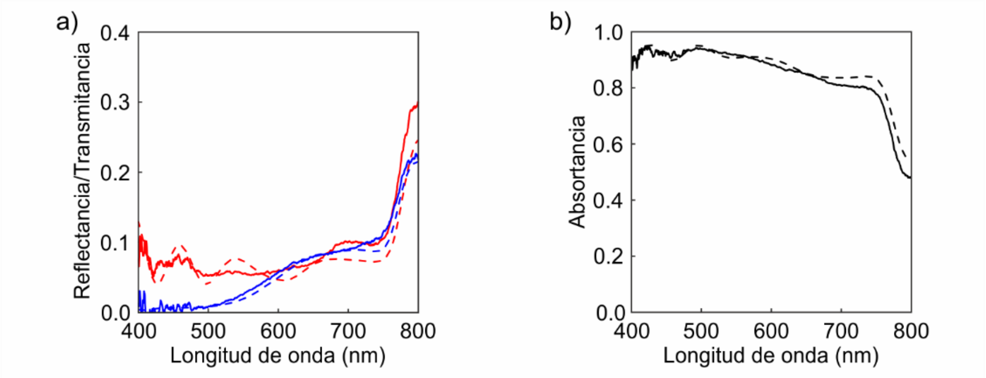

Figura 13. Reflectancia, transmitancia y absortancia de una CSP. a) Espectros de reflectancia (curvas rojas) y transmitancia (curvas azules) calculados (curvas punteadas) y medidos experimentalmente (curvas sólidas) de una CSP. b) Absortancia total del dispositivo calculada a partir de la expresión 1-R-T.

Finalmente se procedió a caracterizar y modelizar una CSP en la que la eficiencia superaba el 20%, un valor que se considera puntero en el campo. Gracias a las virtudes del modelo óptico empleado, se pudo estimar cómo se distribuye la intensidad de campo eléctrico en el interior del dispositivo. Con ello, se procedió a diferenciar la fracción de luz incidente que era empleada por la perovskita para dar lugar a corriente de aquella que se desaprovechada en forma de absorción parasítica. Como se ve en la Figura 14, la corriente extraída del dispositivo crecía a medida que se aumentaba el grosor de la capa de perovskita en el sistema, hasta saturar en un valor de corriente a cortocircuito de 22.5 $mA\cdot cm^{-2}$. De hecho, los valores son tan altos como los límites termodinámicos establecidos por la teoría de Shockley-Queisser estiman que pueden llegar a ser idealmente.[42]

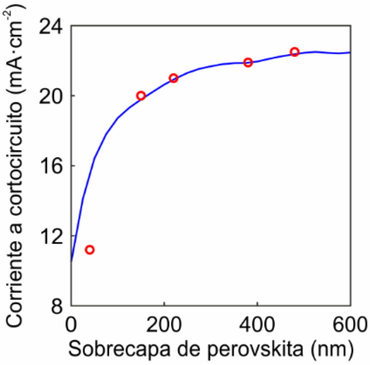

Figure 14. Corriente de una CSP en función del grosor de la capa de perovskita. Corriente a cortocircuito calculada (curva azul) y medida (círculos rojos) en una CSP en la que el grosor de la sobrecapa de perovskita es variado. La arquitectura del dispositivo considerada fue: 1 mm de sustrato de vidrio, 650 nm de FTO, 50 nm de TiO_2 compacta, 85 nm de un andamio de TiO_2 con una porosidad del 50% completamente infiltrado de perovskita $FA_{0.85}MA_{0.15}Pb(I_{0.85}Br_{0.15})_3$, 600 nm de sobrecapa de perovskita $FA_{0.85}MA_{0.15}Pb(I_{0.85}Br_{0.15})_3$, 240 nm de Spiro-OMeTAD, y 50 nm de contacto de oro.

Optimización óptica de celdas solares de perovskita mono-unión y tándem

Diseño óptico de celdas solares basadas en perovskitas $MASn_xPb_{1-x}I_3$

El máximo ideal de eficiencia que se puede obtener de un dispositivo fotovoltaico depende del rango espectral de luz solar que es capaz de absorber el material que conforma la celda, en este caso la perovskita.[42] En particular, para maximizar la capacidad que tienen las perovskitas ABX_3 de transformar la radiación solar en corriente, su borde de absorción ha de desplazarse hacia el rojo, pasando de estar situado a una energía E=1.6 eV a una energía E=1.34 eV. Con tal objetivo en mente, la única aproximación existente hasta la fecha consiste en modificar la composición química de la perovskita mediante la substitución parcial o total del plomo presente en la estructura por estaño. El resultado es una perovskita de composición $MASn_xPb_{1-x}I_3$ en la que la evolución del borde de absorción es el que se muestra en la Figura 15a. Con ello, y siguiendo el protocolo presentado en la sección anterior, se extrajeron las constantes ópticas de la serie de láminas de perovskitas de diferente composición.

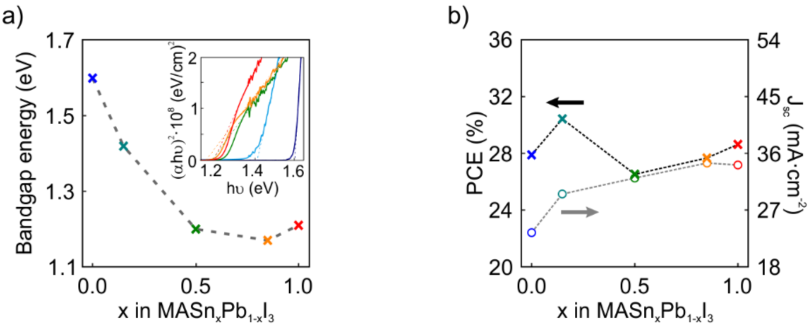

Figura 15. Evolución del borde de absorción en láminas de $MASn_xPb_{1-x}I_3$. a) Energía a la que se encuentra el borde de absorción de perovskitas en las que la relación plomo-estaño se modifica gradualmente: 0% Sn (azul), 15% Sn (azul verde), 50% Sn (verde), 85% Sn (naranja), and 100% Sn (rojo). La línea gris punteada actúa como guía para facilitar la comprensión de la figura. En el recuadro insertado se muestra las gráficas Tauc empleadas para estimar el borde de absorción de los materiales. b) Eficiencia y corriente a cortocircuito calculadas para celdas basadas en perovskitas $MASn_xPb_{1-x}I_3$ con la siguiente arquitectura: 1 mm de sustrato de vidrio, 650 nm de FTO, 50 nm de TiO_2 compacta, 85 nm de un andamio de TiO_2 con una porosidad del 50% completamente infiltrado de perovskita, 600 nm de sobrecapa de perovskita, 240 nm de Spiro-OMeTAD, y 50 nm de contacto de oro.

Mediante el empleo del modelo óptico, se estimó el comportamiento óptico de dispositivos solares basados en estas perovskitas de catión metálico mixto. Con ello se pudo concluir, por ejemplo, que una celda compuesta de una perovskita en la que un 15% de plomo es sustituido por estaño podría sobrepasar el 30% de eficiencia (ver Figura 15b). Esto supondría un incremento considerable si se compara con el 28% de eficiencia ideal para una celda compuesta de una perovskita puramente de plomo.

Celdas solares tándem perovskita/perovskita

Uno de los resultados más importantes extraídos del análisis óptico de las perovskitas $MASn_xPb_{1-x}I_3$ es que cuando el porcentaje de estaño llegó al 85%, se encontró que el borde de absorción presentaba su máximo desplazamiento hacia el infrarrojo (E=1.16 eV). Esto abrió la puerta a proponer una arquitectura tándem en la que dos perovskitas cuyos bordes de absorción se complementan dan lugar a dispositivos con una eficiencia mayor que la máxima alcanzable en una mono-unión. En concreto se propuso un diseño en el que una celda frontal basada en $MAPbI_3$ se combinó con una celda trasera basada en $MAS_{n0.85}Pb_{0.15}I_3$ conectadas en serie. En esta configuración resulta esencial establecer cuáles son los grosores de las diferentes capas de forma que la fracción absorbida en cada subcelda dé lugar a la misma corriente eléctrica. En la Figura 16 se pueden observar los pares de grosores de las láminas de perovskita que componen una celda solar tándem para los que se encuentra una diferencia de fotocorriente generada nula. Con ello se estimó que si la lámina de $MAPbI_3$ era de 240 nm y la de $MAS_{n0.85}Pb_{0.15}I_3$ era de 600 nm, la eficiencia del dispositivo podría alcanzar un 31%.

Finalmente, en este capítulo se analizaron una serie de materiales que se han empleado para fabricar CSPs con el objetivo de proponer un diseño optimizado de una celda solar tándem perovskita/perovskita que podría alcanzar, teniendo en cuenta todas las pérdidas ópticas, un 33.3% de eficiencia.

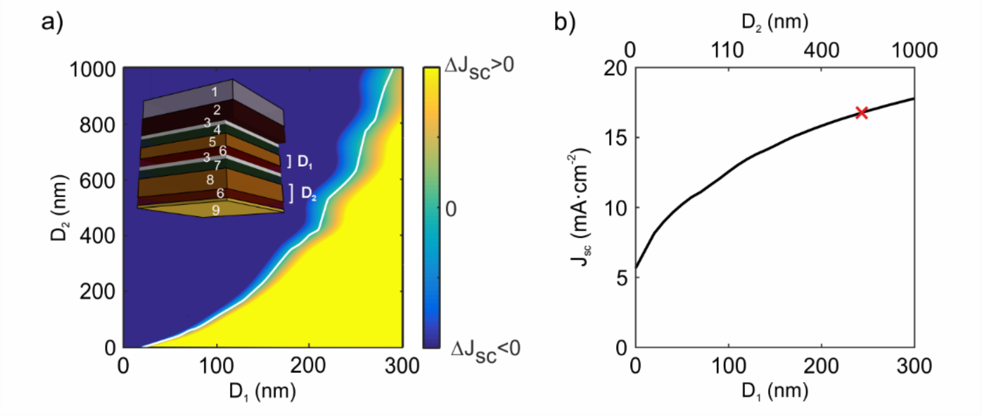

Figura 16. Condiciones para las que las fotocorrientes generadas en una celda frontal y trasera sean coincidentes. a) Diferencia de corriente extraída de una celda frontal y una trasera que componen un dispositivo tándem con la siguiente arquitectura: 1 mm de sustrato de vidrio (1), 650 nm de FTO (2), 50 nm de TiO_2 compacta (3), 85 nm de un andamio de TiO_2 con una porosidad del 50% completamente infiltrado de $MAPbI_3$ (4), D_1 nm de sobrecapa de $MAPbI_3$ (5), 240 nm de Spiro-OMeTAD (6), (3), 85 nm de un andamio de TiO_2 con una porosidad del 50% completamente infiltrado de $MASn_{0.85}Pb_{0.15}I_3$ (7), D_2 nm of $MASn_{0.85}Pb_{0.15}I_3$ capping layer (8), 240 nm of Spiro-OMeTAD (6), and 50 nm of gold contact (9). b) Valores de fotocorriente para cada par de grosores D_1-D_2. La marca roja señala la configuración discutida en el texto (D_1=240 nm and D_2=600 nm). J_{sc} hace referencia a corriente a cortocircuito, por su nomenclatura en inglés.

Celdas solares de perovskita con color estructural

En este capítulo se presenta un método para proveer de color las CSPs. Al contrario de los anteriores capítulos en los que se buscó aumentar el rendimiento del dispositivo desde un aumento de su eficiencia, en este caso se busca otorgarle nuevas cualidades estéticas. Esto es definitivo para su posible integración en elementos cotidianos como son los edificios, lo que daría lugar a un ahorro en los costes de producción semejantes a aquellos logrados a través de un aumento de eficiencia.[43]

La estrategia que se siguió consistió en nanoestructurar el andamio de la CSP en forma de un cristal fotónico. Para ello se diseñó una novedosa técnica que permitió combinar capas de TiO_2 y SiO_2 de forma periódica en las que la porosidad era controlada de forma precisa (ver Figura 17).

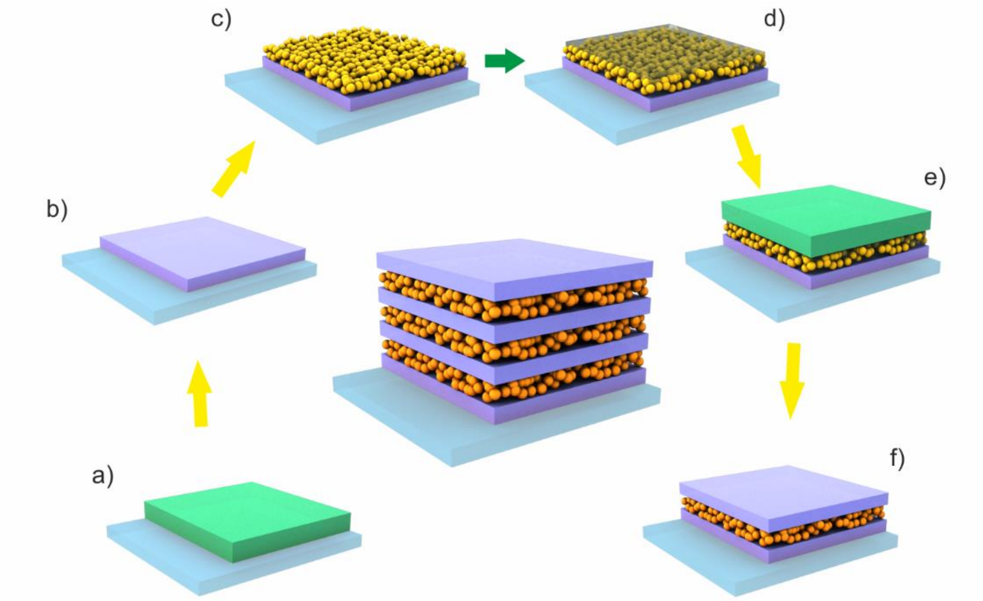

Figura 17. Esquema del proceso de fabricación de un cristal fotónico que combina capas de SiO_2 porosas y capas de TiO_2 cuasidensas. a) Deposición de capa de TiO_2. b) Tratamiento térmico a 500ºC. c) Deposición de nanopartículas de SiO_2. d) Infiltración de poliestireno en la capa de SiO_2. e) Deposición de capa de TiO_2. f) Tratamiento térmico a 500ºC. Una repetición secuencial de estos pasos da lugar a la formación de un cristal fotónico unidimensional.

Tras infiltrar perovskita $MAPbI_3$ en la estructura fotónica y cerrar la CSP, se observó que esta adquiría color sintonizable en todo el espectro visible mientras que mantenía la eficiencia por encima del 5%, alcanzando un máximo cercano al 9% en el azul. Estos valores nunca antes se habían logrado en el campo y supusieron la demostración de las primeras CSPs azules, verdes, amarillas y naranjas con altas eficiencias (ver Figura 18). La caracterización y modelización óptica de los dispositivos permitió concluir que efectivamente el color obtenido era consecuencia de la reflexión producida por el cristal fotónico. Este a su vez modificaba la respuesta espectral de la fotocorriente de la celda de manera que, en los rangos donde se reflejaba la luz, la generación de corriente se reducía por el hecho de darse una menor absorción de fotones. Por otro lado, se analizaron los procesos de inyección y recombinación de carga. Con ello se pudo concluir que la transferencia de carga en el andamio nanoestructurado tenía lugar a través de sucesivos pasos en los que los electrones pasaban de la banda de conducción de la perovskita a la de la TiO_2 y viceversa.

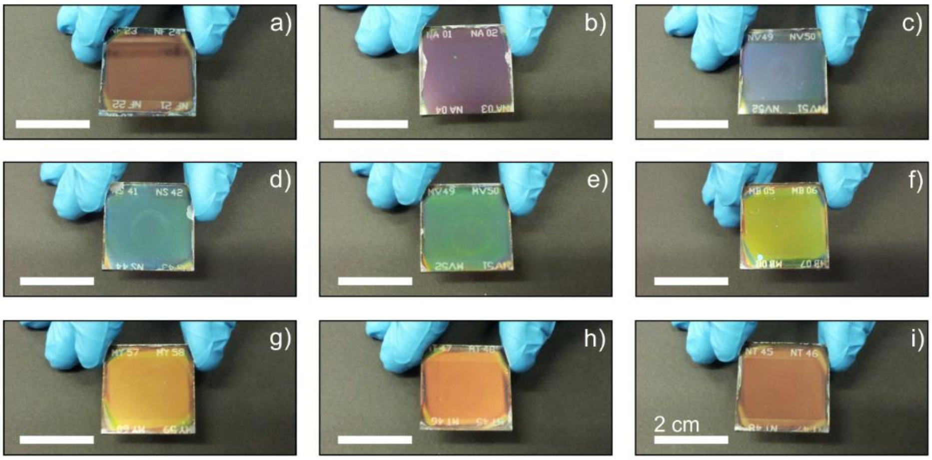

Figura 18. Imágenes tomadas con una cámara digital de CSP incorporando cristales fotónicos diseñados para dar lugar a colores cubriendo todo el espectro visible.

Efectos de confinamiento cuántico fuerte en nanocristales de perovskita sintetizados en andamios mesoporosos

Para ciertas aplicaciones, como la obtención de materiales óptimos para dispositivos tándem o dispositivos emisores de luz, se hace necesario desplazar el borde de absorción de la perovskita hacia el azul. Tradicionalmente, la estrategia empleada consiste en modificar la composición química del material mediante la mezcla de haluros. Si bien de esta manera se logra el objetivo perseguido, la estabilidad de los materiales es muy limitada debido a la aparición de procesos fotoinducidos de segregación de fase.[44-46] En este último capítulo se propuso la síntesis de nanocristales de perovskita $MAPbI_3$ con tamaños en el orden del radio de Bohr de su excitón, entrando en el régimen de confinamiento cuántico fuerte. Esto daría lugar a un desplazamiento hacia el azul en el borde de absorción del material sin necesidad de cambiar la composición química del mismo, asegurándose así su estabilidad en el tiempo. Para ello se sintetizó la perovskita $MAPbI_3$ dentro de una red tridimensional de poros existente en láminas de TiO_2 tal y como se indica en la Figura 19.

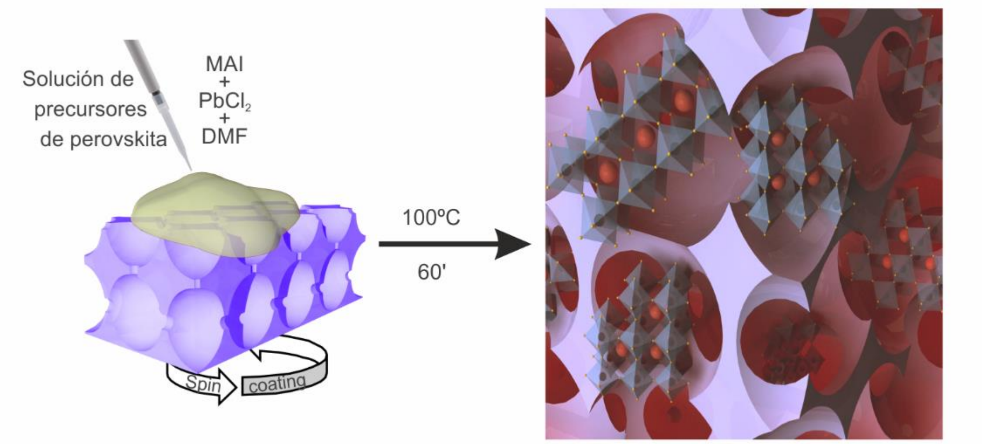

Figura 19. Formación de nanocristales de perovskita $MAPbI_3$ en el interior de nanoreactores.

Se encontró que el tamaño de los nanocristales de perovskita estaba dictado por el tamaño de los poros en los que era sintetizada. Con ello se controló su tamaño para que este fuera de entre 1 nm y 5 nm de radio, lo que se tradujo en un control a la carta en las propiedades ópticas del material. Tanto su borde de absorción como su pico de fotoluminiscencia se desplazaron hacia el azul a medida que el tamaño decrecía, tal y como se muestra en la Figura

20. De hecho, se pudo comprobar que los fenómenos observados seguían la ecuación de Brus que describe cómo se modifica el borde de absorción de un nanocristal de semiconductor a medida que su radio se ve reducido.

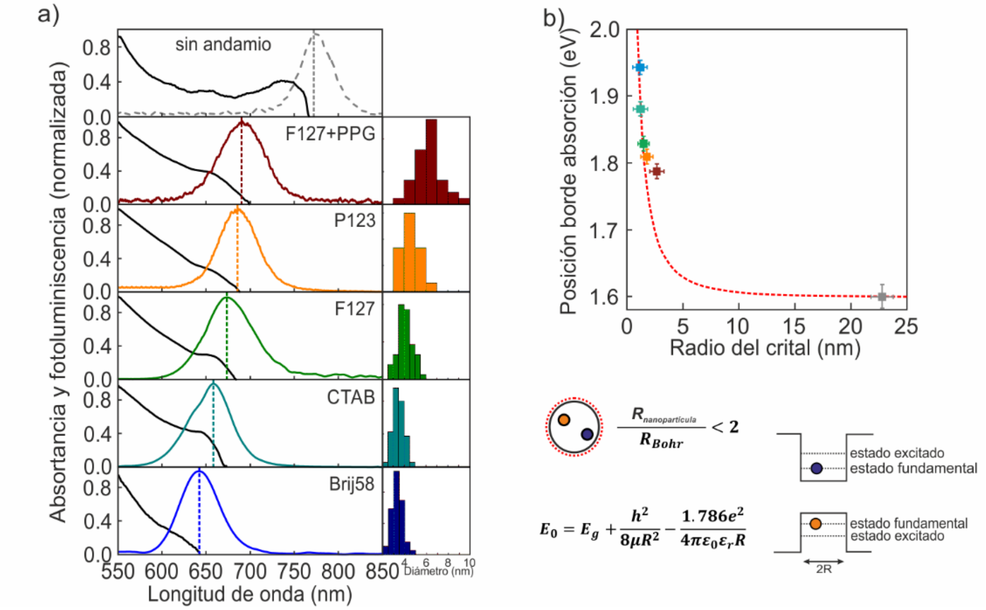

Figura 18. Desplazamiento hacia el azul del borde de absorción de nanocristales de $MAPbI_3$. a) Espectros de absortancia (curvas negras) y fotoluminiscencia (curvas coloreadas) de nanocristales de $MAPbI_3$ sintetizados fuera de andamio (gris), y dentro de un andamio mesostructurado donde el tamaño de poro viene dictado por el uso de los siguientes surfactantes: F127+PPG (curva roja), P123 (curva naranja), F127 (curva verde), CTAB (curva azul verde) y Brij58 (curva azul). Se acompaña el panel con histogramas de distribución de tamaño del nanocristal para cada caso. b) Posición espectral del borde de absorción frente al radio del nanocristal de perovskita $MAPbI_3$ crecidos en láminas de TiO2 de diferente tamaño de poro (el código de color de la Figura 18a se conserva). La línea roja punteada representa el ajuste de la dispersión de puntos a la ecuación de Brus, de la cual se incluye un panel explicativo abajo.

A lo largo del capítulo se mostró cómo esta técnica puede ser extendida al uso de andamios con diferentes composiciones, lo cual influye directamente en el comportamiento óptico del sistema. Además, se demostró que esta estrategia permite conservar las propiedades de los nanocristales a lo largo del tiempo ya que el andamio actúa como encapsulante, aislando el semiconductor de la atmósfera externa. Finalmente, se incluyó una serie de medidas ópticas en la microescala que permitieron concluir que el procedimiento propuesto en el capítulo da lugar a láminas de nanocristales de $MAPbI_3$ confinados de una alta calidad óptica. Esto supuso la apertura de un amplio abanico de posibilidades para proponer estos compuestos para su integración en dispositivos optoelectrónicos.

Referencias

1 Paris Agreement, 21st Conference of the Parties, European Commission **2015**.

2 World energy outlook, *International Energy Agency* **2016**.

3 Perez, R.; Perez, M. A fundamental look at supply side energy reserves for the planet. *The IEA SHC Solar Update* **2015**, *62*, 4–6.

4 Top 10 Emerging Technologies of 2016. *World Economic Forum* **2016**.

5 Onoda-Yamamuro, N.; Matsuo, T.; Suga, H. Dielectric study of $CH_3NH_3PbX_3$ (X = Cl, Br, I). *J. Phys. Chem. Solids.* **1992**, *53*, 935–939.

6 Stoumpos, C. C.; Malliakas, C. D.; Kanatzidis, M. G. Organic tin and lead iodide perovskites with organic cations: unique semiconductors, with phase transitions and near-infrared photoluminescent properties. *Inorg. Chem.* **2013**, *52*, 9019–9038.

7 Baikie, T.; Fang, Y.; Kadro, J. M.; Schreyer, M.; Wei, F.; Mhaisalkar, S. G.; Graetzel, M.; White, T. J. Synthesis and crystal chemistry of the hybrid perovskite $(CH_3NH_3)PbI_3$ for solid-state sensitised solar cell applications. *J. Mater. Chem. A.* **2013**, *1*, 5628–5641.

8 Anaya, M.; Lozano, G.; Calvo, M. E.; Zhang, W.; Johnston, M. B.; Snaith, H. J. Optical description of mesostructured organic-inorganic halide perovskite solar cells. *J. Phys. Chem. Lett.* **2015**, *6*, 48–53.

9 Stranks, S. D.; Eperon, G. E.; Grancini, G.; Menelaou, C.; Alcocer, M. J. P.; Leijtens, T.; Herz, L. M.; Petrozza, A.; Snaith, H. J. Electron-hole diffusion lengths exceeding Micrometer in an Organometal Trihalide Perovskite Absorber. *Science* **2014**, *342,* 341–344.

10 Deschler, F.; Price, M.; Pathak, S.; Klintberg, L. E.; Jarausch, D.; Higler, R.; Hu, S.; Leijtens, T.; Stranks, S. D.; Snaith, H. J.; Atatüre, H. J.; Philips, R. T.; Friends, R. H. High photoluminescence efficiency and optically pumped lasing in solution-processed mixed halide perovskite semiconductors. *J. Phys. Chem. Lett.* **2015**, *5*, 1421–1426.

11 Xing, G.; Mathews, N.; Lim, S. S.; Yantara, N.; Liu, X.; Sabba, D.; Grätzel, M.; Mhaisalkar, S.; Sum, T. C. Low-temperature solution-processed wavelength-tunable perovskites for lasing. *Nat. Mater.* **2014** *13*, 476–480.

12 Tan, Z.-K.; Moghaddam, R. S.; Lai, M. L.; Docampo, P.; Higler, R.; Deschler, F.; Price, M.; Sadhanala, A.; Pazos, L. M.; Credgington, D.; Hanusch, F.; Bein, T.; Snaith, H. J.; Friend, R. H. Bright light-emitting diodes based on organometal halide perovskite. *Nat. Nanotechnol.* **2014**, *9*, 687–692.

13 Cho, H.; Jeong, S.; Park, M.; Kim, Y.; Wolf, C.; Lee, C.; Heo, J. H.; Sadhanala, A.; Myoung, N.; Yoo, S.; Im, S. H.; Friend, R. H.; Lee, T.-W. Overcoming the electroluminescence efficiency limitations of perovskite light-emitting diodes. *Science* **2015**, *350*, 1222–1225.

14 Lee, M. M.; Teuscher, J.; Miyasaka, T.; Murakami, T. N.; Snaith, H. J. Efficient hybrid solar cells based on meso-superstructured organometal halide perovskites. *Science* **2012**, *338*, 643–647.

15 Huang, L.; Li, C.; Sun, X.; Xu, R.; Du, Y.; Ni, J.; Cai, H.; Li, J.; Hu, Z.; Zhang, J. Efficient and hysteresis-less pseudo-planar heterojunction perovskite solar cells fabricated by a facile and solution-saving one-step dip-coating method. *Org. Electron. Physics Mater. Appl.* **2017**, *40*, 13–23.

16 Huang, L.; Li, C.; Sun, X.; Xu, R.; Du, Y.; Ni, J.; Cai, H.; Li, J.; Hu, Z.; Zhang, J. Efficient and hysteresis-less pseudo-planar heterojunction perovskite solar cells fabricated by a facile and solution-saving one-step dip-coating method. *Org. Electron. Physics Mater. Appl.* **2017**, *40*, 13–23.

17 Liu, M.; Johnston, M. B.; Snaith, H. J. Efficient planar heterojunction perovskite solar cells by vapour deposition. *Nature* **2013**, *501*, 395–398.

18 Xiao, M.; Huang, F.; Huang, W.; Dkhissi, Y.; Zhu, Y.; Etheridge, J.; Gray-Weale, A.; Bach, U.; Cheng, Y. B.; Spiccia, L. A fast deposition-crystallization procedure for highly efficient lead iodide perovskite thin-film solar cells. *Angew. Chemie Int. Ed.* **2014**, *53*, 9898–9903.

19 Jeon, N. J.; Noh, J. H.; Kim, Y. C.; Yang, W. S.; Ryu, S.; Seok, S. l. Solvent engineering for high-performance inorganic-organic hybrid perovskite solar cells. *Nat. Mater.* **2014**, *13*, 1–7.

20 Pettersson, L. A. A.; Roman, L. S.; Inganäs, O. Modelling photocurrent action spectra of photovoltaic devices based on organic thin films. *J. Appl. Phys.* **1999**, *487*, 487–496.

21 Burkhard, G. F.; Hoke, E. T.; McGehee, M. D. Accounting for interference, scattering, and electrode absorption to make accurate internal quantum efficiency measurements in organic and other thin solar cells. *Adv. Mater.* **2010**, *22*, 3293–3297.

22 Lozano, G.; Colodrero, S.; Caulier, O.; Calvo, M. E.; Míguez, H. Theoretical analysis of the performance of one-dimensional photonic crystal-based dye-sensitized solar cells. *J. Phys. Chem. C* **2010**, *114*, 3681–3687.

23 Chang, J.-H.; Wang, H.-F.; Lin, W.-C.; Chiang, K.-M.; Chen, K.-C.; Huang, W.-C.; Huang, Z.-Y.; Meng, H.-F.; Ho, R.-M.; Lin, H.-W. Efficient inverted quasi-bilayer organic solar cells fabricated by using non-halogenated solvent processes. *J. Mater. Chem. A* **2014**, *2*, 13398–13406.

24 Enrique Galvez, F.; Kemppainen, E.; Míguez, H.; Halme, J. Effect of diffuse light scattering designs on the efficiency of dye solar cells: an integral optical and electrical description. *J. Phys. Chem. C* **2012**, *116*, 11426-11433.

25 Miranda-Muñoz,J. M.; Carretero-Palacios, S.; Jiménez-Solano, A.; Li, Y.; Lozano, G.; Míguez, H. Efficient bifacial dye-sensitized solar cells through disorder by design. *J. Mater. Chem. A* **2016**, *4*, 1953-1961.

26 Derkacs, D.; Lim, S. H.; Matheu, P.; Mar, M.; Yu, E. T. Improved performance of amorphous silicon solar cells via scattering from surface plasmon polaritons in nearby metallic nanoparticles. *Appl. Phys. Lett*. **2006**, *89*, 093103.

27 Brown, M. D.; Suteewong, T.; Kumar, R. S.; D'Innocenzo, V.; Petrozza, A.; Lee, M. M.; Wiesner, U.; Snaith, H. J. Plasmonic dye-sensitized solar cells using core−shell metal−insulator nanoparticles. *Nano Lett.* **2011**, *11*, 438–445.

28 Yin, J.; Qu, H.; Cao, J.; Tai, H.; Li, J.; Zheng, N. Light absorption enhancement by embedding submicron scattering TiO_2 nanoparticles in perovskite solar cells. *RSC Adv*. **2016**, *6*, 24596-24602.

29 Zhang, W.; Saliba, M.; Stranks, S. D.; Sun, Y.; Shi, X.; Wiesner, U.; Snaith, H. J. Enhancement of perovskite-based solar cells employing core–shell metal nanoparticles. *Nano Lett.* **2013**, *13*, 4505–4510.

30 Saliba, M.; Zhang, W.; Burlakov, V. M.; Stranks, S. D.; Sun, Y.; Ball, J. M.; Johnston, M. B.; Goriely, A.; Wiesner, U.; Snaith, H. J. Plasmonic-induced photon recycling in metal halide perovskite solar cells. *Adv. Func. Mater.* **2015**, *25*, 5038-5046.

31 Jang, S.; Yoon, J.; Ha, K.; Kim, M.; Kim, D. H.; Kim, S. M.; Kang, S. M.; Park, S. J.; Jung, H. S.; Choi, M.. Facile fabrication of three-dimensional TiO_2 structures for highly efficient perovskite solar cells. *Nano Energy* **2016**, *22*, 499–506.

32 Kang, S. M.; Jang, S.; Lee, J. K.; Yoon, J.; Yoo, D. E.; Lee, J. W.; Choi, M.; Park, N. G. Moth-eye TiO_2 layer for improving light harvesting efficiency in perovskite solar cells. *Small* **2016**, *12*, 2443–2449.

33 Paetzold, U. W.; Qiu, W.; Finger, F.; Poortmans, J.; Cheyns, D. Nanophotonic front electrodes for perovskite solar cells. *Appl. Phys. Lett.* **2015**, *106*, 173101.

34 Colonna, D.; Colodrero, S.; Lindstrom, H.; Di Carlo, A.; Míıguez, H. Introducing structural colour in DSCs by using photonic crystals: interplay between conversion efficiency and optical properties. *Energy Environ. Sci.* **2012**, *5*, 8238-8243.

35 Li, Y.; Calvo, M. E.; Míguez, H. Integration of photonic crystals into flexible dye solar cells: a route toward bendable and adaptable optoelectronic devices displaying structural color and enhanced efficiency. *Adv. Opt. Mater.* **2016**, *4*, 464-471

36 Anaya, M.; Calvo, M. E.; Luque-Raigón, J. M.; Míguez, H. Resonant Photocurrent Generation in Dye-Sensitized Periodically Nanostructured Photoconductors by Optical Field Confinement Effects. *J. Am. Chem. Soc.* **2013**, *135*, 7803-7806.

37 Xiao, M.; Huang, F.; Huang, W.; Dkhissi, Y.; Zhu, Y.; Etheridge, J.; Gray-Weale, A.; Bach, U.; Cheng, Y-B.; Spiccia, L. A Fast Deposition-Crystallization Procedure for Highly Efficient Lead Iodide Perovskite Thin-Film Solar Cells. *Angew. Chem.* **2014**, 53, 9898-9903.

38 Löper, P.; Stuckelberger, M.; Niesen, B.; Werner, J.; Filipič, M.; Moon, S.-J.; Yum, J.-H.; Topič, M.; De Wolf, S.; Ballif, C. Complex Refractive Index Spectra of $CH_3NH_3PbI_3$ Perovskite Thin Films Determined by Spectroscopic Ellipsometry and Spectrophotometry. *J. Phys. Chem. Lett.* **2015**, *6*, 66-71.

39 Jiménez-Solano, A.; Anaya, M.; Calvo, M. E.; Alcon-Camas, M.; Alcañiz, C.; Guillén, E.; Martínez, N.; Gallas, M.; Preussner, T.; Escobar-Galindo, R; Míguez, H. Aperiodic Metal-Dielectric Multilayers as Highly Efficient Sunlight Reflectors. *Adv. Opt. Mater*. **2017**, *9*, 1600833

40 Forouhi, A.; Bloomer, I. Optical dispersion relations for amorphous semiconductors and amorphous dielectrics. *Phys. Rev. B* **1986**, *34*, 7018−7026.

41 JobinYvon New Amorphous Dispersion Formula. http://www.horiba.com/fileadmin/uploads/Scientific/Downloads/OpticalSchool_CN/TN/ellipsometer/New_Amorphous_Dispersion_Formula.pdf.

42 Shockley, W.; Queisser, H. J. *J. Appl. Phys.* **1961**, *32*, 510-519.

43 Henemann, A. BIPV: Built-in solar energy. *Renewable Energy Focus* **2008**, *9*, 14-19.

44 Slotcavage, D. J.; Karunadasa, H. I.; McGehee, M. D. Light-induced phase segregation in halide-perovskite absorbers. *ACS Energy Lett.* **2016**, 1, 1199.

45 Brivio, F.; Caetano, C.; Walsh, A. Thermodynamic origin of photoinstability in the $CH_3NH_3Pb(I_{1-x}Br_x)_3$ hybrid halide perovskite alloy. *J. Phys. Chem. Lett.* **2016**, 7, 1083.

46 Barker, A.J.; Sadhanala, A.; Deschler, F.; Gandini, M.; Senanayak, S. P.; Pearce, P. M.; Mosconi, E.; Pearson, A. J.; Wu, Y.; Kandada, A. R. S.; Leijtens, T.; De Angelis, F.; Dutton, S. E.; Petrozza, A.; Friend, R. H. Defect-assisted photoinduced halide segregation in mixed-halide perovskite thin films. *ACS Energy Lett.* **2017**, 2, 1416.

Agradecimientos

Mis primeras palabras de agradecimiento no pueden sino ir dirigidas a mis directores de tesis, mis queridos Hernán y Mauricio. Vuestra confianza en mí desde el primer día, vuestras enseñanzas y vuestra guía me han llevado en volandas hasta este punto y seguido de mi vida como científico. Hernán, tú eres el artífice de algo muy especial que se llama Grupo de Materiales Ópticos Multifuncionales. Siempre te estaré agradecido por dejarme ser partícipe de él, por citarme aquel lunes de Semana Santa de 2011 que yo pensaba pasar con mi familia. Nunca pensé que anular aquel viaje a casa me iba a cambiar la vida hasta tal punto que ahora mi hogar es Sevilla. Sin lugar a dudas eres la persona que más ha influido en el Miguel científico. Eres mi ejemplo y he tratado de asimilar todo lo que me has dicho, por minúsculo que fuera. Mauricio, Coco, tú has sido el equilibrio imprescindible para lograr lo que hemos logrado juntos. Tan sabio como relativizador, ha sido una suerte contar con tu infinito conocimiento. Tú has canalizado mi energía y puesto la cordura en los momentos difíciles. Hernán, Mauricio: os admiro; mucho. Mi singularidad como científico, de existir, es gracias a la combinación de vuestras personalidades y cualidades.

A lo largo de estos años de investigación hay dos personas que destacan en mi carrera por su labor como mentores: Gabriel y Juan. Huelga decir que vosotros habéis sido mucho más que unos *postdocs* al uso –dentro de poco esa situación laboral cambiará para bien, como no podía ser de otra manera–. Vosotros me habéis enseñado y apoyado mucho más de lo que iba con vuestro cargo. Más allá de vuestra indudable calidad como científicos, no es fácil encontrar en este mundo competitivo personas con los valores que vosotros representáis. Quiero decir que esa manera de ser no se puede practicar; vosotros la tenéis innata. Gracias por todo.

Alberto, amigo, compañero de tesis. Hemos hecho este camino juntos, de principio a fin, y no me imagino nadie mejor con quien pudiera haberlo hecho. Eres el motor optimizador del grupo y el adalid del buen hacer. Es increíble cómo dos personas tan diferentes pueden llegar a aguantarse tantas horas. Gracias por estar ahí. Andrea: dos años compartiendo contigo ciencia y vida han sido más que suficientes para saber que siempre serás mi amigo. Tú, como Coco, me has aliviado las *palpitations* en multitud de ocasiones. *Grazie mille*. Gracias al resto de integrantes del MOM que están y que he visto pasar. Todos me habéis ayudado. Me acuerdo especialmente de dos Joses: JR y JM3, artistas.

En el Instituto de Ciencia de Materiales de Sevilla he tenido la oportunidad de departir sobre ciencia con grandes investigadores. Me gustaría agradecer en particular a Manuel y Juan Pedro que me hayan brindado el honor de aprender de ellos. Quiero expresar también mi gratitud a todos los colaboradores científicos que he tenido en el transcurso de estos años: Henry, Anders, Iván y Juanpa en particular. Gracias a todo el personal del cicCartuja y de la Universidad de Sevilla; sé que no he sido precisamente una persona que no haya dado mucho trabajo. Gracias al CITIUS, en especial a Paco Varela por su incansable labor.

Todo lo que he plasmado en esta tesis doctoral no sería lo que es sin las personas que he mencionado, pero tampoco lo podría haber logrado fuera del contexto que ha supuesto para mí la ciudad de Sevilla. En ella he encontrado un grupo de personas maravilloso con las que he madurado y he pasado los mejores momentos de mi vida. He tenido la inmensa fortuna de encontrar una segunda familia más allá de la sangre: María José, Gabri, Laura, Alberto y Andrea. Pero por encima de todos –seguro que lo comprendéis– Martín. He llorado escribiendo estas líneas solo de pensar en lo que os echaré de menos. Mi afecto sincero para Lilian, Miriam y Javi. Estupendos científicos, humanistas, contadores de historias. Esta tesis no se entiende sin las incontables horas en la calle con vosotros y el resto de la gente del Puma. Me acuerdo de vosotros siempre. Y como no, en estas palabras no pueden faltar mi *fratello* Pietro, Moli, Arias y el Ohio B al completo. Amigos de toda la vida que siempre están ahí cuando hacen falta.

Tengo la suerte de tener una familia enorme que me quiere y a la que yo quiero. Estos años os he visto mucho menos de lo que hubiera querido; os agradezco vuestra comprensión y apoyo. Ángel, eres mi hermano y mi mejor amigo. Nunca me has fallado y sé que nunca lo vas a hacer. Eres de las pocas personas que realmente admiro por sus valores y actitud en la vida. Aprendo mucho de ti. Papá, mi personalidad tiene de ti mucho más de lo que crees. Me

has enseñado a saber regatear los envites con torería. Por algo mi nombre “artístico” es el que es.

Finalmente me gustaría manifestar mucho más que agradecimiento a los dos amores de mi vida: mi madre y Elena. Mamá, quiero que sepas que nunca podré devolverte todo tu esfuerzo y dedicación para conmigo. Siempre has sido imprescindible para mí y en estos años de tesis no lo has sido menos. Todos los pasos que voy dando en mi vida tú ya los tenías en mente y has trabajado lo indecible para que logre siempre mis metas. Elena: compañera de viaje, gran científica, amiga y amor infinito. Sin ti no podría haber llegado al final de este camino, imposible. Te quiero, gracias por todo.

Hay que seguir…

UNIVERSIDAD DE SEVILLA

CSIC
CONSEJO SUPERIOR DE INVESTIGACIONES CIENTÍFICAS

MOM
mom.icmse.csic.es

Multifunctional
Optical
Materials
Group

Institute of Materials Science of Seville